ON ENERGY HARVESTING FROM OPEN CHANNEL WATER FLOWS USING PASSIVELY OSCILLATING HYDROFOILS

MUHAMMAD NAFEES MUMTAZ QADRI

PhD

THE HONG KONG POLYTECHNIC UNIVERSITY

2018

The Hong Kong Polytechnic University

Department of Mechanical Engineering

ON ENERGY HARVESTING FROM OPEN CHANNEL WATER FLOWS USING PASSIVELY OSCILLATING HYDROFOILS

MUHAMMAD NAFEES MUMTAZ QADRI

A thesis submitted in partial fulfilment of the requirements for the degree of Doctor of Philosophy

November 2017

CERTIFICATE OF ORIGINALITY

I hereby declare that this thesis is my own work and that, to the best of my knowledge and belief, it reproduces no material previously published or written, nor material that has been accepted for the award of any other degree or diploma, except where due acknowledgement has been made in the text.

________________________________ (Signed)

QADRI, Muhammad Nafees Mumtaz (Name of student)

Dedicated to my maternal grandmother

Mrs. Farkhanda Ishaq (late)

ABSTRACT

Flow energy extraction through flapping foils is a novel concept in the domain of renewable energy. In the past, it was mainly realized using fully or semi prescribed flapping motions, where at least one of the pitching and plunging motions is forced to follow a given profile. Recently, a new type of extractor emerged, which is able to extract flow energy using fully passive flapping motions, i.e., flow-induced pitching and plunging motions. To reveal its underlying fluid-structure interaction (FSI) physics to improve its performance, in this research a prototype equipped with a single flapping hydrofoil was carefully designed, manufactured, and tested in a water tunnel. During the experiments, the hydrofoil's real-time pitching and plunging motions were recorded using two motion sensors, and the instantaneous hydrodynamic forces it experienced were also recorded using a dedicated load cell. With these real-time data, the power and efficiency of the prototype can be evaluated under various conditions. Furthermore, the flow around the hydrofoil was visualized using the laser induced fluorescence (LIF) technique and measured using a time-resolved particle image velocimetry (TR-PIV) system. The flow information was then synchronized with the motion/force information to enable the analysis of FSI physics.

The experimental results revealed that both the pitching and plunging motions of the hydrofoil contributed to the overall energy extraction, and the pitching motion extracted energy only when the hydrofoil underwent the stroke reversal. The energy harvesting performance was observed to increase with the increase of plunging speed and the increase of torque during the stroke reversal. Among all the investigated cases, the device can achieve the best average power coefficient of 1.295 and the best energy extraction efficiency of 60.4%.

The effect of hydrofoil inertia was studied, which was changed by attaching a mass block of different weight. It was found that smaller inertia resulted in a faster plunging motion and a slower stroke reversal. In addition, the effects of the hydrofoil pivot location and pitching amplitude were also investigated in flows of three different free-stream velocities (i.e., U_o = 0.57 m/s, 0.65 m/s and 0.78 m/s). The maximum allowed pitching amplitudes (θ_o) were set at 30°, 43° and 60°, and the pivot location varies between 0.6 and 0.8 chord length from the leading edge. It was found that the hydrofoil

with a higher allowed pitching amplitude generally performed better due to the larger hydrodynamic forces generated from the formation and shedding of a large leading-edge vortex (LEV). The time for stroke reversal decreased as the pivot location increased (i.e., moved away from the leading edge). Energy extraction performance also improved with increase in pivot location distance from leading edge for each pitching amplitude. However, the occasional mismatch in the directions of the transverse force and of the plunging velocity due to the unsteadiness in the flow produced at large allowed pitching amplitudes and increased pivot location led towards lower energy extraction.

The effect of the hydrofoil profile was also studied. Three different foil shapes were chosen: i.e., a flat plate as the baseline, a NACA0006 foil and an elliptical foil. Although manufactured using different materials, these foils have very close total mass. It was found that, at small allowed pitching angels, the change of foil shape did not result in significant change in energy harvesting. But at higher pitching angles, obvious differences were recorded. The low performance of the elliptical foil under all conditions compared to the flat plate and NACA0006 foil was attributed to its relatively sharper leading edge that cause early separation of the LEV, while its trailing edge reduces the interaction between the shedding LEV and the foil surface.

Through this research, a good understanding on the energy extraction performance and FSI physics of a fully passive flow energy extractor was achieved. Although still in its infancy, this device can be further improved in the future research by including foil flexibility, multi-foil configurations etc.

PUBLICATIONS ARISING FROM THE THESIS

CONFERENCE

1. **M. N. Mumtaz Qadri**, H. Tang and Y. Liu, "*Energy Extraction through a Passively Oscillating Hydrofoil*", The 21st Annual Conference of HKSTAM 2017, The 13th Jiangsu-Hong Kong Forum on Mechanics and its Applications, HKPolyU, Hong Kong, April 2017.

2. **M. N. Mumtaz Qadri**, H. Tang and Y. Liu, "*Force and Motion Measurements of a Passively Oscillating Hydrofoil*", 20th Australasian Fluid Mechanics Conference (AFMC), Paper No 448, Perth, Australia, Dec 2016.

3. **M. N. Mumtaz Qadri**, H. Tang, "*Flow Energy Harvesting Using Passively Oscillating Hydrofoils*", 6th Shizuoka University International Symposium, Hamamatsu, Japan, Dec 2016.

JOURNALS

1. **M. N. Mumtaz Qadri**, F. Zhao, H. Tang and Y. Liu, "*Energy Harvesting Performance of a Passively Oscillating Hydrofoil through Force and Motion Measurements*", Renewable Energy, In Preparation (2018).

2. **M. N. Mumtaz Qadri**, F. Zhao, H. Tang and Y. Liu, "*Effect of Pivot location and Pitching amplitude on Energy Harvesting Performance of a Passively Actuated Flapping Hydrofoil under different flow conditions*", Energy, In Preparation (2018).

3. **M. N. Mumtaz Qadri**, F. Zhao, H. Tang and Y. Liu, "*An Experimental Investigation into the Fluid-Solid Interaction of different foil shapes undergoing flapping motion through passive actuation and their effect on Energy Harvesting Performance*", Energy, In Preparation (2018).

ACKNOWLEDGEMENTS

"*Do not let your difficulties fill you with anxiety, after all it is only in the darkest nights that stars shine more brightly.*" **— Hazrat Ali Ibn Abu-Talib A.S**

"*Life consists of two days; one for you, one against you. So, when it's for you don't be proud or reckless, and when it's against you be patient, for both days are test for you.*" **— Hazrat Ali Ibn Abu-Talib A.S**

All praises to Almighty Allah, the creator of the universe, who blessed me with the knowledge and bestowed upon me the will and determination to complete this thesis. All respects to the Holy Prophet Muhammad (May Allah grant peace and honor to him and his family), who is the last messenger and whose life is a perfect model for the whole humanity.

I would like to express my highest respect and profound thanks to my supervisor, Dr. Hui TANG for his kind guidance, support on all fronts, patience and encouragement throughout my Doctoral Research period. I would like to also express my gratitude to my co-supervisor, Dr. Yang LIU for his guidance and support since the early days of my Doctoral Research period.

I am greatly indebted to the DRC chair, Prof Dr. Chih-Yung WEN for his support and encouragement even before coming to Hong Kong, which helped me decide to pursue my Doctoral Research studies in the Mechanical Department at The Hong Kong Polytechnic University. His later support in introducing me to my supervisor deserves the utmost respect which a student, like myself, can give to his teacher.

I am also indebted to Chair Professor San Qiang SHI, Chair Professor Li CHENG and Chair Professor Wallace Woon Fong LEUNG, who served as my temporary chief supervisor and as mentors respectively during my Doctoral Research period as a student and T.A, for their utmost guidance and support.

I would also like to thank the administrative supporting staff of our department's general office under Ms Lily TAM and especially Michelle LAI who worked day and night to support us students in the best way possible. I am very much thankful to Ms Lily TAM for her guidance and support and making time for us whenever possible to listen to our queries and keeping us out of trouble.

I am greatly indebted to the Technical Support staff of the Project Lab of our department including Mr. Jack K. W WONG, Mr. W. C. WOO, Mr. K. K. SHUM and Mr. Max K. F MAN for keeping up to my designs and timetable in the best way possible which enabled me to complete my experiments successfully.

I am thankful to my junior and good friend, Mr. Fuwang ZHAO for his continued support, dedication and hard work to continue this Research Project regarding energy harvesting through flapping foils further and making it as his PhD title. I am also very much indebted to Dr. Bingfu ZHANG and Dr. Shu WANG for their utmost sincerity and guidance throughout my PhD work at the most critical times. I will also not forget the endless eight weeks dedicated by my good friend Mr. Dennis Gallun who helped in laying the foundations in the early stages of this research project including improved design features to the second prototype and data acquisition software for sensor data collection.

I am very thankful to the PolyU Pakistani community and especially Dr. Hafiz Zahoor Ahmad Khan, Dr. Majid Nazeer & family, Dr. Muhammad Bilal & family, Dr. Sawaid Abbas, Mr. Syed Muhammad Irteza, Mr. Ishaq Ahmad, Mr. Adeel Rao Zulfiqar & family, Mr. Muhammad Saleem Sumbal, Dr. Arshad Tipu & family, Dr. Faisal Nouman Baig, Mr. Shakeel Ahmad, Mr. ENGINEER Saad Chugtai & family and Mr. Abdul Mateen Qasim & family from CityU for their utmost sincerity and support during my Doctoral Research Period.

I am very thankful to The Hong Kong Polytechnic University, for awarding me the Teaching Postgraduate Studentship Scheme, which supported and gave me an opportunity to pursue my Doctoral studies.

To my best friends Dr. Aqib Chishty, Dr. Nabeel Qazi, Squadron Leader (Sqd Ldr.) Aamer Shahzad, Dr. Ammar Mushtaq, Dr. Umair Siddique and Dr. Junaid Ahmad Khan and for their sincere support and guidance before and during my Doctoral studies. I also enjoyed Aqib, Aamer bhai and Nabeel bhai's company during my visit to Australia at the 20th AFMC conference in Perth, a gathering not to be forgotten.

I express my indebtedness and my deepest sense of gratitude to my family members including my parents, my younger brother and my extended family for their endless love, moral support, encouragement, and prayers for successful completion of this study.

At last but not the least, I am wholeheartedly indebted to my loving and caring wife Mrs. Mubarak Jaan NAFEES for her endless love, patience and support especially during the dark times in my PhD research. Without her I may not be able to continue my Doctoral degree.

Table of Contents

List of Figures

List of Tables

Nomenclature

U_o	Free stream velocity (m/s)
θ_o	Pitching amplitude (degrees)
x_p	Pivot location (distance from foil's leading edge to where vertical cantilevered shaft is connected
c	Foil's chord length (m)
s	Foil's span length (m)
Re_c	Reynolds number w.r.t chord length
F_x	Body connected force in the chord-wise direction (N)
F_y	Body connected force normal to the foil's chord line (N)
T_z	Torque about the pivot location (parallel to the force sensor z-axis) (N-m)
F_V	Vertical Force (N) or Lift Force normal to the free-stream velocity (N)
F_H	Horizontal Force (N) parallel to the free-stream velocity (N)
L.E	Foil's leading edge
m_f	Mass of foil (kg)
m	Total mass of foil and part of vertical shaft below the force sensor (kg)
$F_{inertial}$	Inertial force (N)
	Plunging velocity (m/s)
$\ddot{y}$	Plunging acceleration (m/s^2)
$F_{V\text{-}Hydro}$	Vertical hydrodynamic force or Net Lift force (N)
$C_{V\text{-}Hydro}$	Coefficient of Vertical hydrodynamic force or Net Lift force
I_z	Mass moment of inertia (kg-m^2)
I_{CM}	Moment of inertia w.r.t. foil's mid-chord
$x_{c\text{-}pv}$	Distance between the pivot location and the mid-chord of the foil
$\dot{\theta}$	Angular velocity (rad/sec)
$\ddot{\theta}$	Angular acceleration (rad/s^2)
$T_{Z\text{-}inertial}$	Inertial moment (N-m)
$T_{Z\text{-}Hydro}$	Hydrodynamic moment or Net torque (N-m)
$C_{Z\text{-}Hydro}$	Coefficient of Hydrodynamic moment or Net torque
P	Instantaneous Power extracted (W)

C_P	Coefficient of instantaneous power extracted
P_y	Instantaneous Power extracted due to plunging motion (W)
C_{Py}	Coefficient of instantaneous power extracted due to plunging motion
P_θ	Instantaneous Power extracted due to pitching motion (W)
$C_{P\theta}$	Coefficient of instantaneous power extracted due to pitching motion
P_{mean}	Time averaged power extracted (W) during flapping cycle
C_{Pmean}	Coefficient of time averaged power extracted during flapping cycle
C_{Pymean}	Coefficient of time averaged power extracted through plunging motion during flapping cycle
$C_{P\theta mean}$	Coefficient of time averaged power extracted through pitching motion during flapping cycle
η (%)	Power or energy extraction efficiency in percentage
ρ	Density of water (kg/m^3)
d	Swept distance (m)
$\Delta T_{linearstroke}$	Time taken for plunging motion during per half flapping cycle (upstroke or downstroke)
ΔT_{SR}	Stroke reversal time per half flapping cycle
$\Delta T_{SR\text{-}TOTAL}$	Total time taken for foil to undergo both stroke reversals in a flapping cycle

CHAPTER 1

INTRODUCTION

1.1 BACKGROUND

With depleting fossil fuel reserves and high energy demand due to increasing world population, there is a commitment to reduce our dependency on such energy sources and a dire need for alternative and innovative energy providing solutions. Renewable energy is such an alternative, which comes from the Earth's resources and is replenished with reference to a human time scale including; the sunlight, wind, rain, tides, oceanic waves and geothermal heat. This form of energy replaces the conventional and commonly used fossil fuels in four distinct domains; electricity generation, hot water/space heating, motor fuels and rural/urban off-grid energy services.

Tidal power is a hopeful renewable energy source and hydrokinetic turbines are being in development and use for electricity production which takes advantage of the kinetic energy of flowing water. These dam-less or zero-head turbines are thus very analogous to wind turbines. However, the hydrokinetic energy offers several advantages compared to the wind, i.e., its high energy density and a much better predictability. Inspired by this very wind turbine industry, most of the hydrokinetic turbine concepts proposed are based on horizontal or vertical axis rotor blade designs. Due to experience gained in the field of wind turbines, the most widespread design of tidal turbine uses a horizontal axis rotor. As for wind turbines, this design typically includes 2 to 4 twisted blades whose shape is designed in such a way that each blade section makes the same angle of attack with the incoming effective velocity. This implies steady hydrodynamics which favours torque constancy if the angle of attack is maintained below the stall angle of the blade. Horizontal axis turbine must be aligned in the direction of the upstream water flow, while vertical axis rotor blade turbines have the advantage to operate with water flow incoming from any angle in the plane perpendicular to its rotation axis. Thus, in a bi-directional tidal current this type of turbine does not require to incorporate a reversal mechanism. The angle of attack of each blade changes over one rotation period resulting in unsteady hydrodynamics.

A study by Climatewire (2011) shows that several organizations are still in the process of developing rotary turbines with improved performance and efficiency. Ragheb (2011) maintained that rotary turbines still operate with efficiencies between 20-45% depending on the tip speed ratio (TSR). For rotary turbines, higher power generation is mostly associated with large size and high tip speed. High tip speeds generate excessive aerodynamic noise and in addition may pose harm to flying/swimming animals. This noise can be reduced by reducing the tip speeds, although according to Jones et al. (2003), the performance of turbines deteriorates due to laminar flow separation. These turbines mostly operate in '*turbine farms*', which are usually located off-shore and mostly away from settlements in most cases, which presents many challenges related to economic and technical viability as well as environmental impact (Westwood, 2004; Kerr, 2007; Langhamer et al., 2011).

An alternative method to the above-mentioned devices for energy harvesting from wind/water are bio-inspired devices. Aquatic animals, as well as flying insects and birds, exploit a different kinetic locomotion mechanism which use oscillatory motions with fins or wings to achieve highly effective propelling and manoeuvring (Triantafyllou et al., 2004). Such inspiration from the evolutionary development in natural flyers/swimmers provides us with opportunities to design and develop not only man-made flyers as effective and agile as the natural ones but also turbines mimicking flapping motion which may be used for energy extraction from fluid flows. At low Reynolds numbers, traditional designs and rotors become less effective due to the increased influence of flow separation (Mueller & DeLaurier, 2003), however natural flyers/swimmers exploit this flow separation phenomenon and use the vortices to create large forces enabling them to fly/swim (Dickinson et al. 1999). The flow separation resulting from such complex flapping kinematics results in beneficial leading-edge vortices (LEVs) being formed in a controlled manner at a certain frequency and amplitude combinations, thereby causing periodic force generation. Furthermore, flapping wing natural flyers not only flap their wings vertically but also rotate in such a manner that generates thrust and lift combined.

Aerodynamic phenomena associated with biological flight prominently features unsteady motions, characterised by large-scale vortex structures, complex flapping kinematics, and flexible wing structures. Moreover, the knowledge gained from studying biological flight shows that the steady-state aerodynamic theory can seriously be challenged to explain the lift needed for biological flyers (Brodsky, 1994; Ellington, 1984a; Ellington et al. 1996). It is expected that understanding the complex unsteady flow physics such as the formation of LEVs and their interaction with the flapping wings and with trailing edge vortices (TEVs) associated with different flow conditions, would enable researchers to develop efficient energy propulsion and above all energy extraction devices. With the understanding that flapping foils produce thrust and lift, turbines based on flapping foil kinematics for energy harvesting has been a keen research interest for at least a decade (Platzer et al., 2009). This was first visited by McKinney and DeLaurier (1981), where they demonstrated the concept of energy harvesting through flapping motion, theoretically and experimentally (Figure 1.1). Their flapping wing wind-mill achieved an efficiency of 16.5%. Subsequently, in the late 1990s and 2000s this concept was revisited in detail where initially and till today, most of the researchers focused on this concept primarily through numerical analysis and few experimental studies. Irrespective of the mode of activation and kinematics (will be discussed in detail in Chapter 2), the flapping motion for energy extraction involves two motion modes: translational/plunging motion and rotational/pitching motion, as shown in Figure 1.2.

The use of such oscillating/flapping rectangular lifting devices or hydrofoils is an interesting alternative to horizontal axis rotor blades (HARBs) and vertical axis rotor blades (VARBs), offering an advantage in shallow waters due to its rectangular extraction plane (Figure 1.3). This rectangular extraction plane allows increasing the rated power of the hydro-generator by a simple extension of the foil span without requiring deeper waters. Furthermore, to use foils of high aspect ratio and endplates amplifies the 2D intrinsic character of the turbine which is beneficial in terms of 3D hydrodynamic losses.

The oscillating foil energy harvester also provides a better *filling factor* when compared to horizontal-axis rotor-blade turbines. This is illustrated in Figure 1.3 which simply states that the area ratio of a circle and a square of side equals to the circle diameter is equal to $\pi/4$ (or 78.5%). This implies that the oscillating foil turbines, shown in Figure 1.3(a) with a power extraction efficiency of 31.4%, would produce the same power as an array of horizontal axis turbine (Figure 1.3(b)) with a power extraction efficiency of 40%. In practice, the oscillating foil turbine has an even greater advantage, considering that too closely packed horizontal axis turbines as shown in Figure 1.3(b) is unrealistic. In fact, the EMEC (European Marine Energy

Centre) guidelines (Legrand and Black & Veatch Ltd, 2009) specify that the lateral spacing between devices should be two and half times the rotor diameter. This is equivalent to Figure 1.3(c) which leads to a filling factor approximately $\pi/10$ (31.42%). Also, without the centrifugal stress associated with rotating blades, the oscillatory devices are structurally robust (Xiao and Zhu, 2014). This allows us to scale up the rated power by simply increasing the hydrofoil span length. Furthermore, untwisted hydrofoils in oscillating concept or bio- inspired energy harvesting oscillatory hydrofoils allow the system to extract energy from incoming vortices or unsteady flows.

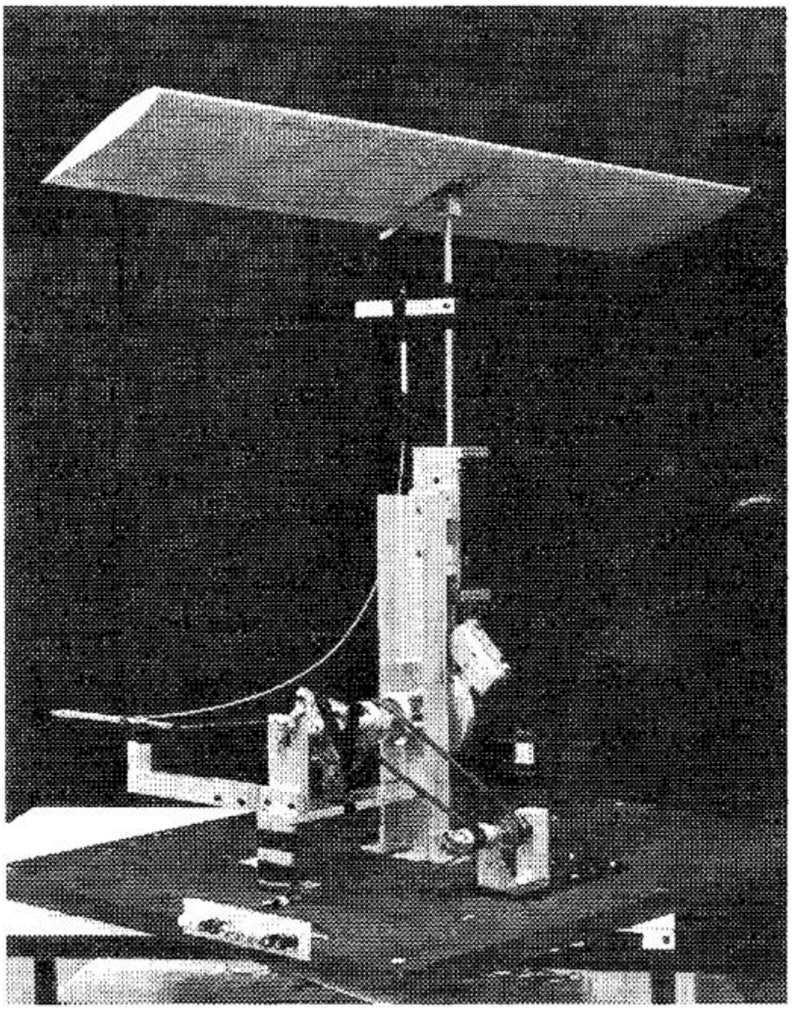

Figure 1.1: Experimental setup of oscillating wing windmill developed by McKinney and DeLaurier at the University of Toronto, Canada in 1981. The system included a wing which would oscillate harmonically to extract wind energy achieving a maximum efficiency of 16.5% (McKinney & DeLaurier, 1981)

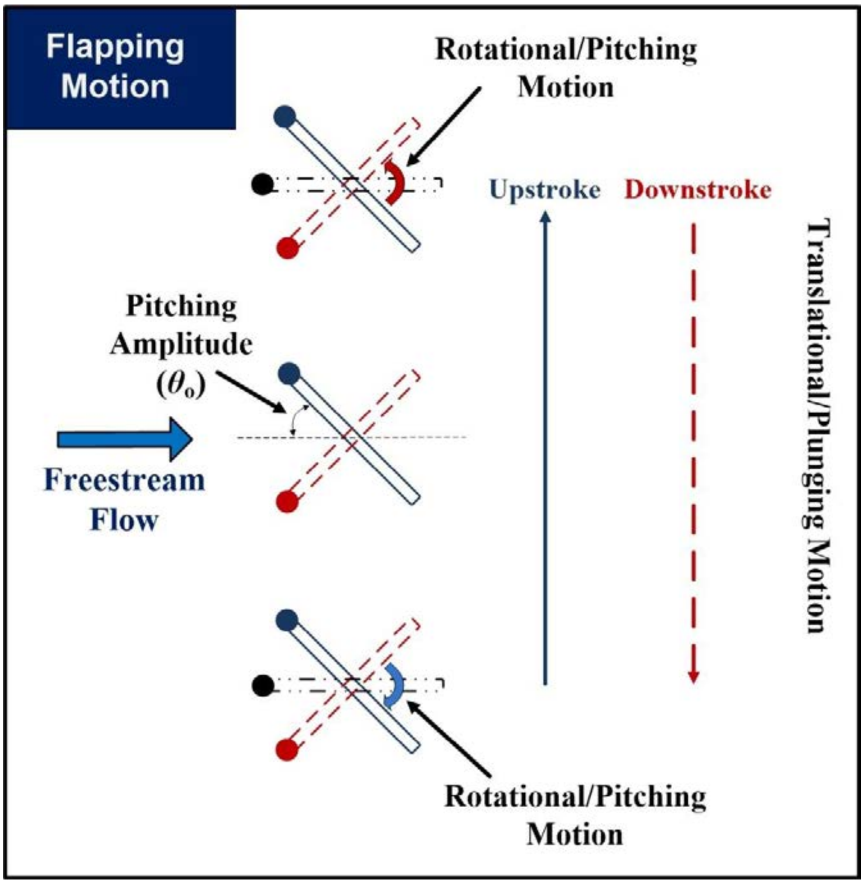

Figure 1.2: Schematic of flapping foil undergoing flapping motion in energy extraction mode and consisting of two motion modes: translational/plunging motion and rotational/pitching motion.

The design and development of successful and competitive flapping wing power generators comparable to the traditional rotary turbines is only possible when several key gaps in the literature are given focus. This may include ensuing fluid-structure interaction (FSI) and the complete understanding of the effects of flow separation and vortex dynamics when subjected to different geometric and kinematic conditions on the energy extraction performance of the harvester. Another important aspect is the kinetics of mode of activation of such flapping wing energy harvesters. As our literature survey will suggest, a majority of research was focused on systems where the flapping motion modes were fully or partially prescribed, whereas rarely a flow induced flapping motion system (passive) has been focused on. What motivates this research is the exploration of this fully passive flapping energy harvester, where the kinematics of the motion modes are unknown since they are flow induced. In such an environment, where upon through variation of different geometric parameters how the energy harvester behaves becomes the major motivational factor

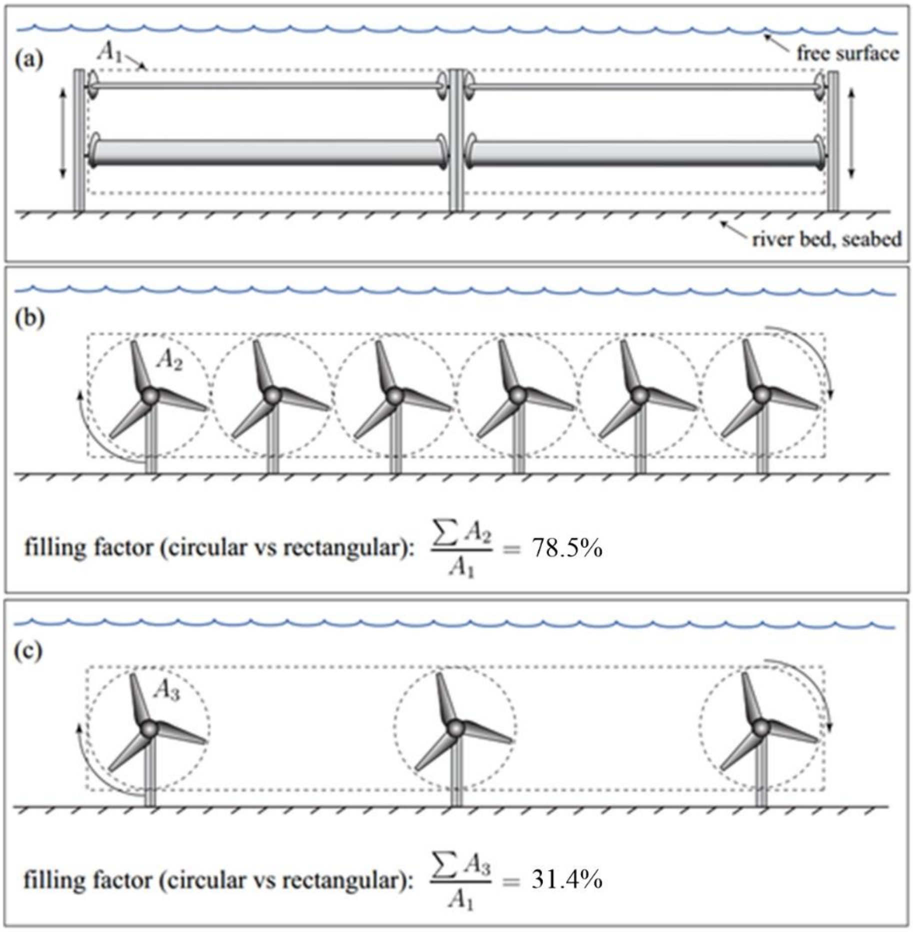

Figure 1.3: Rectangular extraction plane associated with the oscillating foil turbines **(a)** versus the circular extraction plane of horizontal-axis turbines **(b)** and **(c)**. The rectangular extraction plane has a clear advantage in shallow water sites in terms of number of turbines and filling factor.

for this research. Hence, the following research questions arise which need to be investigated to understand the concept of energy harvesting through fully passive flapping foil;

1. How does the flapping hydrofoil interact with the water flow, in terms of the instantaneous kinematics/kinetics of the hydrofoil and the unsteady vortices induced in the water flow?
2. What are the effects of the hydrofoil design features, such as the maximum allowed pitch angle and heave amplitude, pivot location, inertia, and hydrofoil profile, on the energy extraction efficiency?
3. What are the effects of the flow conditions, such as the Reynolds number, on the energy extraction efficiency?

1.2 RESEARCH AIM AND OBJECTIVES

The present research aims to achieve an improved understanding in the role of fluid-structure interaction (FSI) on the performance of a passively oscillating hydrofoil based hydrokinetic energy extractor that operates in an open channel water flow. To achieve this, a series of objectives are specified as follows:

1. To design and develop a water-tunnel test rig that can realize a fully passive flapping motion and simultaneous measurements in water flows
2. To conduct real-time measurements of the test-rig kinematics/kinetics as well as of the surrounding flow field under various geometric and kinematic conditions, including linear and rotary motion measurements, force/torque measurements, flow visualization and velocity measurement using time-resolved particle image velocimetry (TR-PIV).

To make this research focused and in-depth within the limited time frame assumptions have been introduced. Firstly, this study only focuses on a single, rigid hydrofoil. Hence, multi-hydrofoil configurations and flexibility will not be considered. Secondly, the unsteady flow around the hydrofoil is assumed to be two-dimensional, which is achieved through using two end plates in the water tunnel test-rig. Lastly, the test rig is designed in such a way that no actual power-takeoff system is implemented to convert the extracted hydrokinetic energy into electricity. With this setting, the system performance is evaluated through the power and efficiency calculated using measured forces and motion data.

1.3 ORGANIZATION OF THE REPORT

The thesis is organized into 7 chapters.

In chapter 2, a detailed review of the literature on flapping wing aerodynamics, mostly in the energy harvesting mode, will be presented. It will cover the introduction to flapping wing kinematics, along with an insight of the experimental, analytical and computational studies carried out in relation to the power extraction phenomenon through oscillating foils. This will help to identify any gaps in the literature to justify the research questions laid out for this research, as mentioned in the previous section.

In chapter 3, we will discuss the research methodology entailing the details of the experimental test setup including sensors, data acquisition system and flow evolution system both qualitatively and quantitatively.

Chapter 4 will introduce to one flapping foil case, which will be thoroughly discussed focusing on kinematics and kinetics, energy extraction performance, flow visualization and PIV results to establish an understanding how the force-motion and subsequent fluid- structure interaction analysis for such systems will be carried out in the succeeding chapters.

Chapter 5 will discuss the energy extraction performance of the test-rig equipped with flatplate foil through variation of key parameters such as inertial mass, pivot location and pitching amplitude. The tests were conducted at three different free-stream velocities (U_o = 0.57 m/s, 0.65 m/s and 0.78 m/s), which correspond to the chord-length based Reynolds number (Re) of 7.6×10^4, 9.1×10^4 and 1.09×10^5. Coupled effect of pitching amplitude and pivot location variation on energy harvesting performance of the system through detailed quantitative comparative analysis will also be presented in this chapter.

Chapter 6 will focus on the morphological effect on energy harvesting performance for the passively actuated flapping foil energy harvester. As a basis for our future work, three foils will be compared where the flatplate foil, serving as the baseline foil, will be quantitatively compared with NACA0006 and elliptical foil.

In Chapter 7, major conclusions and findings of this thesis will be summarised and recommendations for future work will be proposed.

CHAPTER 2

FUNDAMENTALS & LITERATURE SURVEY

In this chapter, results from numerous studies undertaken on the flapping foil energy extraction concept since 1981 are evaluated. Energy extraction through flapping foil can be broadly grouped into three categories based on kinetics: fully prescribed or fully active system, semi-active system and fully passive system. The literature survey is classified according to the mode of activation (flapping kinetics) and/or flapping kinematics, and the geometric structure of the foil/wing, and introduce to the fundamentals associated with energy extraction through flapping foils and performance evaluation methodology.

2.1 KINEMATICS AND KINETICS OF FLAPPING HYDROFOIL IN ENERGY EXTRACTION MODE

2.1.1 KINEMATICS AND POWER CONSIDERATIONS

Energy extraction from fluid using flapping foil relies for its effectiveness on a mechanism similar to that of so called "*flutter*" in an aircraft wing. Although this phenomenon may trigger structural failure of a wing, it could be exploited for power generation from the kinetic energy of the fluid flow. This "*fluttering*" requires two degrees of freedom motions interacting with phase lag between them: pitching and heaving. As seen in Chapter 1, there are two possible configurations for a flapping foil to achieve these motions and work as an energy extraction device: swing arm configuration and linear guide rail mechanism (see Figure 2.1).

It is also important to understand that how the motion kinematic parameters and forces acting on the foil contribute towards the extraction of power from fluid. As compared to the flapping foil in propulsive mode, where the resultant force points away from the direction of the translational motion, the flapping foil energy extractor has a higher pitching angle and out of phase as compared to it propulsive counterpart. Furthermore, the resultant force points towards the direction of the plunging motion, producing positive power output at the expense of the drag force (Figure 2.2). This leads to the definition of the term "*feathering criterion*" (Equation

2.1) which helps us to identify based on some of the important parameters, whether the flapping foil will work in a propulsive ($\chi < 1$) or energy harvester mode ($\chi > 1$).

$$\chi = \frac{\theta_o}{\arctan\left(2\pi f\, h_o / U_o\right)} \tag{2.1}$$

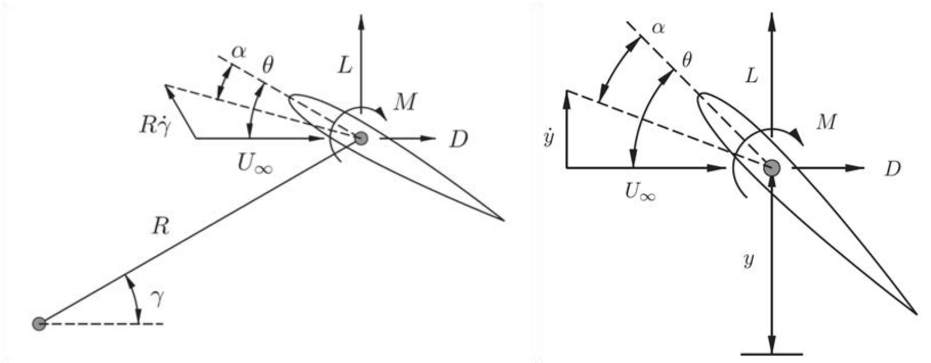

(a) (b)

Figure 2.1: Two different configurations of flapping wing energy harvester system. (a) Swing arm configuration where the flapping angle (γ) of the swing arm plays an important role in the kinematics (heaving and pitching of the foil) of this mechanism, hence making it a 1-DoF system. (b) A non-swing arm (linear guide rail) where although both motions act independent but still coupled. Adapted from Young et al. (2010)

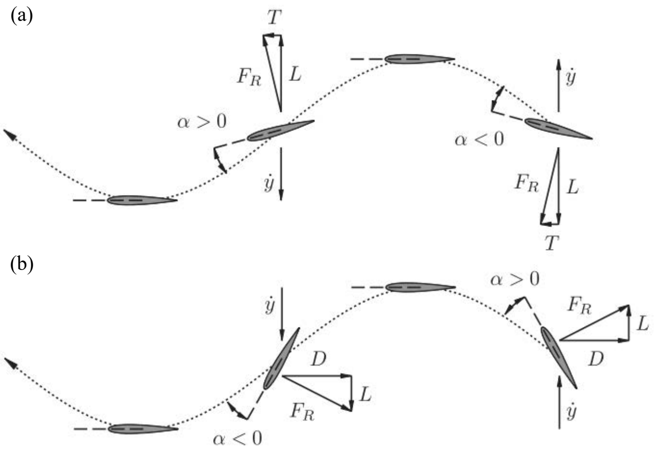

Figure 2.2: Regimes of operation of a flapping foil, the associated angle of attack and force directions throughout the flapping cycle. Adapted from Young et al. (2010). (a) Propulsion mode, (b) Energy harvesting mode.

To evaluate the energy extraction performance of a flapping foil, a number of parameters need to be calculated/measured. Since, our system (which will be introduced in Chapter 3) follows the linear guide flapping motion system as shown in Figure 2.1 (b), our analysis will include lift force or vertical force (L), plunging velocity ( ), torque or moment (*M*) due to pitching motion and angular velocity ($\dot{\theta}$). Through these parameters the instantaneous and cycle (phase) averaged power and ensuing energy extraction efficiency can be calculated. Firstly, instantaneous aero-hydrodynamic power contributed by both plunging and pitching motions is evaluated as shown in Equation 2.2:

$$P(t) = L\dot{y}(t) + M\dot{\theta}(t) \tag{2.2}$$

where *L* is lift force or vertical hydrodynamic force (perpendicular to the incoming horizontal free-stream velocity), *M* is moment or torque because of pitching motion, (t) is the plunging velocity and $\dot{\theta}(t)$ is the angular velocity. If the motions of the flapping foil are assumed to be periodic with time-period *T*, the energy harvesting performance is often characterized by the cycle (phase) averaged power coefficient $\overline{C}_P$ defined as:

$$\overline{C}_P(t) = \frac{1}{T}\int_0^{t+T} C_P(t)dt \tag{2.3}$$

where $C_P(t)$ is defined as:

$$C_P(t) = \frac{P(t)}{\frac{1}{2}\rho s c U_o^3} = C_L \frac{\dot{y}(t)}{U_o} + C_M \frac{c\dot{\theta}(t)}{U_o} \tag{2.4}$$

where, ρ is the density of the fluid (kg/m^3), s is the foil span (m), c is the chord length of the foil (m), U_o is the free-stream velocity of the incoming fluid (m/s), C_L is the coefficient of lift force and C_M is the coefficient of moment which are described as follows:

$$C_L = \frac{L}{\frac{1}{2}\rho U_o^2 s c} \tag{2.5}$$

$$C_M = \frac{M}{\frac{1}{2}\rho U_o^2 s c^2} \tag{2.6}$$

The efficiency of the power generation is usually measured as the ratio of the time average power output ($\overline{P}$) to the power available in the flow through the frontal area swept by the foil (P_a):

$$\eta = \frac{\overline{P}}{P_a} = \frac{\overline{P}}{\frac{1}{2}\rho U_o{}^3 s d} = \overline{C}_P \frac{c}{d} \tag{2.7}$$

where, d is the largest total distance swept by a portion of the foil, where in most cases the trailing edge.

Consider the motions and forces as shown in Figure 2.1(b). The quasi-steady argument suggests that if the angle of attack were maintained at zero throughout the flapping cycle, the power generated would also be zero. Assuming sinusoidal plunge motion $y = hc \sin(\omega t)$ and sinusoidal pitch motion $\theta = \theta_o \sin(\omega t + \varphi)$, with $\varphi = 90^o$, the angle of attack in Figure 2.1(b) is defined as:

$$\alpha(t) = \theta(t) - \arctan\left(\frac{\dot{y}}{U_o}\right) = \theta_o \cos(\omega t) - \arctan\left(\frac{hc\omega\cos(\omega t)}{U_o}\right) \tag{2.8}$$

Davids (1999) noted that the pitch rate $\dot{\theta}$ also has an influence on the angle of attack of the foil. There is an additional velocity component relative to the foil's surface, equal to the distance from the pivot point multiplied by the pitch rate. This additional velocity component is thus not uniform across the length of the foil. Equation 2.7 is seen to be the angle of attack at the pivot point, and the angle of attack at the leading edge is given by:

$$\alpha_{LE}(t) = \theta(t) - \arctan\left(\frac{cx_p\dot{\theta}\cos\theta + \dot{y}}{U_o - cx_p\dot{\theta}\cos\theta}\right) \tag{2.9}$$

2.1.2 KINETICS

Past research has shown that studies in energy extraction through flapping foil(s) classifies these devices into three major categories. This classification is based on the type of activation mechanism applied on either or both of the motion modes: heaving and pitching. These are fully active or fully prescribed method (where the device is used to impose a prescribed flapping motion on the wing), the semi-passive method (where either of the motion modes is subjected to fluid-induced motion while the other is controlled or prescribed) and the fully passive method or flow driven method (where the activation for both motion modes is flow induced).

2.1.2.1 FULLY PRESCRIBED FLAPPING FOIL ENERGY HARVESTER

The fully prescribed method involves the flapping kinematics to be pre-determined. By imposing sinusoidal pitch and plunge motions on a NACA0015 foil in a laminar flow at Re = 1100, for reduced frequency (k) = 0.0 to 1.57 and maximum pitching amplitude (θ_o) = 0º to 90º, Dumas and Kinsey (2006) found efficiencies as high as 34% between θ_o = 70º-80º, k = 0.75-1.13, pivot location (x_p) = 0.333c, plunging amplitude (h_o) = 1.0c and plunge-pitch phase difference (ϕ) = 90º. The best efficiency cases were characterized by: maximum plunge velocity being the same as the free stream velocity, dynamic stall vortex shedding and effective angles of attack as high as 35º. Kinsey and Dumas (2008) noted that shedding of LEVs just before the complete reversal of the pitching stroke would improve power generation and efficiency of a flapping-foil turbine because of the positive suction effect due to low pressure created by LEVs on the foil as noted by Shyy and Liu (2007). Furthermore, the former also showed using NACA0015 foil that power generation increases while the efficiency reduces when h_o was increased from 1.0c to 1.5c. Kinsey and Dumas (2008) also found that for this range of k = 0.75-1.13 is good for power generation for sinusoidal flapping foil turbines.

Additional study on their hydrokinetic turbine was conducted where they compared their results from experiments of a 2kW turbine with numerical simulations (Re = 500,000, k = 0.88, ϕ = 90º, θ_o = 75º, h_o = 1.0c, x_p = 0.333c). The power efficiency results from their 3D analysis compared well with the experimental results, however the 2D CFD analysis over-predicted between k = 0.5-1.0. A maximum difference of 33% was observed at k = 1.0 while for k < 0.5, the numerical 2D and 3D and the experimental results were similar for a single flapping foil. For their tandem configuration experimental tests, they observed the same pattern where with increasing k, the differences between the numerical and experimental results increased. The maximum efficiency achieved shifts from 71% to 45% when simulations change from 2D to 3D at k = 0.88 respectively. This might be attributed to the uncertainties in the estimation of the mechanical losses in the experimental study and the inability of the Unsteady Reynolds Averaged Navier Stokes (URANS) solver to correctly predict the interactions between the wake vortices of the upstream foil with the downstream foil.

The strong effect of k and effective angle of attack (α_{eff}) on the evolution of the upstream wake was also observed by Kinsey and Dumas (2012). It appeared consistent with the numerical study of vortex dynamics by Baik et al. (2012), which stated that the reduced frequency and effective angle of attack are primary determinants in the evolution of the LEVs. 3D losses were also numerically investigated by Kinsey and Dumas (2012) for sinusoidal pitch and plunge kinematics of a NACA0015 foil with different aspect ratios (AR) (5c, 7c and 10c at Re = 500,000) at the best kinematic conditions (k = 0.88, θ_o = 75°, ϕ = 90°, h_o = 1.0c and x_p = 0.333c). Their installation of endplates to the NACA0015 foils showed that the initial 20% and 30% losses due to the 3D effects were reduced to about 10% at AR = 10c.

Deng et al. (2014) numerically investigated the effect of aspect ratio on power generation of a NACA0015 foil using sinusoidal plunge motion and non-sinusoidal pitch motion which was varied from sinusoidal trajectory to trapezoid variation for aspect ratio 1c to 8c at Re = 1100, St = 0.4, θ_o = 81.5°, h_o = 1.23c, x_p = 0.333c, k = 1.02 and ϕ = 90°. They also found that high power generation and efficiency were affected by three dimensional effects, with 4c identified as most appropriate and critical aspect ratio for sinusoidal pitch motion, below which low aspect ratio characteristics dominate the flow field. Aspect ratio of 4c was suggested as most appropriate as a compromise between high power efficiency and lower cost of manufacturing and installation of the flapping system. The 2D results also showed two peaks in the lift time history, with the first peak credited to a good attachment of the flow to the surface of the foil at α_{eff} = 15.4°, while the second peak occurred later as the LEV travelled on the surface of the foil about the trailing edge. The trapezoid pitch motion which performed better in their 2D model had the lift peaks (especially the second peak) eroded in the 3D investigation due to 3D instabilities on the LEV, thus negatively affecting the power generation in 3D.

The wake of a flapping-foil turbine could give us some insight on power extraction performance of a flapping-foil turbine, especially for tandem configuration. By solving the Navier-Stokes equation for power generation and Orr-Sommerfeld equation for stability analysis, Zhu (2011) showed that the wake of a flapping foil was convectively unstable, and when the resonance frequency of the instability in the wake equaled the flapping frequency ($k \approx 0.94$) of the foil, maximum power efficiency is achieved and thus the achievement of an efficient evolution of the wake. Zhu (2011) also observed that pitch power generation was near zero at the optimum kinematic condition ($k = 0.94$, $\theta_o = 70^o$ to 80^o, $\phi = 90^o$, $h_o = 1.0c$, $x_p = 0.333c$) of the flapping-foil turbine. He stated that for large effective angles of attack ($\alpha_{o\text{-}eff} \geq 40$), the flapping frequency of the foil will be higher than the frequency of the instability, while for lower effective angles of attack ($\alpha_{o\text{-}eff} < 40$), it will be lower than the frequency of instability.

Xiao et al. (2012) numerically investigated possible ways of improving power generation through flapping foil by controlling the pitch motion. They studied the effect of several non-sinusoidal pitch motion trajectories on energy extraction of a NACA0012 foil for a range of Strouhal numbers (St = 0 to 0.5) at $Re = 10{,}000$, $\theta_o = 58^o$, $\alpha_{eff} = 10^o$ and 20^o, $h_o = 0.5c$ and $1c$, $x_p = 0.333c$ and $\phi = 90^o$. For different pitch profiles investigated, power generation and efficiency increased with increasing St up to a critical value before dropping. At $\alpha_{o\text{-}eff} = 20^o$, $h_o = 1c$, $St = 0.35$, a trapezoid profile of the pitch motion has been found to generate up to 33% and 39% ($\beta = 1.25$ and 1.5 respectively) more power and efficiency as compared to the sinusoidal pitch motion ($\beta = 1.0$).

Huxham et al. (2012) experimentally studied the influence of the pitch amplitude and reduced frequency on the flapping-foil turbine with sinusoidal pitch and plunge motions, at flow speed of 0.5m/s, $Re = 45{,}000$, $x_p = 0.25c$, for $\theta_o = 4^o$ to 62^o, and $k = 0.16$ to 1.26. He also found that power generation increased with an increase in reduced frequency (from $k = 0.16$ to 0.63), with maximum mean power coefficient of 0.067 achieved at $\theta_o = 62^o$ and $k = 0.63$ and 0.94. On the other hand, maximum efficiency of 23.8% occurred at $k = 0.63$, with maximum $\alpha_{o\text{-}eff} = 46^o$. Although the maximum mean power coefficient of 0.067 is quite low due to mechanical losses, the values of the kinematic parameters were close to the region of best performance as reported in Kinsey and Dumas (2008). Bryant et al. (2012-13) developed a quasi-steady model and a modified quasi-steady model, which incorporated dynamic stall effects, for the study of the flapping-foil energy harvesters at low Re = 1000. The verification of both models with CFD results showed that the dynamic stall model could be an approximate model to the CFD, while the quasi-steady model showed a very poor agreement with the CFD results.

2.1.2.2 SEMI-PASSIVE FLAPPING FOIL ENERGY HARVESTER

The semi-passive flapping foil turbine is another device which incorporates a mix set of activation mechanism for energy extraction. As described, either the heaving or pitching motion is actively controlled while the other motion mode is flow-induced.

Shimizu et al. (2008) designed and numerically studied a semi-passive flapping system with NACA0012 foil, where a sinusoidal pitching trajectory was employed with the help of an actuator (electric motor) of constant frequency and pitching amplitude (θ_o = 0 to 50^o) and the heaving motion being passive, supported by a spring-damper system. Using multi-objective optimization of the design variables (including pivot location, reduced frequency, mass ratio of the wing, damping coefficient and frequency ratio) to maximize the power generation and efficiency. They observed that $\overline{C}_P$ and η decreased linearly with increase in h_o and ϕ respectively, but the optimized results were over predicted when compared with CFD results. They also noted the importance of the LEV and showed that appropriate timing of the formation of the LEV helped the flapping motion of the foil causing a 36.6% increase in mean power coefficient and maximum efficiency of 35% at Tip Speed Ratio (TSR) of 0.58. Hence, flapping foil turbines could have a comparative advantage over the conventional rotary turbines with typical efficiencies of about 0 to 30% at low TSR.

Zhu et al. (2009) through their 2D numerical simulations showed that an increase in θ_o would increase h_o and the efficiency (η) over a range of parameters of a NACA0005 foil at U_o = 1 m/s. These findings are similar to those in Peng and Zhu (2009), Young et al. (2010) and Kinsey et al. (2011). The best efficiency for Zhu et al. (2009) was 25% with x_p = 0.5c, however he did not show a critical value of θ_o beyond which the power efficiency would decline. They also recommended that the 2D results would serve as better guides to the level of energy extraction achieved and the 3D results would offer an accurate prediction of the dynamics of parametric values at best performance. They also observed that when *St* and $\alpha_{o\text{-}eff}$ fall within 0.3-0.5 and 13°-36° respectively, the flow field is dominated by LEVs. They also found out that at θ_o = 30°, $\bar{C}_P$ increases with foil thickness, especially at flapping frequencies greater than 2.

Continuing Zhu et al. (2009) study, Zhu and Peng (2009) put greater emphasis on the interactions of the LEVs and hydrodynamic pressure. From their analysis of power generation using Joukowski foil at *Re* = 1000, θ_o = 15°, with sinusoidal pitch motion and passive heaving motion, C_{Pmean} = 0.6-0.7 was observed at *k* = 0.40-0.70 when pivot location is between 0.2*c* and 0.5*c*. This is because the center of hydrodynamic pressure was located around the pivot location, resulting in good synchronization between the hydrodynamic moment and the pitching motion. They further stated that energy harvesting is most favorable if interactions between LEVs and the foil occur far from the pivot location, preferably around the trailing edge (T.E) of the foil.

Hisanori and Akira (2012) performed an experimental campaign with semi-passive method. By using an actuator to activate the pitching motion of a NACA0015 foil, while the plunge motion was supported by a leaf spring. They investigated the power generation efficiency and the impact of perpendicular distance between the two flapping foils in a bi-plane arrangement with cascade foil flapping motion phase difference (Φ) = 90°. With U_o = 1 m/s, θ_o = 50° and cascade foil interspacing distance (L_x) = 1*c* to 5*c*, the analysis showed that the power generation efficiency increased as L_x increased. The maximum power generation and efficiency was reported in the in-phase mode (35W and 32-33%) with L_x = 4*c*-5*c*. Although the power extraction performance of the two foils were similar to each other in this in-phase mode, the efficiency of the first foil was higher than that of the second foil by about 6%. In the case of anti-phase mode of 90°, maximum power generation and efficiency were about 38W and 37% at gap of 2*c*. There was variation in performance in the anti-phase mode with L_x = 2*c* to 4*c*, where the first foil having higher efficiency than the second one by 6%.

Isogai and Abiru (2012) studied the power generation and efficiency of a multi-foil configuration of 2D NACA0015 foil at *Re* = 38,000 (U_o = 1 m/s) by using an analytical method base d on linear potential aerodynamic theory and numerical method based on N-S equation. Results from the two methods were similar, however different from the experimental results of Hisanori and Akira (2012). They also attributed the difference between the numerical and experimental results to differences in aspect ratios.

Wu et al. (2014) numerically investigated the effect of solid wall boundaries positioned at 0.5c, 1.0c, 1.5c, 3c and 5c from the pivot location x_p = 0.333c, with θ_o = 15°, 30° and 45°, k = 1.26 and Re = 1100 on the power extraction performance of a flapping NACA0015 foil with a prescribed sinusoidal pitch motion and flow driven plunge motion. They found that a solid wall positioned closer to a flapping foil improves the power generation and efficiency over that without a wall/ground effect as θ_o increases from 15° to 45° and the plunge amplitude ho reduced to the chord length. The ground effect on a flapping foil for power generation is similar to that of flapping foil for propulsion in Jones and Platzer (1997), where the propulsive efficiency improved by 20% where the wing was positioned near a wall. Further investigation by them showed that by increasing k, the propulsive efficiency reduced as the wall distance increased from h_o to 10h_o. The increase in power generation efficiency to 40% as observed by Wu et al. (2014) is due to the power consumption increase at high heaving amplitudes up to h_o = 5c as the ground effect reduces. He also found that at θ_o = 45°, $\overline{C}_P$ of about 0.36 and η of 28% were produced by two solid parallel walls separated by 2c and h_o = 1.0c, and 48% higher than the result of a single solid wall at the same condition.

2.1.2.3 FULLY PASSIVE FLAPPING FOIL ENERGY HARVESTER

In this mode the flapping motion is fully flow induced and both motion modes can perform without any form of restriction. McKinney and DeLaurier (1981) undertook the first experimental campaign on a flapping energy harvester in a wind tunnel using a NACA0012 airfoil. The pivot location and frequency of oscillation system was fixed, with wind speeds set at 6 m/s and 8 m/s. Sinusoidal plunge motion was initiated by a falling weight. Power efficiency increased with increasing wind speed and pitching amplitude (θ_o), with the maximum efficiency achieved at 28.3% at θ_o = 30° and U_o = 8 m/s. The phase difference (ϕ) between heave and pitch motion was varied between 0° and 140° with the maximum power generation of 90W being achieved at ϕ = 110° and maximum efficiency of 28.3% at ϕ = 90°.

This early study by McKinney and DeLaurier shows us that flapping wing turbine is a competitive concept against the conventional rotary turbines. It was not until after almost two decades that Jones and Platzer (1997) using an in-house panel code found that for power generation to occur, *the pitch amplitude must exceed the angle of attack due to the heaving motion*. They also found through computations that the maximum power generation occurs at ϕ = 90º. The code also over-predicted the experimental results of McKinney and DeLaurier from ϕ = 60º to 110º with the maximum margin of 11% occurring at ϕ = 90º. This over-prediction is attributed to the effect of flow separation, mechanical losses, viscous effects and three-dimensionality, which was not captured by the panel code. However, in some cases the panel code under-predicted the experimental results at θ_o = 30º, when ϕ was between 90º and 140º. For θ_o = 30º the, the margin between the panel code and experimental results increased as ϕ increased.

In another study, Jones et al. (2003) observed that at $\alpha_{o\text{-}eff}$ = 15º the peak power generation moved from relatively low reduced frequencies to higher reduced frequencies. On the other hand, the location of the peak power efficiency remained at low h_o of 1.25c and high k = 1.4, for phase difference between 80º and 110º. He also undertook a 2D numerical investigation with N-S solver for both laminar and turbulent flow conditions at Re = 20,000 and 1,000,000 respectively to study the effect of flow separation not captured by the panel code. Although they found that flow separation has no adverse effect on the performance of flapping foil turbines, it needs to be ascertained more extensively. they also observed that for k = 0.2 to 1.2, not only that the predicted mean power generated over a cycle for turbulent flows was 33% to 85% lower than those for laminar flows, it was not periodic for k > 0.6.

Peng and Zhu (2009) used numerical simulations with fluid structure interactions (FSI) to study a flapping-foil turbine (Joukowski foil) driven by instability in the flow at Re = 1000. Their design involves a foil mounted on a simple structural system containing a rotational spring in the pitching direction and a damper in the plunge direction. They showed that at large spring stiffness (k_α about 0.1) for a foil pivoted around the leading edge (L.E), a zero-pitch amplitude at the onset repressed the commencement of the flapping motion. Self-starting the flapping motion for Peng and Zhu (2009) was possible when the pivot was located between 0.3c from the L.E and the trailing edge (T.E), while a near stable flapping motion was achieved at pivot location x_p = 0.4c to 0.6c from the L.E. Subsequently, Young et al. (2010-13) and Platzer et al. (2014) numerically studied the fully passive mode at Re = 1100, with a NACA0012 foil with a flywheel rotational viscous damper arrangement pivoted at $x_p = 0.5c$.

Platzer et al. (2009) and Young et al. (2010) considered different pitch motion kinematics from a sinusoidal variation with normal stroke reversal time (ΔT_R = 0.5 for Young et al. (2010)) to a trapezoidal variation with a swift stroke reversal (ΔT_R = 0.1) for $h_o = 1.0c$ and $\phi = 90^{o}$. They found that a pitch motion with moderate stroke reversal time (ΔT_R = 0.3) is preferred for optimum power generation and efficiency. For maximum θ^{o} of 65^{o} and frequencies up to 1.5 Hz, an efficiency as high as 30% could be attained with this fully passive method, which is significant compared to 20% power efficiency (with $\overline{C}_P$ = 0.15) at $\theta_o = 30^{o}$ reported by Peng and Zhu (2009). Ashraf et al. (2011) also found out that for a single NACA0014 flapping foil using ΔT_R = 0.3, there was a 17% and 15% increase in power generation and efficiency respectively over the sinusoidal counterpart.

The control of the effective angle of attack kinematics of a flapping foil is another area of keen interest for improving the performance of a flapping-foil turbine. For this reason, Young et al. (2013) followed up the study in Young et al. (2010) with a direct modification of the α_{eff} of the best pitch control case to a trapezoid variation in a flapping cycle. They found that for a NACA0012 at Re = 1100, a stroke reversal fraction of 0.2, $x_p = 0.5c$, a flywheel rotational damper strength of 3.0, the best effective angle of attack amplitude was 40^{o} resulting in an increase in the power efficiency from about 30% to about 41%.

So far in the fully passive method, achieving high power generation and efficiency by a flapping-foil turbine may be challenging where it is wholly activated and controlled by the flowing fluid. The system, consisting of a Joukowski foil, of Peng and Zhu (2009) was characterized by uncontrollable plunge and pitch motions with unstable and varying frequencies, causing a negative power generation phase for a more than 30% of the flapping cycle. In addition, the evolution of the vortices was chaotic. Furthermore, they also observed that energy recovery from the LEVs enhances power generation, and if not recovered results in a stronger wake. The effect of a linear shear flow on the power extraction performance of a flapping-foil turbine has been studied numerically by Zhu (2012). This study by Zhu (2012) was also a follow up to Peng and Zhu (2009), for the effect of stability of the flapping motion of the foil considering three different shear rates β = 0.05, 0.10 and 0.20. His results showed a periodic response with reliable power generation and efficiency (up to 15% for β = 0.05 and 25% for β = 0.10) compared with 30% for a uniform flow. Furthermore, Zhu (2012) found that the region for periodic response in the parametric space of the pivot location and rotational stiffness was larger than that of a uniform fluid flow. For the fluid flow with a high shear-rate of β = 0.20, the power efficiency was projected to decrease significantly because the region of periodic response that characterizes energy harvesting disappears with increasing shear rate.

Some experimental studies for fully passive flapping-foil turbine include Platzer and Bradley (2009) and Kinsey et al. (2011). The flapping-foil turbine design of Platzer and Bradley (2009) was pitch induced and was used to verify the numerical investigation by Platzer et al. (2008). They found that a pitch motion of trapezoid variation for a fully passive flapping-foil turbine was better for power generation than mechanically induced sinusoidal flapping motion.

Subsequently, Kinsey et al. (2011) designed and tested a 2kW prototype hydrokinetic turbine with two hydrofoils (NACA0015 foil) in tandem configuration separated by 5.4c distance at an average flow speed of 2m/s, flapping sinusoidally with phase difference of 180^{o} between upstream and downstream foils. Their fully passive setups were accomplished by mounting the hydrokinetic turbine on a specially designed pontoon boat and later driving it along a water way. At an average speed of 2m/s, an angular velocity of 6.2 rad/s, a torque of 201 Nm, the 2kW capacity hydrokinetic turbine generated an average power of 1.29kW. Kinsey and Dumas (2010) and Kinsey et al. (2011) also investigated a range of reduced frequencies of which k = 0.75 generated the best power efficiency of 40% for the two hydrofoils in tandem configuration compared with 30% for only the upstream hydrofoil in operation. For the performance in tandem configuration, the upstream and downstream foils generated 67% and 33% of the total power respectively.

Platzer et al. (2009) proposed a fully passive device which require no complex mechanism to enforce the proper phase angle between the heave and pitch motions or create a non-sinusoidal motion profile. The foil plunges on a guide rail and pivoted about a pitch axis that is aft of the mid-chord position, ensuring that the foil is statically unstable and deflects to an increasing pitch angle until it is stopped by a mechanical restraint in the form of a pitch limiter. This drives the upward plunge motion due to the lift on the foil, and the foil is flipped back down at the end of the stroke by an extension rod on the foil contacting another mechanical restraint in the form of a plunge limiter. A non-sinusoidal pitch angle time history with correct phase between the pitch and plunge is automatically generated. It does not rely on a second foil in tandem to be self-starting.

2.2 FOIL SHAPE EFFECT ON ENERGY EXTRACTION

Some amount of work has been done in the effect of foil on power generation performance. Linsdey's (2002) comparative study of NACA 0010, NACA 0014 and NACA 0018 foils through unsteady panel (UPM) calculations and he found measurable effect on power and efficiency by reducing the foil thickness with approximately η = 27% for NACA 0010 to η = 23% for NACA 0018, but it should be noted that the UPM code enforced attached flow at the leading edge and speculated that dynamic stall and LEV formation would likely have a significant effect on these results.

Kinsey and Dumas (2008) used NACA0015 foil as their baseline undergoing prescribed motion using URANS with Re = 1100 with x_p = 1/3. For comparison sake, they also simulated NACA 0002 and NACA 0020 foils, one in which the LEVs were prominent and in the other absent throughout the flapping cycle. The 15% and 20% thickness foils gave similar results, while the 2% exhibited larger extremes in instantaneous aerodynamic forces, however the time averaged values remained similar. It seemed that power generation efficiency is mostly insensitive to the details of foil geometry.

Some work has been done with the 3-D effects on energy extraction performance. With water tank testing and force/load measurement for a NACA 0012 hydrofoil at three different aspect ratios (aspect ratio (AR) = 4.1, 5.9 and 7.9), the results from Simpson et al. (2008 a,b), show clear decrease in efficiency as AR decreases. According to this, the high efficiency around 40% is only present in the high aspect ratio foil. A peak efficiency of 43% was found at the aspect ratio of 7.9, the Strouhal number of 0.4, the maximum angle of attack 34.37^{o} and ϕ = 90^{o}.

Numerical analysis about 3-D effects was also carried out by Kinsey and Dumas (2012), for aspect ratios, 5.0 and 7.0. Similar to the experiments by Simpson et al. (2008 a,b), their simulations demonstrated that maximum cycle averaged power of finite AR wings is lower than that of 2-dimensional wing. Given the flow and flapping conditions of Re = 500,000, reduced flapping frequency f^*=0.14, pitching amplitude θ_o = 75^{o}, and heaving amplitude h_o = c, achieving peak energy harvesting efficiency of 28% for AR = 7.0, and 21% for AR= 5.0. Analysis of the vorticity field along the 3D wing span in one flapping cycle indicates a remarkable difference between 2D and 3D wings at those instants when strong vortex shedding occurs. Similar to a 2-dimensional wing, an enlarged vortex evolves and sheds at mid-span of a 3-dimensional wing, leading to a significant difference between the pressure distributions on top and bottom of the wing, resulting in instantaneous lift force and moment augmentation, enhancing power extraction efficiency. This smoothens out the influence of vortex and reduces the peak instantaneous forces, however at instants where the boundary layer remains attached, there is no difference in the flow structure and pressure distribution as observed in 2-dimensional and 3-dimensional wings.

Usually, a streamlined foil is used for flapping studies in both propulsion and power extraction regimes because according to conventional fluid mechanics, less resistance to fluid flows is desirable, but the manufacturing cost of streamlined is high. By comparison, a simple non-streamlined foil such as a flat plate incurs much less cost to manufacture but its power extraction performance has not been assessed. Kang et al. (2013) recently investigated a flapping flat plate with rounded L.E and T.E numerically and experimentally, in 2D and 3D to understand the influence of geometric, kinematic, 3D effects and Reynolds number on the aerodynamic forces and the flow structures. They showed that compared to a SD7003 foil, the flow field of the flat plate was characterized by early flow separation and stronger LEV especially at maximum effective angle of attack position, because of the smaller radius of curvature at the LE of the flat plate.

This observation is consistent with the effect of the smaller L.E radius on the evolution of LEVs as reported by Kinsey and Dumas (2008) and Ashraf et al. (2011), causing stronger suction on the occurring surface and higher lift peaks than those of the SD7003 foil in Kang et al. (2013). For the flow characteristics of a flat plate at different Reynolds numbers (in the order of 10^4) with low turbulence, the flow characteristics were insensitive to Reynolds number for the flat plate as compared to the SD7003 foil. Consequently Kang et al. (2013) concluded that the L.E of a foil has significant effect on the flow structures and forces produced by a flapping foil.

Usoh et al. (2012) showed that a flat plate may be more advantageous than a NACA or streamlined foil, by promoting the LEV formation, providing more favorable interaction with the trailing edge. For foils at Re = 1100 and x_p = 1/3 they found a slight increase in efficiency (32.5% to 34.2%) in changing from NACA 0012 profile to a rectangular section with same cross-sectional area. With Kinsey and Dumas (2008), the effect in changes in thickness of the rectangular section was found to be minimal. For the flat plate, the LEV was observed to stay closer to the surface of the foil as it convected past the pivot point to the trailing edge as compared to a NACA profile, thus providing some increase in favorable moment and power generation in the second half of the pitch reversal. This seems a promising result, provided that a combination of mechanically simple passive actuation system like Platzer and Bradely (2009), coupled with a flat plate foil, could provide a cheap and robust system with equivalent performance as compared to complex semi-activated designs where pitch actuation motors or fully passive designs with complex mechanical linkages between heave and pitch motions.

Inspired by the structure of a scallop, Le et al. (2013) also investigated the geometric shape of the flapping foil numerically, to determine the effects of the foil with various degrees of camber on its power extraction performance. Their results show that the corrugated structure was advantageous in the control of the vortex activities, especially for a foil (model 008-200) with a combination of a large corrugation and a small degree of camber. A 6% improvement in power generation was achieved over a NACA0012 foil primarily because of enhanced power generation due to the interaction of the free stream velocity with the convex surface of the corrugated foil during the downstroke. They indicated that the improvement due to the corrugated foil could be could be up to 17% if this interaction occurs during both the upstroke and downstroke. Hence, they concluded that geometric wing/foil structures mimicking nature are more beneficial for power generation than conventional foil shapes.

2.3 STRUCTURAL FLEXIBILITY

Structural flexibility is known to have advantages on the performance of flapping foils in force generation. In previous studies on insect wings and fish fins suggest that to a certain degree of flexibility may lead to the generation of higher thrust or lift forces. This could be attributed to the structural resonance, the manipulation of the LEV generation, and the force reorientation effect associated with the deformations (Katz & Weihs, 1978; Zhu, 2007; Michelin et al., 2009; Yin and Luo, 2010; Massoud and Alexeev, 2010). On the other hand, the effect of structural flexibility on the performance of flapping wing energy harvesters is not fully studied. To understand this, Liu et al. (2013) computationally modeled a two-dimensional flexible flapping wings operating within the energy extraction regime. Rather than directly solving the coupled fluid-structure interaction problem, the flexible motion is pre-determined based on priori structural results.

The work of Caracoglia (2010) and Bryant et al. (2011-2013) bridges the gap between the flapping foil power generation literature and the small-scale energy harvesting literature. Caracoglia (2010) used a pivot point at the leading edge, with pitch motion but no plunge motion, to excite bending of an elastic support. Linear potential flow analysis predicted very low efficiency, however an order of magnitude lower than the Betz limit. Bryant and Garcia (2011) used a small (5.9 cm chord) rectangular planform NACA0012 section foil of aspect ratio 2.28, pivoted at the end of a flexible cantilever piezoelectric bimorph beam. They used a modification of the linear potential flow theory, accounting for arbitrary foil motions and for dynamic stall to predict the behavior of the system. Comparison with experiment showed remarkable agreement in time-averaged power generation P_{mean} and very good agreement in flutter frequency, generating just over 2 mW at a flow speed of 8 m/s, vibrating at approximately 4.5 Hz. Bryant et al. (2011-2013) compared the aerodynamic analysis technique to the Navier Stokes results of Kinsey and Dumas (2008) and showed that with sufficient tuning of parameters in empirical dynamic stall models, good agreement could be gained with the Navier Stokes simulations but without the computational expense, allowing for increased utility in design.

Hoke et al. (2014) took the same approach of prescribed deformation superimposed on the motion, for a 2D NACA0015 foil pivoted at s_{piv} =1/3 at Re = 1100 and 2.0×10^4. The motion kinematics were the same as the optimum case in Kinsey and Dumas (2008), that is h = 1.0, θ_o = 76.33°, ϕ = 90° and f^* = 0.14. This work complements that of Liu et al. (2013) as it examined the effect of camber changes, and the ideal phase ϕ_c between the camber deformation and the foil motion (ϕ_c = 90° produced a positive camber at the top of the flapping stroke). Thus, it created foil deformations akin to the Liu et al. work with the LEC amplitude reversed. Values of ϕ_c between -180° and -60° improved the efficiency (from η = 33% to 38% for ϕ_c = -135°). For the best case ϕ_c = -135° plunge power C_{Py} was increased by a camber profile that lowered the instantaneous angle of attack of the leading edge during the upstroke (t/T = 0.25), and then curved the trailing edge towards the LEV, "*cupping*" it as it convected past the foil, increasing pitch power $C_{P\theta}$ at the stroke reversal (t/T = 0.5).

Kedare and Date (1990) reported on the analysis of an oscillating wind energy extraction device, to be used to drive a reciprocating pump. This consisted of a flexible sail mounted on a pivoting frame at one end of a swing-arm. The frame was constrained in the maximum angle of pitch relative to the swing-arm via a cable, which allowed the frame to flip and initiate stroke reversal in response to aerodynamic forces. The principle of operation is very similar to that of Platzer and Bradley (2009), although with a rotating swing-arm rather than vertical motion, and a flexible sail rather than a foil. The analysis used quasi-steady aerodynamics with lift and drag coefficient values for the sail derived from experiment and showed that the device had a lower cut-in speed than a conventional rotational turbine under the same wind conditions.

Using a coupled fluid-structure interaction algorithm, Liu et al. (2016) numerically investigated the effect of structural flexibility upon the energy extraction capacity of an oscillating foil with realistic internal structure, characterized by a stiffener near the trailing edge. The power generation predicted by the model in this study is the net energy flux from the flow field to the foil. Two types of real material were tested out for the stiffener; copper and tungsten carbide with different effective stiffness and density ratios. To distinguish the effects of Young's modulus coefficient and density ratio of the dynamic response and energy extraction efficiency, cases were also studied with the stiffener made of virtual materials with arbitrary Young's modulus and density. Simulation results reveal that the flexibility around the trailing edge could enhance the overall energy extraction performance. For example, with copper stiffener, an increase of 32.2% in efficiency can be reached at high reduced frequency. The performance enhancement is achieved mostly in cases with low Young's modulus and density ratio. A possible underlying mechanism is that the specific foil deformations in these cases encourage the generation and shedding of vortices from the foil leading edge, which is known to be beneficial to flow energy extraction.

2.4 REMARKS

The potential for employing flapping foils in the power generation mode is evident from the literature survey discussed above in detail. The flip-side of the argument is the shortfall in the literature with very little in-depth comparison and placement of flapping foil strategies in context against existing technologies.

Till now, there has been no reported rigorous assessment of the theoretical maximum power extraction capability of flapping foils as there are available for rotary systems. Research indicates that flapping foil design can be significantly superior to rotary turbines at low speeds, however this comparison requires extensive work to quantify performance across the whole range of flow speeds and Reynolds number. Highly efficient fluid dynamic mechanism in natural flyers and swimmers, offers the potential to apply the same in the power generation domain however, this requires new and detailed knowledge of the fundamental problem of interaction between a moving body immersed in a flow, the vortex structures that this motion creates, and the feedback between the motion and the flow structure i.e. more detailed knowledge of the physics of fluid structure interaction. Broad range in reported energy conversion efficiency results in literature shows the system's sensitivity to LEV dynamics and system robustness (from the design concept) to flow conditions.

Also, very much related is the issue of wing profile and planform. A lunate crescent shape has been shown to be optimal for fast swimming fish for propulsion (Chopra, 1974), however a high aspect ratio rectangular wing might be advantageous for power generation, to create as close to two-dimensional conditions on much of the foil as possible and minimize the impact of foil tips. Kinsey et al. (2011) and Kinsey and Dumas (2012) have considered the effect of endplates on the performance of their power generator consisting of a high aspect ratio rectangular foil, but profile shape has not been investigated in great depths in the literature, leading to our second research question (section 1.2).

Furthermore, it is evident from our literature survey and from Table 2.1 that the majority of the numerical and experimental studies related to flapping wing energy harvesters, have only focused fully prescribed (active) or semi-active flapping mechanisms [Kinsey and Dumas (2008), Zhu et al. (2009), Zhu and Peng (2009)). In contrast a fully flow driven flapping wing power generator has only being researched by a few. Neither a detailed fluid-structure interaction analysis nor an extensive parametric study of a passively actuated flapping foil energy harvester has been identified in our literature survey.

It is therefore the focus of this doctoral research to exploit this aforementioned gap in literature and focus on the design and development of a fully passive experimental device which can mimic a 2-DoF flapping motion. Such an experimental device would not include any kind of elaborate mechanical system to prescribe a certain type of kinematics and induce phasing between pitching and plunging motion modes, rather such motion modes should be "*flow-induced*". The test-rig whould also have the room to accommodate sensors for real-time force and motion measurements to analyze the "*hydrodynamic power extraction efficiency*" through variation of key parameters such as pivot location and pitching amplitude. The system will also be able to incorporate different wing profile shapes of the same planform and compare with the baseline flatplate wing. This will also help to determine any effects of morphology on "*hydrodynamic power extraction efficiency*" of this test rig through a thorough experimental qualitative and quantitative assessment.

To provide a comprehensive, yet summarized view of the past research work on flapping foils for energy harvesting, Figure 2.3 provides a pictorial representation of the effects of different parameters such as pivot location (x_p), pitching amplitude (θ_o), phase difference (φ), heaving amplitude (h_o) and reduced frequency (k) against energy extraction efficiency (η) from selected literature sources. Table 2.1 details the literature sources from 1981 till date, tabulating the different geometrical and kinematic parameters used to analyze the energy extraction performance of flapping foils through either numerical, experimental or both in these studies.

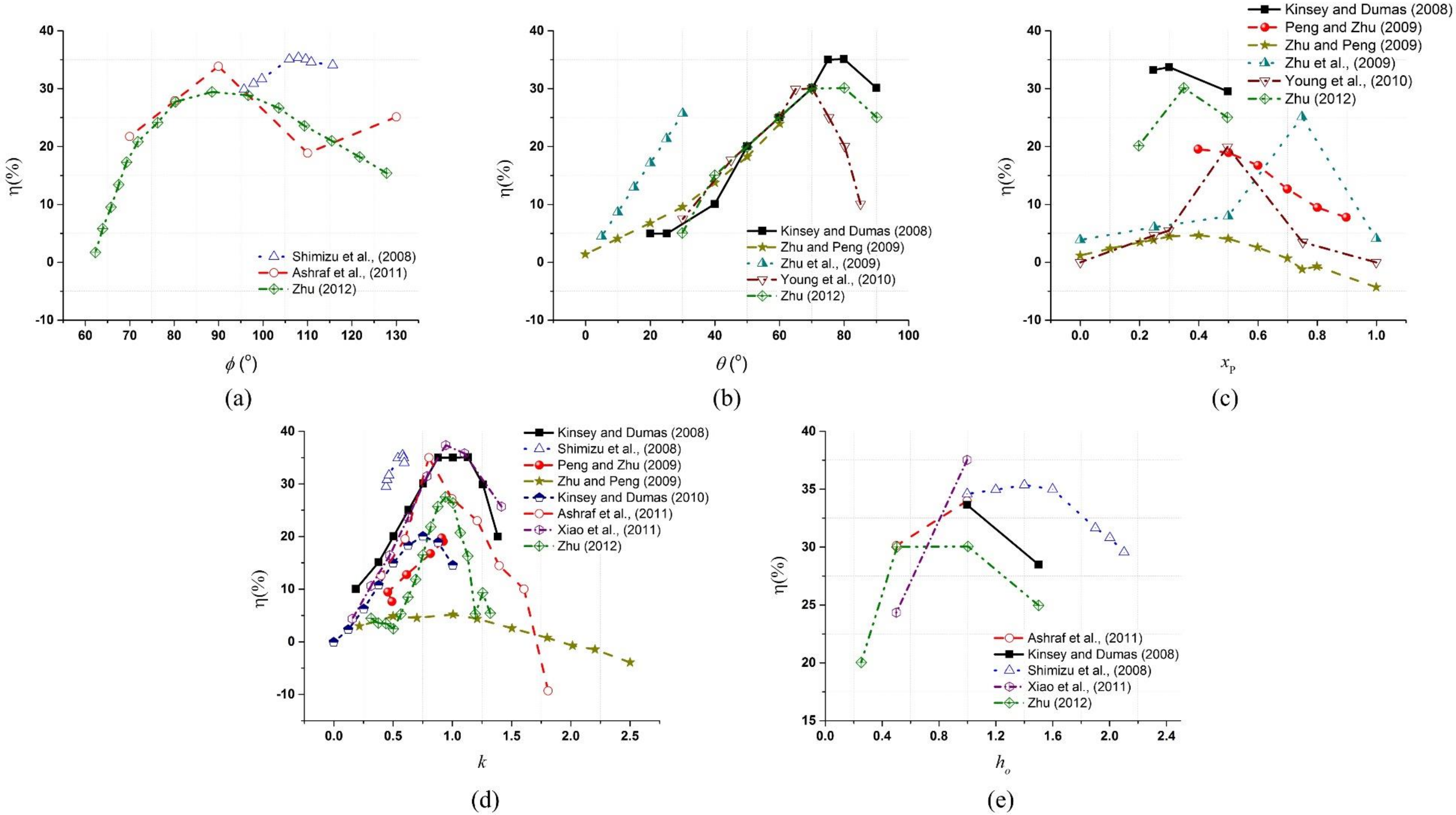

Figure 2.3: Effects of kinematic parameters: **(a)** Phase difference between pitching and heaving motion (ϕ), **(b)** Pitching amplitude (θ_o), **(c)** Pivot location from leading edge (x_p), **(d)** Reduced frequency (k) and **(e)** Heaving amplitude (h_o) on efficiency (η). Results adapted from Kinsey and Dumas (2008) (Re = 1100), Shimizu et al., (2008) (Re = 462,000), Kinsey and Dumas (2010) (Re = 500,000), Young et al., (2010) (Re = 1100), Zhu (2011) (Re = 1000), Xiao et al., (2012) (Re = 10,000), Ashraf et al., (2011) (Re = 20,000) and Peng and Zhu (2009) (Re = 1100).

S/N	Author	Method	Reynolds Number	Wing/Foil Model	Kinematic Parameters	Flapping Kinematics	Performance
1	McKinney & DeLaurier (1981)	Experimental	Re = 85,000, 110,000	NACA0012	Frequency = 2.5 to 3.5Hz, θ_o = 25°, 30°, h_o = 6 cm, x_p = 0.5c, ϕ = 60 to 135°	Fully Passive Sinusoidal	C_{Pmean} = Not given η = 28%
2	Jones and Platzer (1997)	Numerical: 2D Analysis using Panel Code	Re = 1,000,000	NACA0012	k = 0.1 to 20, θ_o = 8°, h_o = 0.2c x_p = 0.25c, ϕ = 100°	Prescribed: Sinusoidal plunge and pitch motions.	C_{Pmean} = -0.0096 η = Not given
3	Jones et al. (1999)	Numerical & Experimental	Re = 30,000	NACA0012	k = 0.5 to 0.8, θ_o = 25°, 30°, h_o = 0.3c, 0.95c x_p = 0.5c, ϕ = 90°	Prescribed: Sinusoidal plunge and pitch motions.	C_{Pmean} = 0.58 η = 26%
4	Davids (1999)	Numerical: Unsteady Panel method	Re = 28,000 to 46,000	NACA0012	k = 2.0, θ_o = 94°, h_o = 0.625cx_p = 0.3c & 0.55c, ϕ = 60° to 130°	Prescribed: Sinusoidal plunge and pitch motions	C_{Pmean} = 0.90 η = 30%
5	Linsdey (2002)	Experimental: Tandem Arrangement	Re = 22,000	NACA0014	k = 0.8 to 1.3, θ_o = 10° to 20°, h_o = 1.0c, x_p = 0.25c & 0.333c, ϕ = 80° to 110°	Fully Passive: Sinusoidal	C_{Pmean} = 0.25 η = 23%

S/N	Author	Method	Reynolds Number	Wing/Foil Model	Kinematic Parameters	Flapping Kinematics	Performance
6	Jones et al. (2003)	Numerical: CFD	Re = 20,000, 1,000,000	NACA0014	$k = 0.65$, $\theta_o = 73^o$, $h_o = 1.3c$, $1.4c$, $x_p = 0.125c$ to $0.8c$, ϕ = 80^o to 110^o	Prescribed: Sinusoidal plunge and pitch motions	C_{Pmean} = 1.48 η = 33%
7	Dumas and Kinsey (2006)	Numerical: CFD 2D Analysis	Re = 500, 1100	NACA0015	$k = 0$ to 1.57, $\theta_o = 0^o$ to 90^o, h_o = $1c$ and $1.5c$, $x_p = 0.333c$, $\phi = 90^o$	Prescribed: Sinusoidal plunge and pitch motions	C_{Pmean} = 0.86 η = 34%
8	Kinsey and Dumas (2008)	Numerical: CFD 2D Analysis	Re = 1100	NACA0015	$k = 0$ to 1.57, $\theta_o = 0^o$ to 90^o, h_o = $0.5c$, $1.0c$ and $1.5c$, x_p = $0.333c$, $\phi = 90^o$	Prescribed: Sinusoidal plunge and pitch motions	C_{Pmean} = 0.86 η = 34%
9	Shimizu et al. (2008)	2D Numerical CFD	Re = 462,000	NACA0012	$k = 0$ to 0.30, $\theta_o = 50^o$, $h_o = 0.5c$ to $2.0c$, $x_p = 0c$ to $1.0c$, $\phi = 95^o$ to 115^o	Plunge motion: Passive Pitch Motion: Sinusoidal	C_{Pmean} = 1.27 η = 35%

S/N	Author	Method	Reynolds Number	Wing/Foil Model	Kinematic Parameters	Flapping Kinematics	Performance
10	Simpson et al. (2008)	Experimental	Re = 13,800	NACA0012	$k = 0.2$ to 0.6, $\theta_o = 11^o$ to 57^o, $h_o = 1.23c$, $x_p = 0.25c$, $\phi = 90^o$	Prescribed: Sinusoidal plunge and pitch motions	C_{Pmean} = Not given $\eta = 57\%$
11	Peng and Zhu (2009)	2D Numerical CFD	$Re = 1000$	Joukowski foil	$k = 0.80$, $\theta_o = 30^o$ to 90^o, $h_o = 1.0c$, $x_p = 0.2c$ to $0.75c$,	Fully Passive Non-Sinusoidal	C_{Pmean} = 0.29 $\eta = 20\%$
12	Zhu and Peng (2009)	2D Numerical CFD	$Re = 1000$	Joukowski foil	$\theta_o = 0^o$ to 60^o $x_p = 0.333c$	Plunge Motion: Passive Pitch Motion: Sinusoidal	C_{Pmean} = 0.36 $\eta = 27\%$
13	Zhu et al. (2009)	2D and 3D Numerical CFD	$Re = \infty$	NACA0005 NACA0025	$k = 0$ to 0.5, $\theta_o = 10^o$ to 30^o, $x_p = 0c$ to $1.0c$	Plunge Motion: Passive Pitch Motion: Sinusoidal	C_{Pmean} = 0.08 $\eta = 25\%$

S/N	Author	Method	Reynolds Number	Wing/Foil Model	Kinematic Parameters	Flapping Kinematics	Performance
14	Platzer et al. (2009)	2D Numerical CFD, Tandem configuration	Re = 20,000	NACA0014	k = 0.80, θ_o = 73°, h_o = 1.05c, x_p = 0.5c, ϕ = 50° to 130°	Prescribed: Sinusoidal plunge and pitch motions	C_{Pmean} = 1.44 η = 54%
15	Platzer et al. (2010)	2D Numerical CFD Tandem configuration	Re = 20,000	NACA0014	k = 0.80, θ_o = 73°, h_o = 1.05c, x_p = 0.5c, ϕ = 50° to 130°	Prescribed, Fully Passive Sinusoidal and Non-sinusoidal	C_{Pmean} = 1.44 η = 54%
16	Kinsey and Dumas (2010)	Numerical: CFD 2D Analysis	Re = 500,000	NACA0015	k = 0.69 to 0.75, θ_o = 75°, h_o = 1.0c, x_p = 0.333c, ϕ = 90°	Fully Passive Sinusoidal	C_{Pmean} = Not given η = 40%
17	Young et al. (2010)	2D Numerical CFD	Re = 1100	NACA0012	$Freq$ = 0 to 1 Hz, x_p = 0.5c, θ_o = 30° to 90°, ϕ = 90°, h_o = 0.5c, 1.0c	Fully Passive Sinusoidal and Non-sinusoidal	C_{Pmean} = 0.79 η = 30%
18	Abiru and Yoshitake (2011)	Experimental	Re = 60,000 to 120,000	NACA0015	k = 1.89, θ_o = 30°, 45°, 50°, h_o = 1.0c, x_p = 0.5c, ϕ = 90°	Plunge motion: Passive Pitch motion: Sinusoidal	C_{Pmean} = Not given η = 32%-37%

S/N	Author	Method	Reynolds Number	Wing/Foil Model	Kinematic Parameters	Flapping Kinematics	Performance
19	Ashraf et al. (2011)	Numerical CFD, Tandem Configuration, 2D Analysis	Re = 20,000	NACA0014	$k = 0.80c$, $\theta_o = 73^o$, $h_o = 1.05c$, $x_p = 0.5c$, $\phi = 90^o$	Prescribed: Sinusoidal and Non-sinusoidal Plunge and Pitch motions	C_{Pmean} = 1.43 $\eta = 54\%$
20	Kinsey et al. (2011)	Experimental: Tandem Configuration	Re = 480,000	NACA0015	k = 0.69 to 0.75, $\theta_o = 75^o$, $h_o = 1.0c$, $x_p = 0.333c$, $\phi = 90^o$	Fully Passive Sinusoidal	C_{Pmean} = Not given $\eta = 40\%$
21	Zhu (2011)	2D Numerical CFD	Re = 100, 500, 1000	Joukowski foil	k = 0.31 to 1.57, $\theta_o = 30^o$ to 90^o, $h_o = 0.5c$ to $2.0c$, $x_p = 0.2c$, $0.35c$ and $0.5c$, ϕ = 30^o to 90^o	Prescribed: Sinusoidal Plunge and Pitch motions	C_{Pmean} = Not given $\eta = 30\%$
22	Bryant et al. (2012)	Numerical 2D Analysis	Re =1000	Not Mentioned	k = 0.31, 0.88, $\theta_o = -60^o$, -76.3^o, $h_o = 1.0c$, $x_p = 0.333c$, $\phi = 90^o$	Prescribed: Sinusoidal Plunge and Pitch Motions	C_{Pmean} = 0.70 $\eta = 27\%$

S/N	Author	Method	Reynolds Number	Wing/Foil Model	Kinematic Parameters	Flapping Kinematics	Performance
23	Campobasso and Drofelnik (2012)	Numerical: CFD 2D Analysis	Re =1100	NACA0015	$k = 0.88$ to 1.13 $\theta_o = 76.33^o$, $h_o = 1.0c$, $x_p = 0.333c$, $\phi = 90^o$	Prescribed: Sinusoidal Plunge and Pitch Motions	$C_{Pmean} = 0.86$ $\eta = 34\%$
24	Hoke and Young (2012)	Numerical: CFD 2D Analysis	Re = 1100	NACA0012	$k = 0.88$ to 1.57 $\theta_o = 76.33^o$, 90^o $h_o = 1.0c$, $x_p = 0.333c$, $0.5c$, $\phi = 90^o$	Fully Passive: Non-Sinusoidal Prescribe: Sinusoidal	C_{Pmean} = Not given $\eta = 38\%$, 47%
25	Huxham et al. (2012)	Experimental	Re = 45,000	NACA0012	$k = 0.025$ to 0.20 $\theta_o = 4^o$ to 62^o $h_o = 1.0c$, $x_p = 0.25c$	Plunge Motion: Passive Pitch Motion: Sinusoidal	$C_{Pmean} = 0.067$ $\eta = 24\%$
26	Isogai and Abiru (2012)	Analytical and Numerical CFD, 2D and 3D Analysis Multi-wing	Re = 38,000	NACA0015	$k = 0.30$ $\theta_o = 50^o$ $h_o = 0.972c$, $x_p = 0.5c$, $\phi = 90^o$	Plunge Motion: Passive Pitch Motion: Sinusoidal	C_{Pmean} = Not given $\eta = 25\%$ to 34%

S/N	Author	Method	Reynolds Number	Wing/Foil Model	Kinematic Parameters	Flapping Kinematics	Performance
27	Kinsey and Dumas (2012)	2D and 3D Numerical CFD Tandem configuration	Re = 500,000	NACA0015	$k = 0.88$ $\theta_o = 75^o$, $h_o = 1.0c$, $x_p = 0.333c, 0.5c$, $\phi = 90^o$	Prescribed: Sinusoidal Plunge and Pitch Motions	C_{Pmean} = 1.6 $\eta = 63\%$
28		2D Numerical CFD Tandem Configuration			$k = 0.25$ to 1.26 $\theta_o = 62^o$ to 75^o, $h_o = 0.75c$, $1.0c$, $x_p = 0.333c$, $\phi = 90^o$		C_{Pmean} = 1.64 $\eta = 64\%$
29		3D Numerical CFD			$k = 0.88$, $\theta_o = 75^o$, $h_o = 1.0c$, $x_p = 0.333c$, $\phi = 90^o$		C_{Pmean} = 0.84, $\eta = 33\%$
30	Xiao et al. (2012)	2D Numerical CFD	Re = 10,000	NACA0012	$St = 0.05$ to 0.6, $\alpha = 10^o, 20^o$, $\theta_o = 58^o$, h_o = $0.5c$, $1.0c$, $x_p = 0.333c$, $\phi = 90^o$	Prescribed: Sinusoidal Plunge and Non-Sinusoidal Pitch Motions	C_{Pmean} = 1.0 $\eta = 39\%$
31	Usoh et al. (2012)	Numerical 2D Analysis	Re = 1100	Flatplate	$k = 0.6$ to 1.2, $\theta_o = 50^o$ to 90^o, $h_o = 1.0c$, $x_p = 0.333$c,	Prescribed: Sinusoidal Plunge and Pitch Motions	$C_{Pmean} = 0.87$ $\eta = 35\%$

S/N	Author	Method	Reynolds Number	Wing/Foil Model	Kinematic Parameters	Flapping Kinematics	Performance
32	Campobasso et al. (2013)	Numerical: CFD 2D Analysis	Re =1,500,000	NACA0015	k = 0.88 to 1.13 θ_o = 76.33°, h_o = 1.0c, x_p = 0.333c, ϕ = 90°	Prescribed: Sinusoidal Plunge and Pitch Motions	C_{Pmean} = 1.01 η = 40%
33	Le et al. (2013)	2D Numerical CFD	Re = 90,000	NACA0012, NACA0008, Corrugated Airfoil	k = 0.63 to 1.57, θ_o = 55° to 65° , h_o = 0.67c to 1.0c, x_p = 0.333c, ϕ = 90°	Prescribed: Sinusoidal Plunge and Pitch Motions	C_{Pmean} = Not given η = 39%
34	Liu et al. (2013)	2D Numerical CFD	Re = 1,000,000	NACA0012	k = 0.31 to 0.94 α = 0°, 5°, 10°, h_o = 0.5c, 1.0c x_p = 0.333c, ϕ = 90°	Prescribed: Sinusoidal Plunge and Pitch Motions	C_{Pmean} = Not given η = 28%
35	Young et al. (2013)	2D Numerical CFD	Re = 1100, 1,100,000	NACA0012	$Freq$ = 0 to 1 Hz, θ_o = 30° to 90° , h_o = 0.5c, 1.0c, x_p = 0.5c, ϕ = 90°	Fully Passive	C_{Pmean} = 1.10 η = 41%

S/N	Author	Method	Reynolds Number	Wing/Foil Model	Kinematic Parameters	Flapping Kinematics	Performance
36	Deng et al. (2014)	Numerical CFD 3D Analysis	$Re = 1100$	NACA0015	$k = 1.02$ $\theta_o = 60.7^o, 73.3^o, 81.5^o$, $h_o = 1.23c$ $x_p = 0.333c$, $\phi = 90^o$, $St = 0.4$	Prescribed: Sinusoidal and Non-Sinusoidal Plunge and Pitch Motions	C_{Pmean} = Not given $\eta = 18\% - 27\%$
37	Platzer et al. (2014)	2D Numerical CFD	$Re = 1100$	NACA0012	$Freq = 0$ to 1 Hz, $\theta_o = 30^o$ to 90^o, $h_o = 0.5c, 1.0c,$ $x_p = 0.5c$, $\phi = 90^o$	Fully Passive	$C_{Pmean} = 0.8$, $\eta = 30\%$
38	Wu et al. (2014)	2D Numerical CFD	$Re = 1100$	NACA0015	$k = 0.63$ to 1.89, $\theta_o = 15^o, 22.5^o, 30^o, 37.5^o, 45^o$, $h_o = 0.5c$, 1.5c, 3c, $x_p = 0.333c$, $\phi = 90^o$	Plunge Motion: Passive Pitch Motion: Sinusoidal	C_{Pmean} = Not Given, $\eta = 28\%$
39	Lu et al. (2014)	2D Numerical CFD	$Re = 20,000$	NACA0012	$\alpha_o = 15^o$, $h_o = 0.8c$ $x_p = 0.333c$, $St = 0.05$ to 0.4	Non-Sinusoidal Plunge and Pitch Motions	C_{Pmean} = Not Given, $\eta = 24\%$

S/N	Author	Method	Reynolds Number	Wing/Foil Model	Kinematic Parameters	Flapping Kinematics	Performance
40	Le et al. (2015)	2D and 3D Numerical CFD	Re = 90,000	NACA0012 Chord-wise and Span-wise Flex	$Freq$ = 0.5 Hz $\alpha = 0^o, 5^o, 10^o$, $h_o = 0.75c$ $x_p = 0.333c$, $\phi = 90^o$	Prescribed: Sinusoidal Plunge and Pitch Motions	C_{Pmean} = Not given η = 33%
41	Xu et al. (2016)	2D Numerical CFD Tandem Configuration	Re = 44,000	NACA0015	k = 0.06 to 0.21 $\theta_o = 70^o$, h_o = 1.0c $\phi = 90^o$	Prescribed: Sinusoidal Plunge and Pitch Motions	C_{Pmean} = Not given η = 53%
42	Wu et al. (2016)	2D Numerical CFD	Re = 1100	NACA0015	k = 0.1 to 0.2, $s_m = 0.05h_o$ to $0.2h_o$, $\theta_o = 75^o$, h_o = 1.0c, x_p = $0.333c$, $\phi = 0^o$ to 315^o (between surging & pitch-plunge)	Prescribed: Sinusoidal Plunge, Pitch and Surging Motions	C_{Pmean} = Not given η = 35.55%

Table 2.1: A summary of studies undertaken on the flapping-foil turbine concept, showing the key operating conditions and performances mentioned in each of the studies.

METHODOLOGY

3.1 TEST MODEL

Experimental study of a passively oscillating energy harvester is carried out in the Water Tunnel Laboratory. The open channel water tunnel has a test section of 0.3 m (W) × 0.6 m (H) × 2.0 m (L) as shown in Figure 3.1. The flow speed can be adjusted from 0.05 m/s to 4 m/s, but flow speeds higher than 1 m/s can only be achieved through sealing the test section and pressurizing the flow.

The tunnel is powered by a 60 hp, 380 V AC, 3-phase, 6 pole motor pump system. The test section of the water tunnel is composed of removable panels on top, bottom and sides which can be removed according to the requirements of the experiment. For this research, only the top acrylic panel is removed since the mechanical test bench is placed on top of the water tunnel test section.

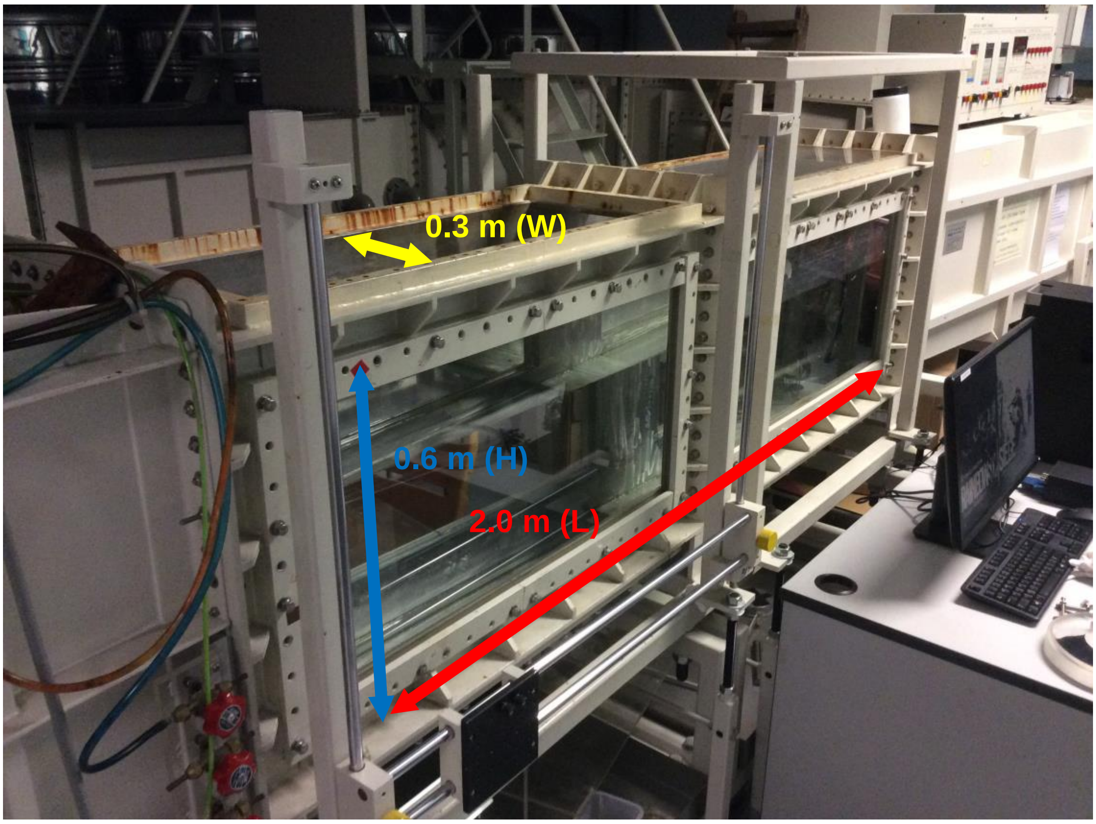

Figure 3.1: Water tunnel test facility in the Department of Mechanical Engineering at The Hong Kong Polytechnic University.

Our main and first objective was to design and develop an energy harvesting device based on a passively flapping foil, where the kinematics are flow induced and the foil is not subjected to any kind of constrained motion or phasing between the two motion modes (plunging and pitching). From our literature survey in Chapter 2, we identified that among the researchers who visited the concept of energy extraction through passively flapping foil, Platzer (2009) was the only one to introduce such a concept for a device.

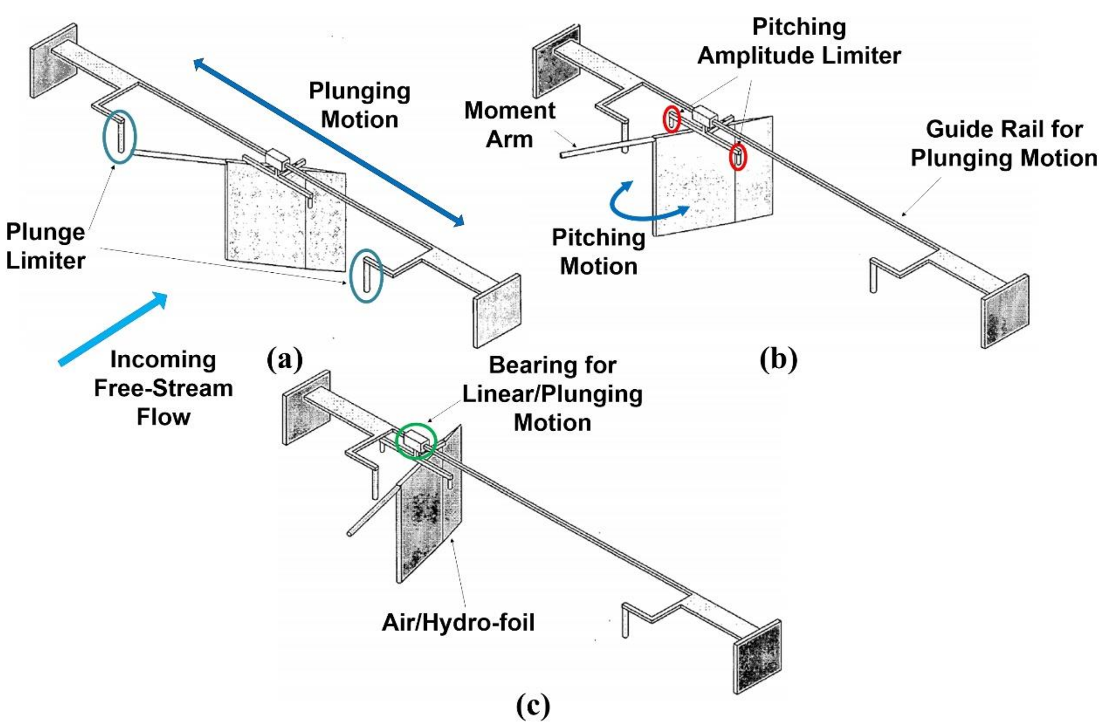

Figure 3.2: Schematic of the design concept for a flow induced flapping foil for energy harvesting introduced by Platzer et al. (2009) in his patent. The schematic shows different and simple mechanical parts of the concept, which can help the foil to perform flapping motion due to aero/hydro-dynamic forces and neither force a specific flapping profile nor induce fixed phasing between the plunging and pitching motions: **(a)** Foil at maximum pitching amplitude set due to the pitching amplitude limiter and moment arm contact and undergoing plunging motion (at Mid-Stroke), **(b)** Foil at start of stroke reversal (pitching motion) when the moment arm contacts the plunge limiter at the end of the plunging stroke, and **(c)** Foil undergoing stroke reversal and at the onset of the plunging motion in the opposite direction.

Figure 3.2 shows such a concept, which he introduced in his patent (Platzer et al., 2009). The concept focuses on a 2-DoF system, where two kinds of limiters are introduced (one for plunging motion (Figure 3.2 (a)) and the other for pitching motion (Figure 3.2(b)). The foil is connected to a bearing which is connected to a guide rail, which allows the foil to perform plunging motion under the influence of aero/hydro-dynamic forces. A moment arm is attached to the top of the foil, which allows it to not only rest pitching amplitude limiter during plunging motion, but also helps the foil to perform pitching motion (stroke reversal) when it contacts the plunger limiter at the end of the stroke (Figure 3.2(b)). As Figure 3.2 suggests, the concept does not consist of any elaborate mechanical systems and the foil’s energy harvesting performance is only dependent on the geometric and kinematic parameters.

Figure 3.3 shows our test rig for the flapping foil based flow energy harvester, which is based on the concept shown in Figure 3.2 and incorporates the same principles of flapping motion as discussed above. Modifications were introduced so that the necessary components may be attached for data logging and analysis. The design does not consist of any mechanical constraints, which make it unique to experimentally study the concept of energy extraction through flow induced flapping motion. The test rig is a two degree-of-freedom (DoF) passive system where the plunge motion, i.e. translation in the cross-flow direction, and pitching motion, i.e. rotation about the hydrofoil span wise axis, can be performed under the influence of hydrodynamic forces. It consists of a small aluminum block with two linear bearings underneath it which helps it to perform plunging motions on two guide rods. The guide rods are supported by four linear mounts which are installed on the main aluminum platform. The small aluminum block houses two sensors: a rotary encoder and an accelerometer. The rotary encoder is a hollow shaft type incremental encoder which helps it to be clamped with the top part of the vertical cantilevered shaft. Hence, when the shaft rotates, the encoder's moving part also rotates with it. The vertical cantilevered shaft is divided into four parts to house the force sensor in between. The test rig consists of two kinds of limiters: plunging limiters (Figure 3.3(a)) and pitching limiters (Figure 3.3(b)). These limiters help in setting the plunging and pitching range. A moment arm is attached to the vertical cantilevered shaft which performs the stroke reversal, at the end of each plunging motion stroke. By contacting the plunge limiter, the hydrofoil flips which is possible due to the inertia of the small aluminum block traveling on the linear guide rail and the hydrodynamic forces from the water flow, allowing the hydrofoil to move in the opposite direction.

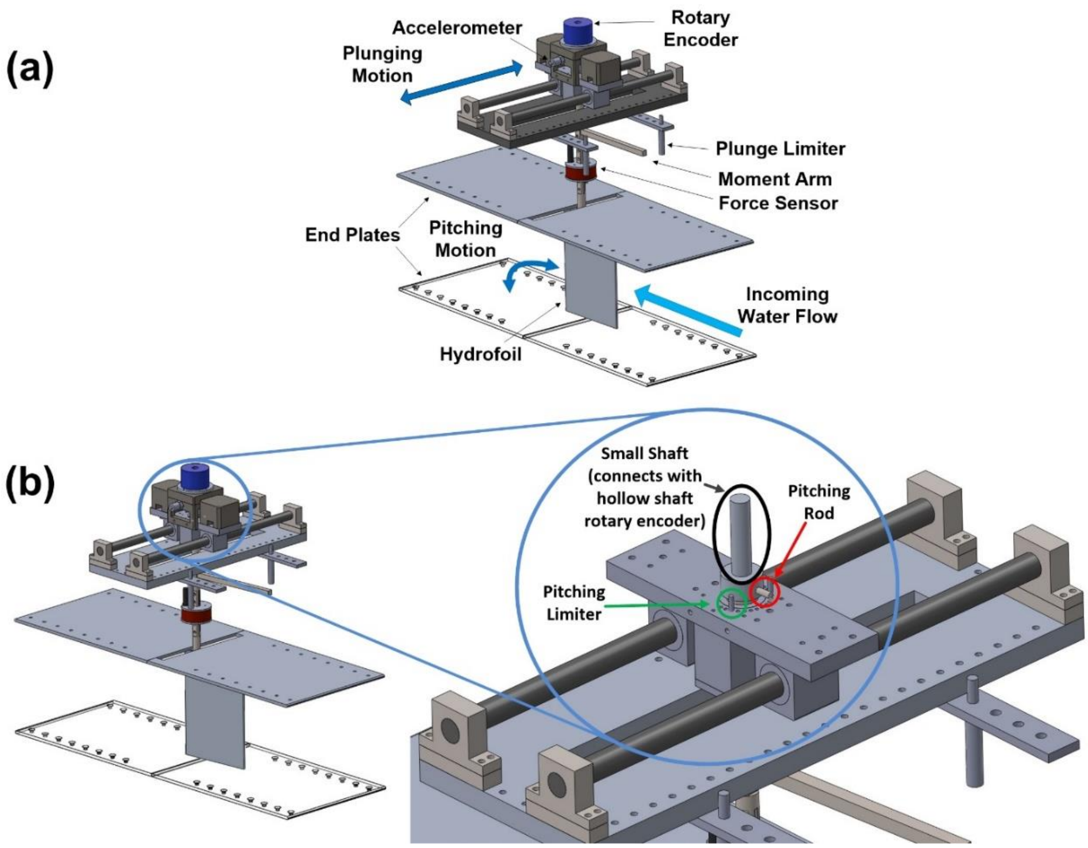

Figure 3.3: (a) Schematic of the experimental setup of a passively oscillating energy harvester with sensors, hydrofoil and endplates installed, **(b)** Exploded view of top of small aluminum block showing the pitching limiter and pitching rod setup.

A similar design was first tested out by Semler & Platzer in 2009 as a part of a MSc thesis research based on Platzer & Bradely patent design (2009). Their main objective at that time was first to investigate the feasibility of such a device, which can be driven into sustainable flow induced flapping motions, determine generally the different geometric and kinematic parameters at which this device works and qualitatively visualize the flow field around it. Figure 3.4 shows the difference between the two devices in terms of design. The approach to our fluid-structure experimental investigation is different and exhaustive compared to what was done by Semler (2009) although a few parameters are common among both studies. Table 3.1 lays out the main differences in mechanical design in detail between the two setups. Further discussion will be carried out at the end of Chapter 5 which will include a detailed comparative analysis of the results obtained in this study and with Semler (2009), Platzer et al. (2010) and Ashraf et al. (2011).

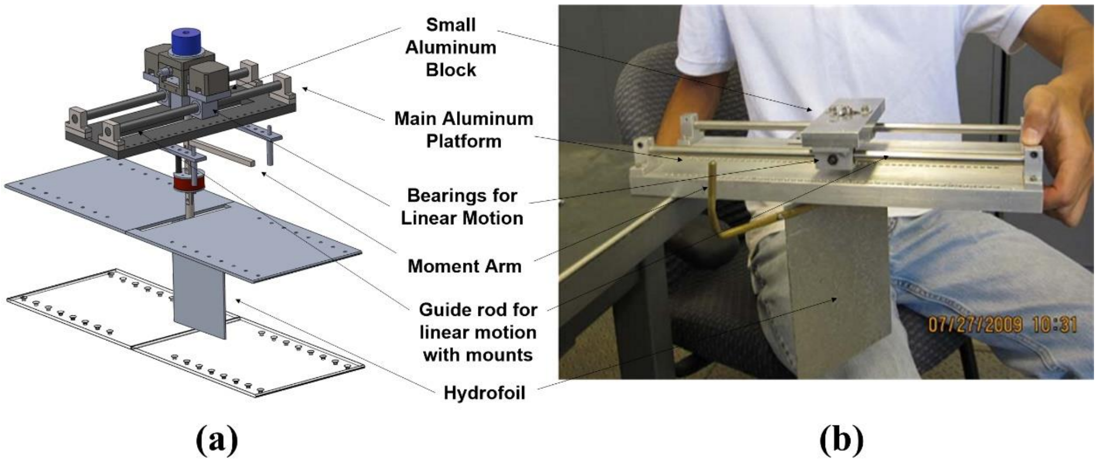

Figure 3.4: Schematic of the experimental setup of **(a)** our passively oscillating energy harvester with sensors, hydrofoil, inertial mass and endplates installed, while **(b)** Semler's setup. The labelled parts show some of the similarities between the two setups, while the ones not labelled shows the absence of parts and devices on Semler's setup.

Design Aspect	M. N. Mumtaz Qadri's Setup	Cogan. S. Semler's Setup
Main Platform	Aluminum Base: 400 mm × 150 mm × 15 mm	Aluminum Base: 381 mm × 153 mm × 21 mm
Small Block on Guide Rail	Aluminum Base: 180 mm × 55 mm × 12 mm	Aluminum Base: 152 mm × 50 mm × 13 mm
Bearings for Linear Motion	2 × SKF LUCE 16-2LS Linear Bearing in Housing	Thomson SPB-6 Super Ball Bushing Pillow Block
Guide Rails and Mounts	2 × SKF LJMR16 Precision Shaft, ESS2 × 400 mm and 4 × SKF LSCS 16 Mounts	Rails with $3/8^{th}$ inch diameter steel and 381 mm long
Bearings for Rotation	1 × Deep Groove Ball Bearings (single row) and 1 × Thrust Ball Bearings (single direction)	Ball Bearing with ½ inch diameter
Vertical Shaft	1 × continuous telescopic stainless-steel shaft with 15 mm dia and then 14 mm dia 1 × telescopic stainless-steel shaft with 15 mm dia and then 14 mm dia divided into two parts to hold Force Sensor with custom made flange. Has a cutout at its end to place the hydrofoil in between	½ inch diameter steel cylindrical shaft. Has a cut through the middle of one end and small holes drilled for the flat plate attachement
Hydrofoil Foil	Acrylic Flat plate foil (140 mm (c) × 200 mm (b) × 5 mm (t))	Aluminum Flat plate (143 mm (c) × 186 mm (b) × 1.5 mm (t))

	3-D printed Elliptical Foil and NACA0006 foil with same chord length and span as flat plate foil All hydrofoils have slits cut out for varying the pitch axis location and connecting to the end of the vertical shaft with screws.	There is a slit that is cut along the upper portion of the flat plate that allows varying the pitch axis location.
Moment Arm	168.5 mm length from vertical shaft stainless steel with square cross section of 90.25 mm^2	13 cm extension from the flatplate shaped like a long "L".
Inertial Mass	3 types of inertial mas blocks; m_{ib} = 0.45 kg, 0.90 kg and 1.35 kg used in pairs	1 type of inertial block used with mass 0.0567 kg.
End Plates	Four end plates; two top (364 mm × 245 mm × 5.5 mm) and two bottom (351 × 245 mm × 5.5 mm). One of top endplates placed in forward position has a special cutout so that the foil can plunge without interfering with it. The top ones are opaque while the bottom ones are transparent.	Nil
Plunge Limiting Method	2 × telescopic rods (6.6 mm to 10 mm) and total length 72 mm. Set by screwing them to a small rectangular and then screwing it to the Main Platform which has M4 screw holes at 15.5 mm apart.	Water Tunnel 1: using the water tunnel test section wall. Water Tunnel 2: Using magnets to allow stroke reversal and limiting the plunge distance Towing Tank: Using metal fingers to limit the plunge distance as the moment arm strikes it at the end of each stroke.
Pitching Amplitude Limiting Method	15 × M3 holes placed in a semi-circular domain offering pitching amplitude ranges from 8° to 82°.	Adjustable piece on the shaft and small block that controls how far the flat plate can rotate. Maximum angle set between 10° and 75°.
Hardware for Performance Analysis	6 – axis force sensor, rotary encoder and uni-axis accelerometer along with Data Acquisition Hardware	Nil

Table 3.1: Comparative analysis of our and Semler's mechanical design and setup of a flow induced/passively flapping foil energy harvester system.

Figure 3.5 shows the kinematics of the passively oscillating hydrofoil performing 2-DoF motion. When the water in the test section reaches a velocity, also known as the cut-off velocity ($U_{o\text{-}cutoff}$), the hydrofoil being at a certain angle of attack (θ_o) will start to move due to the application of hydrodynamic forces of the incoming water flow. The test rig has a pitching limiter which can be used to set the maximum and minimum pitching angle ($+\theta_o$ and $-\theta_o$). Due to the hydrodynamic forces, the hydrofoil will first rotate to $+\theta_o$ or $-\theta_o$ depending on its original orientation and then translate (upstroke or downstroke depending on its original angular orientation). Since the hydrofoil is coupled with the small aluminum block (Figure 3.3) via the vertical cantilevered shaft. The hydrofoil and the small aluminum block together plunge on the guide rod due to the hydrodynamic forces on the hydrofoil. When the moment arm (Figure 3.3), which is attached to the vertical cantilevered shaft touches the plunge limiter, the hydrofoil starts to rotate. This rotation (stroke reversal) continues until the small aluminum block and the hydrofoil decelerate to the point where the hydrofoil pitching angle is almost zero (horizontal with the incoming free-stream water flow). The inertial blocks attached on the small aluminum block provide extra weight to flip the hydrofoil to a few degrees in the opposite direction. Since the free-stream water flow is still incoming and exerting hydrodynamic forces on the hydrofoil, which eventually flips the foil to the opposite direction hence completing the stroke reversal. The lift force is now in the opposite direction which lets the hydrofoil and the small aluminum block to translate (plunge) in the new direction. This process is repeated allowing the hydrofoil to flap in a periodic fashion upon the action of the hydrodynamic forces due to the incoming water flow. The hydrofoil performs a non-sinusoidal pitching motion and sinusoidal plunging motion under the influence of the hydrodynamic forces. Since, the test rig is a fully passive system consisting of very simple mechanical parts, the force and motion kinematics acquired from the sensors are purely dependent on the flow conditions and/or the physical parameters set to study their influence on the energy extraction performance of the system.

To maintain the two dimensionality of the study, four end-plates made from acrylic sheets are suspended from the top of the channel, with two above and two below the fully submerged hydrofoil to reduce the end effects, with a clearance of approximately 3.5 mm. The approximate distance between the leading edge of the front endplate and the leading edge of the foil (when at $\theta_o = 0^{\circ}$ and $x_p = 0.65c$) is 265 mm with variation of ±21mm depending on the pivot location setting. The top end plates are made from black acrylic to avoid background reflection and are arranged to introduce a slit to ensure un-interrupted plunging motion.

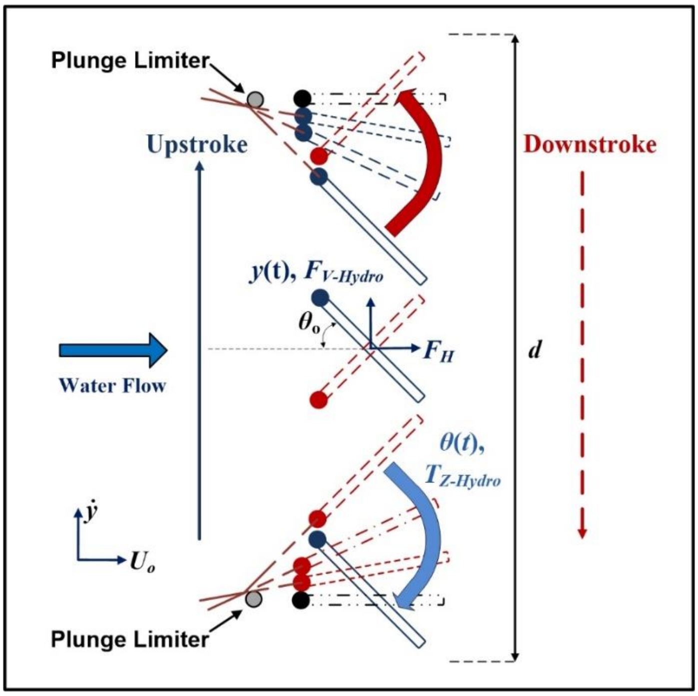

Figure 3.5: Motion kinematics of a passively oscillating hydrofoil in energy extraction mode. The hydrofoil performs a non-sinusoidal angular displacement during both upstroke and downstroke motions. The stroke reversal (pitching motion) is performed with the help of the moment arm and plunge limiter at the both extremes.

Three hydrofoil profiles were selected with rectangular planform to study the energy extraction concept through flapping motion. The flat plate foil was selected as the baseline hydrofoil, while an elliptical shaped foil and NACA 0006 profile were selected to comparatively study the morphological effect on energy harvesting through passively actuated flapping motion. For all three airfoils, the chord length (c) was set to 140 mm, span (s) 200 mm and mass (m_f) 180g. Measurements were conducted at freestream velocity U_o = 0.57, 0.65 and 0.78 ms^{-1}, corresponding to Re_c = 0.7 × 10^5, 0.9 × 10^5 and 1.1 × 10^5.

3.2 SENSORS AND DATA ACQUISITION HARDWARE

To study the performance of the passively oscillating energy harvester, it is important to acquire real-time data for hydrofoil motions, hydrodynamic forces, and surrounding flow field through various sensors and measurement systems. A schematic is shown in Figure 3.6, which shows the data flow between the different sensors and data acquisition module which is connected to a PC.

A six-component ATI Mini-40 SI-80-4 IP68 Force/Torque (F/T) sensor from ATI Industrial Automation Inc. was used to measure the forces and moment on the flapping hydrofoil. The sensing range for the sensor on the F_x and F_y axes was ±80 N with a resolution of 0.02 N and ± 4 N-m measurement range for the torque on the sensor's z-axes (T_z) with a resolution of 5×10^{-4} N-m. The measurement uncertainty on the full-scale load during the calibration tests conducted by ATI Industrial Automation Inc. was 1.5%, 1.25% and 1.5% for F_x, F_y and T_z respectively. Additionally, we also tested out a group of small weights from 0 to 470 g to measure F_x, F_y and T_z and plotted them against the applied weights, as shown in Figure 3.7. After plotting the scatter points, liner curve fit was applied to check the dispersion of the measured force as shown in Figure 3.7, where the measured points have shown a best fit with their respective linear polynomials. Figure 3.8 shows our methodology for applying the weights to the load cell, with the help of a string and a small diameter cylindrical shaft. The force sensor was attached to the vertical cantilevered arrangement between the hydrofoil and the main aluminum platform, oriented with its cylindrical z-axes normal to the pitch-plunge plane, as shown in Figure 3.3.

For the measurement of angular displacement because of pitching motion, a Sendix Incremental 5020 Push Pull configuration rotary encoder with 2000 pulses per revolution from Kubler was chosen. The incremental encoder is hollow shaft type and assembled on top of a mount attached to the top of small aluminum block. The top part of the vertical cantilevered shaft has a small cylindrical metal piece protruding out of it which can be inserted into the hollow section the rotary encoder and secured. This allows the encoder's rotating part to move as the pitching motion occurs, allowing the data acquisition system to acquire the digital signal. For measurements, the initial position of the sensor was set to 0 degrees at the start of the real time measurements, which was done in the acquisition preferences for the sensor in LabView. Although, there was no electronic feedback to verify the angular displacement data the pitching limiters acted as mechanical feedback. The pitching limiters were set in position holes, as shown in Figure 3.3(b), and the angular displacement between each pair holes (mirror image to each other about the H or x axis) was known in the test-rig design stage. After setting them the experiments were conducted and peak to peak angular displacement was checked from the data acquired, which would be in agreement with the angular displacement between the two pitching limiters. In most cases, the angular displacement profile would not have the x-axis as its center line so either it would have moved up or down. Irrespective of that, the peak to peak angular displacement will still be total agreement with the set pitching limiter angular displacement, therefore the data would be centralized about the x-axis.

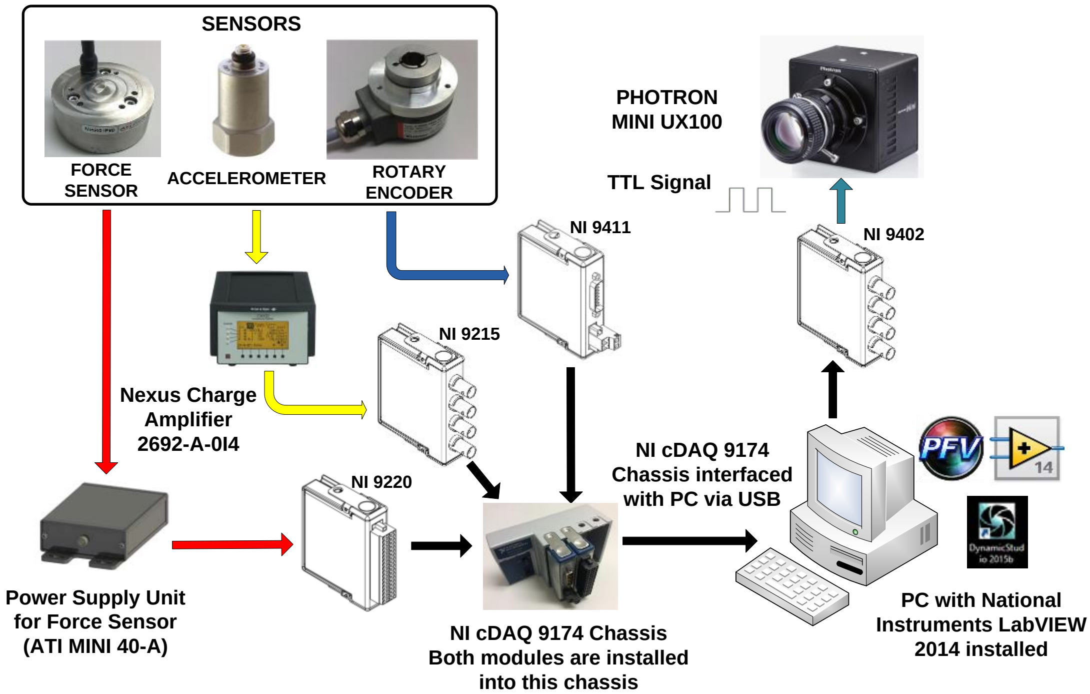

Figure 3.6: Schematic showing interfacing between sensors and their respective DAQ modules, which are then installed into a single NI cDAQ 9174 chassis. The chassis is then connected to the PC with LabVIEW 2014 installed, via a USB cable.

For the linear displacement measurement, a Type 4382V uni-axis charge accelerometer from Bruel & Kjaer was used. The sensor was mounted on one side of the mount as shown in Figure 3.3 and was connected to a Nexus Charge Amplifier 2692-A-0I4. This device is a 4-channel charge conditional amplifier with single and double integration which allows to calculate velocity and displacement information from the accelerometer. The conditioning amplifier was set to double integration so that the displacement information can be sent to the data acquisition system. A Type 4294 accelerometer calibrator from Bruel & Kjaer was used to calibrate the accelerometer. After the calibration, the accelerometer was inserted back onto the test-rig and verification experiments were conducted with image acquisition. Since, the accelerometer was inline with the pivot axis, peak to peak values were verified against peak to peak values attained from two images belonging to the maximum and minimum position of the hydrofoil (i.e. end of stroke). The images were first calibrated in Digimizer v. 4.6.1 and then the peak to peak distance of the pivot position was calculated, and then verified against the displacement data acquired from the sensor, with approximately average percentage error in the range of 0.5-2.5%.

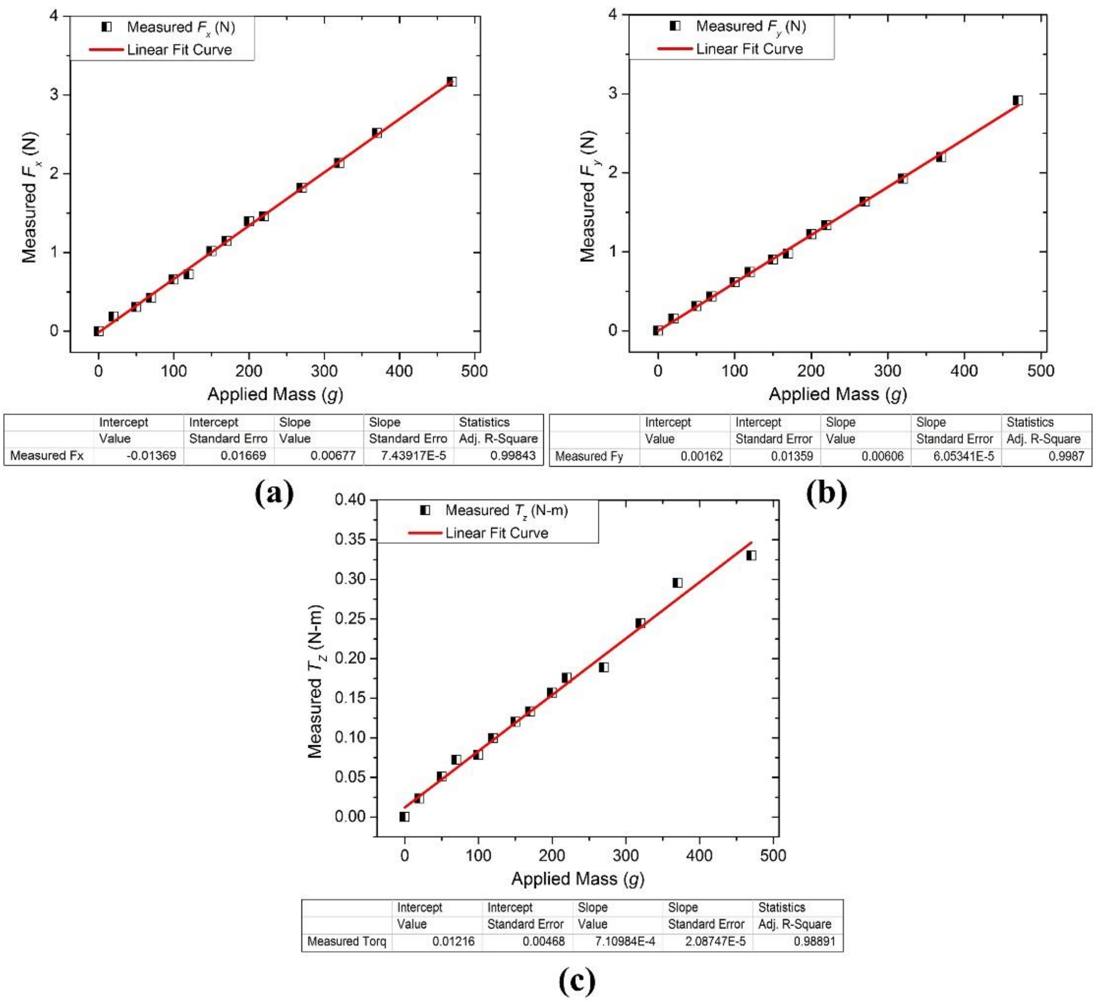

	Intercept Value	Intercept Standard Erro	Slope Value	Slope Standard Erro	Statistics Adj. R-Square
Measured Fx	-0.01369	0.01669	0.00677	7.43917E-5	0.99843

	Intercept Value	Intercept Standard Error	Slope Value	Slope Standard Error	Statistics Adj. R-Square
Measured Fy	0.00162	0.01359	0.00606	6.05341E-5	0.9987

	Intercept Value	Intercept Standard Error	Slope Value	Slope Standard Error	Statistics Adj. R-Square
Measured Torq	0.01216	0.00468	7.10984E-4	2.08747E-5	0.98891

Figure 3.7: Plots showing the dispersion of measured forces **(a)** F_x, **(b)** F_y and **(c)** T_z against small applied mass to the force sensor.

All sensors are connected to a computer via a National Instrument (NI) cDAQ 9174 Compact DAQ chassis which houses three different DAQ modules interfaced with the sensors: two analogue input modules (NI 9220 for the ATI force

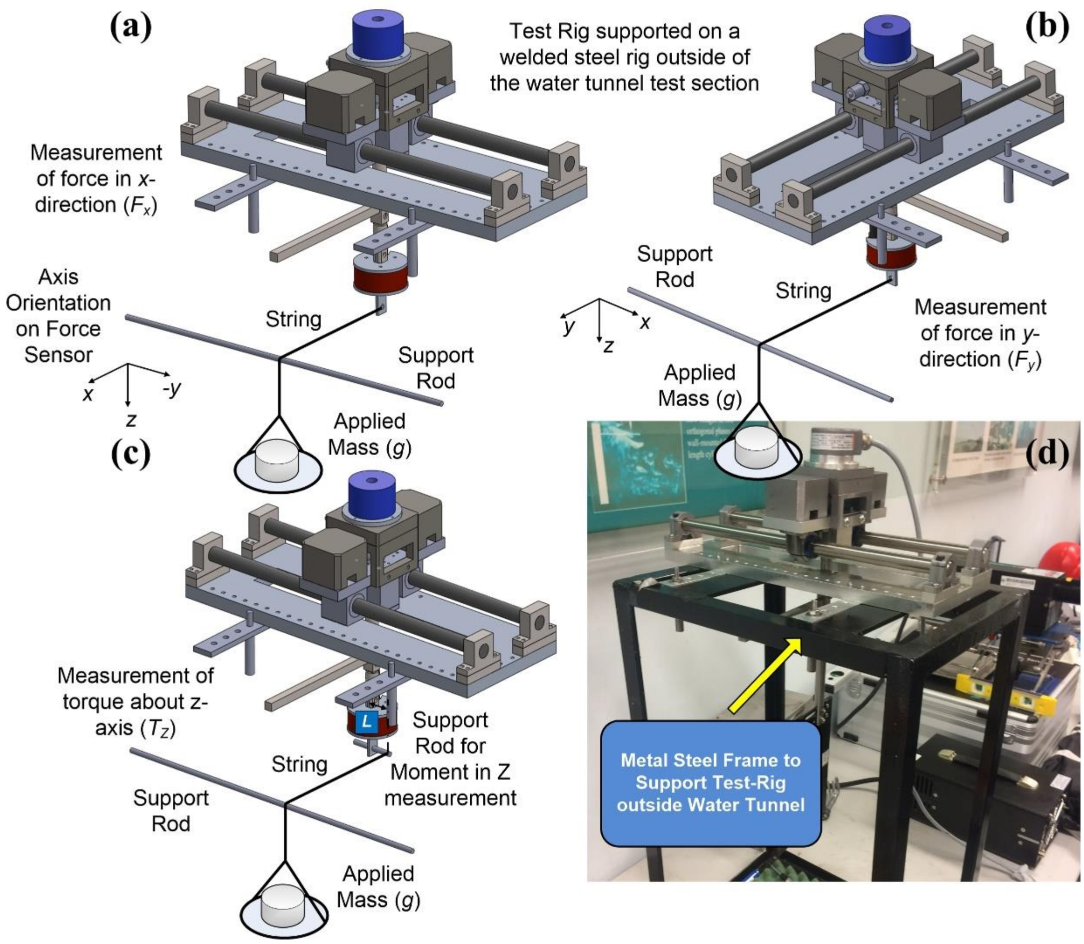

Figure 3.8: Schematics for measuring (a) F_x, (b) F_y and (c) T_z from force sensor in static mode. The test-rig was installed on steel frame specifically made to support it outside the water tunnel for operational reasons as shown in (d). The support rod was installed on the vertical frames of the frame.

sensor and NI 9215 BNC for the charge accelerometer) and one digital input module (NI 9411 for the rotary incremental encoder) as shown in Figure 3.3. The accelerometer was connected to the input section of the channel 1 of the charge amplifier. Since the amplifier was set to double integration, the displacement signal with a gain value set at 1V/m on the conditioning amplifier was sent to the NI 9215 BNC from the conditioning amplifier's output section of its channel 1. The sampling frequency was set to 2000 Hz for all sensors in the LabView program. Two VIs (Virtual Instrument) programs were designed for data acquisition from the sensors. One program was responsible for force and torque data acquisition from the force sensor while the second program for acquisition of displacement signals from the linear and rotary sensors. The second program also consisted of a module which could send TTL signals via NI 9402 BNC to the camera, as will be explained in next section. Both VI were synchronized and to achieve this the force-torque data VI was made as the Master program while the displacement VI was made as the Slave program. Upon activation of the Master VI, both programs would start and simultaneously will receive raw sensor data in real-time and would send TTL signals via the NI 9402 BNC output digital module.

3.3 SENSOR DATA POST PROCESSING

Figure 3.9 shows the assembly and orientation of the force sensor coupled with the hydrofoil. The positive *x* and *y* axes as set by the force sensor manufacturer can be seen in the figure, where the *x*-axis and the *y*-axis are parallel and perpendicular to the chord line respectively. To calculate the lift or vertical force acting on the hydrofoil, the force data from the sensor ($F_{x'}$ and $F_{y'}$) are decoupled using simple trigonometric and algebraic expression as shown in Equation 3.1:

$$\begin{aligned} F_V &= F_{y'} \cos\theta + F_{x'} \sin\theta \\ F_H &= F_{y'} \sin\theta - F_{x'} \cos\theta \end{aligned} \tag{3.1}$$

where F_V and F_H are the vertical (lift) force and horizontal (drag) forces which are parallel and normal to the plunging motion direction, respectively. As mentioned, the dynamic force and moment data acquired from the sensor are synchronized with the motion sensors and the acquired camera images, hence the instantaneous angular displacement data (θ) from the rotary encoder was used to calculate F_V and F_H using Equation 3.1. The *z*-axis of the force sensor was already perpendicular to the pitch-plunge plane and parallel to the vertical cantilevered shaft, hence no such transformation of moment (T_z) data was required.

Before this process of resolving forces, the force-torque (F_x and F_y) and linear displacement (y) data from the sensors were passed through a low pass filter with a cut-off frequency of 10 Hz to remove any noise or high-frequency components without sacrificing the profile and amplitude of the data. Using an in-house Matlab code the linear and angular displacement data were used to calculate the linear and angular velocities and acceleration ($\dot{y}(t), \ddot{y}(t)$ and $\dot{\theta}(t), \ddot{\theta}(t)$). A total of nine parameters including both measured and calculated parameters ($F_{x'}$, $F_{y'}$, T_z, $y(t)$, $\dot{y}(t), \ddot{y}(t)$, $\theta(t)$, $\dot{\theta}(t), \ddot{\theta}(t)$) were then phase-averaged.

In this setup, the forces measured consisted of two components: (i) the hydrodynamic force and (ii) inertial force. The energy extraction performance parameters were calculated using the hydrodynamic force and moment data. Therefore, the inertial forces were subtracted from the measured force and moment data to obtain the hydrodynamic force and moment values. The equations are as follows;

$$F_{inertial} = m\ddot{y}(t)$$
$$F_{V-Hydro} = F_V - F_{inertial} \tag{3.2}$$

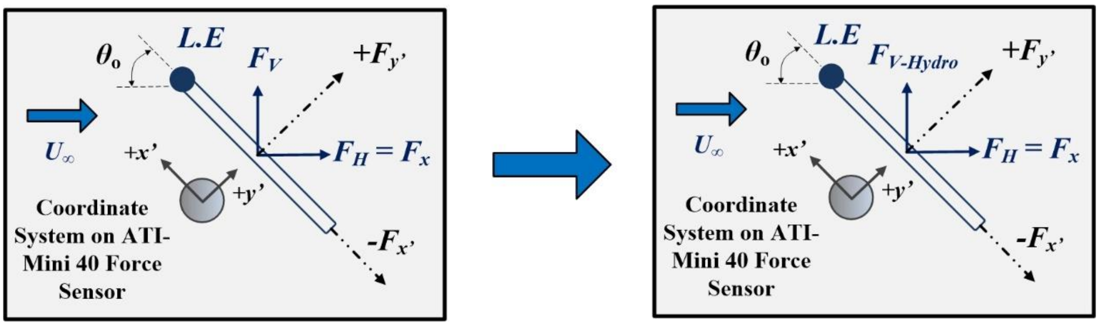

Figure 3.9: Definition of force vectors on the hydrofoil. $F_{x'}$ and $F_{y'}$ are forces parallel and normal to the hydrofoil which are measured by the force sensor directly. F_H and F_V are horizontal and vertical forces which are normal and parallel to the plunging direction, respectively. 'L.E.' represents the leading edge of the flat plate, which is marked by a relatively large color filled circle at one end of the wing.

where, m is the mass of the hydrofoil and the small vertical shaft underneath the force sensor (= 0.20 kg), $\ddot{y}(t)$ is the linear acceleration, $F_{inetial}$ is the linear inertial force and $F_{V\text{-}Hydro}$ is the net vertical hydrodynamic force (hydrodynamic lift force). For the net hydrodynamic moment calculation (Equation 3.3), the same principle was applied as with the calculation of the hydrodynamic lift force;

$$T_{Z-inertial} = I_Z \ddot{\theta}$$
$$T_{Z-Hydro} = T_Z - T_{Z-inertial} \tag{3.3}$$

$$I_Z = I_{CM} + m{x_{c-pv}}^2 \tag{3.4}$$

where I_Z is the mass moment of inertia, which is also dependent on the pivot location where the vertical shaft is attached as given in Equation 3.4 where I_{CM} is the moment of inertia with respect to hydrofoil's mid-chord and x_{c-pv} is the distance between the pivot location and the mid-chord of the hydrofoil, $\ddot{\theta}(t)$ is the angular acceleration, $T_{Z-inertial}$ is the inertial moment and $T_{Z-Hydro}$ is the net hydrodynamic torque about the z-axes (parallel to the vertical cantilevered shaft).

The phase-averaged parameters are then used to evaluate the system performance of the flapping foil energy harvester including; instantaneous total extracted power (P, C_P), instantaneous extracted power due to plunging motion (P_y, C_{Py}), instantaneous power due to pitching motion (P_θ, $C_{P\theta}$), time averaged power and coefficient of power (P_{mean}, C_{Pmean}), efficiency (η) and force-torque parameters ($F_{V-Hydro}$, $C_{V-Hydro}$, $T_{Z-Hydro}$, $C_{Z-Hydro}$), by applying equations 3.5-3.9.

$$P = F_{V-Hydro}\dot{y} + T_{Z-Hydro}\dot{\theta}$$
$$P = P_y + P_\theta \tag{3.5}$$

where, is the plunging velocity and $\dot{\theta}$ is the pitching velocity, $F_{V-Hydro}$ is the hydrodynamic vertical force or net lift force, $T_{Z-Hydro}$ is the hydrodynamic moment or net torque. To calculate the coefficient of power (C_P) and mean coefficient of power (C_{Pmean}), the following equations are as follows:

$$C_P = C_{V-Hydro}\frac{\dot{y}}{U_O} + C_{Z-Hydro}\frac{\dot{\theta}c}{U_O}$$
$$C_P = C_{P_y} + C_{P\theta} \tag{3.6}$$

$$C_{Pmean} = \frac{1}{T}\int_t^{t+T} C_P(t)dt = C_{Pymean} + C_{P\theta mean} \tag{3.7}$$

where, $C_{V-Hydro}$ and $C_{Z-Hydro}$ are the coefficients of vertical hydrodynamic force and hydrodynamic moment respectively and are defined as:

$$C_{V-Hydro} = \frac{F_{V-Hydro}}{\frac{1}{2}\rho U_O^2 sc} \tag{3.8}$$

$$C_{Z-Hydro} = \frac{T_{Z-Hydro}}{\frac{1}{2}\rho U_O^2 sc^2} \tag{3.9}$$

where, ρ is the density of water (kg/m^3), U_o is the free-stream velocity of incoming water flow in the water tunnel (m/s), s is the span of the hydrofoil (m) and c is the chord length of the hydrofoil (m). The efficiency (η) of the energy extraction is measured as the ratio of time-averaged power output to the available power in the flow through the frontal area of the foil;

$$\eta(\%) = \frac{P_{mean}}{\frac{1}{2}\rho U_O^3 sd} \times 100 = C_{Pmean}\frac{c}{d} \times 100 \tag{3.10}$$

where, d is the distance swept by the foil, which is set to 0.3 m. Since the ratio of the efficiency to the mean power coefficient is constant for a given c and d (where both parameters are fixed in this study), discussing only one of them is sufficient in this research.

The Strouhal number is well known for characterizing the vortex dynamics and shedding behaviour for flows around a stationary cylindrical object, such as the von Karman vortex street behind a cylindrical object, and for characterizing induced unsteady flows around 2D airfoils undergoing pitching and plunging motions. Kinsey and Dumas (2008) have previously discussed that the boundary between energy harvesting and thrust production regimes of an oscillating foil relies heavily on the Strouhal number, which is defined as;

$$St = \frac{L_{ref} f}{U_{ref}} = \frac{2h_a f}{U} = \frac{A_{piv} f}{U_\infty} \tag{3.11}$$

where, f is the flapping frequency (Hz), h_a is the stroke (flapping) amplitude and $2h_a = A_{piv}$ and U is the forward velocity or the free stream velocity (m/s). This definition describes a ratio between the oscillating (flapping) speed (fh_a) and the forward speed or free stream speed (U_o), which offers a measure of propulsive or extraction efficiency in flapping wing applications.

3.4 LASER INDUCED FLUORESCENCE (LIF) FLOW VISUALIZATION & PARTICAL IMAGE VELOCIMETRY (PIV) MEASUREMENTS

A laser induced fluorescent (LIF) flow visualization system was used to qualitatively visualize the flow around the flapping hydrofoil in energy extraction mode. To achieve this all hydrofoils presented in this study consisted of a small hole of 3.5 mm diameter at about $0.25c$ from the leading edge to accommodate a small tube used for the dye visualization. The drilled hole extends downwards to the mid span of the foil and then a 1.5 mm diameter hole is drilled through from the leading edge to connect with the long vertical hole. Finally, a 1 mm diameter pin hole is drilled, perpendicular to the span, through the horizontal channel and the hole at the tip of the foil's leading edge is blocked with a small tape, to allow the fluorescent dye to exit through the pin holes (Figure 3.10).

For image acquisition, a Photron FASTCAM Mini (UX100) high speed camera was used (Figure 3.6). It has an internal capacity of 16GB with a frame rate of 4000 frames per second at full resolution of 1024 × 1280 pixels. The camera has BNC input terminals which can be used to activate its image acquisition upon receiving a TTL signal, which was achieved through the NI 9402 BNC digital module (Figure 3.5). Since the VI programs were synchronized, upon the activation of the program, the camera receives the TTL signal to acquire the images while simultaneously the LabView program starts to receive the raw data from the sensors. The camera software used for the image acquisition for qualitative analysis is the Photron FASTCAM Viewer (PFV) v3. The frame rate was set to 125 fps with shutter speed at 1/640 sec and image resolution of 1024 × 1280 pixels, pertaining to approximately 70 seconds of image data.

The dye tracer used in the LIF experiments were fluorescent poster colors from Pentel. These were mixed and stored in a 1L beaker and then extracted using a

50mL syringe. The syringe was connected to thin rubber tubes which were attached carefully to the vertical cantilevered shaft and the end of the tube inserted and secured into the 3.5mm diameter hole on the hydrofoil model. Due to the unavailability of a syringe driver, the dye tracer was inserted manually but carefully (equal constant pressure applied while operating the syringe) to the tube connected to the syringe. To illuminate the dye tracer, a solid state 532 nm green laser with attached optics and with a maximum power of 10.84 W in continuous mode set at mid-span of the foil was used. The arrangement of the LIF system is as shown in Figure 3.11.

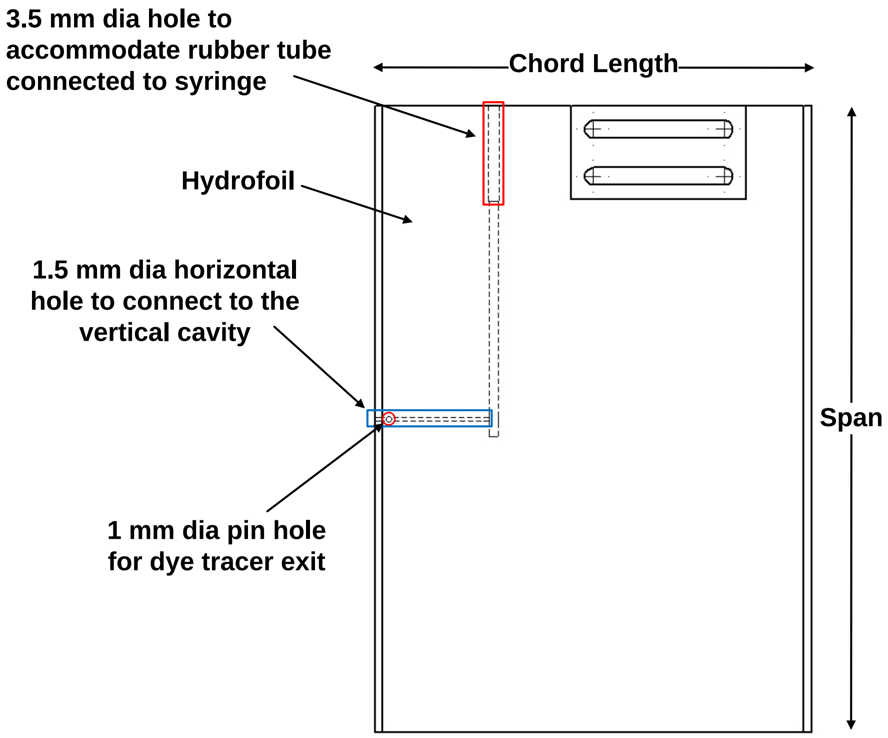

Figure 3.10: Schematic of the arrangement of different holes and cavities to accommodate the rubber tube into the hydrofoil and allow the dye tracer to exit the pin hole situated at the leading edge (L.E) of the hydrofoil.

A Particle Image Velocimetry (PIV) system was used to measure the flow in the *x*-*y* plane at mid-span of the hydrofoil (Figure 3.11). Dynamic studio software (Dantec Dynamics) recorded the detailed quantitative evolution of the flow field around the flapping foil. The water flow was seeded with Polyamid (PSP-20) seeding particles of 20 μm diameter and the same laser and high-speed camera system used for the qualitative LIF experiments were used for the PIV experiments.

The PIV setup is the same as shown in Figure 3.11 only if the syringe with fluorescent dye is removed and the water is filled with the seeding particles. The PIV image size acquired from the camera was by default 1024 × 1280 pixels covering an area of 240 mm × 290 mm. Part of the original image also contains an area which is outside of the water tunnel test section which is about 240 mm × 40 mm, hence using the ROI (Region of Interest) module of the Dantec software this area was excluded before any velocity field processing. Hence, the velocity field was calculated on an approximate image size of 1024 × 1100 pixel.

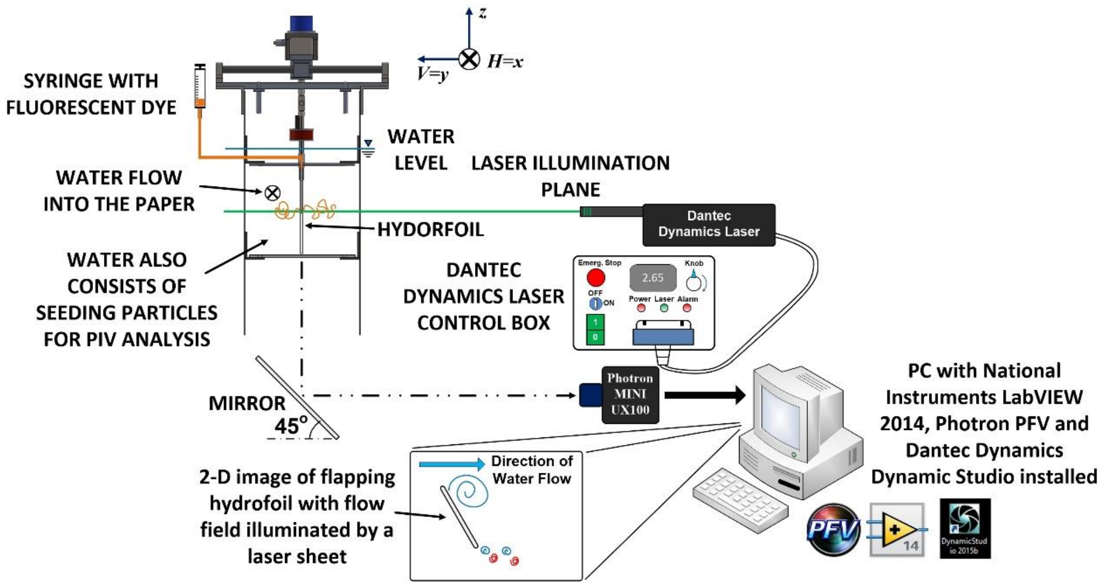

Figure 3.11: Experimental set-up for qualitative assessment of flow structures around a flapping foil in energy extraction mode. The dye used is fluorescent and is illuminated by the laser positioned at mid-span of the oscillating flat plate. Due to space limitations, the camera is placed on the side of the test rig and the profile of the flat plate can be seen using a mirror placed underneath the test-rig at 45° to the horizontal. The Photron PFV software captures the images for detailed qualitative analysis later. The same setup is also being used for PIV analysis. The dye syringe is disconnected, and the water is seeded with 20μm diameter Polyamid particles, which are illuminated by the same laser and acquired by the high-speed camera system respectively on the Dantec Dynamic Studio software.

The images were acquired in single frame mode with a trigger rate of 1000Hz and were interrogated using an Adaptive PIV module in Dantec software with the maximum IA (Interrogation Area) size of 48 × 48 pixels, minimum IA size of 24 × 24 pixels and grid step size of 16 × 16 pixels and a 50% overlapping in each direction. The ensuing in-plane velocity field consists of about 63 × 66 vectors. The average number of erroneous vectors in the captured flow field were about 140 corresponding to about 3.3% of the total. These erroneous vectors occur due to the insufficient light intensity in the shadow of the dye-injection passage built in the hydrofoil especially in the case of the flat plate since the it is being manufactured from transparent Plexiglass. To remove such erroneous vectors, the Moving Average Validation module in Dantec software was used. This method is used to validate vector maps by comparing each vector with the average of other vectors in a defined neighborhood. The vectors that deviate too much from their neighbors can be replaced by the average of the neighbors as a reasonable estimate of true velocities. This was not that much of a major problem in the case of the Ellipse and NACA 0006 foil since they were manufactured using 3-D printing and for full coverage of the upstroke and downstroke motion, two lasers were incorporated (more details will be discussed in Chapter 5). Based on Willert & Gharib (1991), there exists a root-mean-square fluctuation of the PIV measured particle displacement resulting in measurement uncertainties in the streamwise flow approximately close to 1%. Using equation to calculate the uncertainty in the vorticity field (e_ω) from X. Wen et al. (2015), the uncertainty for the resulting vorticity is estimated to be in the range of 4.5%-8.5% of the maximum vorticity in the field.

Since the hydrofoil is moving in a periodic fashion, phase averaging was applied to the acquired images. Eight-time instances (non-dimensional) were selected (t/T = 0.05, 0.10, 0.25, 0.35, 0.45, 0.60, 0.80 and 0.925), where $t/T \approx 0.05$, 0.10 and 0.60 refer to instants when the foil is plunging and is set at maximum pitching amplitude. Other time instants refer to events when the foil is undergoing stroke reversal. In almost all of the cases, the peak values of C_P mostly occur either at or close to these time stamps due to which they are made consistent throughout our discussion. The images were acquired in such a way that the 20 cycles of flapping motion were captured. Images at these time instances for selected cases from each cycle were merged and the above discussed analysis in the Dantec software was applied to get the velocity field and vorticity data around the hydrofoil, which was then exported to Tecplot 360 for post-processing. Due to the unavailability of a suitable Synchronizer or Timer box like the BNC 555 with the PIV system in the lab it was not possible to achieve synchronization between the sensor LabView program and Dantec software for image acquisition and velocity field analysis.

3.5 REMARKS

A detailed discussion has been given in this chapter pertaining to the experimental setup and methodology adopted in this research. The test-rig is designed to mimic a 2-DoF flapping motion which is only applicable when the hydrofoil is subjected to a suitable amount of hydrodynamic force. The magnitude of this hydrodynamic force is dependent on the free-stream velocity of the incoming water flow; hence the test-rig has a cut-off velocity ($U_{o\text{-}cutoff}$) at which starts to perform sustainable flapping motion. Furthermore, the test-rig does not consist of any elaborate mechanical design which may induce phasing between pitching and plunging motion nor any kind of desired flapping motion profile, hence making the energy harvester test-rig a passive system.

As a baseline, a flat-plate shaped hydrofoil was considered and for comparative analysis in the morphological domain, an elliptical and NACA0006 shaped hydrofoils were also added, which will be discussed in detail in Chapter 6. For qualitative analysis, LIF flow visualization technique was employed to identify flow structures while for quantitative analysis PIV and sensor data acquisition were conducted.

A set of equations were formed based on the literature survey in Chapter 2 and used to determine the key parameters to evaluate the performance of the system through in-house MATLAB codes. This included the use of measured quantities from sensors such as force, torque, linear and angular displacement. These quantities were then used, through post-processing and filtration, to calculate subsequent quantities such as velocity, acceleration, net lift force and torque. At the end, performance parameters such as mean coefficient of power (C_{Pmean}) and efficiency (η) were determined for all cases. Since, the swept distance (d) and chord length of foil (c) were fixed, discussing only one performance parameter will be sufficient.

For the test-rig sustainable performance, modifications were employed to the test-rig design to include inertial mass blocks or units. These inertial mass units play an important role in the hydrofoil flapping motion and their main purpose is to provide support to the test rig so that the hydrofoil can perform sustainable flapping motions. Since, the inertial mass blocks are one of the key parameters, results from our preliminary tests will be discussed in detail in Chapter 5, which will precede our discussion on pivot location and pitching amplitude effect. In general, the inertial mass units along with other necessary modifications to the test-rig design, provided us the opportunity to carry out parametric study of passively oscillating hydrofoil for energy extraction in open channel environment.

Figure 3.12 shows the summary of parametric study undertaken during this PhD research. However, in the preceding chapters to bring clarity and summary to our discussion in this thesis, the FSI and coupled dynamics analysis of a few cases have been discussed in detail in the preceding chapters.

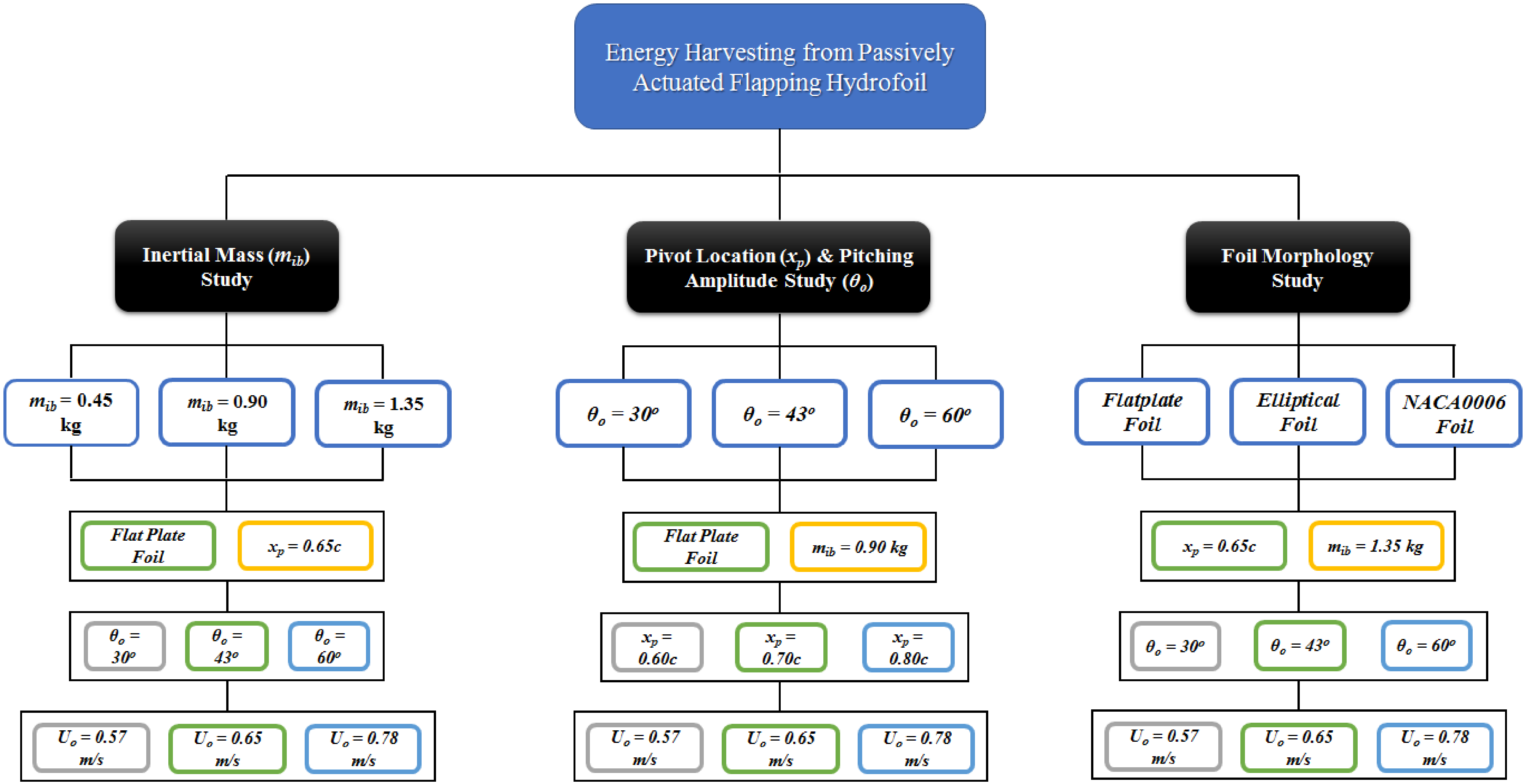

Figure 3.12: Flow chart showing the different geometric and kinematic cases undertaken through an experimental campaign during the PhD research. A few cases will be discussed in the preceding chapters.

CHAPTER 4

ENERGY HARVESTING WITH A FLAPPING FOIL

In this chapter we take a specific case as an example to introduce the flapping wing kinematics, force-moment profile, surrounding flow evolution of the hydrofoil through our PIV and LIF images and eventually its energy extraction performance. The chosen case is the flat-plate hydrofoil operating at pitching amplitude (θ_o = 60°), pivot location (x_p = 0.80c) at freestream velocity (U_o = 0.65 m/s) with test-rig equipped with baseline inertial mass unit (m_{ib} = 0.90 kg). Key observations will be laid out which will provide a basis for understanding the kinetics of the passively flapping foil energy harvesting device concept so that the parametric study in the succeeding chapters is easy to comprehend.

4.1 FLAPPING FOIL KINEMATICS

In chapter 3 we described the working principle of our test-rig, although it is mostly difficult to envision the exact kinematic profile when the hydrofoil's motion modes are flow induced. To visualize such a profile which our motion sensors have acquired and through some post-processing, Figure 4.1 shows both the angular and linear displacement profile of the selected case. The kinematics graph is divided into four zones numbered from 1 to 4. Each of the two halves of the flapping cycle consists of two motion zones, and each motion zone describes the flapping foil's angular and linear kinematics as shown in Figure 4.1.

Figure 4.2 show the kinematics of the hydrofoil, where Figure 4.2(a) shows the first half of the flapping cycle and the Figure 4.2(b) the second half of the flapping cycle. As explained, each of these halves of the flapping cycle consists of two motion modes, which are clearly labelled in Figure 4.2 and are also represented by Figure 4.1 in the form of motion profile. As shown in Figure 4.2(a), the start of the flapping cycle or the initial position of the hydrofoil is when the pitching amplitude is $+\theta_{omax}$ and is positioned at the bottom end of the stroke. With the pitching amplitude set, the incoming water flow applies a hydrodynamic force on the hydrofoil which allows it to start the translational or plunging motion in the upward direction. Since, the maximum pitching amplitude is set by pitching limiters, the angle does not change, which remains until the moment arm gets in contact with the plunge limiter. The moment arm is represented with a dash line protruding out of the hydrofoil and brown in color as shown in Figure 4.2 (See also Figure 3.2(b) and 3.3). Since the hydrofoil did not experience any pitching motion till now, the angular displacement profile shows a horizontal line as shown in Figure 4.1 represented by motion Zone 1 (light green color region).

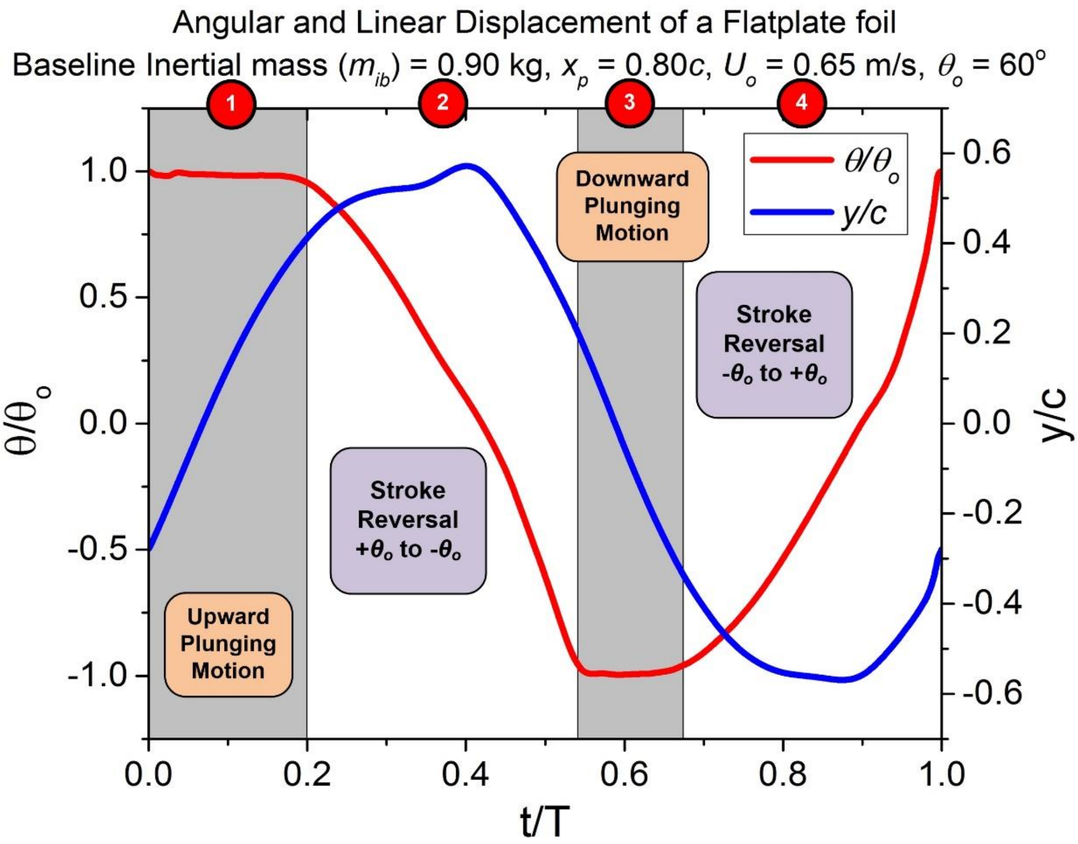

Figure 4.1: The final phase-averaged angular and linear displacement profile of a flatplate hydrofoil with pitching amplitude (θ_o = 60°), at pivot location (x_p = 0.80c) at freestream velocity (U_o = 0.65 m/s) with test-rig equipped with baseline inertial mass unit (m_{ib} = 0.90 kg). The plot is divided into four zones indicating the different events occurring during a flapping motion. Both angular displacement and linear velocity are dimensionalized with respect to maximum pitching amplitude ((θ_o = 60° in this case) and hydrofoil's chord length (c = 0.14m), respectively.

As the moment arm comes in contact with the upper plunge limiter, the hydrofoil starts to perform the pitching motion/stroke reversal, represented by Zone 2. The first half of the stroke reversal process, i.e. from $+\theta_{omax}$ to near zero is due to the momentum gained by the hydrofoil during the upstroke plunging motion and the inertial mass block attached on top of the test-rig. As the hydrofoil pitching amplitude is near zero, and in the negative pitching amplitude regime, the incoming water flow rotates the hydrofoil further to -θ_{omax}, hence the end of first half of flapping cycle and start of the second (See black hydrofoil and red hydrofoil on top of upstroke in Figure 4.2(a)). This motion profile of pitching amplitude change is shown in Figure 4.1 represented by Zone 2 (light cyan color region).

Since the hydrofoil is not at -θ_{omax}, the incoming water flow applies a hydrodynamic force in the form of vertical lift force but now in the downward direction as shown in Figure 4.2(b). Due to this vertical hydrodynamic force the hydrofoil undergoes plunging motion in the downward direction (downstroke). The pitching amplitude is fixed at -θ_{omax} since it cannot change further due to the presence of a pitching limiter, indicating that it will remain constant as shown in Figure 4.1 represented by Zone 3 (light yellow color region). We also observe that the time taken to undergo this downstroke plunging motion is not the same as the upstroke plunging motion shown in Zone 1 in Figure 4.1, indicating difference in linear/plunging velocity between both upstroke and downstroke motion.

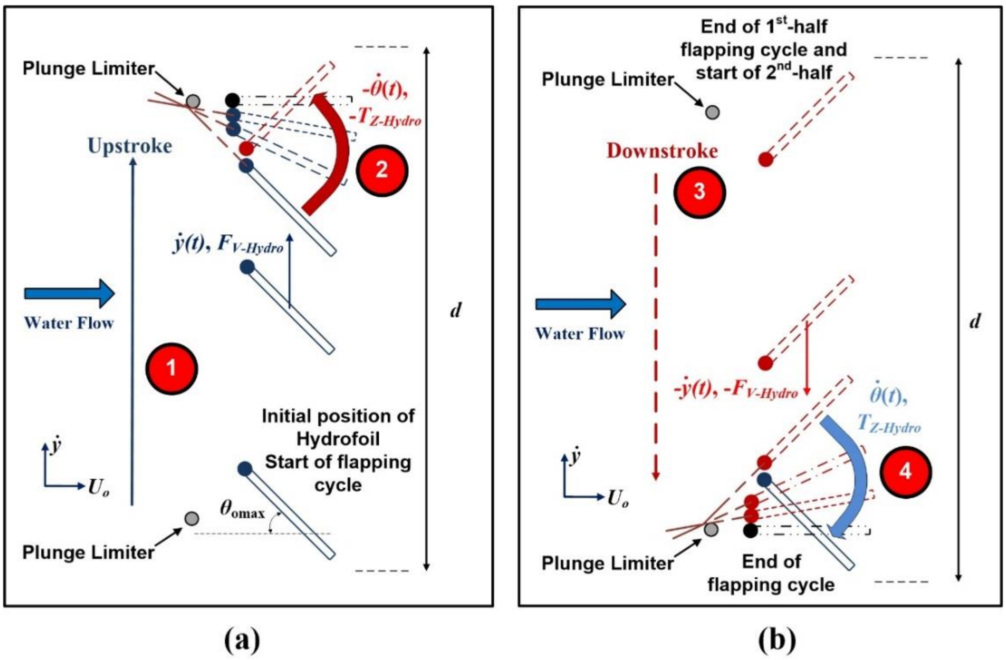

Figure 4.2: Schematic showing the **(a)** first half of the flapping cycle which is divided into two motion zones 1 and 2. Zone 1 is upstroke plunging motion with hydrofoil set at maximum pitching amplitude while zone 2 is stroke reversal or pitching motion of hydrofoil due to the contact between the moment arm and upper plunge limiter from +θ_{omax} to -θ_{omax}, **(b)** Second half of flapping cycle with motion zones 3 and 4. Zone 3 is downstroke plunging motion with hydrofoil now set at negative maximum pitching amplitude while zone 4 is the second stroke reversal of the flapping cycle due to the contact between the moment arm and lower plunger limiter from -θ_{omax} to +θ_{omax}.

The hydrofoil continues to plunge downwards until the moment arm comes in contact with the lower plunge limiter, indicating the end of motion Zone 3 and start of motion Zone 4. Due to the contact of the moment arm with the plunge limiter, the momentum gained by the hydrofoil due to the downstroke plunging motion and the support of the inertial mass block, the foil undergoes pitching motion (stroke reversal). As before, half of the second stroke reversal is due to the factors just described and as the foil rotates beyond the zero-angle mark (as shown in Figure 4.2(b) by black foil) the hydrodynamic forces due to the incoming water flow helps the hydrofoil to rotate back to $+\theta_{omax}$, which is set by the pitching limiter, marking the end of the flapping cycle (position indicated by blue foil in Figure 4.2(b) marked with Zone 4). This second stroke reversal ($-\theta_{omax}$ to $+\theta_{omax}$) is defined by the angular displacement plot, marked as Zone 4 in the Figure 4.1 (light blue color region). The time taken for the second stroke reversal compared to the first one is slightly smaller as observed in the case of upstroke and downstroke plunging motion, indicating the system's asymmetricity about the centerline of the water tunnel due to its design features and motion kinematics which are dependent on the flow condition.

4.2 FLUID STRUCTURE INTERACTION

In this section, we will discuss the force-motion correlation and flow evolution around the hydrofoil with the help of LIF and vorticity images acquired through PIV methodology. The LIF images give us a platform to observe the flow field qualitatively, while through PIV we see the quantitative aspect of the flow field around the hydrofoil.

Figure 4.3 shows the plunging kinematics and kinetics, synchronized with angular displacement profile. The plot consists of coefficient of net vertical hydrodynamic force ($C_{V\text{-}Hydro}$), also known as coefficient of lift force, non-dimensional plunging velocity ($/U_o$) and the resulting energy extraction profile due to the plunging motion (C_{Py}). The plot is also marked with eight distinct time stamps which will correlate to the flow evolution at those instants, shown in Figure 4.4. Correspondingly, Figure 4.5 shows the angular kinematics and kinetics and synchronized with angular displacement data. Like Figure 4.3, the plot consists of coefficient of net hydrodynamic moment ($C_{Z\text{-}Hydro}$), non-dimensional angular velocity ($\omega c/U_o$) and resulting energy extraction due to pitching motion ($C_{P\theta}$).

From Figures 4.3 and 4.4 we can see that the hydrofoil is at $+\theta_{omax}$ and starts to undergo upward plunge motion. Due to the high angle of attack (in this case 60º) a separation region is formed on the foil's upper surface. This separation region allows the formation of a vortex at the leading edge of the flatplate foil, known as leading edge vortex or LEV. At $t/T \approx 0.05$ in Figure 4.4 that LEV starts to form up, which causes the pressure on the foil's upper and lower surface to decrease and increase, respectively. This change in pressure on the foil's surface leads to the generation of a net vertical force or lift force, as can be seen in Figure 4.3 at $t/T \approx 0.05$ ($C_{V\text{-}Hydro}$). Due to the continued plunging motion of the hydrofoil at maximum pitching amplitude, the size of the LEV grows as shown at $t/T \approx 0.10$ in Figure 4.4 allowing the lift force to continuously increase, which can be seen at the same time instant marked in Figure 4.3. Sometime between $0.10 < t/T < 0.25$, this primary LEV fully forms up and sheds into the wake. Due to the separation of the LEV from the hydrofoil's upper surface the lift force decreases as it can be seen in Figure 4.3 in this time range. At approximately $t/T \approx 0.21$, the moment arm of attached to the vertical cantilevered shaft comes in contact with the upper plunge limiter, which initiates the stroke reversal/pitching motion of the hydrofoil. At $t/T \approx 0.25$ as shown in Figure 4.4, the flow on the foil's upper surface starts to get pushed against the tunnel wall. Also, just after the primary LEV sheds, a second LEV starts to form up as can be seen in Figure 4.4 at $t/T \approx 0.25$. However, since there is not enough plunging distance, the secondary LEV doesn't mature enough and as the hydrofoil continues its stroke reversal the flow structures start to break down and shed in to the wake. Due to this the hydrodynamic lift force keeps on decreasing and eventually shifts to the opposite direction due to the change in the hydrofoil's orientation. At $t/T \approx 0.35$, the hydrofoil continues to rotate and is nearing the zero-angle mark, while pushing the fluid on top of its surface against the tunnel wall. The first large spike in $C_{V\text{-}Hydro}$ shown at $t/T \approx 0.35$ in Figure 4.3 is due to the hydrofoil experiencing a slight jerk during the rotational motion. This is due to the foil reaching the end of the stroke, the type of linear bearings (SKF LUCE-16-2LS) used in our test-rig and the foil's higher rate of pitch reversal due to larger pivot location (more about pivot location effect in Chapter 5). No obvious flow structures are formed, and the vorticity plot shown in Figure 4.4 at $t/T \approx 0.35$ indicates the continuation of the breakdown of the flow structures which were observed at $t/T \approx 0.25$. Around $t/T \approx 0.45$, the hydrofoil continues its pitching motion and passes the zero-angle mark with no obvious flow changes around the hydrofoil as can be seen in Figure 4.4. At this point, we observe a large peak in $C_{V\text{-}Hydro}$ in Figure 4.3 and $C_{Z\text{-}Hydro}$ in Figure 4.5. The direction of the hydrodynamic force is now in the downward direction and since the hydrofoil is nearing stroke reversal completion, it experiences a sudden surge in the hydrodynamic lift force due to this rapid stroke reversal, leading to increase in both hydrodynamic lift force and torque (Figure 4.3 and 4.5).

At approximately $t/T \approx 0.54$ the first stroke reversal is completed and the first half of the flapping cycle finishes leading to the onset of the second half of the flapping cycle, with the hydrofoil is now set at $-\theta_{omax}$. Same as in the first half of the flapping cycle, due to the hydrofoil now set at high pitching amplitude, the incoming free-stream flow will apply the hydrodynamic force on the foil. This will start the downward plunging motion and similarly lead to the formation of the leading-edge

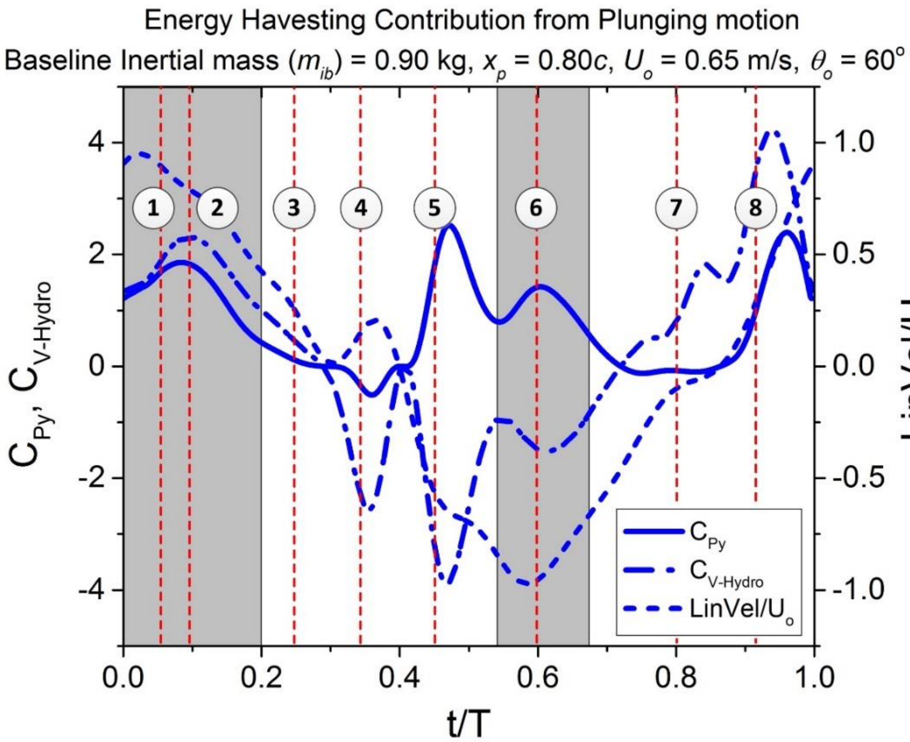

Figure 4.3: Plot showing the phase-averaged net vertical hydrodynamic force ($C_{V\text{-}Hydro}$), plunging velocity dimensionalized against free-stream velocity ($/U_o$ or $LinVel/U_o$), energy extraction profile due to plunging motion (C_{Py}) and angular displacement on the right-hand axis dimensionalized against maximum pitching amplitude (θ/θ_o) of a flatplate hydrofoil with pitching amplitude pitching amplitude (θ_o = 60º), at pivot location (x_p = 0.80c) at freestream velocity (U_o = 0.65 m/s) with test-rig equipped with baseline inertial mass unit (m_{ib} = 0.90 kg).

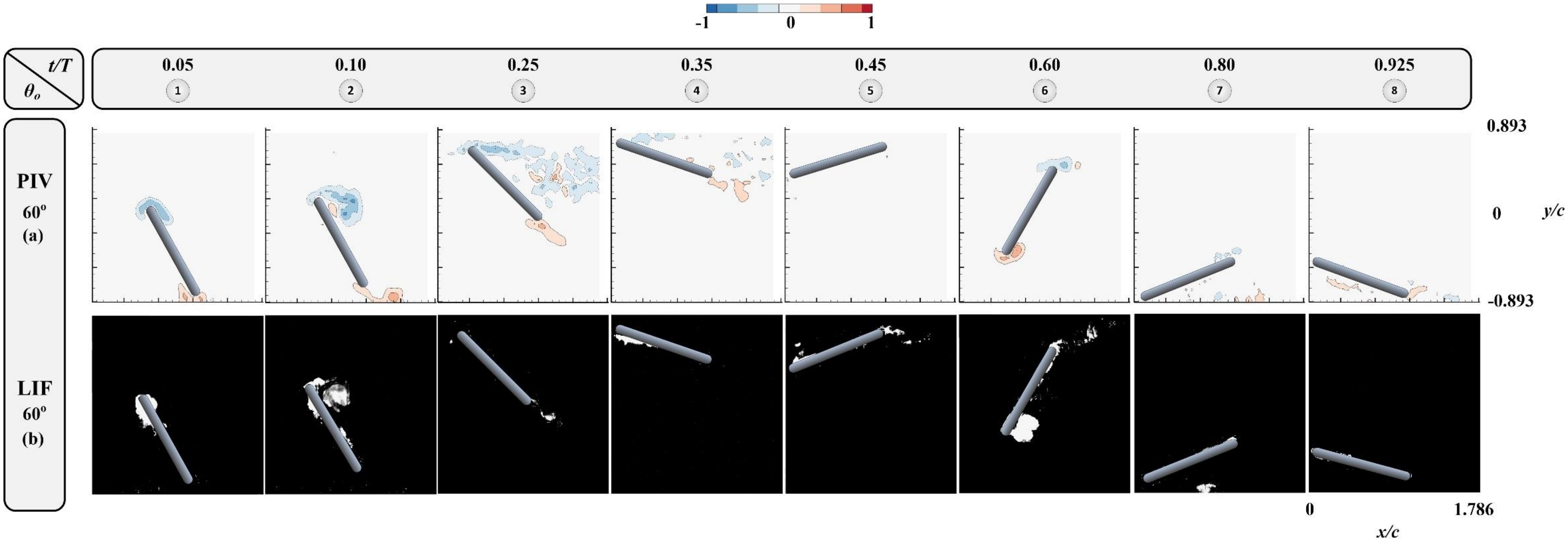

Figure 4.4: Figure showing **(a)** vorticity contours, and **(b)** LIF images of of flat-plate hydrofoil at eight different time instants during one flapping cycle with free-stream velocity U_o = 0.65 m/s, pitching amplitude θ_o = 43° and pivot location x_p = 0.70c. The x and y scale are dimensionalized with reference to the chord length (c = 0.14 m) of the hydrofoil.

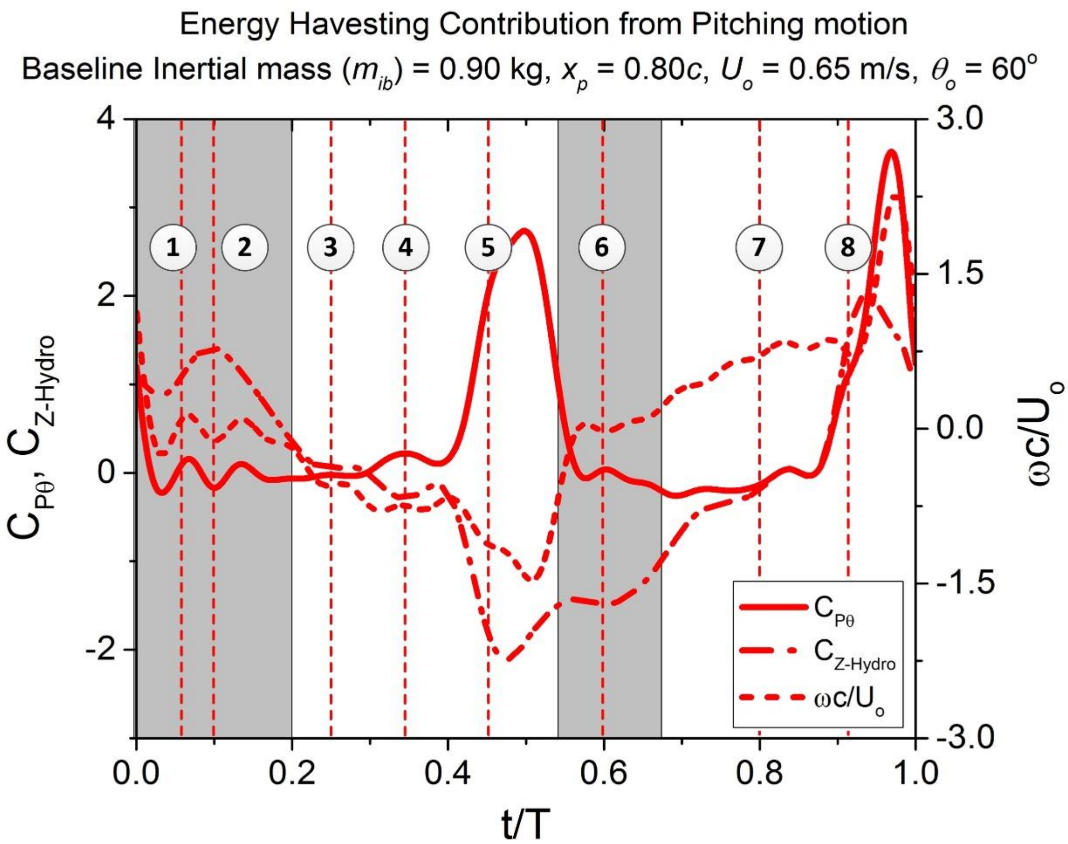

Figure 4.5: Plot showing the phase-averaged net hydrodynamic moment ($C_{Z\text{-}Hydro}$), angular velocity dimensionalized against free-stream velocity ($\omega c/U_o$), energy extraction profile due to pitching motion ($C_{P\theta}$) and angular displacement on the right-hand axis dimensionalized against maximum pitching amplitude (θ/θ_o) of a flatplate hydrofoil with pitching amplitude pitching amplitude (θ_o = 60°), at pivot location (x_p = 0.80c) at freestream velocity (U_o = 0.65 m/s) with test-rig equipped with baseline inertial mass unit (m_{ib} = 0.90 kg).

vortex on the foil's bottom surface. This leading-edge vortex starts to grow due to the hydrofoil's plunging motion. At $t/T \approx 0.60$ from Figure 4.4, we can observe the formation of flow structure at the foil's leading edge. Due to the generation of such flow structure, the hydrodynamic force experiences an increase in the downward direction as shown in Figure 4.3. As the foil plunges further, this leading-edge vortex grows in size and eventually sheds into the wake. From our analysis of kinematics in the previous section, we saw that the hydrofoil in this case is covering the same distance in the downstroke phase is less time than in the upstroke phase. Due to the relatively higher velocity in the second half of the flapping cycle, the hydrofoil reaches the point at which the moment comes in contact with the lower plunge limiter quickly (at approximately $t/T \approx 0.69$). The total time taken in this case for the downstroke motion is about $\Delta T_{linearstroke} \approx 0.15$ as compared to the upstroke motion $\Delta T_{linearstroke} \approx 0.21$.

The hydrofoil undergoes a second stroke reversal in the flapping cycle due to the contact between the moment arm and the lower plunge limiter. The foil also plunges/translates simultaneously, eventually leading to deceleration as it approaches the zero-angle mark. From Figure 4.4 we can see that at $t/T \approx 0.80$ the foil is nearing the zero-angle mark and no evident flow structures can be seen around the hydrofoil. The hydrodynamic force is declining in the downward direction and with the hydrofoil changing its orientation, it reverses its direction to upwards. By $t/T \approx 0.925$, the foil has crossed the zero-angle mark and its pitching amplitude is now in the positive region. As in the first half of the flapping cycle, the foil upon nearing completion of its stroke reversal, experiences a sudden surge in lift force which leads to increase in both net vertical hydrodynamic force and moment as shown by a second peak in Figures 4.3 and 4.5 at and near $t/T \approx 0.925$.

4.3 ENERGY EXTRACTION

In the previous section we have described the force and motion correlation along with the description of the flow field around the hydrofoil. We will extend that in this section by discussing about the hydrofoil's energy extraction profile in a flapping cycle due to the correlation between the force and motion.

Since the hydrofoil performs two motion modes (plunging and pitching), both contribute to the total energy extraction profile of the passively oscillating foil in a flapping cycle. Figure 4.6 shows the C_P profile marked with black line, while the blue line represents the energy extraction profile due to plunging motion (C_{Py}) which is also shown in Figure 4.3 and the red line shows the energy extraction profile due to pitching motion ($C_{P\theta}$), which is also shown in Figure 4.5. In the case of energy extraction from both pitching and plunging motion (Figure 4.3 & 4.5 respectively and Figure 4.6), the correlation between the hydrodynamic torque and lift force with the angular velocity and linear velocity, respectively is very important where they are shown in Figure 4.3 and 4.5, respectively.

Through observing Figure 4.3, we can see that the hydrodynamic lift force ($C_{V\text{-}Hydro}$) and plunging velocity have very good synchronization with each other. By synchronization it means that both parameters have the same sign. This indicates that the value of the calculated power is positive. This synchronization leads to increase in C_{Py} where the profile has its first high peak at $t/T \approx 0.10$, since the hydrofoil is undergoing plunging motion at maximum pitching amplitude. After $t/T \approx 0.10$, the hydrodynamic lift force starts to decrease due to the onset of stroke reversal. The plunging velocity also decreases with the hydrodynamic lift force and goes to zero around $t/T \approx 0.38$, eventually leading to decline in C_{Py} at around $t/T \approx 0.40$. As for $C_{P\theta}$ in Figures 4.5 & 4.6, energy extraction remains almost zero due to the constant pitching amplitude of the hydrofoil during the plunging motion and at some points during the initiation of the stroke reversal the desynchronization between the hydrodynamic torque and angular velocity. Hence during this phase of the upstroke motion, pitching motion contributes very little to the total energy extraction of the system.

As the hydrofoil undergoes stroke reversal and passes through the zero-angle mark, it experiences a sudden increase in lift force (in the downward direction due to the foil's new orientation) as well as torque as result of rapid stroke reversal experience. The plunging velocity in Figure 4.3 and the angular velocity in Figure 4.5 have also the same signs as their force counterparts. This synchronization between the force and velocity leads to positive peaks in C_{Py} (Figure 4.3 & 4.6) and $C_{P\theta}$ (Figure 4.5 & 4.6) at $t/T \approx 0.47$ and 0.50 respectively. After the first stroke reversal is complete, the foil starts to move downward with pitching amplitude set at $-\theta_{omax}$. The pitching angle allows the foil to form a separation region on the its lower side, causing the flow to rotate which eventually leads to the formation of a leading-edge vortex (LEV). As the hydrofoil plunges downwards, the LEV grows in size and strength which leads to the increase in hydrodynamic lift force as shown at $t/T \approx 0.60$ in Figure 4.3. Since both the hydrodynamic lift force and plunging velocity have the same sign, they synchronize which results in positive energy extraction. This is represented by a third peak at $t/T \approx 0.60$ in C_{Py} in Figure 4.3 & 4.6. Since there is no pitching motion, $C_{P\theta}$ at this point remains zero. A little later after this, the LEV sheds into the wake which leads to the decline in hydrodynamic lift force and around $t/T \approx$ 0.69 the second stroke reversal of the flapping cycle begins. Due to the change in foil's angular orientation along with linear deceleration in the first half of the second stroke reversal, the energy extraction declines (C_{Py} in Figure 4.3 & 4.6), which for C_{Py} remains till $t/T \approx 0.90$. In the case of $C_{P\theta}$, at around $t/T \approx 0.90$ the foil is crossing

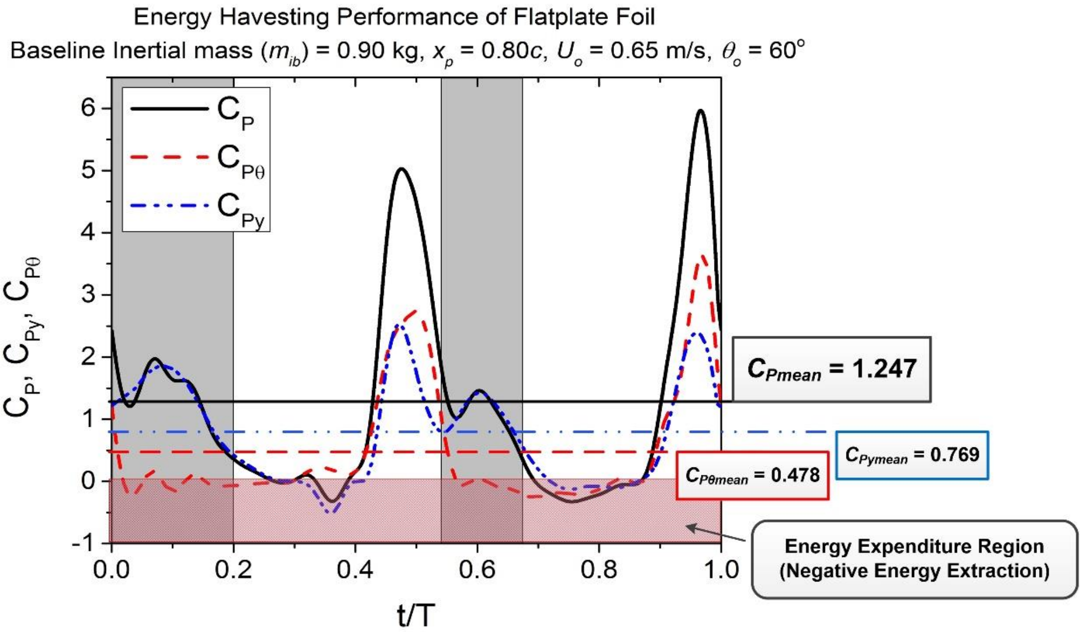

Figure 4.6: Plot showing the phase-averaged energy extraction profile (C_P) with energy extraction due to plunging motion (C_{Py}) and energy extraction due to pitching motion ($C_{P\theta}$) of a flatplate hydrofoil with pitching amplitude pitching amplitude (θ_o = 60º), at pivot location (x_p = 0.80c) at freestream velocity (U_o = 0.65 m/s) with test-rig equipped with baseline inertial mass unit (m_{ib} = 0.90 kg). C_{Pmean}, C_{Pymean} and $C_{P\theta mean}$ are also marked in the plot.

the zero-angle mark which leads to the change in hydrodynamic force direction. Due to the higher free-stream velocity and longer pivot distance from leading edge, the foil undergoes a rapid pitch reversal generating a high torque and increasing the lift force because of this (Figures 4.3 & 4.5). The good synchronization between the velocities and the force leads to very large peaks especially for $C_{P\theta}$ at $t/T \approx 0.97$.

The C_P profile in Figure 4.6 shows the overall energy extraction by the hydrofoil in a flapping cycle and it is made up by both C_{Py} and $C_{P\theta}$ combined as shown by Equation 3.6. From Figure 4.6 we can see that the C_P profile follows the profile of C_{Py} throughout the flapping cycle, and the high peaks at $t/T \approx 0.48$ and $t/T \approx 0.97$ resulting in $C_P \approx 5$ and $C_P \approx 6$ respectively, is due to the energy extraction enhancement provided by $C_{P\theta}$ to C_{Py} at those time instants. The red zone marked in Figure 4.6 is the region of energy expenditure or negative energy extraction. Although, the C_P profile remains positive for most of the time during the flapping cycle, it does cross into this red zone at two instants; $0.33 < t/T < 0.38$ and $0.7 < t/T < 0.85$. We can also see that the C_P profile during these time zones follows the C_{Py}

profile, and the reason for this crossing is due to the de-synchronization between the hydrodynamic lift force and plunging velocity as shown in Figure 4.3.

To determine the energy harvesting performance of the system, we calculate the mean coefficient of power extraction (C_{Pmean}) and efficiency (η), as shown in Table 4.1 and Figure 4.6. The C_{Pmean} is the algebraic sum of C_{Pymean} and $C_{P\theta mean}$, with the plunging motion contributing about 61.67 % and pitching motion about 38.33 % to total energy extraction in this case, where this ratio can change depending on different geometric and kinematic parameters. A C_{Pmean} value of 1.247 was achieved as shown in Table 4.1, which compared to previous studies (Table 2.1) is higher than most cases. Although, there are some studies where the C_{Pmean} values (Table 2.1) are higher than the case discussed in this chapter (2nd highest among all our cases combined), but their efficiency is lower compared to the case discussed here (58.19% as in Table 4.1). This is due to the values chosen by for foil's chord length and swept distance, which is different among all studies. It should be noted that the performance analysis for all our cases in this research refers to the "*hydrodynamic power extraction efficiency*" rather than "*water-to-wire efficiency*" due to the lack of a power-takeoff system.

Case	Performance Parameters			
Flatplate foil θ_o = 60°, x_p = 0.80c U_o = 0.65 m/s, m_{ib} = 0.90 kg	C_{Pymean}	$C_{P\theta mean}$	C_{Pmean}	η (%)
	0.769	0.478	1.247	58.19

Table 4.1: Table showing performance parameters of a flatplate hydrofoil with pitching amplitude (θ_o = 60°), at pivot location (x_p = 0.80c) at freestream velocity (U_o = 0.65 m/s) with test-rig equipped with baseline inertial mass unit (m_{ib} = 0.90 kg).

4.4 REMARKS

The purpose of this chapter was to provide a basic understanding of the methodology of analyzing the force-motion behavior and the energy extraction performance of the system, which will be almost similar when discussing the effect of different geometric and kinematic parameters on test-rig's energy harvesting performance in the succeeding chapters. For this reason, we chose one case and explained the important aspects in detail to provide such prior understanding.

As part of our analysis, we discovered that the hydrofoil undergoes a flapping motion where during the upstroke plunging motion its pitching amplitude remains constant. This is due to the presence of a pitching limiter, which can be used to set the value of $\pm\theta_{omax}$ and would only change when the moment arm attached to a vertical cantilevered shaft comes in contact with the plunge limiter, causing the hydrofoil to undergo stroke reversal (pitching motion). We also observed that as the hydrofoil plunges (upstroke or downstroke), the separation region because of its set pitching amplitude leading to the generation of leading edge vortex (LEV). As the hydrofoil plunges further, the LEV grows in size resulting in the increase of hydrodynamic lift force and then a decline due to it shedding into the wake.

For positive power generation, both from plunging and pitching motion, synchronization between the force and respective velocity is very important and can only happen if the signs of both parameters are the same. Any de-synchronization would either lead to negative energy extraction or zero, depending on the values of the force and velocity. We also observed that C_P during a flapping cycle follows the profile of C_{Py}, while $C_{P\theta}$ enhances the energy extraction performance at two instances during the flapping cycle, which is when the hydrofoil is about to complete its stroke reversal. The performance parameters for energy harvesting include the mean coefficient of power (C_{Pmean}) and efficiency (η), which can be calculated using equations given in Chapter 3. For the case discussed in this chapter, of a flatplate foil at θ_o = 60º, x_p = 0.80c and U_o = 0.65 m/s and test-rig equipped with baseline inertial block of mass (m_{ib}) 0.90 kg, the system achieved a C_{Pmean} of 1.247 and energy extraction efficiency of 58.19%.

EFFECT OF SEVERAL KEY PARAMETERS

The pivot location and pitching amplitude of the flapping foil are very important parameters for the energy extraction performance of flapping foil harvesters. It has been illustrated that in these flapping foil turbines, adjusting the pivot location has a similar effect as changing the phase lag between pitch and heave (Davids, 1999; Kinsey and Dumas, 2008). A systematic study by Davids (1999) on the relation between phase lag and pivot point location shows an obvious interdependency. Other studies done by Asharf et al. (2011), Isogai et al. (2003), Zhu and Peng (2009) and Xiao et al. (2012) have also employed different pivot locations between 0.333*c* and 1.0*c* from the L.E. as suitable for high performance of the flapping foil turbine. This may be related to the difference in the kinematics such as prescribed/semi-passive/fully passive motion used in their respective studies. In most flapping wing studies, the dynamics of the system is determined by the combination of kinematic parameters so that they often need to be considered in an integrated way, where the effective angle of attack (α_{eff}) or the nominal angle of attack comes into play. Although effective angle of attack is more physically relevant due to its close correlation with leading edge separation (Zhu, 2011), in most previous experimental investigations the pitching amplitude (rather than the effective AoA) was utilized as a characteristic parameter (Jones and Platzer, 1997; Jones et al., 2003; Dumas and Kinsey 2006; Kinsey and Dumas, 2008; Simpson et al., 2008 and Ashraf et al., 2011).

Numerical simulations aside, it is important that both these geometric parameters be investigated in an experimental campaign as to fully understand how it affects the energy extraction performance of a passively actuated flapping foil. Before this, we will first visit the methods which will help the test-rig to perform viable flapping motions without any external help. This will include modifications such as length setting of vertical cantilevered shaft and inertial blocks or units of different mass to the help the foil to flap and extract energy from incoming free-stream flow. Three different inertial mass units were tested; small inertial block (m_{ib} = 0.45 kg), baseline inertial block (m_{ib} = 0.90 kg) and big inertial block (m_{ib} = 1.35 kg). Preliminary tests with these inertial mass blocks were carried out at three different freestream velocities (U_o = 0.57 m/s, 0.65 m/s and 0.78 m/s) with varying pitching amplitudes (θ_o = 30°, 43° and 60°) and pivot location fixed at 0.65*c*.

Later in this chapter, we will discuss in detail the effect of varying pivot location on energy extraction performance of a flatplate hydrofoil cantilevered at different pivot locations (x_p = 0.60*c*, 0.70*c* & 0.80*c*). We will also focus on how this energy harvesting behavior changes when pitching amplitude is changed as the pivot location is varied (coupled effect) at different freestream velocities. For these two analysis (pivot location and pitching amplitude variation) the test-rig was equipped with baseline inertia (m_{ib} = 0.90 kg).

5.1 TEST-RIG VIABILITY

5.1.1 METHODS TO ENSURE TEST-RIG VIABILITY

As a first step we first performed various methods and tests to ensure that our test-rig would be able perform sustainable and viable flapping motions in energy harvesting mode. During our preliminary experiments to check the viability of the test rig, we observed that with certain hardware configurations the test-rig would require support in the form of additional mass to able to perform plunging motion and stroke reversal under the influence of the hydrodynamic forces. These inertial mass blocks would be attached on the top of the small aluminum block which is connected to a linear guide rail using linear bearings. These hardware configurations included the test rig without sensors and with sensors which would also affect the length of the vertical cantilevered shaft. This in turn determined the cut-off water velocity ($U_{o\text{-}cutoff}$) of the test rig, the minimum free-stream velocity at which the hydrofoil would perform sustainable flapping motions without any external support. The design of the test-rig was such that the hollow shaft rotary encoder sensor (for measuring angular displacement) was attached on top of the vertical cantilevered shaft and the sensor placed on small platform attached to the translating aluminum block. The screw in the sensor, which allows to secure the vertical cantilevered shaft inside the hollow shaft of the sensor influenced the mass blocks and eventually the $U_{o\text{-}cutoff}$. The screw was to be secured in a such a way that it allowed the vertical shaft to perform pitching motions without too much applied torque but would also rotate the hollow shaft section of the sensor (coupled with the vertical cantilevered shaft) to acquire good digital signal for measurement.

Another important factor was the length of the vertical cantilevered shaft, which houses the moment arm, the force sensor and the hydrofoil as shown in Figure 5.1 (a). This configuration was used in all our experiments, whose results and analysis will be discussed in this thesis. However, before the configuration in 5.1 (a) was finalized, our preliminary experiments for the test rig's sustainability were carried out by first the configuration in Figure 3.9 (b) and a similar configuration as in Figure 5.1 (a) but without the force sensor housing.

Initial tests revealed that the configuration in Figure 5.1 (b) required little assistance of inertial blocks, specifically of low mass (< 150 g for one block) to perform self-sustainable flapping motions for energy extraction. This was performed without the coupling of the rotary encoder on top of the cantilevered shaft, allowing to test-rig to start self-sustained flapping motions at about $U_{o\text{-}cutoff}$ = 0.37 m/s ~ 0.40 m/s. Future experiments could have been performed with this configuration, however since the system was passive (no actuators) and to calculate the energy extraction performance, synchronized sensor data (as discussed in Chapter 3) was required. Hence, to incorporate the sensors especially the force sensor since it had to be placed within the cantilevered shaft, the length of the shaft was increased from 186 mm to 274 mm. By increasing the length of the vertical cantilevered shaft, it was observed that inertial blocks with small masses (< 150 g for one block) were insufficient to allow the hydrofoil to perform flapping motions. Hence, to deal with this the mass of the inertial blocks were increased appropriately to allow the hydrofoil to perform self-sustained flapping motion due to the application of hydrodynamic forces (≈ 300 g for one block). Furthermore, by adding the rotary encoder to the top of the vertical shaft the minimum mass of the inertial blocks, required for the hydrofoil to perform self-sustained flapping motion, was increased to approximately 400 g. This increased the cut-off velocity of the energy harvester to approximately 0.50 m/s, which meant that future parametric analysis was to be conducted at free-stream velocities greater than 0.50 m/s.

It is to be kept in mind that the flapping motion performed by the test-rig in energy extraction mode is in 2-DoF (plunging and pitching motions). Although, once the hydrofoil is at its maximum pitching angle (set by a mechanical limiter) it can translate regardless of the presence or absence of additional inertial mass and/or change of length of the vertical cantilevered shaft and/or the presence or absence of sensors. However, the test-rig faces a challenge when it is about to perform the stroke reversal (pitching motion with the help of moment arm touching the plunging limiter as explained in Section 3.1.1). It is because of the coupling of the rotary encoder attachment with the vertical cantilevered shaft, that with the addition of the appropriate inertial mass units helps the hydrofoil to perform the stroke reversal and translate in the opposite direction, with the process repeating itself resulting in a periodic flapping motion.

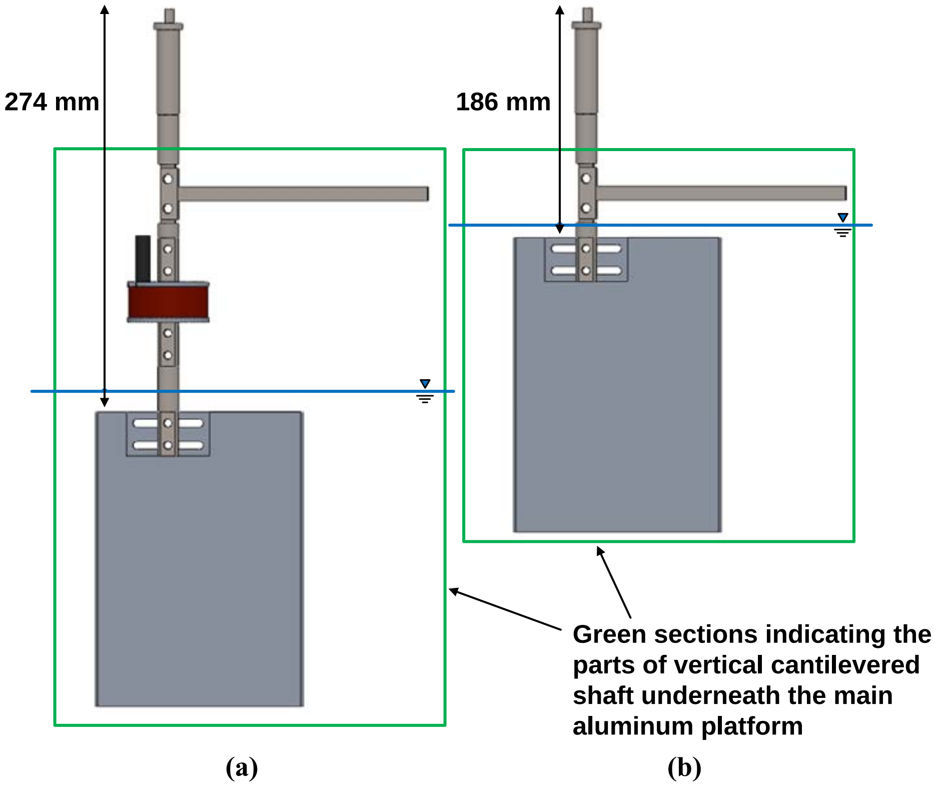

Figure 5.1: Schematic of vertical cantilevered shaft used in experiments. **(a)** Current configuration of the vertical cantilevered shaft including the force sensor attached with a custom-made flange and **(b)** initial configuration of the vertical cantilevered shaft used in our preliminary experiments to determine the suitable set up for the test-rig to perform self-sustained flapping motions.

Three different inertial mass unit configurations were tested. The mass blocks were made of mild steel with the small inertial block weighing $m_{ib} \approx 0.45$ kg, baseline inertial block $m_{ib} \approx 0.90$ kg and big inertial block $m_{ib} \approx 1.35$ kg (which is the coupling of the small and baseline inertial block). A pair of same inertial mass blocks were used to provide equal mass distribution on the small aluminum block. In the next sections we will discuss the effect of these inertial mass blocks on energy harvesting performance while varying the pitching amplitude (θ_o = 30°, 43° and 60°) at three different free-stream velocities (U_o = 0.57 m/s, 0.65 m/s and 0.78 m/s). The reason for choosing these free-stream velocities is that they are higher than the cut-off velocity ($U_{o\text{-}cutoff} \approx 0.50$ m/s) of the sensor equipped test-rig, hence $U_o < U_{o\text{-}cutoff}$ cannot be used in our experiments. Higher velocities may also have been included, but to study how a passively actuated flapping foil behaves at relatively lower velocities led us to choose these values. Furthermore, through some of our initial tests, we observed that at very high velocities the test-rig would perform erratically and, in most cases, frequently damaged some of our mechanical parts.

5.1.2 EFFECT OF FLOW VELOCITY AND PITCHING AMPLITUDE

In this section we will first analyze how the test-rig performs when equipped with an inertial mass block. For simplicity, we first choose the small inertial mass block for our analysis at different pitching amplitudes and varying free-stream velocity. Later in the next section, we will perform a comparative analysis as we change the inertial block mass linearly.

Figure 5.2 shows the performance of the test rig equipped with small inertial blocks, at three different pitching amplitudes (θ_o = 30º, 43º and 60º) at three different free stream velocities. The graph shows a steady linear increase in C_{Pmean} and power extraction efficiency (η) with the increase in pitching amplitude. It is also evident from Figure 5.2 that with the increase in free-stream velocity, the slope with which the C_{Pmean} increases with increasing pitching amplitude, decreases significantly.

To understand this trend, it is important to study the behavior of the force and motion components which are solved together using the equations in Section 3.1.4 to give us the performance parameters. Figure 5.3 shows such an example of force and motion behavior and their correlation for the small inertia case at θ_o = 43º for all free-stream velocities.

From equations 3.4 and 3.5 the sum of power extracted due to the plunging motion (C_{Py}) and pitching motion ($C_{P\theta}$) results in the total power extracted from the fluid (C_P) indicated by blue, red and black spark lines in Figure 5.3(a) respectively. It can also be observed that C_P follows C_{Py} profile while $C_{P\theta}$ enhances the energy extraction performance at particular time instants ($t/T \approx 0.45$ and 0.90 for this example), while the latter remains zero during the remainder of the flapping cycle. These time stamps correspond to when the hydrofoil has almost completed its stroke reversal (pitching motion). It can be deduced then that most of the energy extracted from the incoming free-stream water flow is due to the plunging motion of the hydrofoil, while the pitching motion only contributes when the hydrofoil has almost completed its stroke reversal.

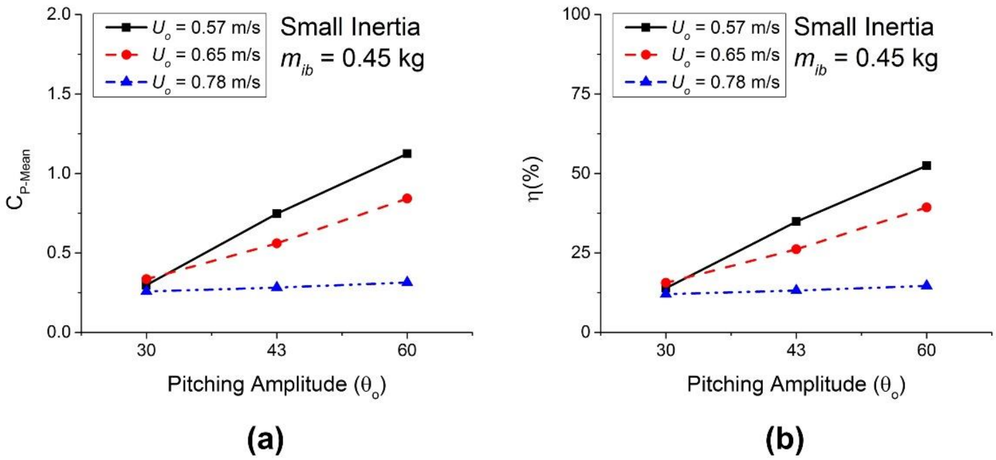

Figure 5.2: Graphs showing performance analysis in the form of, **(a)** Mean coefficient of power (C_{Pmean}) and **(b)** Energy extraction efficiency (η), of test-rig equipped with small inertial blocks for energy extraction at θ_o = 30°, 43° and 60° at three different free-stream velocities.

From Figure 5.2 (a) we see that the C_{Pmean} (θ_o = 43°) with increasing free-stream velocity decreases, which is also supported by the phase-averaged C_P graph in Figure 5.3 (a). C_P values tend to decline as the free-stream velocity increases, which affects the mean power coefficient (C_{Pmean}) as observed in Figure 5.2 (a) As discussed, this can be attributed to the individual contributions by the plunging and pitching motions since force and motion of the flapping foil is affected by the incoming free-stream. Another important observation in this case is that as the free-stream velocity increases, evidently part of the C_P trend line crosses the zero mark (Figure 5.3 (a)-II and III) and remains negative for a moment of flapping time, indicating loss of energy extraction.

Refer to Figure 5.3 (b), which shows the energy extraction due to plunging motion and its corresponding vertical hydrodynamic force (lift force) and linear (plunging) velocity. At U_o = 0.57 m/s, C_P graph (Figure 5.3 (a-I) has multiple high peaks and remains positive for almost the whole flapping cycle, which is due to the synchronization achieved by the hydrodynamic lift force and linear velocity, as shown Figure 5.3 (b-I). Synchronization between the two parameters correspond to their signs remaining the same during the flapping motion. Due to this, positive energy extraction due to plunging motion was achieved as seen in Figure 5.3 (b-I).

From Figure 5.3 (c-I), due to the non-sinusoidal motion of the hydrofoil, the angular velocity mostly remain zero (due to constant pitching angle during the plunging motion) and only shows a change when the hydrofoil is performing the stroke reversal. The concept of synchronization can also be applied between the hydrodynamic moment and angular velocity. Since, in this case positive $C_{P\theta}$ is only achieved when $C_{Z\text{-}hydro}$ and $\omega c/U_o$ (non-dimensional angular velocity) are synchronized (positive power extraction) at $t/T \approx 0.45$ and 0.90, while for the rest of the flapping motion $C_{P\theta}$ is almost at the zero-line, due to angular velocity being zero for most part of the flapping motion. When adding both C_{Py} and $C_{P\theta}$ together, which which has both higher peak values and a positive trend.

For cases at $U_o = 0.65$ and 0.78 m/s (Figures 5.3 (II) and (III)), the decrease in peak values in C_P and part of it being negative during some duration of the flapping cycle is attributed mostly to the contribution by the plunging motion, since there exist similarities in $C_{P\theta}$ at all free-stream velocities as observed in Figure 5.3 (c). With the increase in free-stream velocity there is a small increase in the vertical hydrodynamic force (lift force) as shown in Figure 5.3 (b), however the reason due to which C_P in Figure 5.3 (a-II & III), is showing lower peak values and some negative trend during the flapping cycle is because of the de-synchronization between the linear velocity and the hydrodynamic lift force. For time ranges $0.20 < t/T < 0.40$ and $0.70 < t/T < 0.90$ for both $U_o = 0.65$ m/s and 0.78 m/s C_{Py} remains negative because of the opposite signs of the linear velocity and the hydrodynamic lift force, with the highest de-synchronization occurring at $U_o = 0.78$ m/s. Furthermore, when calculating C_P using Equation 3.5, the common multiplication factor ($1/U_o$) decreases from 1.7544 to 1.2821 with increasing U_o, which reduces the force, moment and kinematic values to some extent.

It can be deduced from this observation that for energy extraction from fluid (positive power coefficient) synchronization between the hydrodynamic force and moment and their associated velocities play a vital role. Anything from a de-synchronization to a velocity being zero can contribute towards energy lost rather than energy extracted from the moving fluid system. It was observed that the plunging motion contributes the most towards energy extraction from flow and for this test-rig, the pitching motion only contributes when the hydrofoil has almost completed its stroke reversal since the change in pitching angle is only observed during this process. Free-stream velocity is another major factor in energy extraction through passive flapping motion. In this case we observed that with increasing free-stream velocity, total energy extracted decreased due to the addition of unsteadiness affecting the kinematics of the test rig, which may bring de-synchronization between the forces and their associated velocities.

Figure 5.4 shows the energy extraction, force-moment and motion kinematics at of the flapping energy harvester system equipped with small inertial blocks for three different pitching amplitudes at free-stream velocity of U_o = 0.65 m/s. Time stamps are also marked in Figure 5.4(a) which correspond to the flow evolution (LIF) shown in Figure 5.5.

Referring to Figure 5.2, we observed that in the case of the test-rig equipped with small inertial blocks with the increase in pitching amplitude the energy extraction performance parameters (C_{Pmean} & η) increase in a linear fashion irrespective of the free-stream velocity. This is supported by the trend exhibited in Figure 5.4 (a) where the peak values and amplitude of the C_P is increasing with increasing pitching amplitude. We also observe that most of the contribution to total energy extraction is by the plunging motion, while the pitching motion contributes mostly when the hydrofoil is almost about to complete its stroke reversal ($t/T \approx 0.45$ and 0.90) as discussed earlier and now both increase in amplitude with increasing pitching amplitude resulting in increasing C_{Pmean}.

Figure 5.4 (b) shows the hydrodynamic lift force and linear velocity and its effect on the calculated energy extraction due to plunging motion. We observe that with increasing pitching amplitude, power extracted through plunging motion increases with peak values occurring mostly at time instants when the hydrofoil starts its plunging motion (end or about at the end of the stroke reversal). Plunging velocity also increases slightly with increasing pitching amplitude, however the main contribution towards increasing energy extraction through plunging motion is due to the hydrodynamic lift force. The hydrodynamic lift force also exhibits undulations in its trend in a flapping cycle, which increases with increasing pitching amplitude because of flow separation leading to the formation of leading edge vortices (LEVs).

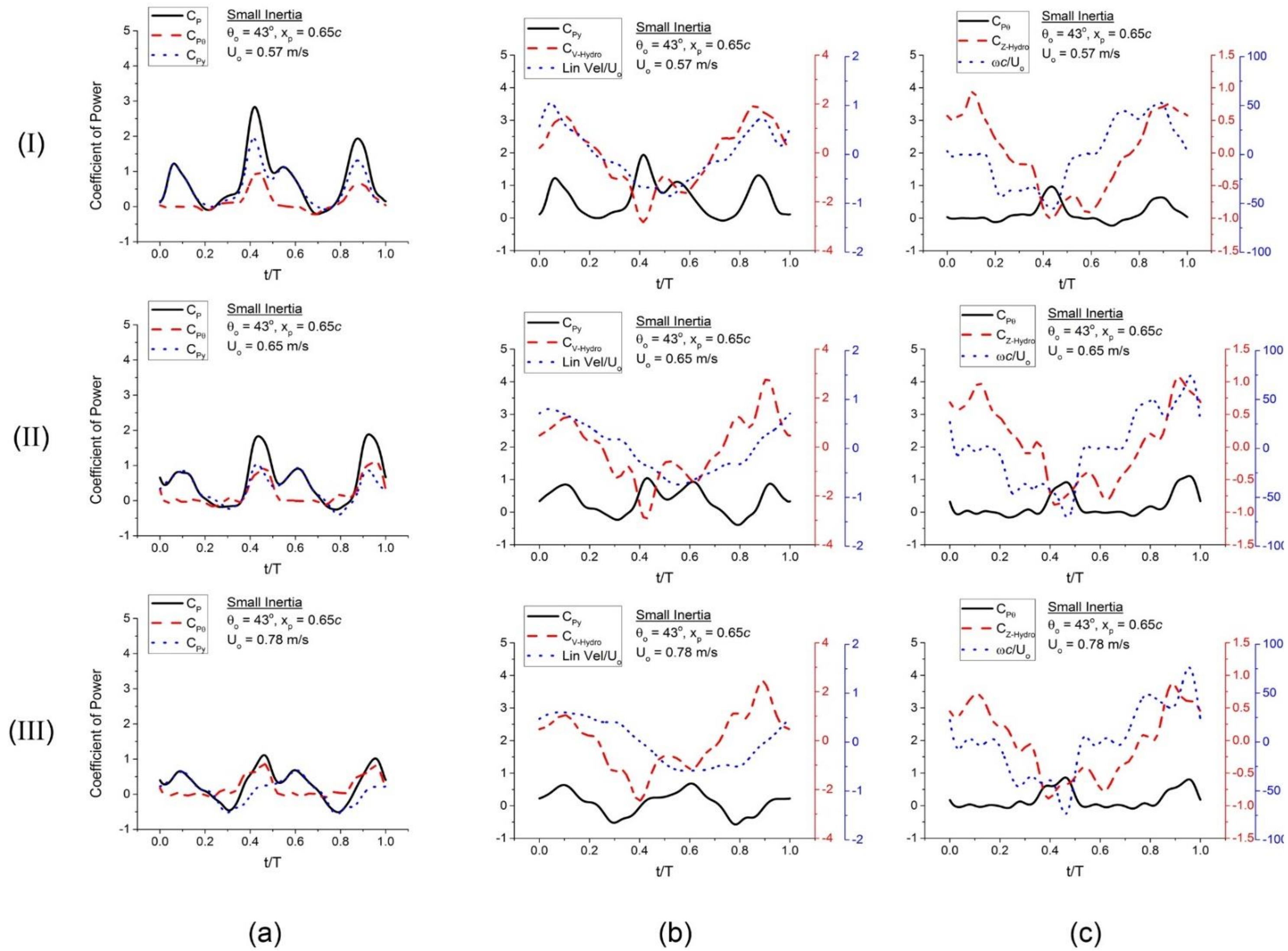

Figure 5.3: Graphs showing phase-averaged **(a)** Coefficient of Power (Total, Plunging and Pitching), **(b)** Coefficient of Power due to Plunging motion with corresponding Coefficient of Hydrodynamic Vertical Force and Linear Velocity and **(c)** Coefficient of Power due to Pitching Motion with corresponding Coefficient of Hydrodynamic Moment and Angular Velocity, for θ_o = 43° at, **(I)** U_o = 0.57 m/s, **(II)** U_o = 0.65 m/s and **(III)** U_o = 0.78 m/s.

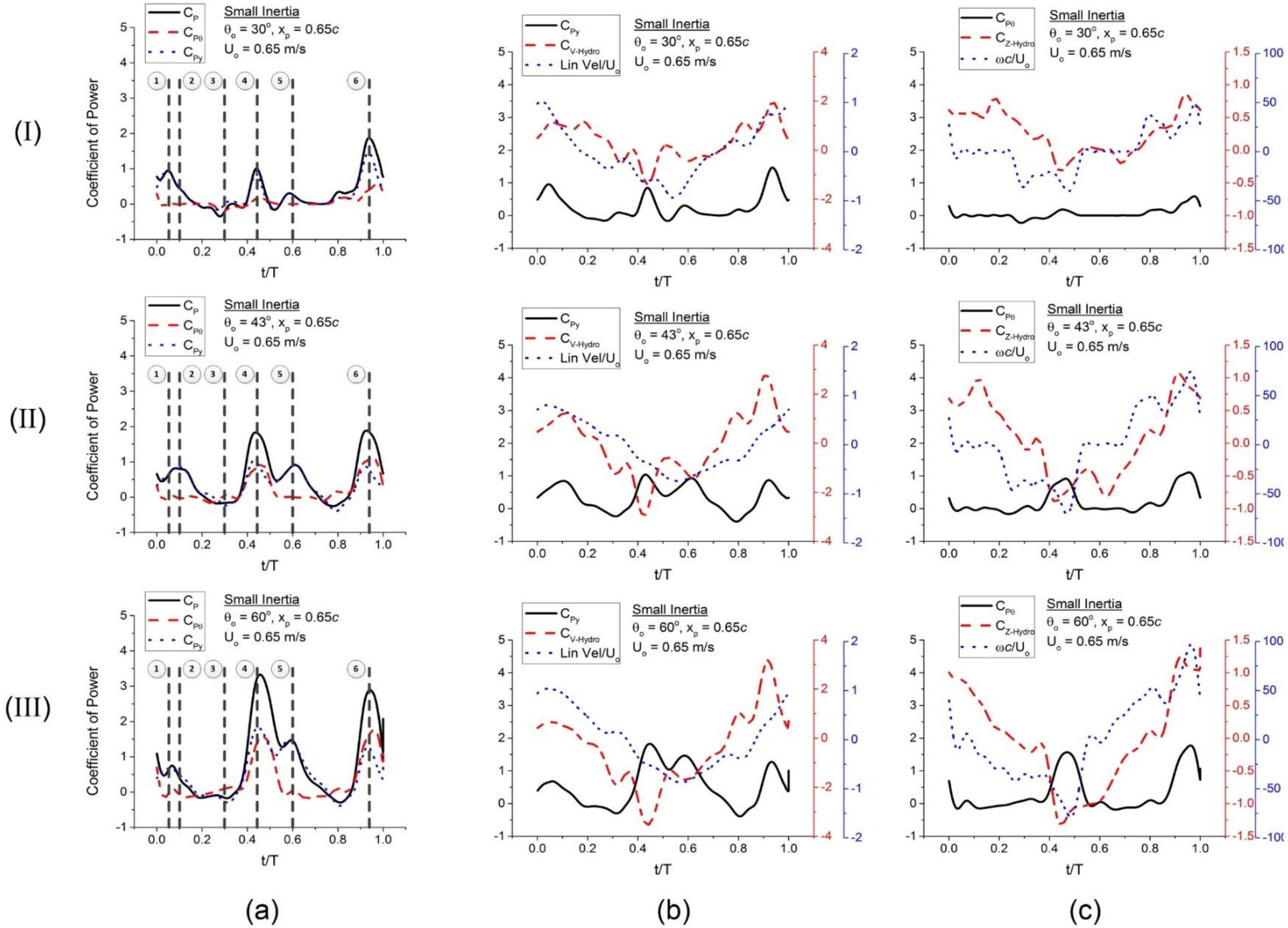

Figure 5.4: Graphs showing phase-averaged **(a)** Coefficient of Power (Total, Plunging and Pitching), **(b)** Coefficient of Power due to Plunging motion with corresponding Coefficient of Hydrodynamic Vertical Force and Linear Velocity and **(c)** Coefficient of Power due to Pitching Motion with corresponding Coefficient of Hydrodynamic Moment and Angular Velocity, at U_o = 0.65 m/s for, **(I)** θ_o = 30°, **(II)** θ_o = 43° and **(III)** θ_o = 60°. Time stamps marked in (a) are as follows t/T = (1) 0.05, (2) 0.10, (3) 0.30, (4) 0.45, (5) 0.60 and (6) 0.95.

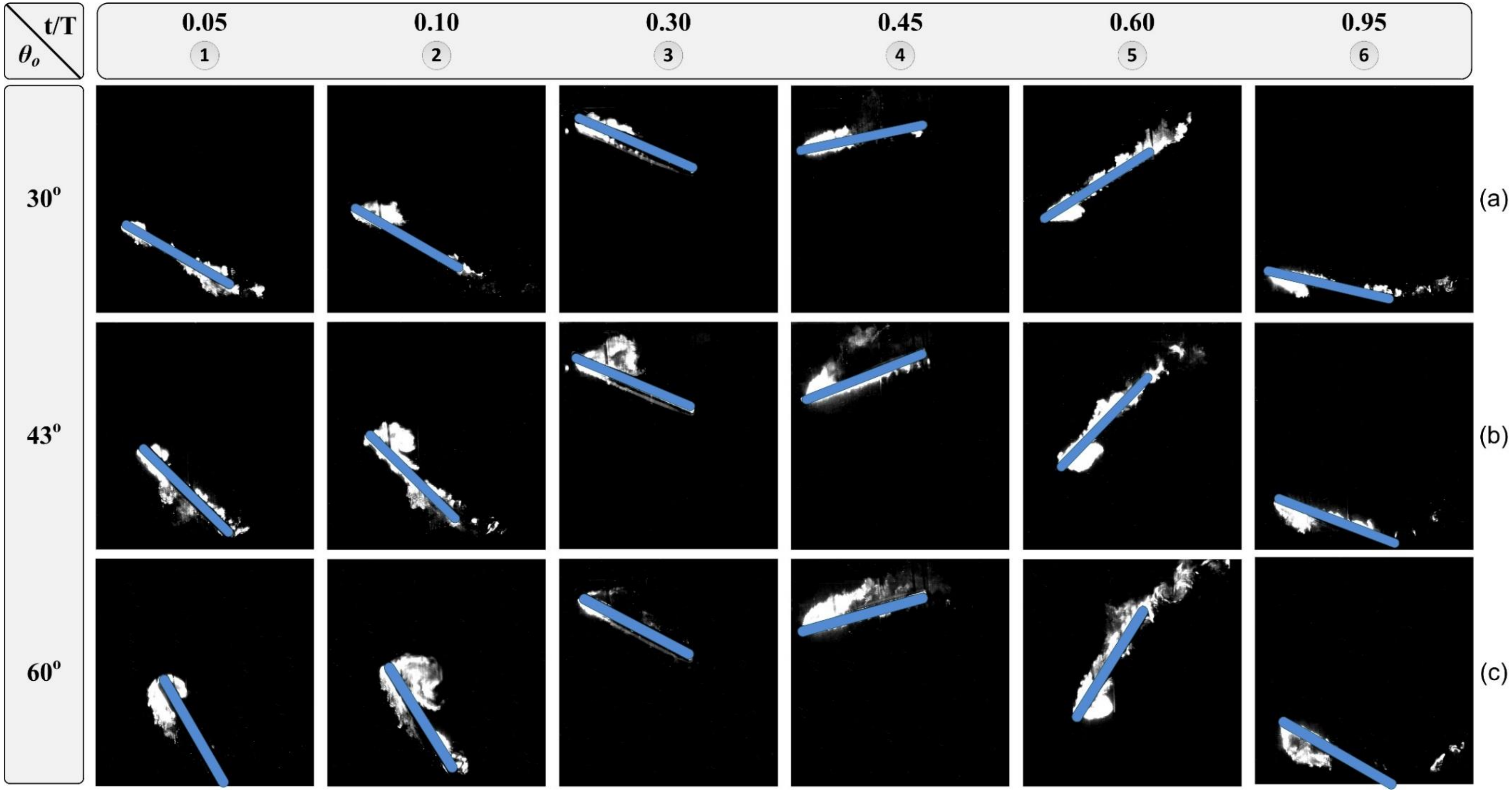

Figure 5.5: Figure showing LIF visualization images of hydrofoil at different time instants during one flapping cycle, where the test rig is equipped with small inertial blocks (m_{ib} = 0.45 kg) with free-stream velocity of U_o = 0.65 m/s and three different pitching amplitudes: **(a)** θ_o = 30°, **(b)** θ_o = 43° and **(c)** θ_o = 60°.

This could be referred to the LIF images in Figure 5.5, which show the changes in the flow, at different time instants during a flapping cycle, surrounding the hydrofoil in energy extraction mode at different pitching amplitudes. Leading edge separation is evident in all three pitching amplitudes, with the largest separation region occurring at θ_o = 60º. For θ_o = 30º in Figure 5.5 (a) the comparatively low angle of attack forms a small separation region which results in the formation of the LEV. However, during its upstroke motion (with constant pitching amplitude), the LEV convects downstream on the hydrofoil's upper surface only to detach itself just at the pivot location and in to the wake. Comparatively, for pitching amplitudes θ_o = 43º and 60º (Figure 5.5 (b) & (c)) due to large angles of attack, the separation region increases significantly. The size of the LEV becomes larger with increasing pitching amplitude and as the hydrofoil starts its plunging motion (both upstroke and downstroke), the flow separates the leading edge, forming an LEV that almost covers the whole of the hydrofoil. Furthermore, the flow separates earlier during both upstroke and downstroke motions for the flat plate hydrofoil, which may be due to the small radius of curvature at the hydrofoil's leading edge, letting the flow around the L.E. experience a stronger adverse pressure gradient which increases with increasing pitching amplitude. As a result, increased hydrodynamic lift force values are observed with increasing pitching amplitudes in Figure 5.4 (b) at t/T = 0.05, 0.10 (initiation of upstroke) and t/T = 0.60 (initiation of downstroke). Larger peaks in Figure 5.3 (b) during 0.40 < t/T < 0.50 and 0.85 < t/T < 0.95 were observed when the hydrofoil experienced a sudden jerk (vibration) at the end of its stroke reversal.

The intensity of this vibration increases with pitching amplitude, which is also due to the rapid stroke reversal experienced by the hydrofoil as augmented by angular velocity and hydrodynamic torque data in Figure 5.4 (c). Since the magnitude of applied hydrodynamic forces increase with increasing pitching amplitude (leading to larger and rapid LEV formation, convection and detachment), which results in larger values of hydrodynamic torque. As a result, the hydrofoil experiences rapid pitch reversals (stroke reversals) which lead to increase in angular velocity significantly. Additionally, the synchronization of angular velocity and hydrodynamic torque during 0.40 < t/T < 0.50 and 0.85 < t/T < 0.95 results in large improvements in energy extraction due to pitching motion ($C_{P\theta}$), which contributes significantly to the large peaks at t/T = 0.45 and t/T = 0.95 in Figure 5.4 (a) with increasing pitching amplitude.

5.2 EFFECT OF LINEAR INERTIA

In this section, we comparatively analyze how by increasing the inertial mass on the test rig affects its kinematics, force generation and eventually energy extraction performance. Figure 5.6 shows the C_{Pmean} plots for the different inertial mass systems at varying pitching amplitudes at different free-stream water velocities.

At low free stream velocity (Figure 5.6(a)) all three inertial systems show a similar trend at all pitching amplitudes, with the energy extraction with small inertial block being the highest compared to the other two inertial systems with the same pitching amplitude. Furthermore, the mean coefficient of power extraction also increases in an almost linear fashion for each inertial system as the pitching amplitude increases, which is due to formation of increasing large and shedding of LEV from the hydrofoil upper surface. This results in the production of higher lift forces, augmented by the rapid pitch reversal (stroke reversal) resulting in higher values of hydrodynamic torque and eventually generating higher peaks in $C_{P\theta}$ which contributes towards to the total energy extraction. It can be hypothesized that at lower water speeds the test-rig does not perform in an erratic fashion allowing it to undergo kinetics, which predictably will perform almost linearly with changing physical parameters.

As the free-stream velocity is increased (Figure 5.6(b)), we notice some changes in trend across the board. Small inertial block system still exhibits a typical linear behavior of increasing energy extraction with increasing pitching amplitude however, it's different in the case of baseline and big inertial blocks. Big inertial block case does also show an increasing C_{Pmean} with increasing pitching amplitude although the difference is not that significant when $\theta_o = 30^o$ to $\theta_o = 43^o$ since the values are almost closer to each other. For baseline case, C_{Pmean} values at all pitching amplitude cases lie in a very small range ($C_{Pmean} \approx 0.35$-0.40), showing no significant improvement in energy extraction with increasing pitching amplitude. To augment this, lets refer to Figure 5.7 which shows the variation of C_P in one flapping cycle for all inertial blocks with varying pitching amplitudes at $U_o = 0.65$ m/s. In Figure 5.6(b) for $\theta_o = 30^o$ C_{Pmean} values almost remains constant, with a very slight increase but not significant as the inertial mass is increased. This is also supported by C_P graph for $\theta_o = 30^o$ in Figure 5.7, where for all inertial mass units trend in C_P fairly remains similar during most of the time during the constant line in Figure 5.6(b). At

θ_o = 43º, the C_P peaks for all inertial mass units increase compared to the θ_o = 30º counterpart, suggesting increase in hydrodynamic lift force and torque.

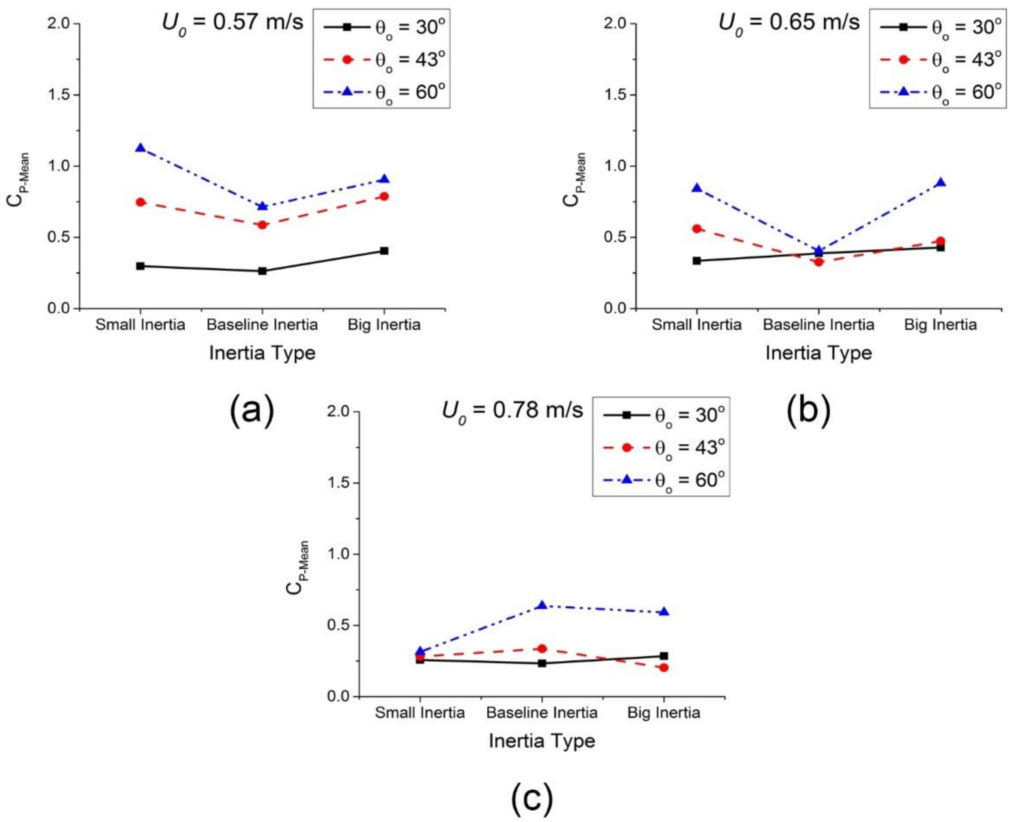

Figure 5.6: Mean coefficient of power (C_{Pmean}) for the different inertial blocks with varying pitching amplitudes at **(a)** U_o = 0.57 m/s, **(b)** U_o = 0.65 m/s and **(c)** U_o = 0.78 m/s.

For the small inertial block system, C_P remains positive for most part of the flapping cycle, however when the inertial mass is increased the system expends energy to the fluid rather than extracting from it. The slightly higher value of C_{Pmean} of the big inertial unit in Figure 5.6(b) for θ_o = 43º is due to the higher peak values in C_P in Figure 5.7 than the baseline inertial unit. This can be attributed to increased hydrodynamic lift force at most time instants and hydrodynamic torque during rapid stroke reversals due to increased inertial mass on the system. A somewhat similar trend is also observed for θ_o = 60º in Figure 5.7, but with some increased energy extraction performance as shown in Figure 5.6(b) due to higher pitching amplitude, early formation and shedding of a large LEV resulting in the production of large hydrodynamic lift force.

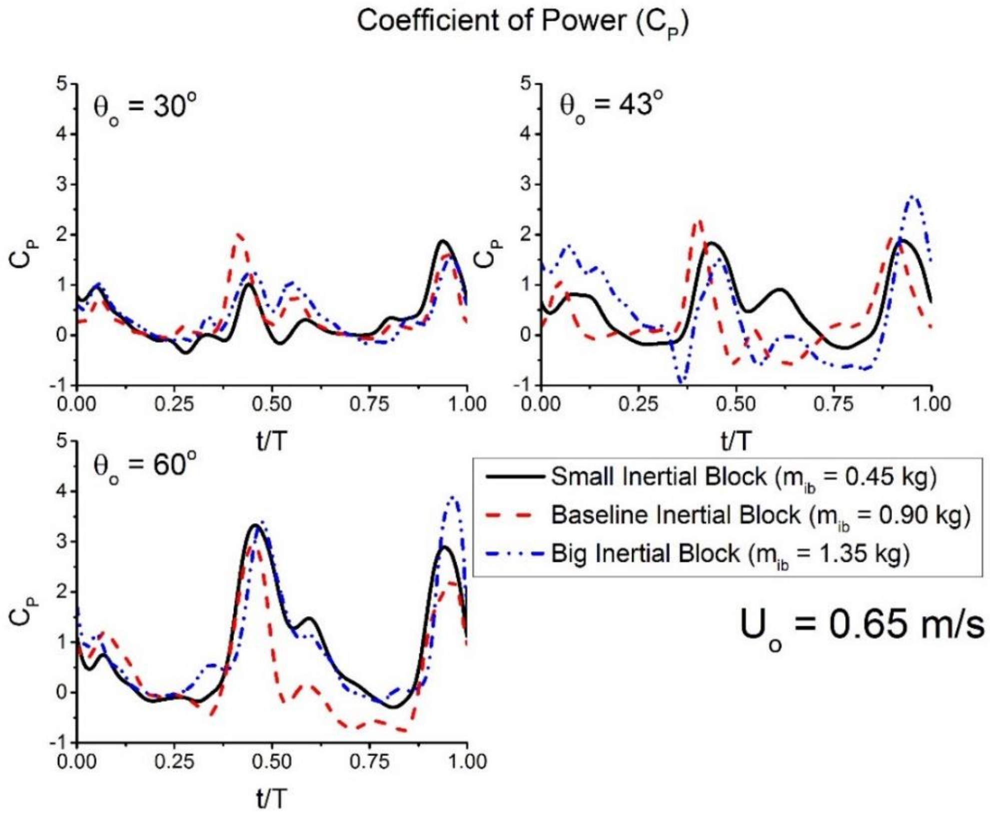

Figure 5.7: Phase-averaged C_P for the different inertial blocks with varying pitching amplitudes at $U_o = 0.65$ m/s.

From Figure 5.6(b) we also observe that for the baseline inertial mass unit, C_{Pmean} is much lower than the other two inertial mass units and in the same proximity as the smaller two pitching amplitudes ($C_{Pmean} \approx 0.35$-0.40). This could be attributed to the increase in energy expenditure during most of the flapping cycle as shown in Figure 5.7, even though the peak values have increased compared to the previous two pitching amplitudes. C_P for small and big inertial units do also cross the zero mark for a short amount of time, but the negative peak values of the baseline inertial unit case are larger and as discussed indicating energy expenditure (more during downstroke and positive stroke reversal $0.50 < t/T < 0.90$).

As discussed, we observed that with increasing pitching amplitude the energy extraction performance increases which in general is happening in all the inertial mass unit cases (Figure 5.6). However, we did also observe the behavior of the test rig when equipped with the baseline inertial mass unit at $U_o = 0.65$ m/s where C_{Pmean} values are in a very narrow region ($C_{Pmean} \approx 0.35$-0.40). Figure 5.8 shows the power, force and kinematic parameters associated with the plunging motion for the baseline inertial unit at U_o = 0.65 m/s at different pitching amplitudes.

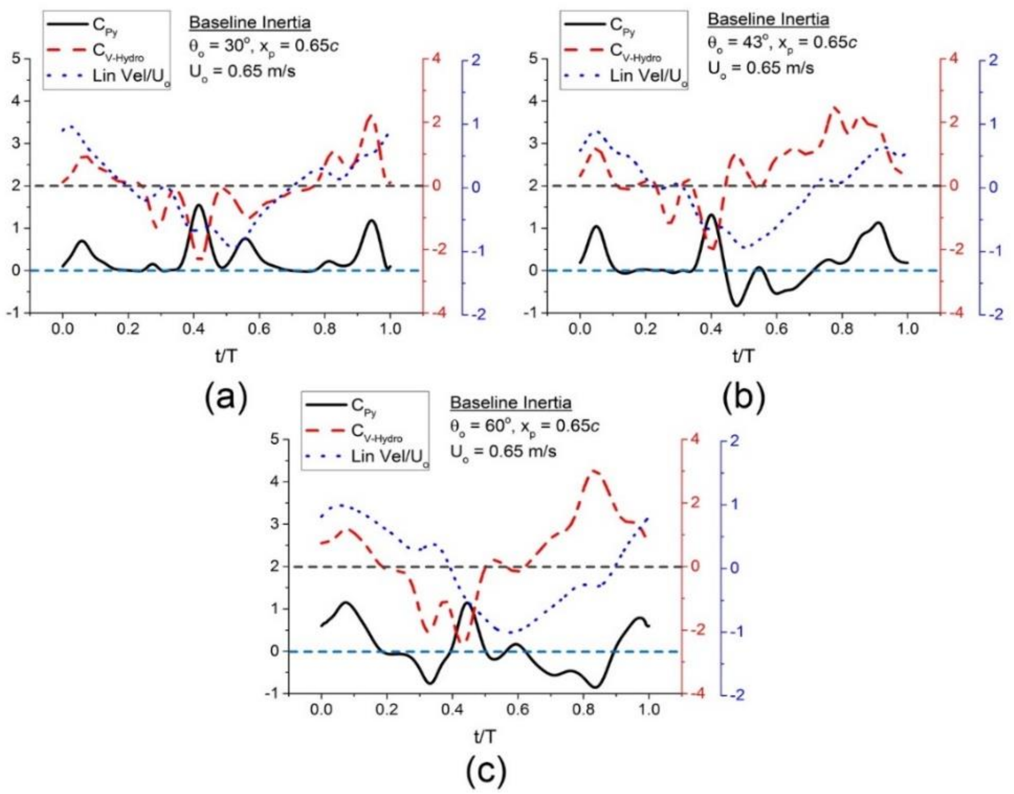

Figure 5.8: Phase-averaged $C_{V\text{-}Hydro,}$ Lin Vel/U_o and C_{Py} for the baseline inertial block at U_o = 0.65 m/s for **(a)** θ_o = 30°, **(b)** θ_o = 43° and **(c)** θ_o = 60°.

At θ_o = 30° in Figure 5.8 (a) we see that the linear velocity and hydrodynamic lift force have good synchronization, due to which C_{Py} remains positive during the whole flapping cycle. For θ_o = 43°, the synchronization remains for first half of the flapping cycle, but the linear velocity and hydrodynamic lift de-synchronize during the second half, which results in energy expenditure by the hydrofoil for the time range 0.45 < t/T < 0.70. Even though the hydrodynamic lift force values are greater than θ_o = 30°, the de-synchronization results to negative C_{Py} values, due to which C_{Pmean} for θ_o = 43° is slightly less than that for θ_o = 30°. For θ_o = 60°, hydrodynamic force values increase which also increase the plunging velocity of the hydrofoil, but we observe more desynchronization between the linear velocity and the hydrodynamic lift causing energy expenditure between 0.20 < t/T < 0.40 and 0.60 < t/T < 0.90. However, C_{Pmean} is still slightly more than the θ_o = 43° and almost close to θ_o = 30° since the time for which the system can extract energy from the fluid for θ_o = 60° is slightly greater than for θ_o = 43° as seen in Figure 5.8(b) and (c).

When compared with the other two inertial blocks' plunging kinetic parameters, as shown in Figure 5.9 for θ_o = 43° and U_o = 0.65 m/s, we observe that even though the hydrodynamic lift forces are somewhat similar, with slightly decreasing plunging velocity with increasing inertial mass, the apparent desynchronization between the lift force and plunging velocity for baseline inertial system takes the toll in its energy extraction performance as seen in Figure 5.6(b).

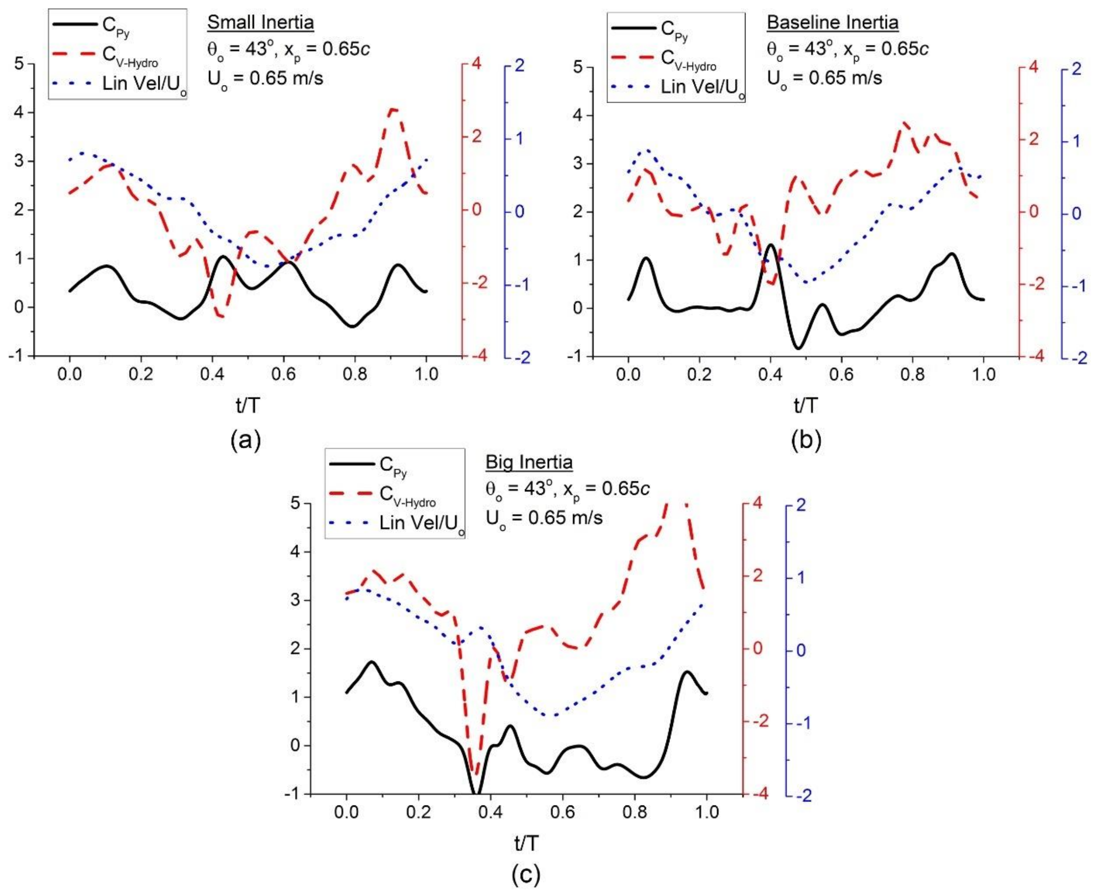

Figure 5.9: Phase-averaged $C_{V\text{-}Hydro}$, Lin Vel/U_o and C_{Py} at U_o = 0.65 m/s and θ_o = 43° for **(a)** Small inertial block **(b)** Baseline inertial block and, **(c)** Big inertial block.

Figure 5.10 (a) shows the Strouhal number and the flapping frequency for different inertia types at three different free-stream velocities (U_o = 0.57, 0.65 and 0.78 m/s) at θ_o = 43°. At very high Strouhal numbers, the shed vortices in the wake of an oscillating wing take the form of a reverse Karman street. In this condition, the vortices induce a jet like pattern near the center of the oscillating wing, thus providing a momentum surplus, and hence thrust is generated. In the study of natural flyers and swimmers in cruising condition, it was found that the Strouhal number is often within a narrow range of 0.2 < *St* < 0.4 (Taylor et al., 2003; Triantafyllou et al., 2000). On the other hand, at lower Strouhal numbers, the wake takes the form of the standard Karman street, where momentum deficit exists near the centre of the wing. This momentum deficit is believed to be related to the amount of energy extraction, however the exact relationship is unknown (F. Siala, J. A. Liburdy, 2015). In our experiments we have observed the formation of drag type vortices making a Karman street in the wake of the flapping foil, and *St* calculations through our measured quantities as shown in Figure 5.10 (a) lie within the smaller *St* ranges and not in the natural flyers and swimmers, indicating that the flapping foil in an energy harvesting mode generates a drag type von Karman vortex street. However, the exact range of *St* for energy harvesting flapping like that for natural flyers has not yet been determined and needs a more comprehensive parametric study to determine this range.

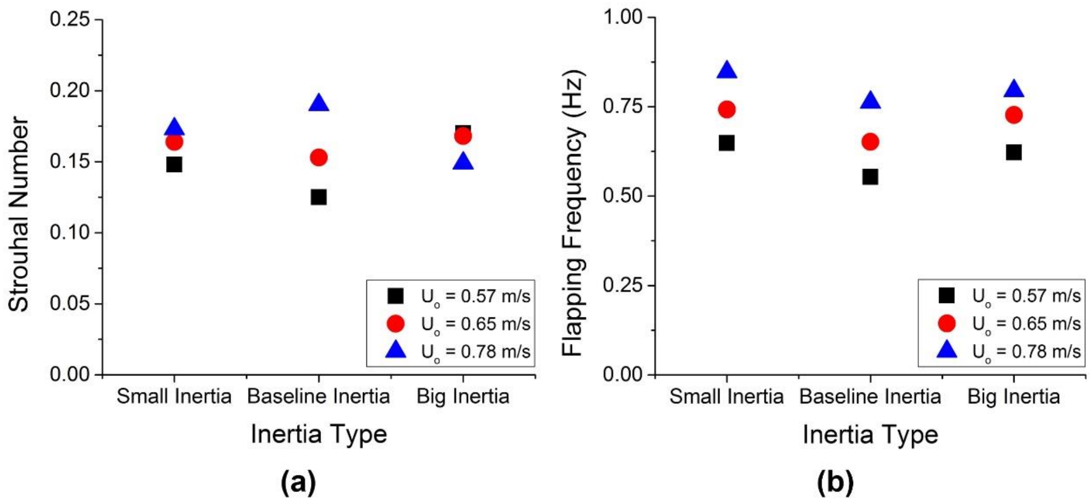

Figure 5.10: Scatter plot showing; (a) Strouhal number (*St*) and (b) flapping frequency (f – *Hz*) of a flatplate foil at θ_o = 43° at three different freestream velocities (U_o = 0.57, 0.65 and 0.78 m/s) for all three inertial mass types (Small Inertia (m_{ib} = 0.45 kg), Baseline Inertia (m_{ib} = 0.90 kg) and Big Inertia (m_{ib} = 1.35 kg)).

5.3 EFFECT OF PIVOT LOCATION

In the previous section, we have established different methods to make our test-rig viable for sustainable energy harvesting through flapping motion. This included modifications to the vertical cantilevered shaft and inclusion of inertial mass units on the test-rig to maintain this viability. Through experimenting with different inertial mass blocks, we were able to determine their effect on the test-rig's behavior in energy extraction mode.

We continue our experimental investigation by adopting one of the inertial mass units and investigate further the effect of other key parameters on the energy harvesting performance of the test-rig. In this section we will focus the effect of pivot location (x_p), which is defined as the distance from the foil's leading edge (L.E) to where the vertical cantilevered shaft is attached to the foil. We will analyze the passively flapping foil's kinematics and subsequent force generation, necessary for energy extraction as the pivot location is varied. For our discussion in this chapter, we have chosen three different pivot locations (x_p = 0.60c, 0.70c and 0.80c) tested at three different free-stream velocities (U_o = 0.57 m/s, 0.65 m/s and 0.78 m/s) and test-rig equipped with baseline inertial mass block (m_{ib} = 0.90 kg). Force-motion time history and subsequent flow evolution through our PIV results for fluid-structure interaction analysis will be presented in detail.

Before we present our results, it is important to note that as part of our preliminary testing, a flatplate hydrofoil with slits varying from 0.20c to 0.80c was initially designed, fabricated and experimentally tested to check the range of pivot locations, which would allow the foil to perform flapping motion. It was observed that pivot locations preceding 0.50c (inclusive) did not allow the foil to perform sustainable flapping motions, irrespective of different free-stream velocities, pitching amplitudes and inertial mass blocks. This could be attributed to the position of the center of gravity (C.G) and aerodynamic center (A.C) of the flatplate hydrofoil, which is at mid-chord. When the pivot location is x_p < 0.50c, we observed that the hydrofoil does rotates fully to the set pitching amplitude, rather it opposes the change and almost remains at near zero-degree angle. This could be due to the opposing moment produced by lift force as a result of the pivot location. Even, if the foil plunges due to the non-zero but very small pitching amplitude, it does not possess enough velocity to ensure change in angular direction (stroke reversal). With external help to ensure a complete pitching amplitude change at the end of the stroke, the foil would rotate in the opposite direction due to the opposing moment. At x_p = 0.50c since the vertical cantilevered shaft is set at the foil's C.G/A.C, the absence of any distance between the hydrodynamic force and pivot point leads to zero moment, hence no angular displacement. It was of this reason that for our detailed study, pivot locations aft of mid-chord were chosen where values have already been defined in the previous paragraph.

5.3.1 EFFECT ON STROKE REVERSAL TIME (ΔT_{SR})

Stroke reversal time (ΔT_{SR}) is an important parameter, which corresponds to the rotational speed of the flapping foil and is sensitive to change due to variation in geometric and kinematics parameters. Table 5.1 shows the stroke reversal time for three pivot locations (x_p = 0.60c, 0.70c and 0.80c) for different free-stream velocities (U_o = 0.57 m/s, 0.65 m/s and 0.78 m/s) at pitching amplitudes θ_o = 30º, 43º and 60º. Values from all three tables show that as free-stream velocity increases, with varying pivot location aft of the mid-chord, there is a decrease in ΔT_{SR}, indicating rapid pitch reversals due to increasing flapping frequencies. It is also observed that for U_o = 0.65 and 0.78 m/s, although negligible enough to be ignored but in quantitative terms, with increasing pivot location from the leading edge (L.E) there seems to be a slight decrease in ΔT_{SR} for both positive and negative angular change which may be attributed due to the static instability caused by the pivot location moving in the aft direction from the mid-chord.

θ_o	x_p	Stroke Reversal Time (ΔT_{SR})					
		U_o = 0.57 m/s		U_o = 0.65 m/s		U_o = 0.78 m/s	
		θ_o to - θ_o	-θ_o to θ_o	θ_o to - θ_o	-θ_o to θ_o	θ_o to - θ_o	-θ_o to θ_o
30º	0.60c	0.3562	0.3544	0.3281	0.3181	0.2948	0.3239
	0.70c	0.3293	0.352	0.2977	0.336	0.2765	0.3122
	0.80c	0.3128	0.3019	0.2925	0.2779	0.2773	0.2655
43º	0.60c	0.3598	0.4237	0.3471	0.3868	0.3092	0.3233
	0.70c	0.3196	0.3415	0.3005	0.3197	0.3045	0.3143
	0.80c	0.3411	0.3009	0.3196	0.2890	0.2984	0.2813
60º	0.60c	0.3777	0.3900	0.3848	0.3779	0.3590	0.3990
	0.70c	0.3595	0.3966	0.3498	0.395	0.3383	0.3854
	0.80c	0.3721	0.3534	0.3392	0.3817	0.3457	0.3737

Table 5.1: ΔT_{SR} for pivot locations x_p = 0.60c, 0.70c and 0.80c for three different free-stream velocities at θ_o = 30º, 43º and 60º. Two-time instants are noted in this table which shows that during one flapping cycle, the hydrofoil undergoes two stroke reversals.

Although the trend observed for ΔT_{SR} in Table 5.1 for both negative and positive angular displacement change, the total time taken to perform the stroke reversal during one cycle flapping cycle is clear. Figure 5.11 shows the plots for total stroke reversal time ($\Delta T_{SR\text{-}TOTAL}$) for all cases described in Table 5.1. At all pitching amplitudes it can be observed that with increasing free-stream velocity $\Delta T_{SR\text{-}TOTAL}$ decreases, indicating that the stroke reversal takes less portion of the flapping cycle time.

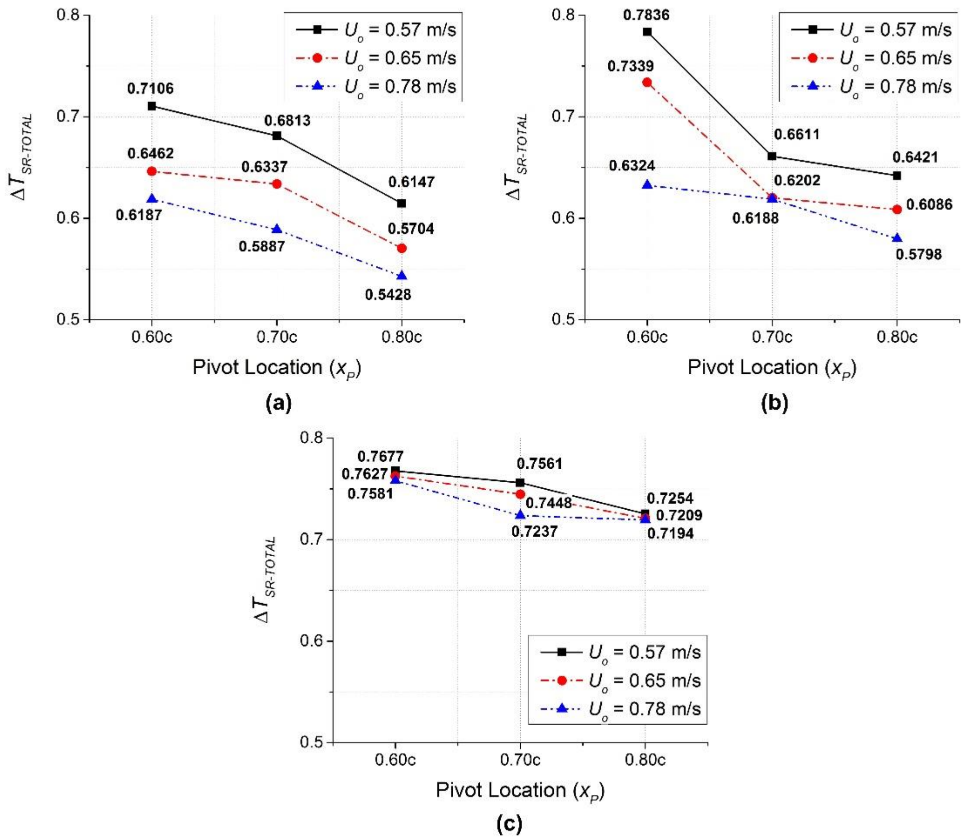

Figure 5.11: $\Delta T_{SR\text{-}TOTAL}$ at pivot locations $x_p = 0.60c$, $0.70c$ and $0.80c$ for three different free-stream velocities (U_o = 0.57 m/s, 0.65 m/s and 0.78 m/s) at **(a)** $\theta_o = 30^o$, **(b)** $\theta_o = 43^o$ and **(c)** $\theta_o = 60^o$. It is evident from the figure that with increasing water velocity and within, moving the pivot location aft of the mid-chord allows the hydrofoil to perform both stroke reversals quicker in a flapping cycle, hence more time spent in plunging motion. Furthermore, with increasing pitching amplitude the total stroke reversal time ($\Delta T_{SR\text{-}TOTAL}$) increases at each pivot location and tends to fall into a narrow range of values (becoming closer to each other), where this is more evident at $\theta_o = 60^o$.

Furthermore, for one free-stream velocity, as the pivot location moves further aft of the mid-chord, the $\Delta T_{SR\text{-}TOTAL}$ decreases which may be due to the increasing torque generated by the hydrofoil due to increasing distance of the aerodynamic center from the cantilevered pivot location. Two things can be deduced from this; increasing the free-stream velocity and within, moving the pivot location aft of the mid-chord reduces the stroke reversal time within the flapping cycle allowing the airfoil more time to perform the plunging motion and secondly it allows the airfoil to perform the 2-DoF flapping motions faster, hence the increase in flapping frequencies.

It can also be observed from Figure 5.11 that with increasing pitching amplitude, the total stroke reversal time ($\Delta T_{SR\text{-}TOTAL}$) also increases at each pivot location, indicating that the increased flapping frequency allows the hydrofoil to cover the linear distance in less time during the flapping cycle. The total stroke reversal time ($\Delta T_{SR\text{-}TOTAL}$) values also lie within a very narrow range with increasing pitching amplitude, as it is quite evident in Figure 5.11 (c) for θ_o = 60°, although it still follows a gradual decline in ($\Delta T_{SR\text{-}TOTAL}$) as observed at other pitching amplitudes. It should be noted that the calculations for ΔT_{SR} and $\Delta T_{SR\text{-}TOTAL}$ were all done from the angular displacement profile (*y*-axis) against non-dimensional time (*t/T*) (*x*-axis). Hence, the values given in Table 5.1 and Figure 5.11 represent the ratio of the flapping period.

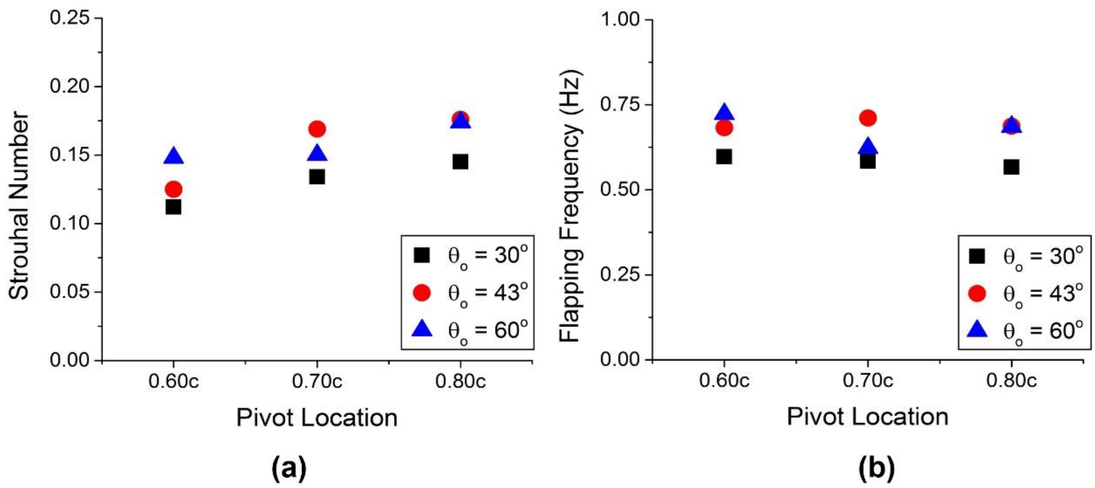

Figure 5.12: Scatter plot showing; (a) Strouhal number (*St*) and (b) flapping frequency (*f – Hz*) of a flatplate foil at U_o = 0.65 m/s at three different pitching amplitudes (θ_o = 30°, 43° and 60°) and equipped with Baseline Inertia (m_{ib} = 0.90 kg).

Figure 5.12 shows the Strouhal number (*St*) and flapping frequency (f) trend for a flatplate foil with varying pitching amplitude θ_o = 30°, 43° and 60° at x_p = 0.60*c*, 0.70*c* and 0.80*c* at U_o = 0.65 m/s and m_{ib} = 0.90 kg. Although the oscillating frequency lie within a very narrow range for each pitching amplitude in Figure 5.12 (b), the St on the other hand gradually increases as the pivot location is moved towards the trailing edge for each pitching amplitude. This suggests that the dimensionless quantity representing oscillating flow mechanisms is mostly dependent on the total straight-line distance between the extremes of the pivot location position throughout the flapping cycle (A_{piv}) as shown in Table 5.2. The A_{piv} values were determined from linear displacement data from the accelerometer as it was fixed on the small aluminum block and in-line with the foil's pivot location. From Table 5.2 it can be observed that at smaller fixed pivot location, there is an increase in A_{piv} as pitching amplitude increases and as the pivot location moves to the x_p = 0.80c, A_{piv} almost remains consistent with increase in pitching amplitude. However, at each pitching amplitude with increase in pivot location distance from leading edge, shows a gradual and consistent increase in A_{piv}. This increase in linear distance may be attributed towards the relatively increasing plunging velocity experienced by the flatplate foil as the pivot location increases, eventually impacting the vorticity around the foil where the vortex formation and shedding becomes stronger and faster due to increase in plunging velocity.

5.3.2 CHANGE ON ENERGY EXTRACTION PERFORMANCE AND FLUID-STRUCTURE INTERACTION

We have discussed that how by varying the pivot location as well as the pitching amplitude at different free-stream velocities affects the kinematics of a flapping foil in energy harvesting mode. In this section, we will try to fully understand that how by varying the pivot location can affect the force generation capacity and energy extraction performance of a passively actuated flapping foil and the underlying fluid-structure interaction. For simplicity, in this section we will discuss the θ_o = 43° case for pivot locations x_p = 0.60c, 0.70c and 0.80c at free-stream velocities U_o = 0.57 m/s, 0.65 m/s and 0.78 m/s.

Figure 5.13 shows the performance of the test-rig at θ_o = 43° with varying free-stream velocity at three different pivot locations (x_p = 0.60c, 0.70c and 0.80c). The graph shows a steady and gradual increase in energy extraction performance as the pivot location is moved aft of the mid-chord towards the hydrofoil's trailing edge (T.E). The energy extraction performance is also dependent on the free-stream velocity, indicating a decrease in performance and efficiency as it is increased. At lower free-stream velocities, the energy extraction performance also seems more sensitive to changes in pivot location as indicated in Figure 4.1, although this may vary when other geometric parameters change such as pitching amplitude, which will be discussed in detail later.

To understand how by varying the pivot location can affect the energy extraction performance of the flapping foil test-rig, it is important to analyze how this geometrical aspect affects the force and kinematic parameters of a flapping hydrofoil. Figure 5.14 shows the force and motion behavior and their correlation for pitching amplitude θ_o = 43°, U_o = 0.65 m/s at three different pivot locations (x_p = 0.60c, 0.70c and 0.80c).

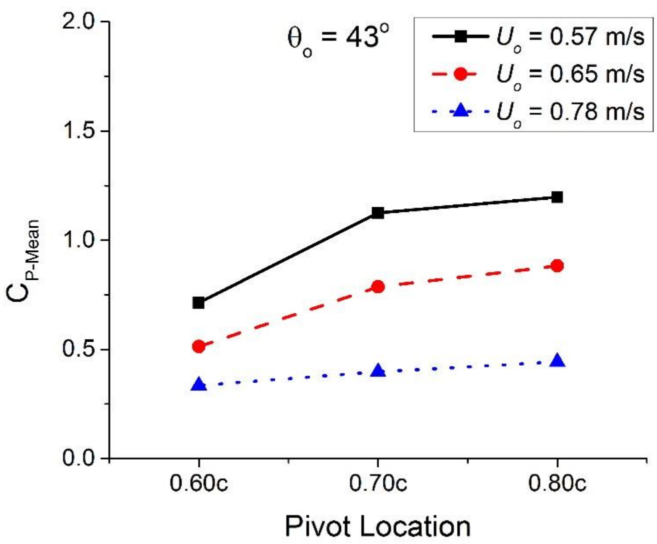

Figure 5.13: C_{Pmean} variation of flat-plate hydrofoil with varying pivot locations (x_p = 0.60c, 0.70c and 0.80c) at three different free-stream velocities (U_o = 0.57 m/s, 0.65 m/s and 0.78 m/s) with pitching amplitude set at θ_o = 43°. A gradual increase in performance is observed as the pivot location is moved more in aft direction from mid-chord (C.G and A.C of flat-plate).

From Figure 5.14 (a) we see an increase in C_P as the pivot location distance from the leading edge is increased. The peak values, which are also increasing with increasing pivot location, are mostly occurring between 0.4 < t/T < 0.55 and 0.8 < t/T < 0.95 i.e. during the end of the stroke reversal. Furthermore, as already discussed in Chapter 4 and section 5.1 that most of the energy extraction contribution is from the plunging motion and the pitching motion only enhances this performance during the end of each stroke reversal during each flapping cycle. For a very brief period (0.2 <

$t/T < 0.275$ for $x_p = 0.60c$ and $0.3 < t/T < 0.35$ for $x_p = 0.70c$ and $0.80c$) during the flapping cycle, C_P remains in the negative regime with comparatively smaller values indicating energy expenditure however for the rest of the flapping cycle it remains positive. This does very little to affect the overall mean energy extraction performance of the flapping foil and shows a gradual increase as shown in Figure 5.13.

This energy expenditure, even for a brief amount of time, as well as the sudden increase in peak values is mostly due to the contribution from the plunging motion as shown in Figure 5.15 (b), which shows the hydrodynamic lift force ($C_{V\text{-}hydro}$), corresponding plunging velocity (Lin Vel/U_o) and C_{Py} as a result. With increasing pivot location, we observe an increase in hydrodynamic lift force and a gradual increase in plunging velocity, although this increase is not the only determining factor in the enhancement of energy extraction performance. Synchronization between the forces and their corresponding velocities plays an important role, and we see that for all three pivot locations this synchronization between the hydrodynamic lift force and plunging velocity is quite good, except for instants where it is negative for a brief time and has small negative values indicating not too much energy has been expedited. Not only the peak values which occur due to the end of the stroke reversal are increased with increasing pivot location, but during the plunging motion (with the hydrofoil at its maximum set pitching amplitude) the acting hydrodynamic forces also increase considerably. With good synchronization with the plunging velocity, C_{Py} in Figure 5.14 (b) during these time periods of plunging motion remain positive, which enhances the energy extraction performance as observed in C_P trend in Figure 5.14 (a).

Figure 5.14 (c) shows $C_{P\theta}$ and the corresponding hydrodynamic torque and angular velocity. As observed in Chapter 4 and Section 5.1 the energy extraction from pitching motion is only contributed during the ending stages of the stroke reversal, while at other time instants the angular velocity is zero since the hydrofoil is plunging with the set maximum pitching amplitude. As the pivot location is moved towards the trailing edge, the hydrodynamic torque is increased as shown in Figure 5.14 (c). Since the hydrodynamic lift force is acting on the flat plate hydrofoil's mid-chord where its aerodynamic center (A.C) and center of gravity (C.G) are located. As the distance between the A.C and the cantilevered pivot location is increased, the moment arm increases which increases the net torque acting on the hydrofoil. Due to this increased net hydrodynamic torque, the total time taken for the stroke reversal (ΔT_{SR}) is reduced indicating that the hydrofoil spends the most of its flapping cycle portion undergoing plunging motion. Depending on other parameters, this indicates that the hydrofoil then can extract more energy from the surrounding fluid. Because of this increased net hydrodynamic torque and subsequent increased angular velocity experienced by the hydrofoil leads to larger peaks in $C_{P\theta}$ as shown in Figure 5.14 (c), which augments C_{Py} resulting in higher C_P values as shown in Figure 5.14 (a).

Figure 5.14 shows the plunging motion force and motion parameters for x_p = 0.60c, 0.70c and 0.80c at U_o = 0.65 m/s and θ_o = 43°, and correspondingly Figure 5.16 shows the vorticity contours at eight different time instants as labelled in Figure 5.15. As already discussed, we observe a gradual increase in peak values in hydrodynamic lift force and plunging velocity as the pivot location of the vertical cantilevered shaft is moved aft of the flat-plate hydrofoil's mid-chord. With good synchronization between the lift force and plunging velocity ensues larger peaks in C_{Py} as observed in Figure 5.15. At t/T = 0.05, the hydrofoil is at its maximum set pitching amplitude which in this case is θ_o = 43° and has just initiated the upstroke motion. Due to a high pitching amplitude and the initiation of the plunging motion the LEV forms up for all three pivot locations. However, the evolution is different since for x_p = 0.60c the plunging velocity is comparatively slower than the other two pivot locations the hydrofoil allowing the LEV to form up early than at 0.70c and 0.80c as shown in Figure 5.16. At t/T = 0.10 for 0.60c pivot location the LEV starts to detach from the foil's upper surface, however for the 0.70c and 0.80c pivot locations the LEV has formed but not shed completely. Furthermore, from Figure 5.16 the size of LEV at t/T = 0.10 shows some similarities in terms of size for all pivot locations. In correlation with Figure 5.15, since the LEV starts to detach early for 0.60c, the hydrodynamic lift force decreases at **(2)** in Figure 5.15 (a), while since the LEV is still attached to the foil's upper surface for 0.70c there is a sudden rise in hydrodynamic lift force, while it is much higher for 0.80c due to the presence of greater inner core strength as shown in Figure 5.16 and slightly larger size of LEV as compared to 0.70c. For both 0.70c and 0.80c the shedding time for the LEV during this upstroke motion are almost close spanning in the time range $0.115 < t/T < 0.135$ which can be seen due to the sudden decline in hydrodynamic lift force in Figure 5.15 (b) and (c).

Between $0.10 < t/T < 0.25$ for all three pivot locations, the first LEV has detached from the hydrofoil's upper surface and sheds into the wake which is followed by the initiation of the second LEV. Subsequently, upon contact of the moment arm with the plunge limiter the hydrofoil starts to decelerate and initiates stroke reversal. The second LEV is still on the upper surface of the hydrofoil and slowly moves along the chord line. However, due to the linear deceleration and stroke reversal, the flow on the upper side of the hydrofoil gets pushed against the side wall of the water tunnel as can be seen at $t/T = 0.35$. Subsequently, the hydrodynamic lift force and the plunging velocity declines because of this deceleration, where after $t/T = 0.35$ the hydrofoil almost comes to a halt briefly. The flow structures, especially the second LEV, on the upper side of the hydrofoil break down eventually and are shed into the wake as shown in Figure 5.16. As the hydrofoil performs the stroke reversal past its zero-degree angular position due to the presence of inertial block attached on the test-rig, the continuous presence of the hydrodynamic force on the hydrofoil takes over the stroke reversal, as already discussed in detail in Section 5.1. Since, the hydrofoil is not performing any significant plunging motion during its second half of its stroke reversal, no evident flow structures are observed in Figure 5.16 at $t/T = 0.45$ and little beyond for all three pivot locations. However, due to the hydrofoil's change of direction and the force sensor being coupled with the hydrofoil, we observe large peaks in hydrodynamic lift force curves in Figure 5.15. The size of these peaks especially observed between $0.4 < t/T < 0.5$ for $0.70c$ and $0.80c$ is due to the large torque because of increased moment arm distance between A.C/C.G and the cantilevered pivot location. As the hydrofoil completes its stroke reversal and is set to its maximum pitching amplitude, its starts its downstroke motion. $t/T = 0.60$ in Figure 5.16 shows the hydrofoil in its negative maximum pitching amplitude position and already undergoing plunging motion. The hydrofoil experiences the same kind of flow evolution as already discussed in its first half of its flapping cycle, where for $0.60c$ due to its relatively lower plunging velocity has more time to perform its downstroke motion hence, the LEV is formed on the foil's lower surface and gets ready to detach from the surface. The hydrodynamic lift force experiences a similar fate as in the first half of the flapping cycle, where due to the early shedding of the LEV, there is a sudden decline as shown in Figure 5.16 (a). As for $0.70c$ and $0.80c$ pivot location cases, since the LEV is still forming on the foil's lower surface, the lift force is still comparatively higher. With its good synchronization with the plunging velocity, we observe higher peaks at t/T = 0.60 in Figure 5.15 (b) and (c) in C_{Py} which eventually contributes towards enhancement in energy extraction performance as observed in Figure 5.14 (a)-II & III.

As the moment arm comes in contact with the downward plunge limiter, the second stroke reversal of the flapping cycle starts and the foil experiences linear deceleration and change in angular displacement. The first LEV already sheds before the hydrofoil starts its stroke reversal and as the second LEV starts to form up the foil has started its second stroke reversal. With its changing angular displacement, the foil pushes the flow on its lower surface against the other side of the wall, which eventually breaks down the flow structures including the second LEV and dispersed into the wake as observed at t/T = 0.80 in Figure 5.16. Since the foil approaches the zero-degree mark around t/T = 0.80 and subsequent after, the foil briefly stops its plunging motion due to which the hydrodynamic lift force reaches near its zero-mark as observed in Figure 5.15. However, due to the presence of inertial blocks the foil passes its zero-degree marks by a few degrees and due to the continuous action of the hydrodynamic forces by the water flow, the foil completes its stroke reversal, as experienced in its first half of flapping cycle. The hydrodynamic lift force continues to increase in its new direction (now upstroke) and upon its end of the stroke reversal a large peak is observed around t/T = 0.95, which leads to another increase in C_{Py} as observed in Figure 5.15. No evident flow structures are observed at this moment since the hydrofoil is not performing plunging motion at large pitching amplitudes, nor the foil is experiencing high frequency pitching motions as seen by rapid pitching foils. Subsequent augmentation in C_P graph in Figure 5.14 (a), which increases as the pivot location distance increases from the leading edge.

5.4 EFFECT OF PITCHING AMPLITUDE

In the previous section we discussed as how by changing the pivot location affects the kinematics of the flapping plate hydrofoil and subsequently the net hydrodynamic lift and ensuing energy extraction from the flow. The flow evolution was also analyzed and its correlation with the hydrodynamic lift force and flapping foil kinematics. To further our analysis, in this section we will discuss that how can the variation in pitching amplitude across different pivot locations can affect the flapping foil kinetics and its energy extraction performance. Although, we

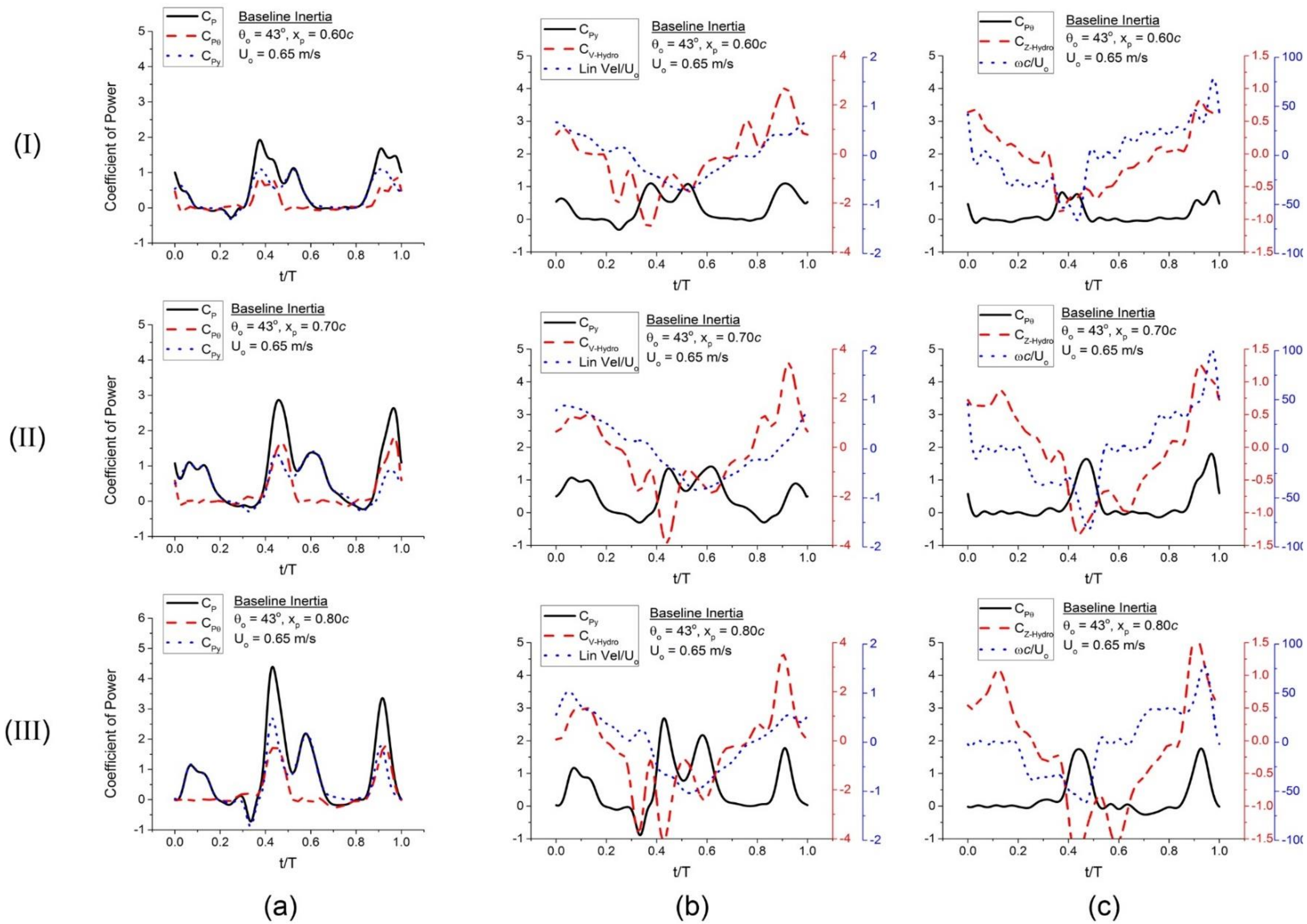

Figure 5.14: Graphs showing phase-averaged **(a)** Coefficient of Power (Total, Plunging and Pitching), **(b)** Coefficient of Power due to Plunging motion with corresponding Coefficient of Hydrodynamic Vertical Force and Linear Velocity and **(c)** Coefficient of Power due to Pitching Motion with corresponding Coefficient of Hydrodynamic Moment and Angular Velocity, for θ_o = 43° and U_o = 0.65 m/s at pivot locations, **(I)** $x_p = 0.60c$, **(II)** $x_p = 0.70c$ and **(III)** $x_p = 0.80c$.

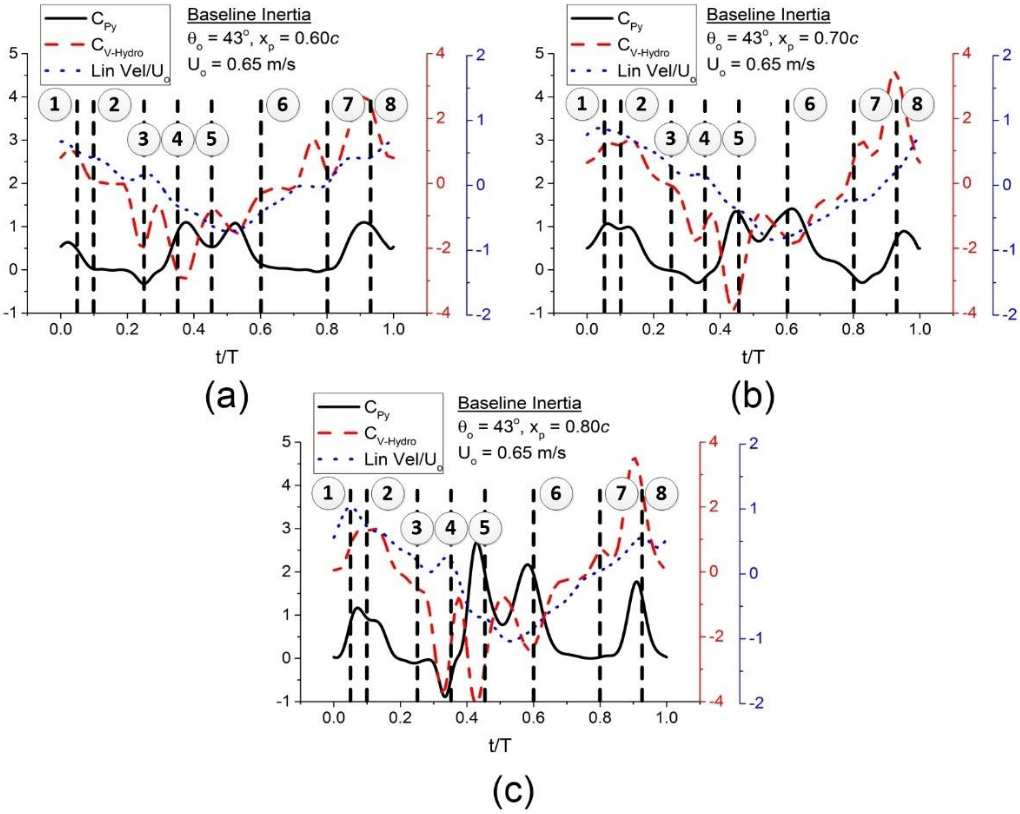

Figure 5.15: Phase-averaged C_{Py}, $C_{V\text{-}hydro}$ and Lin Vel/U_o variation of flat-plate hydrofoil with pitching amplitude set at θ_o = 43° and U_o = 0.65 m/s for pivot locations: **(a)** x_p = 0.60c, **(b)** x_p = 0.70c and **(c)** x_p = 0.80c. Eight different time instants are marked on all three graphs which correlates with flow evolution in Figure 4.5 because of changes observed in hydrodynamic lift force.

have discussed up to some extent as how by increasing the pitching amplitude can affect the flow evolution and energy extraction performance in Section 5.1.2, this chapter will explore its correlation with varying pivot location on the energy extraction process.

Figure 5.17 shows the variation of C_{Pmean} at different pivot locations for the three different pitching amplitudes at different free-stream velocities. Irrespective of the pivot location and pitching amplitude, we observe in Figure 5.17 that with the increase in free-stream velocity, C_{Pmean} tends to decrease implying that energy extraction efficiency also decreases. This was also observed in our discussion in Section 5.1.2 when exploring the effects of the variation in mass of inertial blocks on system's energy extraction performance.

For all free-stream velocities and pivot locations in Figure 5.17, the hydrofoil when set at θ_o = 30° and 43° shows a similar gradual increase in C_{Pmean} with increase in pivot location distance from leading edge however, for 60° the trend is comparatively erratic. Normally, at each pivot location for all free-stream velocities C_{Pmean} should increase as exhibited by 30° and 43°. However, when increased to 60° the trend becomes erratic where at 0.80c C_{Pmean} increases with increasing pitching amplitude at all free-stream velocities (Figure 5.15) and at 0.60c at U_o = 0.57 m/s (Figure 5.17 (a)), while it is either lower than both 30° and 43° at 0.60c (Figure 5.17 (b) & (c)) or almost in between the two at 0.70c for U_o = 0.65 m/s and 0.78 m/s (Figure 5.17 (b) & (c)).

Figure 5.18 shows the C_P graph at U_o = 0.65 m/s for the three different pitching amplitudes at pivot location cases 0.60c and 0.70c, where it was observed that the foil at pitching amplitude 60° had lower energy extraction performance than at other two pitching amplitudes at this free-stream velocity (Figure 5.17 (b)). At 0.60c at $0 < t/T < 0.25$, C_P starts to decline and scratches the zero-mark line for all three pitching amplitudes, with the 60° case starting off with the highest value at $t/T = 0$ followed by 43° and 30° cases. However, for $0.25 < t/T < 0.375$ 60° case remains in the negative region while 43° and 30° make a steady increase in energy extraction. 60° case is able to recover a positive energy extraction performance for $0.375 < t/T < 0.55$ however, compared to the other pitching amplitudes it does not attain the same peak value.

Roughly after $t/T \approx 0.55$, 60° case goes deeper into the red zone as marked in Figure 5.18 (a) and expends energy to its surrounding till $t/T \approx 0.90$ and then recovers with a comparatively large positive peak than the other pitching amplitude cases. This loss of energy for most part of the time during the flapping cycle as compared to the other two pitching amplitude cases pertains to the lower C_{Pmean} value at 0.60c pivot location as seen in Figure 5.17 (b). At pivot location 0.70c in Figure 5.17 (b), although C_P for all pitching amplitudes remain in the positive region and hardly going into the red zone as marked, C_{Pmean} for $\theta_o = 60°$ is greater than $\theta_o =$ 30° but smaller than $\theta_o = 43°$. For $0 < t/T < 0.25$ in Figure 5.18 (b) C_P values are greater for $\theta_o = 43°$ and remain so till right before $t/T \approx 0.25$, while for 30° and 60° the peak remains for half of this time and remain zero till $t/T \approx 0.325$.

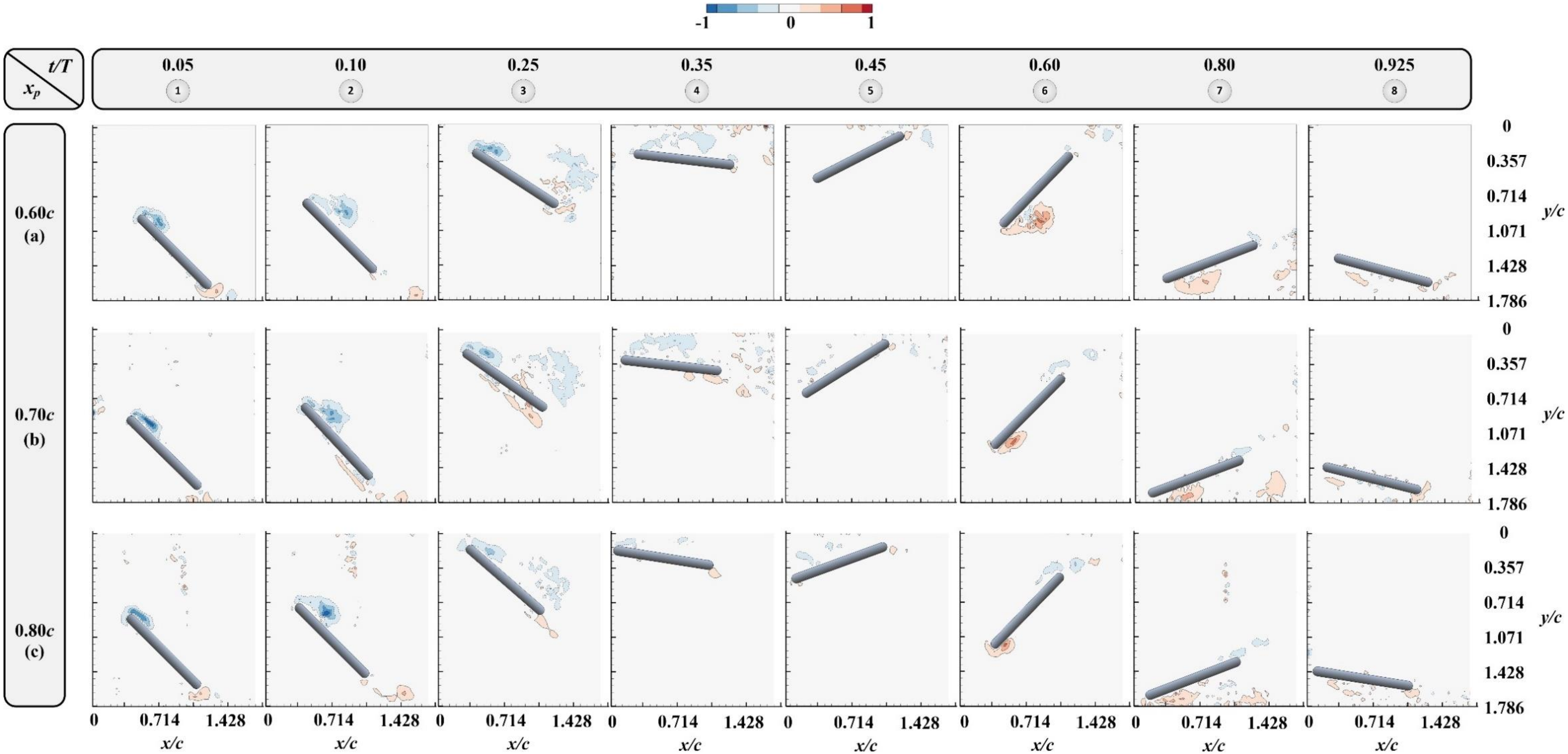

Figure 5.16: Figure showing vorticity contours of flat-plate hydrofoil at eight different time instants during one flapping cycle with free-stream velocity of U_o = 0.65 m/s and pitching amplitude θ_o = 43° at three different pivot locations: **(a)** x_p = 0.60c, **(b)** x_p = 0.70c and **(c)** x_p = 0.80c. The x and y scale are dimensionalized with reference to the chord length (c = 0.14 m) of the hydrofoil.

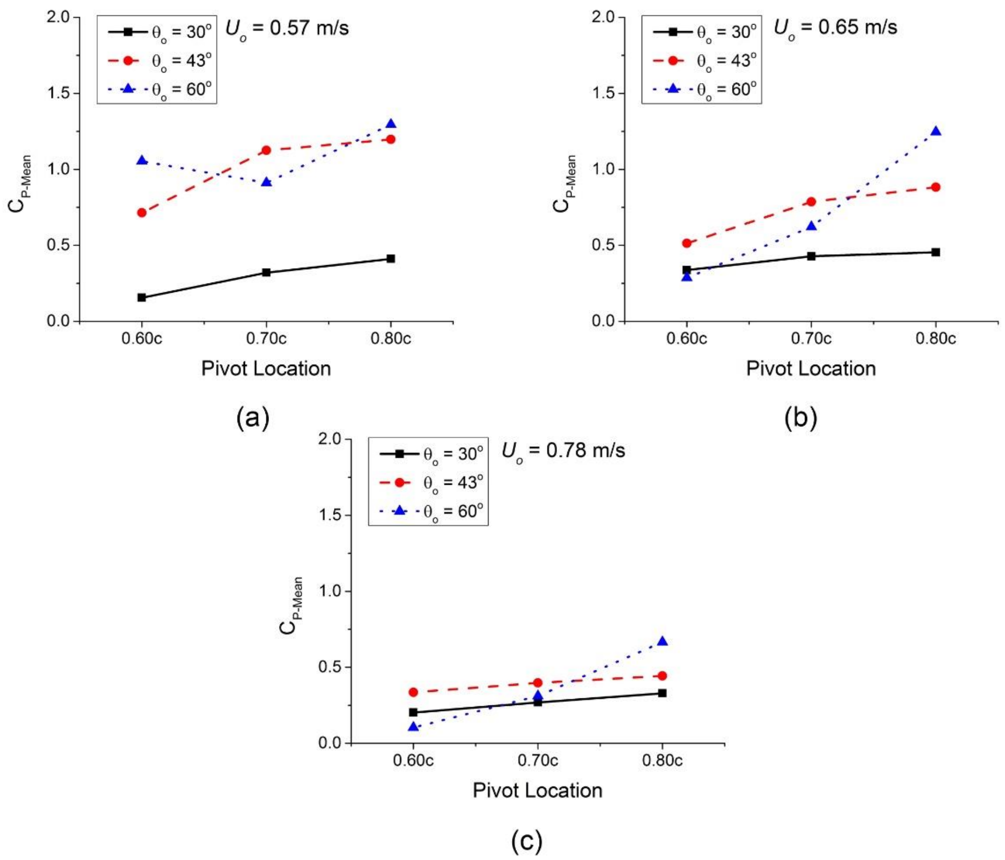

Figure 5.17: C_{Pmean} variation of flat-plate hydrofoil with varying pivot locations (x_p = 0.60c, 0.70c and 0.80c) at three different pitching amplitudes (θ_o = 30°, 43° and 60°) at **(a)** U_o = 0.57 m/s, **(b)** U_o = 0.65 m/s and **(c)** U_o = 0.78 m/s.

Between 0.3 < t/T < 0.5 the C_P values increase to their respective peak values for all pitching amplitudes with θ_o = 43° being the highest before θ_o = 60° and 30°, which also goes for the second bump in C_P values observed in Figure 5.18 (b) right after the first peak (0.475 < t/T < 0.75 for all pitching amplitude cases). The same behavior is being exhibited where this small increase in C_P is higher and remains for a longer time for θ_o = 43° as compared to the other two pitching amplitudes. The last peak values due to the second stroke reversal of the flapping foil exhibit the trend where the peak values for θ_o = 60° is higher followed by 43° and 30°. Although this helps the θ_o = 60° case to enhance its mean energy extraction performance, the longer time spent, and slightly higher C_P values exhibited by θ_o = 43° for most part of flapping cycle allows it to have an edge over the θ_o = 43° case. It is due to this that the θ_o = 43° case has a higher C_{Pmean} value than the θ_o = 60° case as seen in Figure 5.17 (b) for x_p = 0.70c.

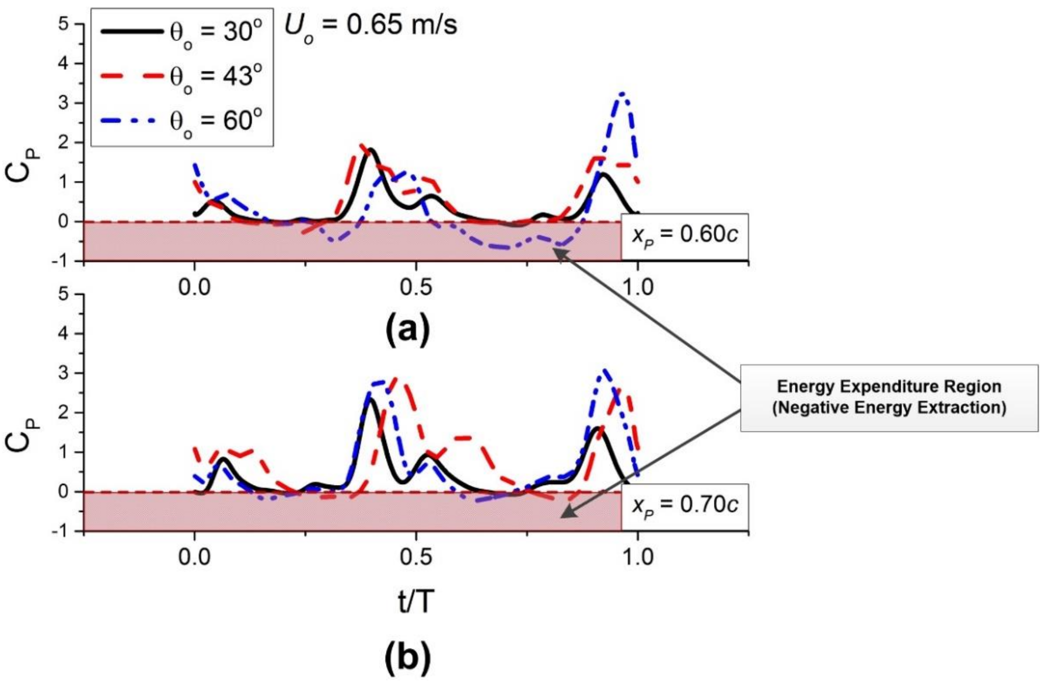

Figure 5.18: Phase-averaged C_P at U_o = 0.65 m/s for three different pitching amplitudes at pivot locations **(a)** x_p = 0.60c and **(b)** x_p = 0.70c. Red regions marked in red below the zero line indicates the region where the flapping foil starts to expend energy from the system rather than extracting it from the surrounding fluid.

To complement the previous discussion of flapping foil energy extraction behavior for different pitching amplitudes and pivot locations 0.60c and 0.70c, Figure 5.19 (a) and (b) shows the energy extraction contribution due to plunging (C_{Py}) and pitching motion ($C_{P\theta}$) at U_o = 0.65 m/s and θ_o = 30º, 43º and 60º respectively. C_{Py} plots are also marked with eight different time instants to correlate the hydrodynamic lift fore behavior with the flow evolution for x_p = 0.60c and 0.70c in Figure 5.22 and Figure 5.23 respectively.

$C_{P\theta}$ in Figure 5.19 (b) exhibits a normal trend at both pivot locations, where the energy extraction contribution increases with increasing pitching amplitude. Furthermore, energy extraction peaks are higher in the 0.70c case relative to the 0.60c pivot location case due to the high torque experienced by the hydrofoil and higher angular velocity as a result. As observed previously, the pitching contribution towards total energy extraction by the hydrofoil is positive twice during the flapping cycle when the foil is about to complete its stroke reversal, while it remains zero during the plunging phase since the hydrofoil is set at its maximum pitching amplitude. Hence, the main part is played by the plunging motion which determines the trend of the total energy extraction during the flapping cycle, as is in this case. We observe in Figure 5.19 (a)-I where for θ_o = 60° C_{Py} is negative for most part of the flapping cycle (0.2 < t/T < 0.9) indicating huge energy loss by the system during its flapping motion. This could be attributed towards the de-synchronization between the hydrodynamic lift force and plunging velocity resulting in negative energy extraction through plunging motion in this case as seen in Figure 5.20 (c). The only way C_{Pmean} is positive in Figure 5.17 (b) for θ_o = 60° at x_p = 0.60c is due to the augmentation of positive $C_{P\theta}$ seen in Figure 5.19 (b)-I. While at other pitching amplitudes C_{Py} shows a more positive trend due to good synchronization between their respective hydrodynamic lift force and plunging velocity, irrespective of the fact that comparatively hydrodynamic lift force for θ_o = 30° and 43° is lower than for θ_o = 60°. When changed from x_p = 0.60c to 0.70c, C_{Py} peak values increase and show better performance by staying above the red-zone (energy expenditure zone) for almost the whole of the flapping cycle. This was possible due to good synchronization between the hydrodynamic lift force and plunging velocity at all pitching amplitudes as shown in Figure 5.21. Augmented by higher $C_{P\theta}$ in Figure 5.19 (b)-II, C_P trend in Figure 5.18 (b) shows higher peak values resulting in higher C_{Pmean} for all pitching amplitudes than at x_p = 0.60c as shown in Figure 5.18 (b).

However, at x_p = 0.70c (Figure 5.17 (b)) C_{Pmean} for θ_o = 60° is lower than θ_o = 43° which is due to the lower hydrodynamic lift force values at θ_o = 60° than θ_o = 43° observed in Figure 5.21 (b) and (c) respectively. To fully understand the hydrodynamic force behavior and its effect on the energy extraction performance of the passively flapping foil, Figure 5.22 and 5.23 shows the flow evolution in terms of vorticity contours with three pitching amplitudes (θ_o = 30°, 43° and 60°) for two pivot locations x_p = 0.60c and 0.70c at U_o = 0.65 m/s. These time instants in Figure 5.22 and 5.23 are the same as marked in the C_{Py} graphs in Figure 5.19 (a) to correlate the force and energy extraction behavior with the flow evolution at those moments.

Leading edge separation is quite evident for both pivot locations and it increases as the pitching amplitude increases. For θ_o = 30° in Figure 5.22 & 5.23 (a) a small LEV forms at t/T = 0.05, which goes on to increase in size by t/T = 0.10 as the hydrofoil plunges in the upstroke motion. The vortex core strength as indicated by the vorticity level for θ_o = 30° seem similar which suggests similar trend in hydrodynamic lift force behavior between 0 < t/T < 0.2 in Figures 5.20 (a) & 5.23 (a)

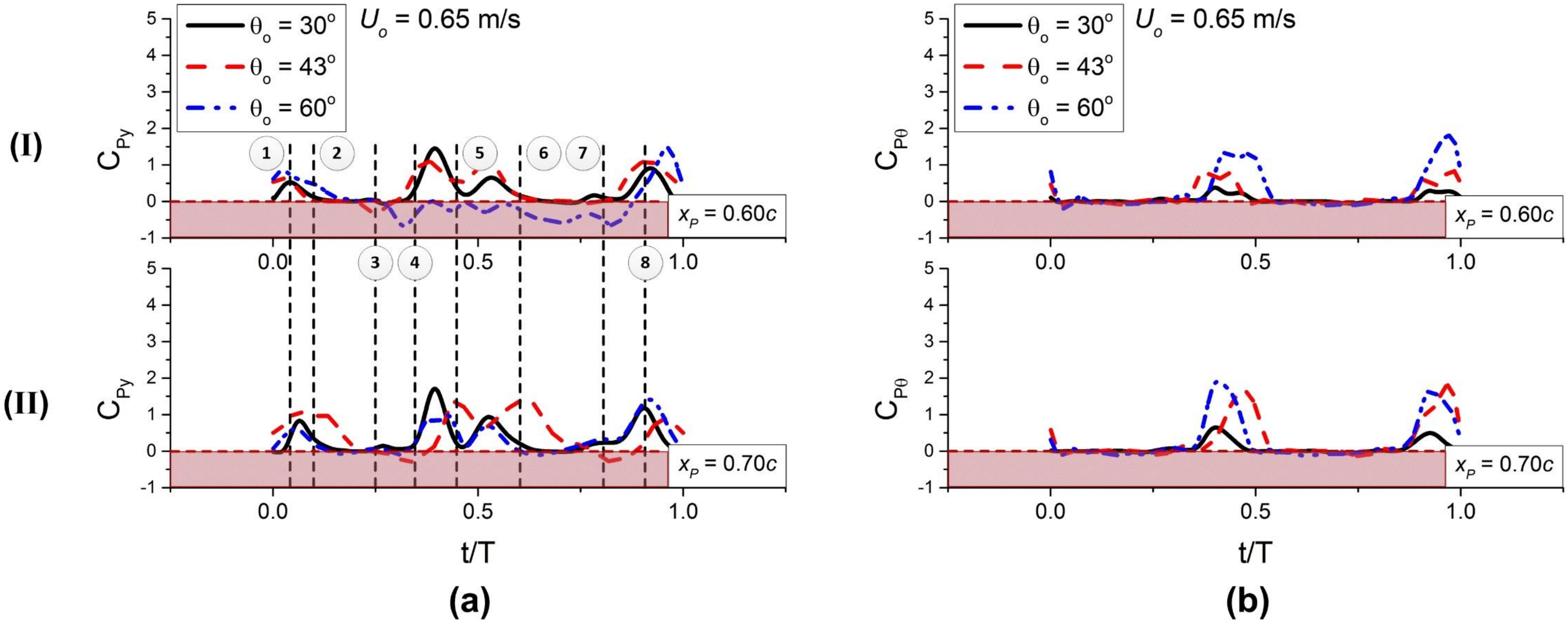

Figure 5.19: Phase-averaged **(a)** C_{Py} and **(b)** $C_{P\theta}$ at U_o = 0.65 m/s for three different pitching amplitudes (θ_o = 30°, 43° and 60°) at pivot locations **(I)** x_p = 0.60c and **(II)** x_p = 0.70c. Red regions marked in red below the zero line indicates the region where the flapping foil starts to expend energy from the system rather than extracting it from the surrounding fluid. Furthermore, eight different time instants are marked in **(a)** to correlate the behaviour of C_{Py} with the flow evolution of the flapping foil in energy harvesting mode for both pivot locations.

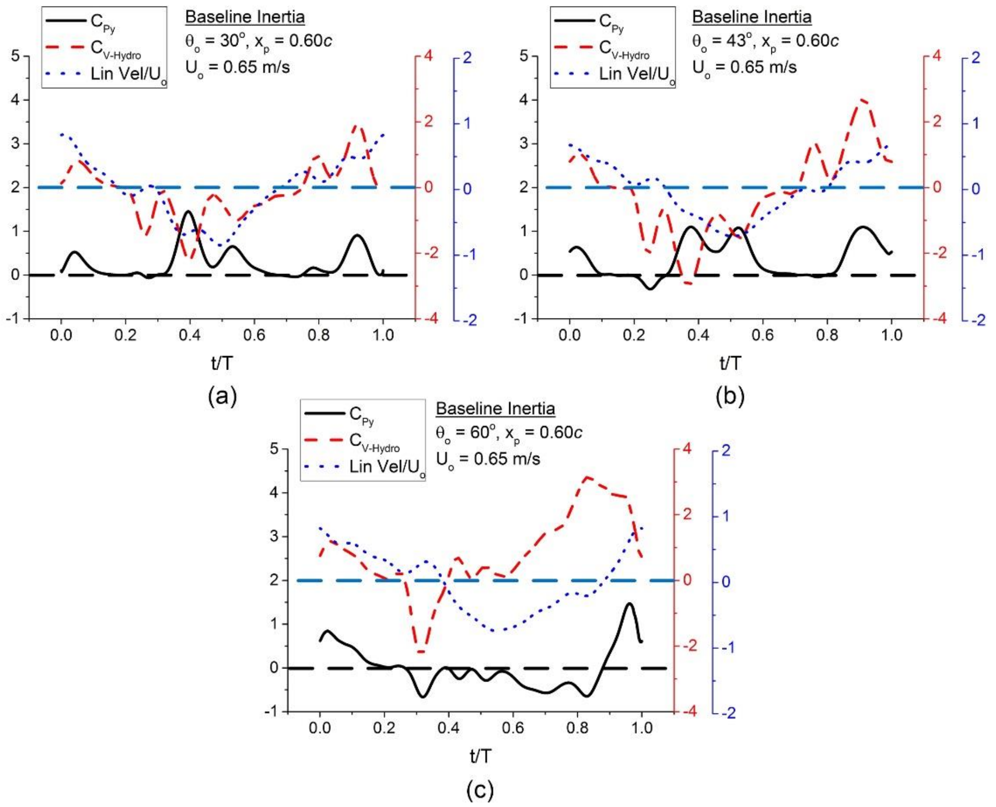

Figure 5.20: Phase-averaged C_{Py}, $C_{V\text{-}hydro}$ and Lin Vel/U_o of a flat-plate hydrofoil with pivot location x_p = 0.60c, free stream velocity U_o = 0.65 m/s for pitching amplitudes **(a)** θ_o = 30°, **(b)** θ_o = 43° and **(c)** θ_o = 60°.

however the size is slightly larger for x_p = 0.70c case due to which the peak value of the hydrodynamic lift force is slightly higher at t/T = 0.10. By around t/T = 0.25 the LEV formed travels downstream on the hydrofoil's upper surface, separates around the pivot location from the surface and convects into the wake.

This leads to a decrease in lift force which we can be observed in both Figure 5.22 (a) & Figure 5.23 (b). By after t/T = 0.25, the hydrofoil as it plunges in the upstroke motion another LEV starts to form up while the hydrofoil also starts its stroke reversal as seen in Figures 5.22 (a) & 5.23 (a) between 0.28 < t/T < 0.48. The hydrofoil pushes the flow on its upper side against the wall and impedes the second LEV to form fully. The flow eventually breaks down into small incoherent structures as witnessed at t/T = 0.35 and 0.45. The hydrofoil performs a low frequency pitching motion, which does not lead to any development of obvious flow structure(s). As the hydrofoil achieves its maximum pitching amplitude in the small peak seen in the hydrodynamic lift force is because of the formation of the counter-clockwise LEV, as seen in t/T = 0.60 for both x_p = 0.60c & 0.70c. Comparatively, the counter-clockwise LEV for x_p = 0.70c is properly formed as compared to the one for x_p = 0.60c where the flow structure seems to have shrunk or deformed, hence the comparative low lift force in Figure 5.21 (a) between 0.55 < t/T < 0.65. By $t/T \approx 0.72$ the hydrofoil initiates its second stroke reversal during which and by the end of it experiences another surge in hydrodynamic lift force between 0.85 < t/T < 0.95.

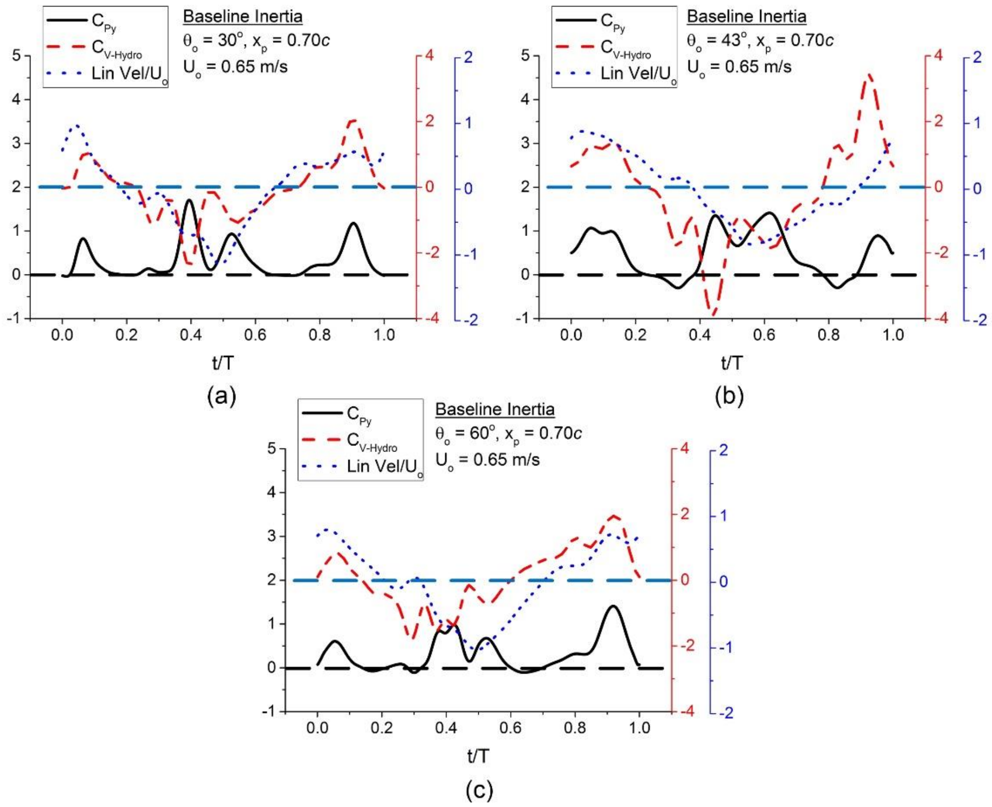

Figure 5.21: Phase-averaged C_{Py}, $C_{V\text{-}hydro}$ and Lin Vel/U_o of a flat-plate hydrofoil with pivot location x_p = 0.70c, free stream velocity U_o = 0.65 m/s for pitching amplitudes **(a)** $\theta_o = 30^o$, **(b)** $\theta_o = 43^o$ and **(c)** $\theta_o = 60^o$.

As the pitching amplitude is further increased to $\theta_o = 43^o$ and 60^o, the separation region on the hydrofoil's surface (upper during upstroke and lower during downstroke) increases, as seen in Figure 5.22 & 5.23 (b) & (c). The large separation region leads to the formation of a large size LEV, which is formed when the hydrofoil is at its maximum pitching amplitude and initiates its plunging motion. The LEV size at t/T = 0.10 for $\theta_o = 43^o$ in Figure 5.22 (b) is a little smaller in size than in Figure 5.23 (b), which could be the reason for the difference in hydrodynamic lift force as seen in Figure 5.20 (b) & 5.21 (b) between 0 < t/T < 0.175.

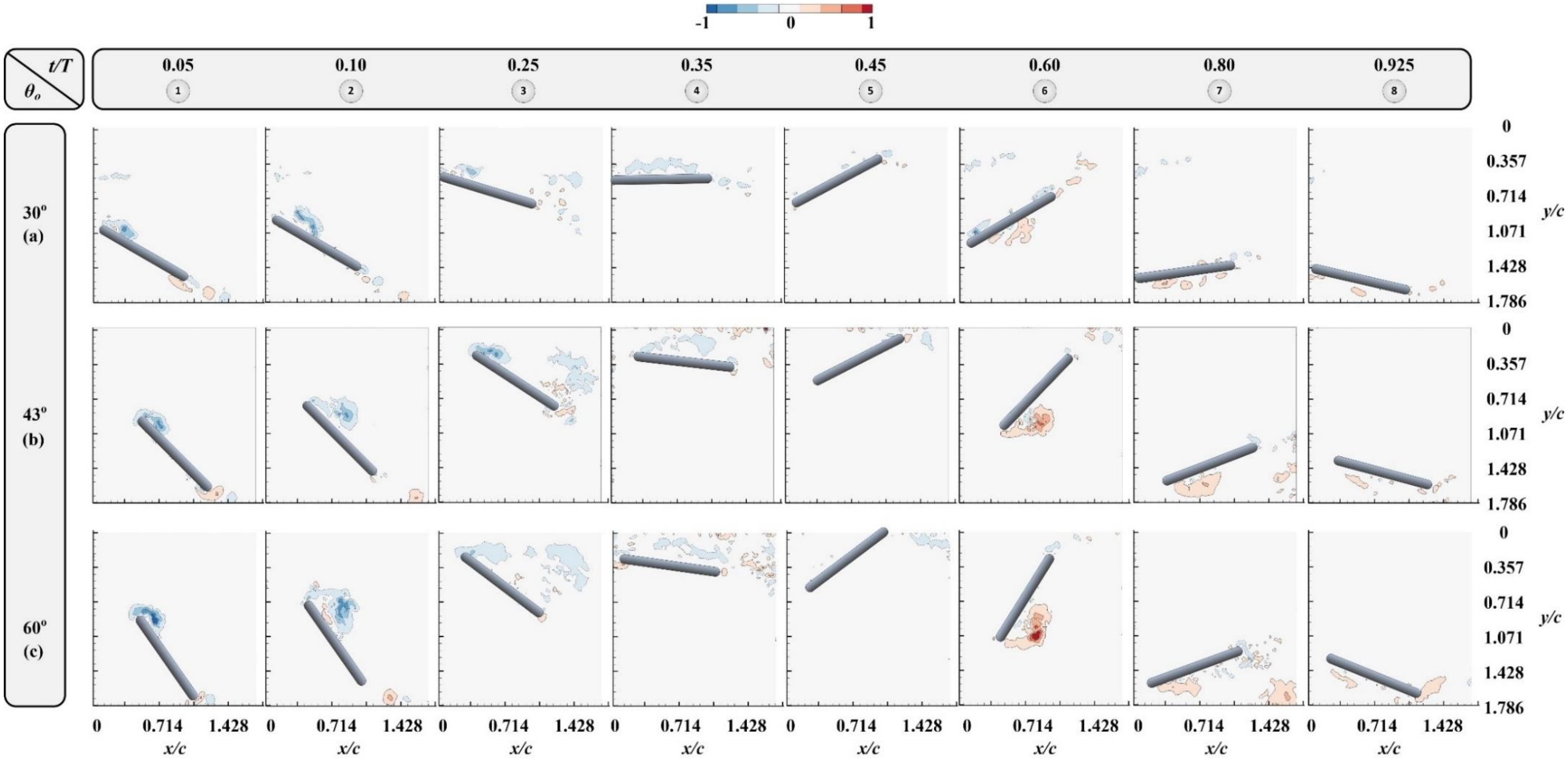

Figure 5.22: Figure showing vorticity contours of flat-plate hydrofoil at eight different time instants during one flapping cycle with free-stream velocity of U_o = 0.65 m/s and pivot location x_p = 0.60c at three different pitching amplitudes: **(a)** θ_o = 30°, **(b)** θ_o = 43° and **(c)** θ_o = 60°. The x and y scale are dimensionalized with reference to the chord length (c = 0.14 m) of the hydrofoil.

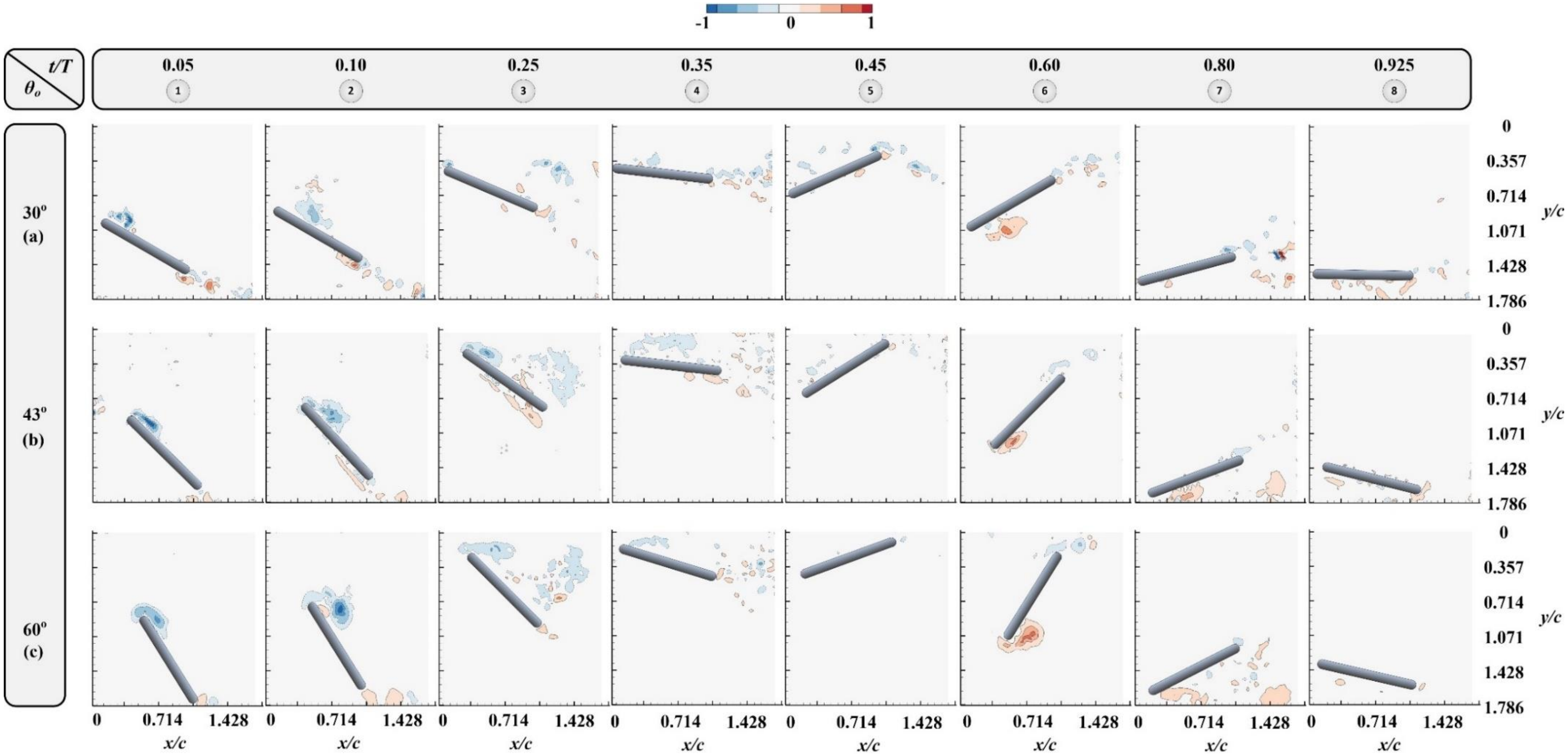

Figure 5.23: Figure showing vorticity contours of flat-plate hydrofoil at eight different time instants during one flapping cycle with free-stream velocity of U_o = 0.65 m/s and pivot location x_p = 0.70c at three different pitching amplitudes: **(a)** θ_o = 30°, **(b)** θ_o = 43° and **(c)** θ_o = 60°. The x and y scale are dimensionalized with reference to the chord length (c = 0.14 m) of the hydrofoil.

The LEV in x_p = 0.70c case stays on the hydrofoil's upper surface for a little longer than on the x_p = 0.60c case where it starts to shed around $t/T \approx 0.12$ allowing the hydrofoil in the former case to have the hydrodynamic lift force for a longer time. As both LEVs shed in to the wake with the hydrofoil plunging upwards, a sudden drop in lift force is observed and by $t/T \approx 0.23$ the hydrofoil starts its stroke reversal while plunging. This initiates a deceleration process allowing the lift force to decrease until the foil crosses its zero-degree mark which leads to a sudden shift in direction of the lift force acting on the hydrofoil. The foil when about to complete its stroke reversal, experiences a sudden surge in lift force magnitude due to it experiencing a slight jolt upon its stroke reversal completion. Similar events are also experienced by the hydrofoil at $\theta_o = 60^o$ as can be seen in Figure 5.22 (c) & 5.23 (c). As the hydrofoil starts its downstroke motion, it experiences the same LEV formation where its size and strength depend on the hydrofoil's pitching amplitude and the pivot location since both have a coupling effect on the foil's plunging velocity, which tend to increase as the pitching amplitude and pivot location distance from foil's leading-edge increase. The formation of LEV for x_p = 0.60c during both upstroke and downstroke motions is early due to relatively low plunging velocity of the hydrofoil as compared to the x_p = 0.70c, which also leads to early separation and formation of a secondary LEV. These flow evolution events are also quite sensitive when the pitching amplitude is increased, causing the formation and action of large forces on the flapping foil in energy harvesting mode. For $\theta_o = 60^o$, although we observe a larger separation area and formation and shedding of a large LEV from the foil's surface (Figures 5.22 (c) & 5.23 (c)) which leads to the formation of the large lift forces acting on the foil as observed in Figures 5.20 (c) and 5.21 (c). However, the de-synchronization during most part of the flapping cycle between the lift force and plunging velocity contributes towards a lower energy extraction performance by plunging motion at both x_p = 0.60c and 0.70c (Figures 5.20 (c) and 5.21 (c)), eventually affecting C_{Pmean} (Figure 5.17 (b)) where it is lower than its smaller pitching amplitude counterparts.

5.5 COMPARISON WITH OTHER WORKS

As discussed in Chapter 3, a similar design was made and tested out by Semler (2009) although the objectives and the methodology implemented were different compared to our study. To validate Semler's study, numerical computations were carried out at a later stage by J. Lai's group, which have been mentioned in Platzer et al. (2010), Ashraf et al. (2011) and Young et al. (2013). In this section we will lay out a comparative picture of results and performance attained by our group against some of these works, which could provide the basic and helpful platform to the scientific society investigating such fully passive flapping energy harvesting systems in the future.

Table 3.1 already has laid out the major differences and similarities of the mechanical design and setup of the passively flapping energy harvester between our and Semler's. Compared to us, Semler tested out his test-rig with different mechanical setups in two Water Tunnel test facilities. For each facility, the test-rig was mechanically adjusted to meet the test section requirements. Also, for all studies combined, the pitching amplitude was set to $\theta_o = 40^o$, while in our research we visited three different pitching amplitudes; $\theta_o = 30^o$, 43^o and 60^o for which their analysis has already been discussed in the previous section. Different pivot locations and water speeds have been analyzed in Semler's work during their tests in all three of their facilities. The chord length of the flat plate foil in both works are very similar as well as the span. Hence, where kinematic and geometric parameters align a comparative analysis can be given between both works. Due to the lack of appropriate data acquisition system, Semler (2009) does not provide any evidence of force and motion measurements and eventual energy extraction performance computations. However, Semler (2009) does provide observational analysis on the behavior of the test-rig under different geometric and flow conditions.

Initial experiments were carried out in Water Tunnel A with a dense screen with free-stream velocities ranging between 0.29 and 0.35 m/s. The test section is 685.8 mm high and 381 mm wide compared to our water tunnel test section of 600 mm high and 300 mm wide. The water speeds were measured using a digital electromagnetic velocimeter at different dial settings of the water tunnel. Experiments were carried out at different pivot locations and water speeds with a flat plate foil. Table 5.2 shows the different observations which are categorized based on; sustainability and consistency, amount of deflection or pitching motion and smoothness of the hydrofoil traverse on the guide rail. The water tunnel walls were used as plunge limiter and served the purpose of allowing the moment arm to rotate to initiate the stroke reversal process, as compared to cylindrical plunge limiters in our test-setup (see Table 3.1 for detailed comparison).

Water Speed (dial setting)	x_p (with cm)	Average Travel Time (s)	Average Linear Velocity (cm/s)	Description
1.1 (0.29 m/s)	0.357c (5.1)	n/a	n/a	Too inconsistent for analysis
	0.497c (7.1)	5.10	7.06	Needs manual assistance. Quarter deflection. Travel not smooth.
	0.629c (9.0)	4.14	8.70	Needs manual assistance. Full deflection. Travel smooth.
	0.769c (11.0)	3.51	10.26	Needs manual assistance. Full deflection. Travel smooth.
	0.839c (12.0)	3.74	9.63	Needs manual assistance. Full deflection. Travel smooth.
1.6 (0.35 m/s)	0.357c (5.1)	n/a	n/a	Too inconsistent for analysis
	0.497c (7.1)	2.83	12.72	Works on its own inconsistently. Half deflection. Travel not smooth.
	0.629c (9.0)	2.54	14.17	Works on its own inconsistently. Half deflection. Travel not smooth.
	0.769c (11.0)	2.68	13.43	Works on its own inconsistently. Full deflection. Smooth travel.
	0.839c (12.0)	2.77	13.0	Works on its own consistently. Full deflection. Travel smooth.
2.1 (0.34 m/s)	0.357c (5.1)	n/a	n/a	Too inconsistent for analysis
	0.497c (7.1)	n/a	n/a	Too inconsistent for analysis
	0.629c (9.0)	2.78	12.95	Works on its own inconsistently. Half deflection. Travel not smooth.
	0.769c (11.0)	2.96	12.16	Works on its own inconsistently. Half defection. Smooth travel.
	0.839c (12.0)	2.83	12.72	Works on its own consistently. Half deflection. Travel not smooth.
2.3 (0.34 m/s)	0.357c (5.1)	n/a	n/a	Too inconsistent for analysis
	0.497c (7.1)	n/a	n/a	Too inconsistent for analysis
	0.629c (9.0)	**Data not given**		
	0.769c (11.0)	2.61	13.79	Works on its own consistently. Half deflection. Travel not smooth.
	0.839c (12.0)	2.72	13.24	Works on its own consistently. Half deflection. Travel not smooth.

Table 5.2: Summary of observations for experiments carried out in Water Tunnel A. (Semler, 2009).

Second set of experiments were carried out in Water Tunnel B with a cross section of 450 mm (height) and 382 mm (width). Water speeds could be varied from 0 to 0.40 m/s and had a linear relationship with the operating frequencies of the water tunnel test section (0-40 Hz). Since the test-rig could not be set up on top of the water tunnel test section due to the comparatively longer inner walls, it was setup with the help of sheet metal cut and shaped in a manner to hold the test rig. Instead of using the water tunnel side walls, this time they have installed magnets on the side walls and a coupled magnet attached to the hydrofoil itself. As the hydrofoil approaches the wall, the moment arm would begin to rotate and to complete this rotation, the magnet on the wall opposes the magnet on the hydrofoil, hence repelling it past the zero-angle position. For the first set of experiments in this water tunnel facility, three different pivot locations and three different water speeds were tested. Table 5.3 summarizes the observations for this set of experiments. Second set of experiments were carried out one fixed pivot location of x_p = 0.699c and θ_o = 40^0 at three different free-stream velocities (U_o = 0.20 m/s, 0.30 m/s and 0.40 m/s) and inertial mass unit of 0.0566 kg (used in pairs). The purpose of this test was to check if adding a load or mass affects the behavior of passively flapping foil energy harvester. Observations for this test is shown in Table 5.4.

Water Speed (m/s)	x_p (with cm)	Average Travel Time (s)	Average Linear Velocity (cm/s)	Description
0.20	0.559c (8)	3.67	9.81	Near Full Deflection
	0.699c (10)	3.5	10.29	Full Deflection
	0.804c (11.5)	**Data not given**		
0.30	0.559c (8)	3.06	11.76	Half Deflection. Stalls when crossing from left to right every time.
	0.699c (10)	3.27	11.01	Full Deflection
	0.804c (11.5)	**Data not given**		
0.40	0.559c (8)	2.81	12.81	Quarter deflection. Stalls when crossing from left to right every time.
	0.699c (10)	2.81	12.81	Near Full deflection
	0.804c (11.5)	2.41	14.94	Full Deflection

Table 5.3: Summary of observations for first set of experiments carried out in Water Tunnel B. (Semler, 2009).

Flow visualization testing was also carried out in this water tunnel facility with colored dye, which is equipped with dye injection. The facility has six dye containers that are pressurized with air from a compressor and the dye is transported from the containers through a tygon tube where it can be released in to the water though a small metal port connected to the end of the tube. Each dye container is of different color and can be brought on or off by a series of valve manipulations. Flow visualization was carried out at a water speed of 0.20 m/s and dye was released into the flow just upstream of the hydrofoil and at various distances off the plate. Tests were carried out with static and dynamic conditions to observe the behavior of the flow around the hydrofoil.

Water Speed (m/s)	x_p (with cm)	Average Travel Time (s)	Average Linear Velocity (cm/s)	Description
0.20	0.699*c* (10)	3.31	10.88	Full Deflection
0.30		3.14	11.46	Full Deflection
0.40		3.04	11.84	Near Full Deflection

Table 5.4: Summary of observations for second set of experiments carried out in Water Tunnel B with added inertial weights (Semler, 2009).

From observations and analysis, the flat plate foil in Water Tunnel A was subjected to water flow with ripples and noticeable imperfections. This non-uniform flow created inconsistent behavior during the flapping motion. At some geometric and kinematic parameter combinations, the hydrofoil would inch its way across in spurts, sometimes it would go half way across and reverse back without making it to the other wall. Deflection or pitching angle sometimes varied for each traverse on the same run. In Water Tunnel B, the flow was uniform, and the hydrofoil traversed with nice "smooth" strokes in this flow allowing it to give relatively consistent data. The oscillator worked on a consistent basis at different pivot locations, water speeds and inertial weight.

Comparatively, in our study before we carried out the detailed parametric analysis of this passively flapping foil energy harvester device, detailed sustainability and viability tests were carried out to ensure that during the main phase of the research, the test-rig will perform in a consistent and sustainable manner. In the start of this chapter a section is dedicated to this discussion outlying the necessary steps to taken to ensure this sustainability. Since our test-rig was different in design due to the addition of sensors, additional inertial mass blocks were placed on top of the small aluminum block to ensure that the foil performs both plunging and pitching motions without any external help, as was the case in some experiments in Semler's work. Another major difference is the cutoff velocity ($U_{o\text{-}cutoff}$) of both test-rigs. Although, it is not mentioned clearly in Semler's work the device can work at very lower free-stream velocities (U_o = 0.20 m/s), while for our test-rig it can go as low as $U_{o\text{-}cutoff} \approx 0.37$ m/s (without sensor configuration) while $U_{o\text{-}cutoff} \approx 0.50$ m/s (with sensors configuration). Semler (2009) also carried out his experiments without any endplates placed at the wing tips, which means that 3D effects were very much involved in affecting the performance of the passively flapping foil energy harvester, while in our study 3D effects were negated by including the endplates and performing 2-D analysis of the flow field.

No work was carried out by Semler regarding pitching amplitude variation to see its effects on the flapping foil energy harvester. The pitching amplitude was fixed at $\theta_o = 40^0$ for all experimental investigations and pivot location and water speed was varied instead. For pivot locations analysis, we found that the general observations made by Semler were consistent with our observations and results. We know that pivot location affects how much moment is created by the flow to rotate the hydrofoil in this case. The lift force acts near the mid-chord in the case of flat plate foil, hence if the pivot location is located at the mid-chord, then the flow will not impart a moment to rotate the flat plate foil. If the pitch axis is forward of the mid-chord (toward the leading edge), then the flat plate foil will remain in the neutral position like a weather vane that points in the direction of the flow. A similar observation was made in our experiments, where during the initial phases of our testing the foil would not move or perform sustainable flapping motions if the pivot location was forward of the flat plate foil. However, as the pivot location was moved aft of the mid-chord the hydrofoil would start to perform flapping motions when subjected to incoming flow, a similar observation also made by Semler in his experiments. The moment arm that the lift force used to rotate the flat plate is equal to the distance of the pitch axis from the mid-chord. The more the pivot location moved further back (towards the trailing edge), the higher the average traverse velocity of the hydrofoil. This is like flapping frequency (f) in our study as shown in Table 5.2 where the increase in pivot location distance at a fixed free-stream velocity and pitching amplitude leads to increase in flapping frequency.

Similarly, for water speed study in both researches, experiments demonstrate a similar observation pertaining to increase in hydrofoil traverse velocity (Semler (2009) or flapping frequency (M. N. Mumtaz Qadri (2018)) with increase in free-stream velocity. Higher free-stream velocities allow for higher power extraction, which is also evident in our results as shown in Table 5.2, where P_{mean} (W) has shown an increase with increase in free-stream velocity when pivot location and pitching amplitude are fixed.

Semler (2009) carried out only one set of experiment related to additional weight placed on the small aluminum block travelling on the guide rail. His main purpose was to investigate how the system performs when subjected to a load (mechanical). In our case it was related to the viability and sustainability of the flow induced flapping foil energy harvester and for this study we tested three different inertial mass units (see Section 5.1). However, these additional weights or inertial mass units in our study can also be referred as a "load" and its effects can be studied, which have been done. In this regard, Semler's and our observations are consistent. Semler (2009) states that from his experiments, the system without weights had more consistent performance than with weights, indicated that added load did hamper oscillator performance. In our case, the system without weights did not work, so additional inertial mass units were necessary. With Small Inertial Mass unit (m_{ib} = 0.45 kg), the passively flapping foil energy harvester was consistent and gave a linear response as the geometric and kinematic parameters were changed (Figure 5.2), however as m_{ib} increased the system still performed sustainable flapping motions but showed irregular trends with varying kinematic and geometric parameters.

Similar computational work pertaining to passively flapping foils for energy harvesting has been carried out by J. Lai's group as mentioned earlier. First, Ashraf et al. (2011) studied the power extraction potential of flapping foils in different configurations using NS 2-D laminar flow calculations for a NACA 0014 foil at Re = 20,000 and x_p = 0.5c, although both the foil and Re is different compared to our study. He studied the effect of phase difference between pitching and plunging motion on power extraction through a sinusoidally flapping foil and showed that power output and efficiency peak is in the range of ϕ = 90-110°. Then, using an aerohydronamically inspired non-sinusoidal motion from Platzer (2009), achieved a power extraction efficiency of 34% at C_{pmean} = 0.89, with ΔT_R = 0.3 and ϕ = 90°, θ_o = 73° and h = 1.05. Compared to our experimental investigations the maximum energy extraction efficiency was 73.03% at C_{pmean} = 1.565 with m_{ib} =

0.90 kg, θ_o = 60º, x_p = 0.80c and U_o = 0.57 m/s and generating an average power (P_{mean}) of 4.057 W. However, the highest Pmean of 4.703 W was achieved at m_{ib} = 0.90 kg, θ_o = 60º, x_p = 0.80c and U_o = 0.65 m/s with energy extraction efficiency of 57.08% at C_{pmean} = 1.223. ΔT_R refers to time taken for one stroke reversal and is similar to our ΔT_{SR} shown in Table 5.1. It can be observed that our ΔT_{SR} values are close to the ΔT_R = 0.3 at which Ashraf et al. achieved good energy harvesting performance. However, it must be noted that ΔT_R values in this study is imposed by the user compared to our ΔT_{SR} values which are produced because of the flow affecting the flapping foil kinematics. For the non-sinusoidal single foil study, the plunging component of power output dominates the overall power output from the oscillating foil. In our case, the plunging motion defines the trend of the C_P profile and contributes more towards total energy extraction, however pitching motion also contributes at two distinct instants during the flapping cycle. Ashraf et al. (2011) states that the results for a single NACA 0014 wing power generator undergoing non-sinusoidal pitch plunge motion indicates around 17% increase in power generated and around 15% increase in efficiency over that for sinusoidal motion. Ashraf et al. generated the non-sinusoidal motion of the generator through equations given in the Appendix of Ashraf et al. (2011).

Young et al. (2010) also numerically investigated a fully flow driven flapping motion for a single foil. Figure 5.24 shows the schematic diagram for this fully flow driven power generator. The hydrofoil undergoes both plunge and pitch degrees of freedom and the conservation of energy equation for this system can be written as follows:

$$(L - C\dot{y})\dot{y} + M\dot{\theta} = m\dot{y}\ddot{y} + I\dot{\theta}\ddot{\theta} \tag{5.1}$$

where, L is the aerodynamic lift, M is the aerodynamic moment, m is the mass of the airfoil, I is the moment of inertia about the pivot point and C is the viscous damper which is used to extract the power from the plunging motion only. No power is extracted from the pitching component as it provides much less power than the plunge component, and it also simplifies analysis (Ashraf et al., 2010; Young et al., 2010 & 2013).

The frequency at which the flow-driven foil will oscillate is a function of the incoming flow speed, the mass and inertial of the foil and supporting mechanism, and the pitch and plunge amplitudes. Additional though was given as to the way the power was extracted, as measuring only the power generated by the aerodynamic forces and moment on the foil is like what is done in the prescribed motion cases and results in a no-load situation. Accordingly, the load on the foil from the power extraction mechanism must be built into the simulation.

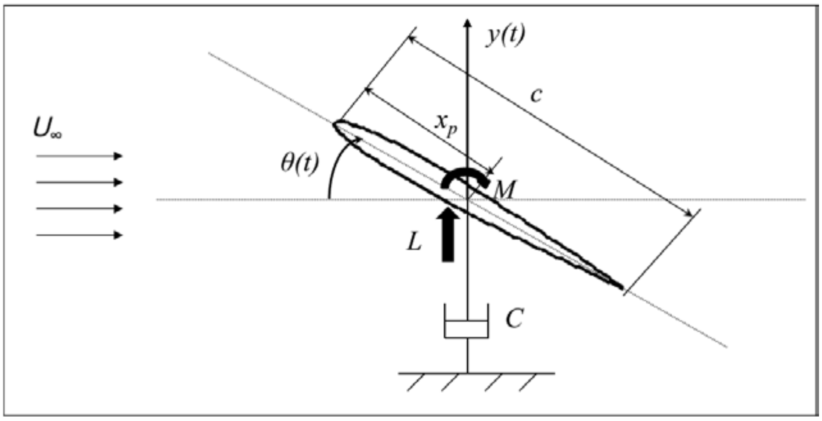

Figure 5.24: Schematic diagram of a fully flow – driven power generator (Ashraf et al., 2010)

To implement this fully flow driven flapping motion, both pitch and plunge positions are considered as a function of a mechanism angle β using the methodology described in Young et al. (2010) with schematics shown in Figure 5.25 such that,

$$\begin{aligned} y &= f(\beta) \\ \theta &= g(\beta) \end{aligned} \tag{5.2}$$

Since, now the system is based on the flywheel system, the power extraction from the system is modelled as a rotational viscous damper attached to the flywheel. The equation of motion of the combined foil-flywheel (ignoring the mass of the moving linkage elements) is determined via conservation of energy as (Young et al., 2010):

$$L\dot{y} + M\dot{\theta} - c_b(\dot{\beta})^2 = m_a\dot{y}\ddot{y} + I_a\dot{\theta}\ddot{\theta} + I_b\dot{\beta}\ddot{\beta} \tag{5.3}$$

where, $y(t)$ = vertical position of the foil, $\theta(t)$ = foil pitch angle, I_a = foil moment of inertia about pivot point, I_b = moment of inertia of the flywheel, m_a = foil mass, c_b = strength of rotational damper on flywheel, $\beta(t)$ = flywheel rotation angle.

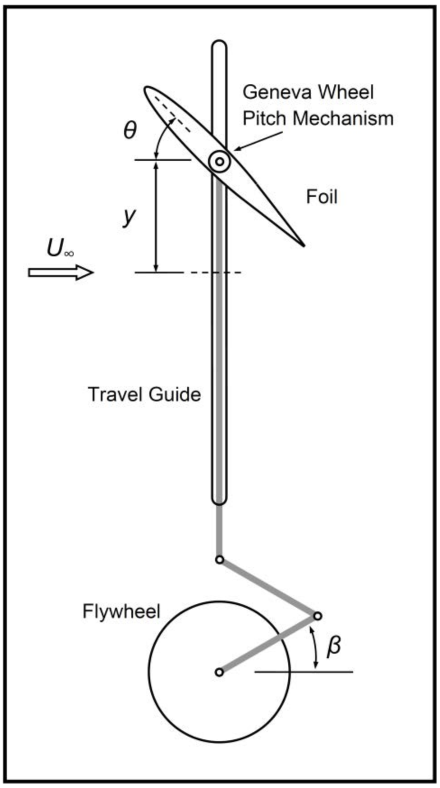

Figure 5.25: Schematic diagram of a fully flow – driven power generator (Young et al., 2010 & 2013)

Equations 5.2 are referred to as linkage functions and the equation of motion of the foil is solved in terms of β:

$$\ddot{\beta} = \frac{1}{[m_a(f_\beta)^2 + I_a(g_\beta)^2 + I_b]}[Lf_\beta + Mg_\beta - c_b\dot{\beta} \\ -(m_a f_\beta f_{\beta\beta} + I_a g_\beta g_{\beta\beta})(\dot{\beta})^2] \tag{5.4}$$

where, $f_\beta = \partial f/\partial\beta$, $f_{\beta\beta} = \partial^2 f/\partial\beta^2$, etc.

The relationship between plunge and pitch motions is encompassed within the definition of the linkage functions. If the flywheel is rotated at a constant rate, the plunge and pitch motions would be sinusoidal in time, but this is not guaranteed by the solution of equation 5.4, and hence non-sinusoidal motions may be achieved even with sinusoidal linkage functions (Young et al., 2010).

The generality of the formulations shown by Young et al. (2010) allows a much wider range of flapping kinematics considered, however the motion of the foil in the water tunnel experiments by Semler (2009) is characterized by translation of the foil at constant pitching amplitude, with periods of rapid rotation of the foil at the top and bottom of the stroke, similar to our kinematics. This may be incorporated into the pitch angle linkage function via a stroke reversal fraction $\Delta\hat{\beta}_R$, representing the fraction of the total flapping cycle over which the foil reverses pitch angle and for plunge motion, $y = hc \sin\beta$, the pitch motion at the top of the upstroke is given by;

$$\begin{gathered}\theta = -\theta_o \sin\left(\frac{\beta+\phi-\pi}{2\Delta\hat{\beta}_R}\right) \\ (1-\Delta\hat{\beta}_R)\pi - \phi < \beta \le (1+\Delta\hat{\beta}_R)\pi - \phi\end{gathered} \tag{5.5}$$

A NACA0012 airfoil section was used with chord length (c) = 0.15 m and a free stream velocity of U_o = 1.0 m/s in water is assumed. Reynolds number is set to Re = 1100 and plunge amplitude fixed at h = 1.0c and ϕ = 90°. For further reduction of the number of free parameters, the mas and inertia of the foil were ignored in comparison to the inertia of the flywheel. The damper strength is non-dimensionalized (c') by the idealized fluid damping on a flat plate rotating about its mid-chord, according to the linearlized theory of Theodorsen (1935), by analogy with the approach used by Zhu et al. (2009) and Zhu & Peng (2009) for a linear damper (for equations see Young et al., 2010). Similarly, flywheel inertia is also non-dimensionalized (I') by considering the ratio of kinetic energy in the flywheel and moving foil, compared to the kinetic energy of the ideal fluid added mass and inertial of a plunging and pitching plate (Brennen, 1982) (for equations see Young et al., 2010). The optimum pitch amplitude, pivot location and stroke reversal function $\Delta\hat{\beta}_R$ were first determined. The effect of $\Delta\hat{\beta}_R$ was evaluated for several different flywheel inertias and damper strengths as shown in Figure 5.26 (a) and non-sinusoidal pitching by $\Delta\hat{\beta}_R$=0.2 showed better results and was used for remaining numerical simulations. As reported before, the majority of the power production occurs during the translation phase, keeping the stroke reversals short is advantageous, but not so short that the power requirement to turn a rapidly rotating foil becomes too high. Effect of flywheel inertia was evaluated for two pitching amplitudes and c' = 1.209 as shown in Figure 5.26 (b) and I' = 5.67 was selected for further runs. Pivot point location was evaluated for $\theta_o = 75^o$, I' = 5.67 and c' = 1.209 as shown in Figure 5.26 (c), with $x_{piv} = 0.50c$ showing the clear advantage and was selected for further runs. After this, the effect of pitch amplitude and damper strength were evaluated, and a contour map (Figure 5.26 (d)) was drawn up of efficiency and all runs used $\Delta\hat{\beta}_R = 0.2$, I' = 5.67 and $x_{piv} = 0.50c$. From the contour map it can be seen that the maximum efficiency obtained is around 30%, which is less than Ashraf et al. (2010) prescribed non-sinusoidal flapping motion of 34% discussed before and even lower than what we have achieved in our experimental investigations. Optimum performance is achieved at higher pitching amplitudes, like our results as reported at $\theta_o = 60^o$ but with a different pivot location ($x_p = 0.80c$ in our case). Still, higher pitch amplitudes for better energy extraction performance are an indication of the importance of the leading-edge separation.

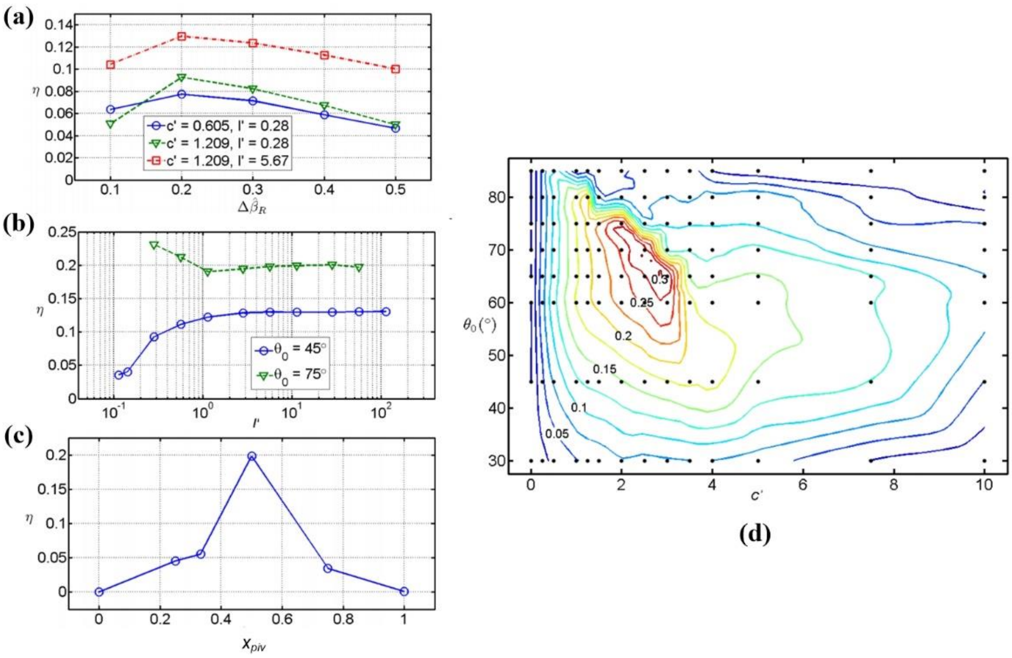

Figure 5.26: **(a)** Efficiency versus stroke reversal fraction, for $\theta_o = 45^o$, $x_{piv} = 0.50c$, **(b)** Efficiency versus non-dimensional flywheel inertia for two pitch amplitudes, **(c)** Efficiency versus foil pivot point location, **(d)** Contours of turbine efficiency vs non-dimensional damper coefficient strength and foil pitch angle. (Young et al., 2010)

5.6 REMARKS

A detailed account of the effect of key parameters such as inertial mass units, pivot location and pitching amplitude on the energy extraction performance of a passively flapping foil has been given in this chapter. At first three different inertial blocks were tested at three different pitching amplitudes including θ_o = 30°, 43° and 60°, while keeping pivot location fixed at 0.65c at three different free-stream velocities (U_o = 0.57 m/s, 0.65 m/s & 0.78 m/s). Later the effect of pivot location was studied, and a total five pivot locations were chosen out of which three (x_p = 0.60c, 0.70c & 0.80c) were discussed in this chapter. Although energy harvesting performance parameters were shown for all the above parameters at three different free-stream velocities, for consistency U_o = 0.65 m/s was chosen for fluid-structure interaction discussion. A summary of important parameters for all categories of cases pertaining to this chapter are shown in Tables 5.5 and 5.6, where Table 5.5 summarizes the pitching amplitude and pivot location study at baseline inertia (m_{ib} = 0.90 kg), while Table 5.6 shows the inertial mass variation study.

As part of our analysis to determine as to what kinematic factors contribute towards energy extraction, we observed in our C_P plots that the majority of the its trend was dependent on the plunging motion. The pitching motion would only contribute toward energy extraction during time instants when the hydrofoil would be completing its stroke reversal. There were instants depending on parametric configuration of the test-rig that the hydrofoil would expend energy rather than extract during the flapping cycle, however due to the major and minor contributions by both plunging and pitching motion respectively the mean coefficient of energy extraction has been positive, indicating good energy extraction performance by the passively oscillating foil energy harvester system.

The part of selecting three different inertial mass unit was to demonstrate how the test-rig performs when the mass on its plunging system is increased. As demonstrated, the small inertial mass unit performed in an almost linear fashion with different flow conditions and parametric configuration. With the increase in inertial mass on the system as some point the test-rig did start to perform in an erratic fashion. Although, it did impact the stroke reversal by allowing it to flip quickly depending on other configurations also, but also influenced the plunging motion due to which in some cases we observed poor synchronization between the hydrodynamic lift force and plunging velocity.

In retrospect, the small inertial mass unit will seem to be the optional choice due to its linearly fashioned results however, in our other experimental regimes involving different shape hydrofoils (more details in Chapter 6) we observed that they had difficulty performing with smaller parametric configurations, hence the foil morphology analysis was done using big inertial mass unit (m_{ib} = 1.35 kg), while pivot and pitching amplitude analysis with the baseline foil (flatplate) was done using the baseline inertial mass unit (m_{ib} = 0.90 kg).

We also observed during our analysis that pivot location and pitching amplitude contribute extensively to flapping foil kinematics and force generation, which affects energy harvesting performance. By keeping the pitching amplitude constant and varying the pivot location a considerable change in kinematics and force behavior was observed as the pivot location distance from the leading edge was increased. Total stroke reversal time $\Delta T_{SRTOTAL}$ was influenced by change in pivot location, where in each free-stream velocity it decreased with increase in pivot location indicating a quick change in pitching amplitude and more time spent undergoing plunging motion in one flapping cycle. Furthermore, an increase in energy extraction performance was observed as the pivot location distance from leading edge was increased due to increase in plunging velocity magnitude and high torque (during stroke reversal) leading to increase contribution to C_P by $C_{P\theta}$ during stroke reversal periods. Similar behavior was observed at all pitching amplitudes as the pivot location distances were increased and change in energy extraction performance became more sensitive as the pitching amplitude was increased from θ_o = 30° (gradual increase in C_{Pmean}) to θ_o = 60° (steep increase in C_{Pmean}) as pivot location varied. This indicates that the change in pitching amplitude coupled with change in pivot location effects the energy extraction performance of the flapping foil.

In most cases we observed that a higher pitching amplitude at any given pivot location performs better due to the generation of large forces because of increased separation area and formation and shedding of LEV. However, the de-synchronization between the forces and velocities due to unsteadiness in the flow around the flapping foil created at large pitching amplitudes and increased pivot location distances has led towards lower energy extraction performance.

A comparative analysis has also been carried out between our research and related works by Semler (2009), Ashraf et al. (2010) and Young et al. (2010). The focus on passively flapping foil energy harvester system was common among all our research, although there were differences in methodology and parameters hence, the comparison cannot be done on an exhaustive quantitative level. Although, in terms of performance our energy harvester system gave a maximum efficiency of 73%, followed by Ashraf et al. and Young et al. of 34% and 30% respectively. In terms of observational analysis, similarities were found between our research and Semler's in terms of test-rig behavior when subjected to increase in pivot location, water speed and added weight, although qualitatively. Still, this analysis provides a somewhat better understanding when compared amongst similar system (passively flapping foil energy harvester) and could help the scientific community in providing insight when researching such a fully passive flapping energy device(s).

Inertia Type	Water Speed (U_∞)	Pivot Location (x_p)	Pitching Amplitude (θ_o)	P_{mean} (W)	C_{pmean}	η	C_{pymean}	$C_{p\theta mean}$	St	f (Hz)	A_{piv} (m)	ω	χ
Baseline Inertia (m_{ib})	0.57 m/s	0.60c	30	0.403	0.155	7.252	0.112	0.043	0.097	0.464	0.119	2.914	1.765
			43	1.917	0.739	34.501	0.611	0.128	0.128	0.596	0.123	3.747	1.933
			60	2.733	1.054	49.190	0.764	0.290	0.148	0.666	0.127	4.185	2.230
		0.70c	30	0.830	0.320	14.941	0.271	0.049	0.112	0.454	0.141	2.851	1.542
			43	2.909	1.122	52.366	0.847	0.276	0.174	0.629	0.158	3.950	1.488
			60	2.363	0.911	42.530	0.582	0.330	0.155	0.590	0.149	3.710	2.161
		0.80c	30	1.066	0.411	19.192	0.308	0.103	0.139	0.491	0.162	3.083	1.288
			43	3.188	0.829	38.692	0.647	0.183	0.147	0.590	0.161	3.709	1.727
			60	4.057	1.565	73.026	1.116	0.449	0.171	0.596	0.164	3.742	1.967
	0.65 m/s	0.60c	30	1.294	0.337	15.709	0.281	0.056	0.112	0.597	0.122	3.748	1.551
			43	2.007	0.522	24.361	0.373	0.149	0.125	0.682	0.119	4.286	1.983
			60	1.100	0.286	13.349	-0.006	0.292	0.148	0.723	0.133	4.541	2.251
		0.70c	30	1.789	0.465	21.711	0.382	0.083	0.134	0.584	0.149	3.670	1.323
			43	3.054	0.794	37.073	0.506	0.288	0.169	0.711	0.154	4.469	1.526
			60	2.471	0.643	29.988	0.353	0.289	0.150	0.623	0.156	3.916	2.221
		0.80c	30	2.227	0.579	27.033	0.462	0.118	0.145	0.567	0.167	3.560	1.205
			43	3.543	0.922	43.004	0.646	0.275	0.176	0.687	0.167	4.318	1.463
			60	4.703	1.223	57.080	0.746	0.478	0.174	0.685	0.165	4.303	1.956
	0.78 m/s	0.60c	30	1.341	0.202	9.419	0.147	0.054	0.112	0.693	0.126	4.351	1.569
			43	2.263	0.341	15.894	0.156	0.184	0.110	0.752	0.114	4.725	2.232
			60	0.683	0.103	4.795	-0.117	0.220	0.133	0.787	0.132	4.946	2.476
		0.70c	30	1.785	0.269	12.539	0.181	0.087	0.132	0.692	0.149	4.345	1.361
			43	2.686	0.404	18.867	0.173	0.231	0.164	0.787	0.162	4.944	1.583
			60	2.063	0.311	14.494	0.068	0.242	0.134	0.701	0.149	4.405	2.471
		0.80c	30	2.189	0.330	15.379	0.215	0.115	0.150	0.649	0.180	4.075	1.213
			43	3.074	0.800	37.310	0.406	0.393	0.191	0.773	0.161	4.854	1.378
			60	4.428	0.666	31.102	0.315	0.351	0.152	0.751	0.158	4.719	2.174

Table 5.5: Summary of key parameters for Baseline Inertia (m_{ib} = 0.90 kg) for three different free-stream velocities (Uo = 0.57, 0.65 and 0.78 m/s), three different pivot locations (x_p = 0.60c, 0.70c and 0.80c) and three different pitching amplitudes (θ_o = 30°, 43° and 60°).

Pivot Location (x_p)	Inertia Type	Water Speed (U_∞)	Pitching Amplitude (θ_o)	P_{mean} (W)	C_{pmean}	η	C_{pymean}	$C_{p\theta mean}$	St	f (Hz)	A_{piv} (m)	ω	χ
0.65c	Small Inertia (m_{ib} = 0.45 kg)	0.57 m/s	30	0.774	0.298	13.926	0.255	0.044	0.116	0.507	0.131	3.183	1.480
			43	1.937	0.747	34.863	0.592	0.155	0.148	0.648	0.130	4.071	1.742
			60	2.915	1.124	52.464	0.838	0.286	0.159	0.642	0.141	4.033	2.101
		0.65 m/s	30	1.288	0.335	15.637	0.280	0.055	0.130	0.590	0.143	3.706	1.295
			43	2.146	0.558	26.051	0.356	0.202	0.164	0.742	0.144	4.660	1.603
			60	3.239	0.842	39.313	0.524	0.318	0.193	0.732	0.171	4.599	1.797
		0.78 m/s	30	1.713	0.258	12.030	0.203	0.054	0.125	0.679	0.144	4.266	1.406
			43	1.873	0.282	13.154	0.090	0.192	0.173	0.847	0.159	5.322	1.521
			60	2.083	0.314	14.632	0.032	0.281	0.102	0.827	0.096	5.198	3.151
	Baseline Inertia (m_{ib} = 0.90 kg)	0.57 m/s	30	0.682	0.177	8.281	0.152	0.025	0.092	0.446	0.133	2.804	1.854
			43	1.521	0.395	18.456	0.317	0.079	0.125	0.553	0.147	3.473	2.014
			60	1.851	0.714	33.321	0.417	0.297	0.164	0.612	0.153	3.843	2.007
		0.65 m/s	30	1.493	0.388	18.122	0.316	0.073	0.123	0.593	0.135	3.724	1.435
			43	1.272	0.331	15.444	0.179	0.152	0.153	0.652	0.152	4.096	1.679
			60	1.557	0.405	18.902	0.064	0.341	0.212	0.725	0.190	4.553	1.599
		0.78 m/s	30	1.549	0.403	18.806	0.271	0.132	0.157	0.701	0.146	4.403	1.156
			43	2.216	0.576	26.902	0.326	0.251	0.190	0.762	0.163	4.785	1.412
			60	4.231	0.637	29.719	0.419	0.218	0.146	0.705	0.161	4.428	2.294
	Big Inertia (m_{ib} = 1.35 kg)	0.57 m/s	30	1.051	0.405	18.917	0.316	0.090	0.142	0.505	0.160	3.170	1.259
			43	2.041	0.787	36.728	0.632	0.155	0.170	0.622	0.156	3.908	1.548
			60	2.347	0.905	42.251	0.678	0.227	0.131	0.525	0.143	3.296	2.520
		0.65 m/s	30	1.652	0.430	20.047	0.335	0.095	0.138	0.575	0.156	3.612	1.291
			43	2.052	0.534	24.912	0.298	0.236	0.168	0.727	0.150	4.566	1.568
			60	3.298	0.858	40.035	0.609	0.249	0.124	0.586	0.138	3.679	2.658
		0.78 m/s	30	1.886	0.284	13.250	0.204	0.080	0.129	0.640	0.158	4.024	1.384
			43	1.349	0.203	9.473	0.018	0.185	0.149	0.794	0.146	4.991	1.754
			60	3.922	0.590	27.551	0.367	0.223	0.138	0.693	0.156	4.353	2.415

Table 5.6: Summary of key parameters for different inertial mass; Small Inertia (m_{ib} = 0.45 kg), Baseline Inertia (m_{ib} = 0.90 kg) and Big Inertia (m_{ib} = 1.35 kg) at three different free-stream velocities (U_o = 0.57, 0.65 and 0.78 m/s) and three different pitching amplitudes (θ_o = 30°, 43° and 60°) at fixed pivot location x_p = 0.65c.

CHAPTER 6

EFFECT OF HYDROFOIL PROFILE

The main component of any energy harvester is the air/hydro-foil which is driven by the incoming free-stream flow, and the geometric aspect of this component affects the flow evolution around it, which generates hydrodynamic forces resulting in energy extraction. Hence, the profile of the foil design is an important parameter which can contribute towards the performance of an energy harvester. Most of the existing studies are based on NACA 00 series foils, and a small number of them have investigated the foil thickness and its impact on energy harvesting. Lindsey (2002) through his numerical work via the panel method showed that foil thickness did not have effect if the flow remains attached to the foil's surface. It also appeared that thinner foils can enhance energy extraction performance although an inviscid flow model was adopted, which affected the accuracy of the results. Dumas and Kinsey (2006) adopted a viscous N-S solver to overcome this problem and found that the overall efficiency and dynamic stall occurrence were not sensitive to foil geometry. In their follow-up studies, they noticed that although the details of leading edge vortex shedding, shear layer rolling up, and instantaneous forces are different among the tested foil shapes (NACA0002, 0015 and 0020), time averaged efficiency remained unchanged. Usoh et al. (2014) performed a comparative numerical study between a flatplate and two streamline foils (NACA0012 and LENS), where they found that a simple flatplate foil is advantageous over other streamline foils. The numerical study was performed at Re = 1100 with x_p = 0.333 and slight increase in energy extraction performance was observed when foil shape was changed from a NACA0012 section to a rectangular section (with the same cross-sectional area). Another interesting study inspired from nature involving camber and corrugations was performed by Le et al. (2013). Scallop shells provided a useful model for the corrugations and camber designed embedded in a flatplate foil and numerically investigated and compared with NACA0008 and 0012 sections. Its energy extraction performance was found to be better than NACA0012 but inferior to NACA0008 foil sections. They concluded that energy harvesting performance was primarily dependent on flapping foil kinematics and section shape provided a secondary effect.

From our literature survey it can be seen that most of foil shape analyses for energy harvesting through flapping motion was focused on NACA 00 series foils, other than Usoh et al. (2014) and Lee et al. (2013). This provides us with an opportunity to exploit this domain of morphology effect on energy extraction and provides us with a basis for our future experiments which may include permutations of foil and wing geometries for energy harvesting through passive flapping motion. As a start, we experimentally investigated two different foil sections, an elliptical foil and NACA 0006 foil, and compared their energy harvesting performance against the flatplate foil, which is the baseline foil shape in this research. The pivot location was fixed at $x_p = 0.65c$ with varying pitching amplitudes ($\theta_o = 30^o$, 43^o and 60^o) at three free stream velocities (U_o = 0.57 m/s, 0.65 m/s and 0.78 m/s). The small aluminum block on the guide rail was equipped with baseline inertial (m_{ib} = 0.90 kg) blocks for uniformity in our comparative analysis in this chapter.

6.1 SELECTION OF HYDROFOIL PROFILES

For our experiments focusing on impact of the shape of hydrofoil sections on energy harvesting from free-stream fluid, we choose two different streamlined foil sections; an elliptical foil and a NACA 0006 foil. To bring consistency to our experiments, the mass of all foil sections was fixed at $m_{foil} \approx 0.175$ kg, while the moment of inertia (I_{CM}), as given in Equation 3.4 and described in Section 3.1.4, was between 3.5-4.7 × 10^{-4} kg-m^2. The total mass below the force sensor, which included the hydrofoil and small shaft connected to it was around $m \approx 0.20$ kg. Other parameters such as chord length and span length were also kept constant (c = 0.14 m and s = 0.20 m, respectively). For the flatplate foil this was achieved through fabricating using plexiglass, which was possible due to its simple design making it easy to fabricate. However, this was not possible for the other two streamlined foil sections using plexiglass due to manufacturing complexities involved. Aluminum could also be used to manufacture the two foil sections. However, it was not possible due to the unavailability of machining process to manufacture such complex foil sections using any metal in our department's workshop.

Another option to solve this problem was to take advantage of 3D printing systems. Since, the other two foils had to be in the same mass range as the acrylic/plexiglass flatplate foil, foil section dimensions could not be selected at random. Instead of the conventional thicker airfoils such as NACA 0012 and NACA

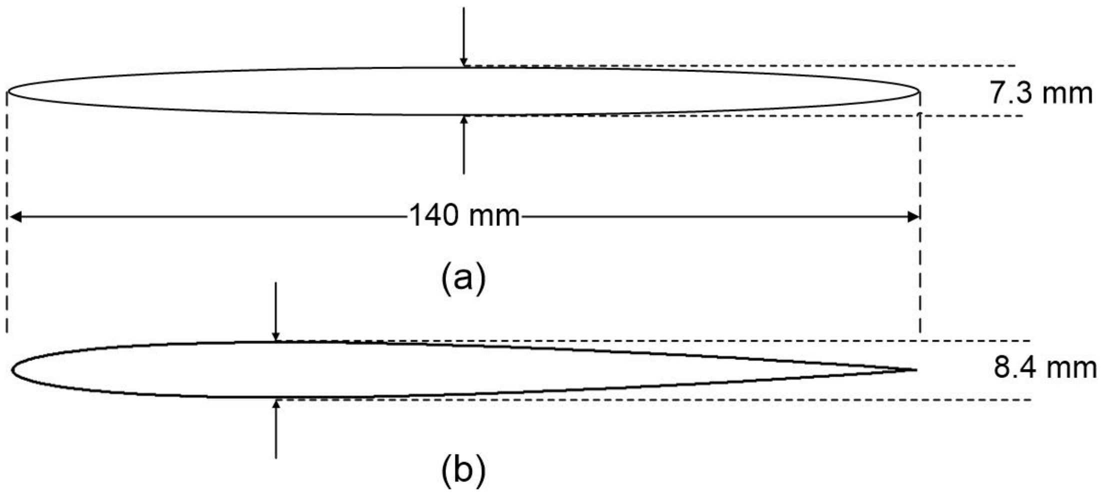

Figure 6.1: Schematic of **(a)** Elliptical foil with minor axis length (diameter) set at 7.3 mm which accounts to about 5.2% thickness with reference to chord length and **(b)** NACA 0006 foil section amounting to about 8.4 mm thickness at roughly 0.29c corresponding to about 6% thickness with reference to chord length. Both hydrofoils after 3D printing and pivot location plate inserted to them weighed around 165 *g* and 174 *g* respectively.

0015, which have been used as baseline foils in numerous studies till now in this research domain, a thinner foil was the only option. For the NACA profile, five different foil sections (NACA 0004, 0006, 0008, 0010 & 0012) were designed to test their mass properties using Solidworks and CatalystEX software before printing. The 3D printer is UPrint SE from Stratasys and uses Fused Deposition modeling (FDM) technology, which is an additive manufacturing (AM) process commonly used for prototyping, modelling and production applications. The FDM thermoplastic used by this 3D printer is ABS*plus* and through CatalystEX software we could determine the final mass of the hydrofoil. Finally, NACA 0006 foil section was chosen. The same technique was applied to the elliptical foil section. Since, there is no series which differentiates among different elliptical foil sections the parametric equation of ellipse was used to generate coordinates for the foil section. Since the chord length (c) was set at 0.14 m for all foils, the major axis of the ellipse was set to 0.14 m. Different minor axis lengths were tested to determine the mass of the elliptical foil section within the mass range of the flatplate foil and NACA 0006 by applying the same methodology as implemented in the case of NACA foil. Five different minor axis lengths were tested (0.0055 m, 0.0062 m, 0.0068 m, 0.0073 m & 0.008 m) from which 0.0073 m was the most suitable one. Figure 6.1 (a) and (b) shows the profile for the selected elliptical and NACA 0006 foils used in our experiments.

Since the ABS*plus* material is not transparent unlike plexiglass and a detailed analysis of flow evolution in both upstroke and downstroke motion was required, two lasers were used PIV experiments. Figure 6.2 shows the LIF/PIV experimental setup, which is like the one in Figure 3.7 except for the presence of an additional laser system on the other side of the test rig. Care was taken, and multiple pre-experiment tests were conducted to make sure that the laser sheets from both lasers were properly aligned and at the same height level. Post processing procedure as described in Section 3.1.3 for flow evolution via PIV experiments which was used for flatplate foil was adopted for these two foil sections.

6.2 PERFORMANCE OF ELLIPTICAL HYDROFOIL

Figure 6.3 shows the performance of an elliptical foil with big inertia (m_{ib} = 1.35 kg) attached to the top of the small aluminum block travelling on the guide rail, at three different pitching amplitudes (θ_o = 30°, 43° and 60°) at three different free stream velocities (U_o = 0.57 m/s, 0.65 m/s and 0.78 m/s). Figure 5.3 also consists of a star symbol at θ_o = 30°, with the caption in the figure referring to the inability of the elliptical foil to perform sustainable flapping motions for energy harvesting at U_o = 0.57 m/s. Hence, we were unable to acquire the force-motion data since the test-rig required external help to perform sustainable flapping motion. The test-rig was first equipped with baseline inertial blocks (m_{ib} = 0.90 kg) to check whether the elliptical hydrofoil can perform, however at some parameters it was unable to fully perform sustainable operation. Hence, the morphological study was carried out using big inertial blocks and later performance of these hydrofoils will be compared with the flatplate case equipped with big inertial blocks for systematic comparative analysis. Although we cannot determine the whole trend at the smallest free-stream velocity, at other parameters the elliptical hydrofoil was able to perform sustainable energy harvesting through flapping motion. As observed in most of our previous cases, the elliptical hydrofoil exhibits comparatively good energy harvesting performance at lower free-stream velocities, where with the increase in U_o, C_{Pmean} decreases at each pitching amplitude.

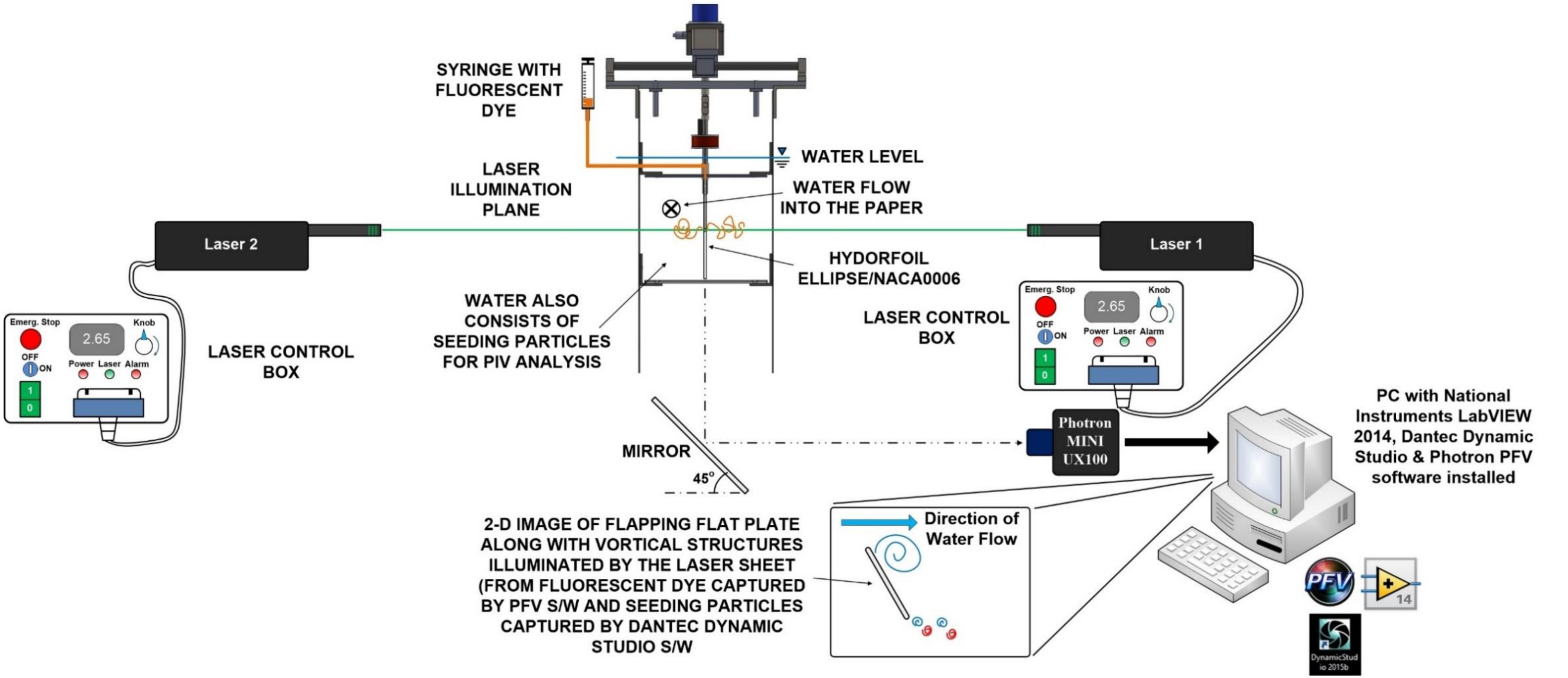

Figure 6.2: Experimental set-up for qualitative assessment of flow structures around a flapping foil (elliptical foil and NACA 0006 foil) in energy extraction mode. The dye used is fluorescent and is illuminated by two lasers positioned at mid-span of the oscillating flat plate on each side of the test rig. Due to space limitations underneath the test section, the camera is placed on the side of the test rig and the profile of the flat plate can be seen using a mirror placed underneath the test-rig at 45° to the horizontal. The Photron PFV software captures the images for detailed qualitative analysis later. The same setup is also being used for PIV analysis. The dye syringe is disconnected, and the water is seeded with 20µm diameter Polyamid particles, which are illuminated by the same laser and acquired by the high-speed camera system respectively on the Dantec Dynamic Studio software.

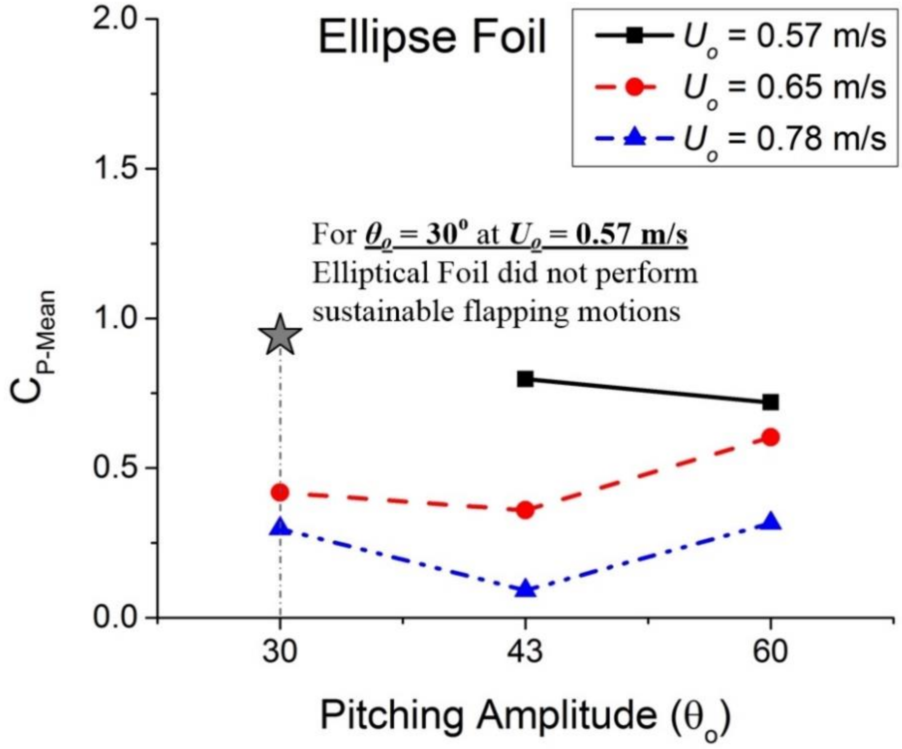

Figure 6.3: Graph showing performance of the elliptical foil for three different pitching amplitudes (θ_o = 30°, 43° and 60°) at different free-stream velocities (U_o = 0.57 m/s, 0.65 m/s and 0.78 m/s). Notice the Star symbol at θ_o = 30° indicating that the test-rig with the elliptical foil did not perform sustainable flapping motions at U_o = 0.57 m/s, hence no force-kinematics data could be acquired for energy harvesting performance analysis.

Figure 6.4 shows the force-motion behavior and the corresponding energy harvesting performance from both motion modes in a flapping cycle at U_o = 0.65 m/s at three different pitching amplitudes (θ_o = 30°, 43° & 60°). Figure 5.4 (a) shows the phase-averaged C_P and contributions from both plunging and pitching motions C_{Py} and $C_{P\theta}$ at three different pitching amplitudes. With increasing pitching amplitude, it can be observed that the peak values in C_P at different time instances during the flapping cycle increases, attributing towards the formation of large separation areas at the leading edge of the foil leading to decrease in pressure and increase in lift force consequently. Most of the contribution is from the plunging motion since the C_P graph follows the C_{Py} trend except in peak values. Increase in peak values is not only observed during stroke reversal (0.375 < t/T < 0.435 and 0.875 < t/T < 0.975) but also evident during some parts of plunging motion. However, for Figure 5.4 (a-II) during we observe a severe drop in energy harvesting performance during the

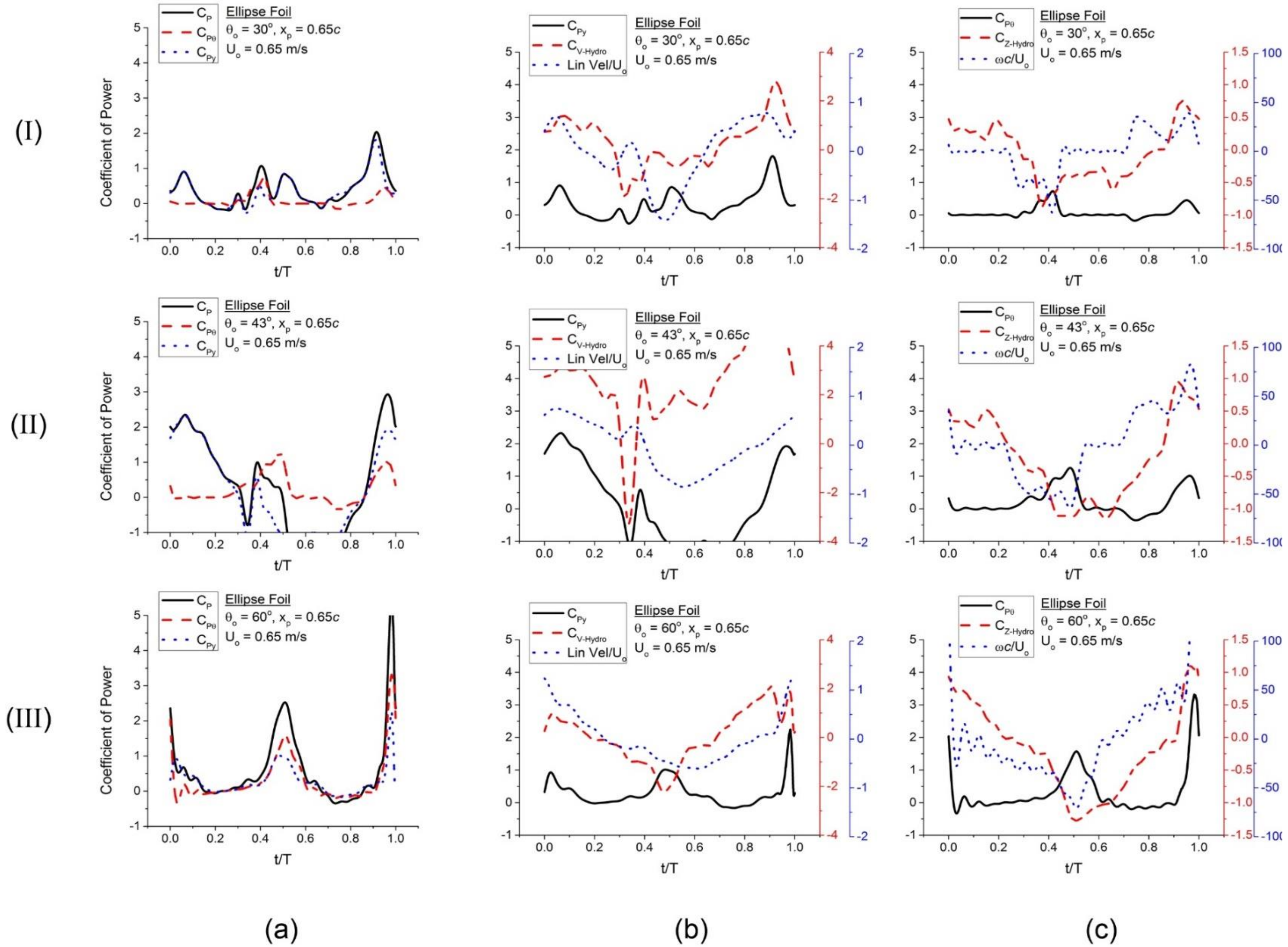

Figure 6.4: Graphs showing phase-averaged **(a)** Coefficient of Power (Total, Plunging and Pitching), **(b)** Coefficient of Power due to Plunging motion with corresponding Coefficient of Hydrodynamic Vertical Force and Linear Velocity and **(c)** Coefficient of Power due to Pitching Motion with corresponding Coefficient of Hydrodynamic Moment and Angular Velocity of an Elliptical Hydrofoil at U_o = 0.65 m/s for, **(I)** θ_o = 30°, **(II)** θ_o = 43° and **(III)** θ_o = 60°.

downstroke phase of the flapping elliptical foil at θ_o = 43°, leading to energy expenditure. The C_P trend witnessed here was not only at this free-stream velocity but also seen in the other two free-stream velocities (U_o = 0.57 m/s and 0.78 m/s) at this pitching amplitude (θ_o = 43°). The elliptical hydrofoil was not able to perform sustainable symmetrical plunging motion during the downstroke motion as compared to its upstroke motion leading toward considerable loss of energy from the system.

This energy expenditure which spans almost the whole of the downstroke motion for an elliptical hydrofoil at θ_o = 43° as well as peak values and trend line followed by the C_P graph for other pitching amplitudes is mainly due to C_{Py}. Figure 6.4 (b) shows the phase-averaged C_{Py}, $C_{V\text{-}hydro}$ and LinVel/U_o for an elliptical hydrofoil at different pitching amplitudes at U_o = 0.65 m/s. For the hydrofoil at θ_o = 30°, we observe good synchronization between the hydrodynamic lift force and plunging velocity. Peaks in hydrodynamic lift force are also visible during parts of plunging motion, mostly during its initiation period right after the stroke reversal stops, while other peaks during time ranges mentioned in the previous paragraph is mostly due to the sudden change in direction because of stroke reversal. Due to these peak values in hydrodynamic lift force and good synchronization with the plunging velocity, C_{Py} remains positive throughout the flapping cycle. A similar behavior but with comparatively increased hydrodynamic lift force due to a higher angle of attack is observed in θ_o = 60° case. Compared to its upstroke motion, the lift force rises at a higher gradient during its downstroke motion and suddenly leading to a higher small during peak due to the stroke reversal. Synchronization with the plunging velocity during the initiation of both upstroke and downstroke motion is better but suddenly decreases leading to almost zero energy extraction between $0.1 < t/T < 0.35$ and $0.7 < t/T < 0.875$. However, for θ_o = 43° the profile of lift force during the flapping cycle is purely a-symmetrical as compared to all the cases we have discussed here and observed during our experimental campaign.

Upon our analysis of the associated PIV images, it revealed that although the motion kinematics (plunging motion) were some-what symmetrical, flow evolution during the upstroke and downstroke motion were not entirely identical. A fully developed LEV was formed at the onset of upstroke motion, which as the foil plunged upwards was shed into the wake followed by the formation of a second LEV. This secondary LEV fully develops and starts to travel on the hydrofoil's upper side, however since by this time the foil has already started its stroke reversal, the shed secondary LEV almost breaks down due to the flow being pushed against the tunnel wall and the foil undergoing stroke reversal. As the hydrofoil starts its downstroke motion, it is not until after the mid-stroke position that the onset of LEV is observed, however not as fully developed as the one in the upstroke motion. This LEV eventually breaks down as the hydrofoil reaches the end of the stroke and undergoes stroke reversal. This difference in flow evolution during the two strokes of the flapping cycle leads to an a-symmetrical lift force variation as observed in Figure 6.4 (b-II). Because of a such a trend, the synchronization with the normal plunging velocity profile of the elliptical hydrofoil at θ_o = 43° as seen in Figure 6.4 (b-II) is not good especially during the downstroke phase till the start of the second stroke reversal during the flapping cycle (0.45 < t/T < 0.85). This leads to very poor energy extraction performance during the second half of the flapping cycle, such that even the contribution by the pitching motion does not improve the performance during the downstroke motion. However, the overall performance (C_{Pmean}) for θ_o = 43° at U_o = 0.65 m/s, as seen in Figure 6.3, is still positive and almost at the same level as of at θ_o = 30° but both still lower than θ_o = 60°. This can be attributed towards the C_{Py} peaks during the upstroke motion between 0 < t/T < 0.3 due to the subsequent onset and shedding of two LEVs resulting in the generation of very high forces and between 0.875 < t/T < 1.0 because of the stroke reversal.

Figure 6.4 (c) shows the contribution from pitching motion of the elliptical foil at all three pitching amplitudes at U_o = 0.65 m/s. $C_{P\theta}$ at all pitching amplitudes for the elliptical hydrofoil exhibits a similar behavior shown by the flapping foil as witnessed in our experimental campaign i.e. non-sinusoidal motion, where the foil plunges at a constant max pitching amplitude and undergoes pitching motion only during stroke reversal. Since there is no change in pitching amplitude during plunging motion, $C_{P\theta}$ remains zero hence the peaks in $C_{P\theta}$ only appear twice since the hydrofoil undergoes stroke reversal twice during the flapping cycle. Furthermore, because of increased pitching amplitude the hydrofoil experiences increase in torque which also increases the angular velocity profile as seen in Figure 6.4 (c). Good synchronization between hydrodynamic moment and angular velocity especially during stroke reversal time zones leads to increase in $C_{P\theta}$ with increasing pitching amplitude. This enhances the overall energy extraction performance of the flapping elliptical hydrofoil which eventually increases C_{Pmean} in Figure 6.3.

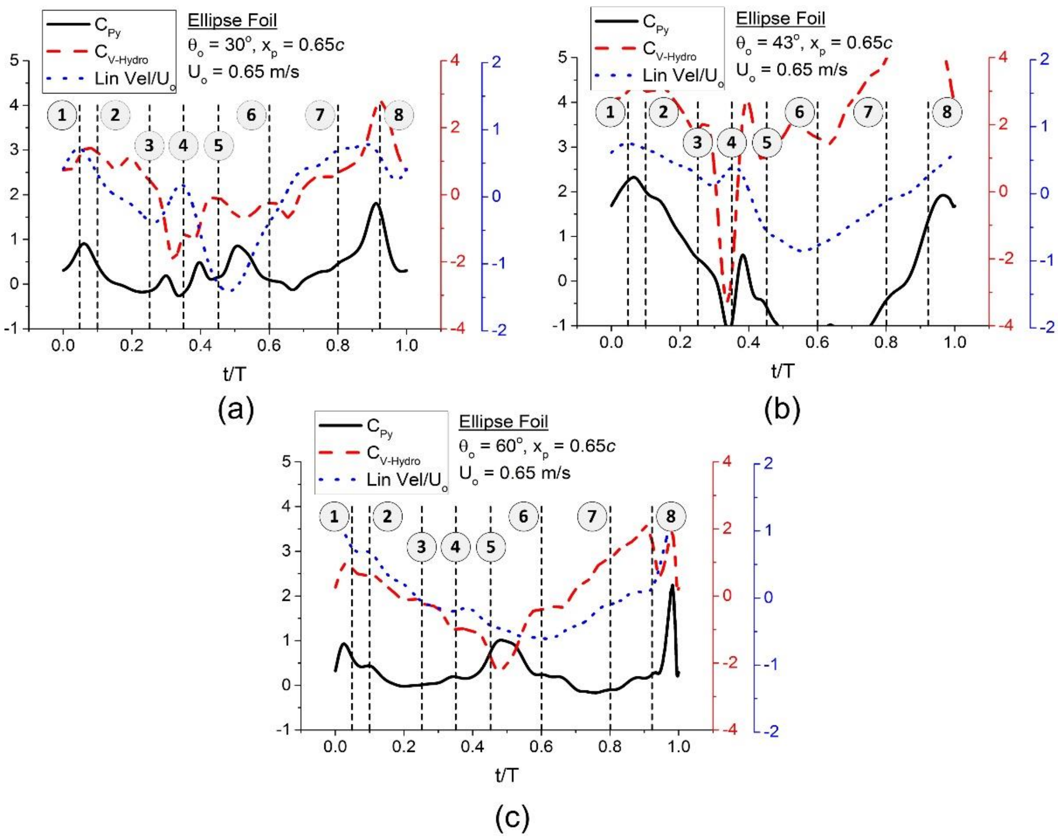

Figure 6.5: Graph showing phased average C_{Py}, $C_{V\text{-}hydro}$ and LinVel/U_o of an elliptical foil at U_o = 0.65 m/s for pitching amplitudes **(a)** θ_o = 30°, **(b)** θ_o = 43° and **(c)** θ_o = 60°. Each of the plots consist of eight marked time stamps which correlate to the flow evolution behaviour at those instants in Figure 6.6.

Figure 6.5 shows C_{Py} plots of the elliptical hydrofoil for all pitching amplitudes marked with eight distinct time stamps, whereas Figure 6.6 shows the flow evolution in terms of vorticity contours around the elliptical hydrofoil correlating with these time stamps. Time stamp $t/T \approx 0.05$ corresponds to the hydrofoil in the initial phase of its upstroke motion. As shown in Figure 6.6, for all three pitching amplitudes, the LEV starts to form up where its size depending on the pitching amplitude. Around this time stamp the hydrodynamic lift force starts to increase as in Figure 6.5. As the hydrofoil plunges further, the LEV starts to grow which is proportional to the separation region size which increases because of increasing pitching amplitude. For θ_o = 30°, the LEV stretches across more than half of the hydrofoil's upper surface around $t/T \approx 0.10$ and between $0.10 < t/T < 0.25$ this primary LEV sheds aft of the pivot location into the wake. While, at θ_o = 43° the LEV grows more rapidly in size as compared to the θ_o = 30° case although it doesn't

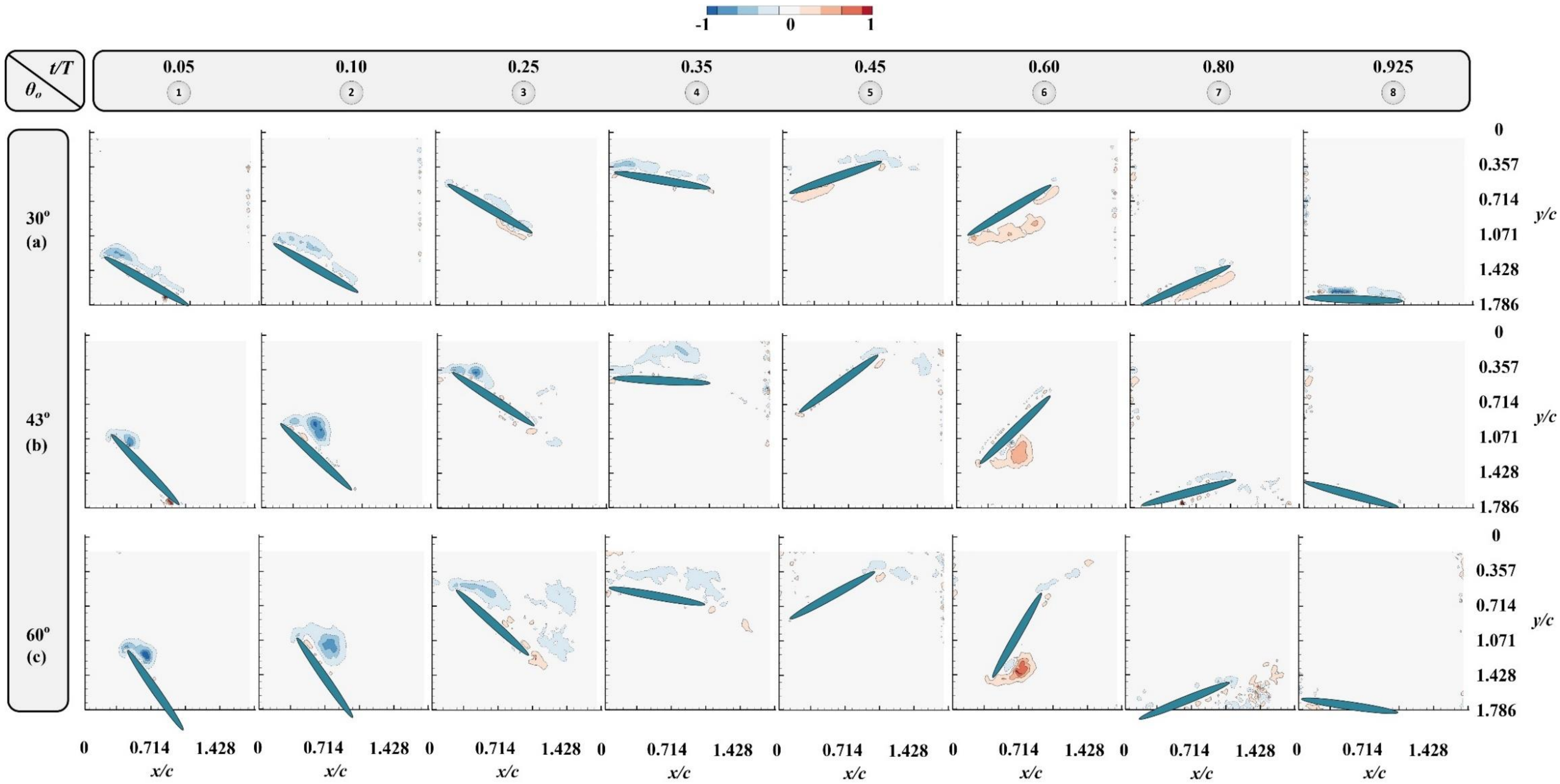

Figure 6.6: Figure showing vorticity contours of elliptical hydrofoil at eight different time instants during one flapping cycle with free-stream velocity of U_o = 0.65 m/s and pivot location x_p = 0.65c at three different pitching amplitudes: **(a)** θ_o = 30°, **(b)** θ_o = 43° and **(c)** θ_o = 60°. The x and y scale are dimensionalized with reference to the chord length (c = 0.14 m) of the hydrofoil.

stretch out completely over the upper surface of the foil. As the foil plunges further upwards, this primary LEV sheds into the wake about upstream of the pivot location between $0.10 < t/T < 0.25$ and just before $t/T \approx 0.25$ the secondary LEV has already taken shape. A similar situation between these time instants ensues in the case of $\theta_o = 60^o$, except the size of the primary LEV which is followed by the formation of a secondary LEV which has developed faster than its $\theta_o = 43^o$ counterpart and about to shed into the wake by $t/T \approx 0.25$. Since the primary LEV is still on the foil's upper surface, we observe the increase in hydrodynamic lift force profile in Figure 6.5 which then declines due to the shedding of the primary LEV and then increases slightly just before $t/T \approx 0.25$ due to the formation of the secondary LEV.

Between $0.25 < t/T < 0.35$ the foil starts the stroke reversal because of the moment arm touching the plunge limiter. At $t/T \approx 0.25$ for $\theta_o = 30^o$, the secondary LEV has not started to form, which happens so around $t/T \approx 0.30$. By this time the hydrofoil is undergoing stroke reversal and the secondary LEV starts to stretch along the foil's upper surface which then almost into the wake by $t/T \approx 0.45$. At $t/T \approx 0.35$ for $\theta_o = 43^o$ the secondary LEV starts to shed in to the wake while the foil undergoes stroke reversal, which indicates a decline in hydrodynamic lift force as seen in Figure 6.5 (b). A similar scenario is witnessed for $\theta_o = 60^o$ where the secondary LEV sheds into the wake except it's broken down as compared to the $\theta_o = 43^o$ where the vortex is almost intact. As the hydrofoil continues its stroke reversal around $t/T \approx 0.45$, no further change in the flow around the foil for all pitching amplitudes is observed. Between $0.45 < t/T < 0.60$ the foil completes its stroke reversal and initiates its downstroke plunging motion. For the $\theta_o = 30^o$ we see a similar flow structure as was during its upstroke motion although in this case we identify three distinct vortex cores in cascade and covering more than half of the foil's lower surface. Presence of these multiple vortex cores allows the foil to experience and increase in lift force which then suddenly decreases as LEV sheds in to the wake. For $\theta_o = 43^o$ around $t/T \approx 0.60$, the formation of a very large LEV is observed in Figure 6.6 (b). The size of this LEV is slightly bigger than what was observed at t/T 0.10 and $\theta_o = 60^o$ at $t/T \approx 0.60$ indicating that during the downstroke motion the generation of lift force is slightly higher than the upstroke motion and its $\theta_o = 60^o$ counterpart as observed in Figure 6.5 (b) and (c). Although there is difference in generated forces between $\theta_o = 43^o$ and $\theta_o = 60^o$, the de-synchronization between the lift force and plunging velocity during the downstroke motion (Figure 5.5 (b)) for θ_o

= 43° leads to poor energy harvesting performance during that period. Between 0.70 < t/T < 1.0 the foil undergoes a second stroke reversal and during this pitching amplitude change no evident flow structures are formed around the foil. The change in lift force and the sudden spike is due to the sudden change in direction by the foil during the stroke reversal.

6.3 PERFORMANCE OF NACA0006 HYDROFOIL

Figure 6.7 shows the mean energy harvesting performance (C_{Pmean}) of NACA 0006 hydrofoil for all pitching amplitudes (θ_o = 30°, 43° and 60°) at three different free-stream velocities (U_o = 0.57 m/s, 0.65 m/s and 0.78 m/s) with pivot location fixed at 0.65c. Except at U_o = 0.57 and 0.78 m/s, the NACA hydrofoil shows a linear increase in energy extraction performance with increasing pitching amplitude at U_o = 0.65 m/s. At θ_o = 30°, energy extraction performance remains almost in a very small range with almost similar numbers (C_{Pmean}) for U_o = 0.57 m/s and 0.65 m/s, a small decline at U_o = 0.78 m/s. As the pitching amplitude is increased to θ_o = 43°, mean energy extraction performance shows a near linear decline with increasing free-stream velocity, while at θ_o = 60° the foil underperforms at U_o = 0.57 m/s compared to at θ_o = 43°, while at U_o = 0.65 m/s and 0.78 m/s C_{Pmean} increases as the pitching amplitude is increased to θ_o = 60°.

Figure 6.8 shows the phase averaged force and kinematics profile of a NACA0006 foil at different free-stream velocities for θ_o = 30° with pivot location fixed at 0.65c. As discussed, C_{Pmean} at this pitching amplitude for U_o = 0.57 and 0.65 m/s are in very close proximity to each other. Referring to Figure 6.8 (c), which shows the pitching motion contribution, peak values and overall trend of $C_{P\theta}$ is quite small. Even with increasing free-stream velocity, $C_{P\theta}$ profile looks somewhat identical showing no significant improvement in energy extraction performance with increasing free-stream velocity from the pitching motion.

From Figure 6.8 (a), C_P profile mostly follows the C_{Py} trend due to less contribution from the pitching motion. High C_P peaks are only witnessed at U_o = 0.57 and 0.65 m/s, while at U_o = 0.78 m/s C_P profile is quite smaller leading to decrease in C_{Pmean} compared to the two smaller free-stream velocities. Furthermore, C_P profile for NACA0006 foil at U_o = 0.57 m/s is different than at U_o = 0.65 and 0.78 m/s indicating some change in lift and plunging velocity profile at the smallest

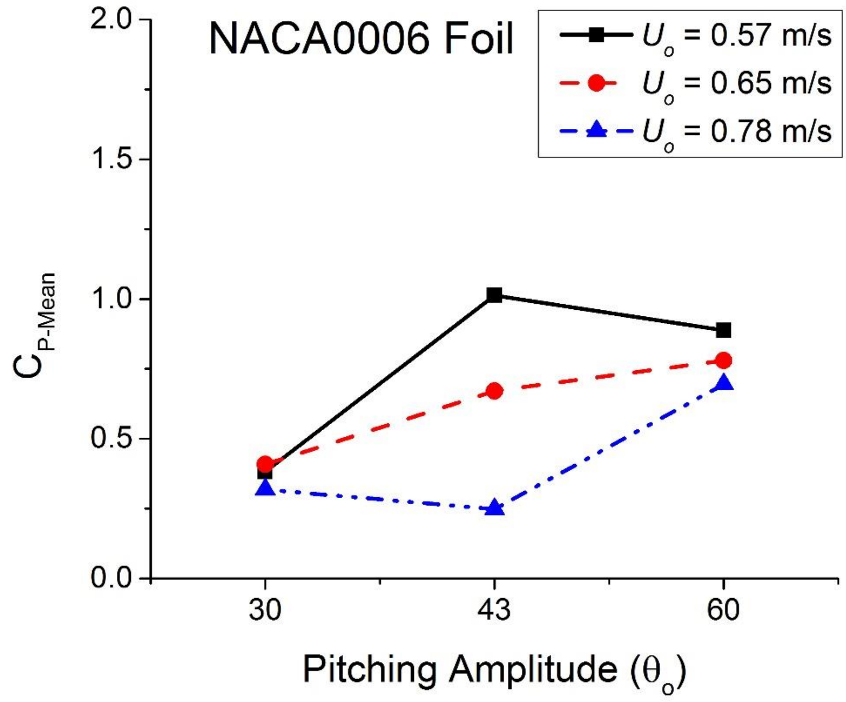

Figure 6.7: Graph showing performance of the NACA 0006 foil for three different pitching amplitudes (θ_o = 30°, 43° and 60°) at different free-stream velocities (U_o = 0.57 m/s, 0.65 m/s and 0.78 m/s) at $x_p = 0.65c$.

free-stream velocity as shown in Figure 6.8 (b)-I. Two very distinctive peaks are observed at U_o = 0.57 m/s (Figure 6.8 (b)-I), mostly occurring almost during the last phases of the plunging motion (upstroke and downstroke) and at the onset of stroke reversal. Although, during the onset of upstroke motion a positive hydrodynamic lift force is generated ($0 < t/T < 0.1$), however there is fluctuation in the plunging velocity and during this time range has the opposite sign. This de- synchronization leads to negative energy harvesting performance which remains for some part of the upstroke motion. As the foil is about to complete its plunging motion and initiates its stroke reversal, a sudden change in direction in lift force and plunging velocity (both in same direction) synchronizes both parameters. This causes an increase in C_{Py} which spans from $0.15 < t/T < 0.45$. As the foil completes its first stroke reversal and initiates its downstroke motion, the lift force (which is now in the downstroke direction) starts to increase as well as the plunging velocity. Between $0.45 < t/T < 0.625$, both parameters are not synchronized due to which the energy extraction is minimal, but it then starts to increase in a similar fashion as during upstroke motion and due to sudden recovery in synchronization between hydrodynamic lift force and plunging velocity.

In Figure 6.8 (a)-II at U_o = 0.65 m/s, we observe multiple peaks in C_P during the flapping cycle. These peaks are not only during the stroke reversal but also during the plunging phase of the flapping cycle. The profile is different than what we witnessed at U_o = 0.57 m/s and similar to at U_o = 0.78 m/s as seen in Figure 6.8 (a)-III even though the peak values are smaller than at U_o = 0.65 m/s, and other flapping foil energy harvesting cases which we have discussed in our experimental campaign. In Figure 6.8 (b)-II we observe good synchronization between hydrodynamic lift force and plunging velocity during the initial phases of the upstroke motion ($0 < t/T < 0.15$). After mid-upstroke, although the hydrodynamic lift force continues to increase there is a sudden decrease in plunging velocity is observed ($0.17 < t/T < 0.3$) which causes de-synchronization between the lift force and the plunging velocity affecting energy harvesting performance. The hydrofoil starts to decelerate due to the onset of stroke reversal, which causes the change in direction of the hydrodynamic lift force and a sudden spike due to the stroke reversal process coming to an end. Good synchronization between hydrodynamic lift force and plunging velocity is observed between $0.35 < t/T < 0.60$ hence two positive peaks in C_{Py} are observed. As the first stroke reversal is completed and the downstroke motion starts the hydrodynamic lift force starts to increase in the downstroke direction along with the plunging velocity. Although both parameters are in synch with each other hence there is a gradual increase in C_{Py} ($0.65 < t/T < 0.85$) followed by a sudden spike between $0.85 < t/T < 1.0$ in hydrodynamic lift force due to the second stroke reversal. The good synchronization between the lift force and plunging velocity leads to fourth positive peak in C_{Py} as seen in Figure 6.8 (b)-II. It may be because of these multiple positive peaks for U_o = 0.65 m/s case and two big peaks for U_o = 0.57 m/s, that the C_{Pmean} for both cases are very close to each other as seen in Figure 6.7. As for U_o = 0.78 m/s case the hydrodynamic lift force is somewhat smaller as compared to the other two free-stream velocities. We do observe almost the same number of peaks in C_{Py} as seen in Figure 6.8 (b)-II, however due to smaller hydrodynamic lift force C_{Py} peaks are comparatively smaller. Furthermore, we also noticed mediocre energy harvesting performance by the pitching motion (Figure 6.8 (c)-III hence it didn't augment to the energy harvesting

(I)

(II)

(III)

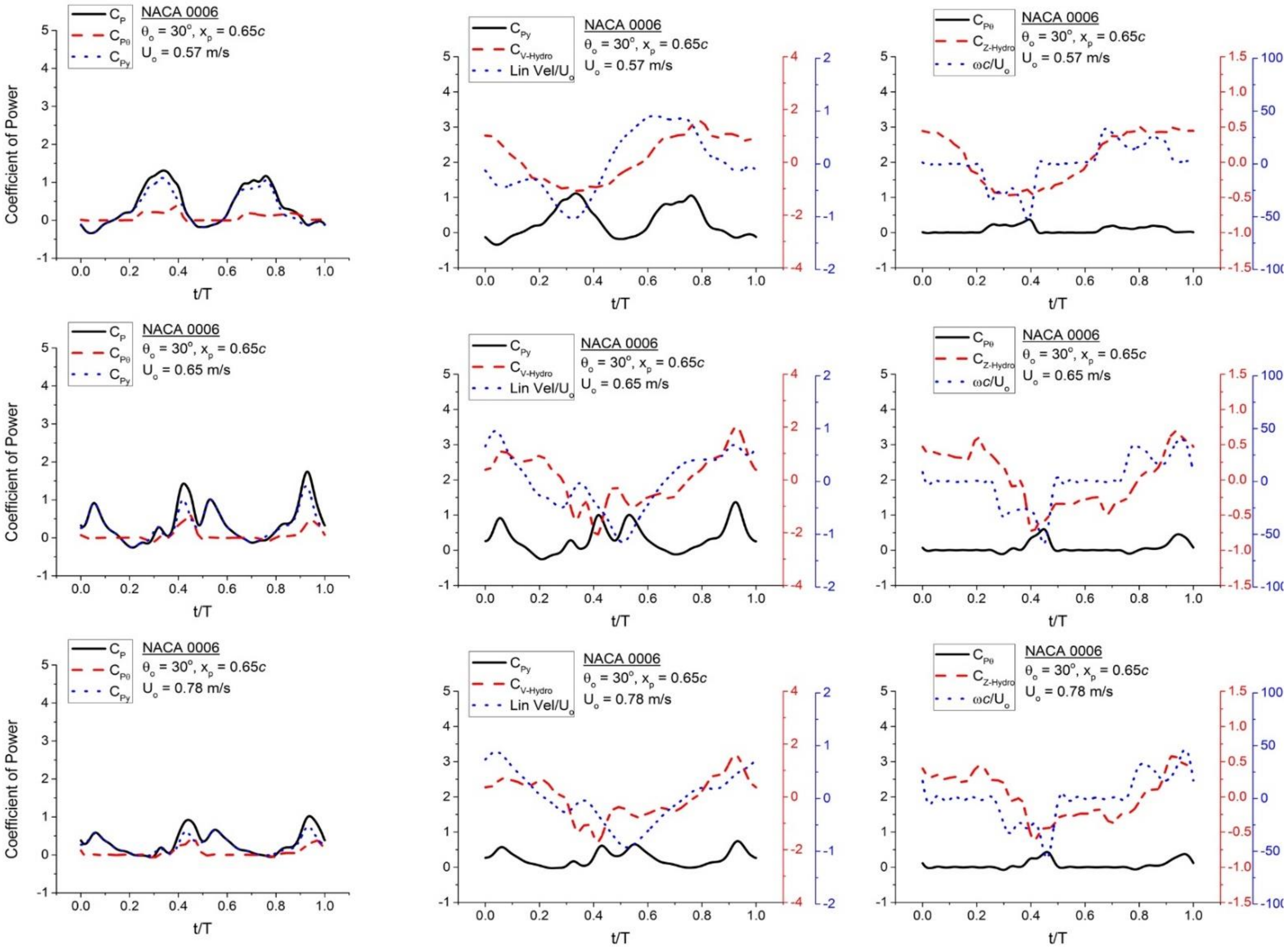

(a) (b) (c)

Figure 6.8: Graphs showing phase-averaged **(a)** Coefficient of Power (Total, Plunging and Pitching), **(b)** Coefficient of Power due to Plunging motion with corresponding Coefficient of Hydrodynamic Vertical Force and Linear Velocity and **(c)** Coefficient of Power due to Pitching Motion with corresponding Coefficient of Hydrodynamic Moment and Angular Velocity of an Elliptical Hydrofoil for pitching amplitude θ_o = 30º at, **(I)** U_o = 0.57 m/s, **(II)** U_o = 0.65 m/s and **(III)** U_o = 0.78 m/s.

from plunging motion and to the overall energy harvesting performance of the NACA0006 foil at U_o = 0.78 m/s. Because of this the overall profile of C_P in Figure 6.8 (a)-I is smaller as compared to resulting in a smaller C_{Pmean} as compared to U_o = 0.57 and 0.65 m/s cases as seen in Figure 6.7.

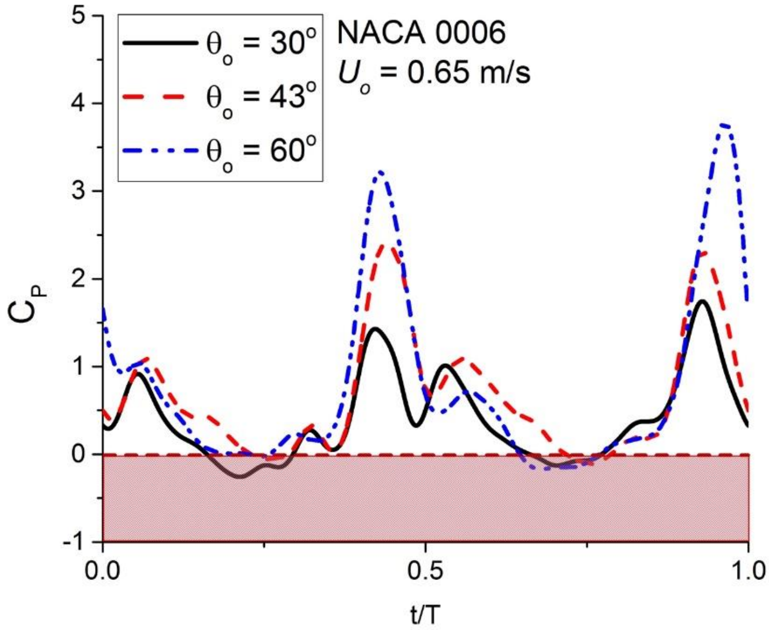

Figure 6.9: Phase-averaged C_P at U_o = 0.65 m/s for three different pitching amplitudes at pivot location x_p = 0.65c for NACA0006 foil. Red regions marked in red below the zero line indicates the region where the flapping foil starts to expend energy from the system rather than extracting it from the surrounding fluid.

Figure 6.9 shows the C_P profile of NACA0006 hydrofoil at different pitching amplitudes for free-stream velocity U_o = 0.65 m/s. From Figure 6.7 we see that for U_o = 0.65 m/s, NACA0006 exhibits an increase in energy extraction performance with increasing pitching amplitude in an almost linear fashion. C_P profiles for all pitching amplitudes are similar within the flapping cycle, with the only difference in magnitude which increases with increasing pitching amplitude. Between $0 < t/T < 0.23$, the C_P values first increases indicating that the foil has initiated its plunging motion regardless of pitching amplitude. As the foil starts plunges further, C_P starts to decline indicating that the vortical structures (LEV) which were formed at the onset of the plunging motion, have shed into the wake hence affecting the hydrodynamic lift force. Furthermore, the foil also starts to decelerate due to the initiation of the stroke reversal as observed for all pitching amplitudes between 0.24

< t/T < 0.45. Although the foil is still plunging, it decelerates almost to a stop as it passes its zero-angle mark and rotates further (after $t/T \approx 0.45$) set maximum pitching amplitude in opposite direction. As the foil is undergoing stroke reversal, the change in direction experienced by the foil and coupled force sensor allows it to reach peak values in the downstroke direction. In Figure 6.9 at $\theta_o = 30^{\circ}$, we observe two peaks in C_P, with the first peak because of directional change experienced by the foil (pitching motion due to stroke reversal), while the second peak is due to formation of flow structures because of the foil initiating downstroke motion (plunging motion). The magnitude of the first peak as compared to the second peak increases considerably as the pitching amplitude of the foil is increased. Evidently, as the foil plunges downstroke, the acting hydrodynamic forces increase, but due to the small translational distance, the foil already starts to decelerate due to the contact of the moment arm with the plunge limiter (an action which occurs early when the pitching amplitude of the foil is increased). This lets the foil to decelerate, eventually following the same sequence as it experiences during the first half of its flapping cycle.

Figure 6.10 shows the corresponding C_{Py} and $C_{P\theta}$ of the pitching amplitude cases for NACA0006 foil at U_o = 0.65 m/s, while Figure 6.11 shows the detailed hydrodynamic lift force and plunging velocity time history for these cases in one flapping cycle. From Figure 6.9 and 6.10 (a) we observe that for both $\theta_o = 43^{\circ}$ and 60° cases C_P profile does not cross the red zone while for $\theta_o = 30^{\circ}$, although positive for maximum amount of the flapping cycle, it goes negative for a brief moment at two separate occasions; $0.18 < t/T < 0.29$ and $0.65 < t/T < 0.75$. This could be attributed to the de-synchronization between the hydrodynamic lift force and plunging velocity during the mentioned time ranges as seen in Figure 6.11 (a). For $\theta_o = 43^{\circ}$ and 60° good synchronization is observed between the hydrodynamic lift force and plunging velocity resulting in a C_{Py} profile which either remain positive in the form of peaks or near the zero-line mark as seen in Figure 6.11 (b) and (c).

From Figures 6.9 and 6.10 we can also see that the C_P profile totally follows the C_{Py} profile at all pitching amplitudes, while the $C_{P\theta}$ augments the energy extraction capability of the NACA0006 foil at two distinct time instants during the flapping cycle as can be seen in Figure 6.10 (b). From $0 < t/T < 0.40$ approximately, the hydrofoil is undergoing plunging motion with set maximum pitching amplitude

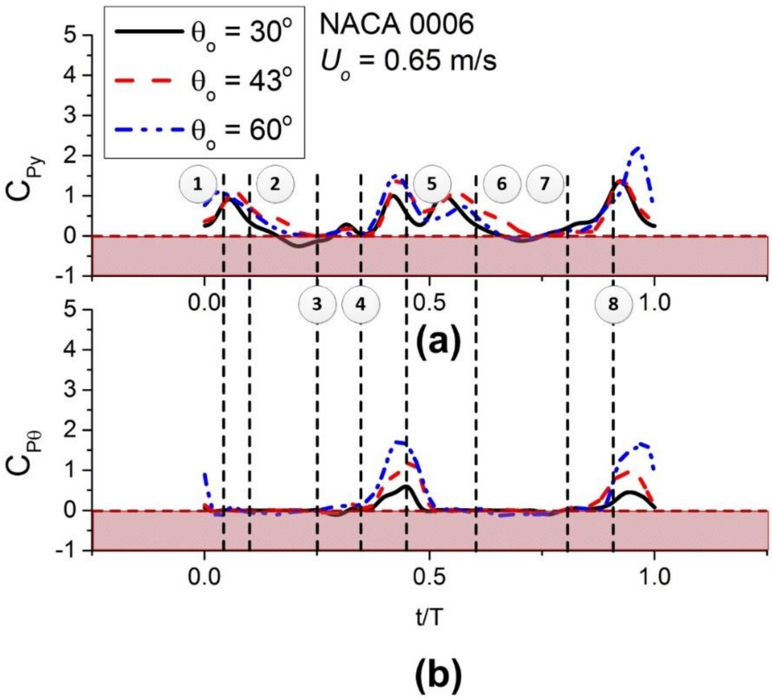

Figure 6.10: Phase-averaged **(a)** C_{Py} and **(b)** $C_{P\theta}$ at U_o = 0.65 m/s for three different pitching amplitudes at pivot location $x_p = 0.65c$ for NACA0006 foil. Eight-time stamps are marked to correlate to the flow evolution around the NACA0006 foil as shown in Figure 6.12.

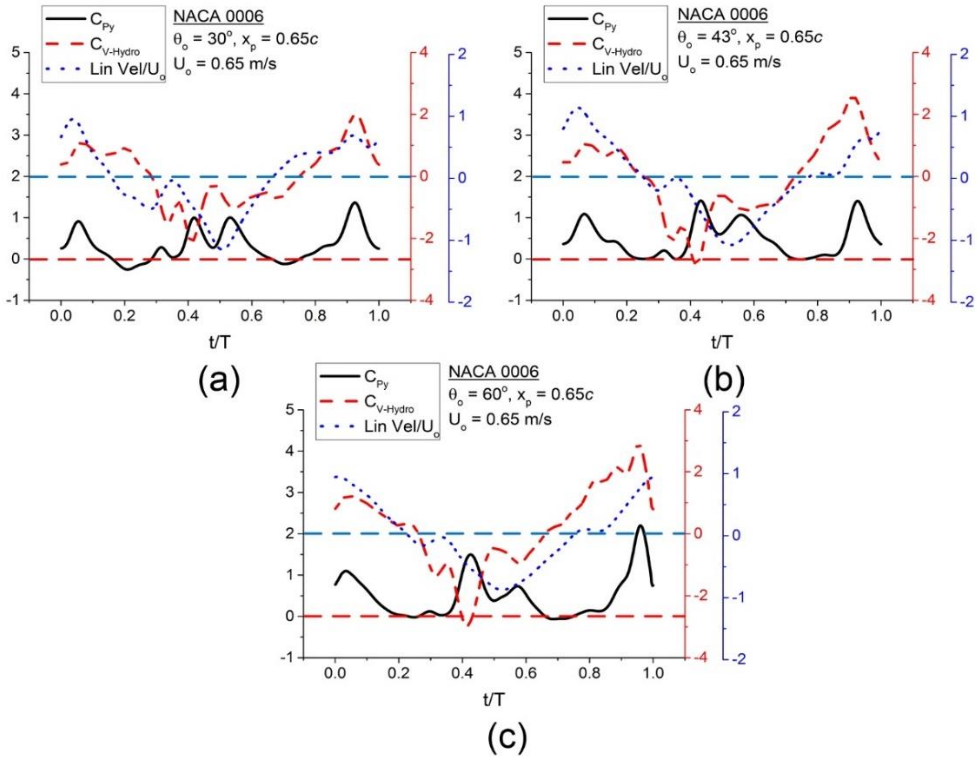

Figure 6.11: Phase-averaged C_{Py}, $C_{V\text{-}hydro}$ and Lin Vel/U_o of NACA0006 hydrofoil with pivot location $x_p = 0.65c$, free stream velocity U_o = 0.65 m/s for pitching amplitudes **(a)** $\theta_o = 30^o$, **(b)** $\theta_o = 43^o$ and **(c)** $\theta_o = 60^o$.

hence not change in angular kinematics, leading to zero contribution to total energy extraction. When the foil starts the stroke reversal process, it experiences not only the hydrodynamic lift force due to the continuous translational motion but hydrodynamic moment which results in pitching motion. The magnitude of the hydrodynamic torque and the resulting pitching motion depends on the pitching amplitude, which increases as the pitching amplitude is increased as shown in Figure 6.10 (b). The first half of the stroke reversal is the result of the momentum gained by the foil due to the plunging motion in the first stroke of the flapping cycle. Since, a greater pitching amplitude generates larger hydrodynamic forces (Figure 6.11) the resulting increased plunging velocity augmented by the inertial block generates a higher angular velocity as the foil performs the stroke reversal. When the foil halts and almost passes the zero-angle mark, the acting hydrodynamic forces further rotates the foil to the set pitching amplitude. The angular velocity in the second half of the stroke reversal and the resulting hydrodynamic torque values increase if the set pitching amplitude value is higher. With good synchronization between hydrodynamic torque and angular velocity, it eventually generates positive energy harvesting performance with $C_{P\theta}$ peaks increasing with increasing pitching amplitude. This then further augments the C_{Py} profile leading to better energy harvesting performance with increasing pitching amplitude as observed in Figure 6.9 and Figure 6.7 in the form of C_{Pmean}.

Figure 6.12 shows the vorticity plots of the flow evolution at eight different time stamps during the flapping cycle, around the NACA0006 foil at three different pitching amplitudes (θ_o = 30°, 43° and 60°), which correlate to the same marked time stamps in C_{Py} plots as shown in Figure 5.11. As seen in Figure 6.12 at $t/T \approx 0.05$, as the foil commences the plunging motion, due to the separation area caused by the foil at fixed maximum pitching angle, the LEV starts to form up. For θ_o = 30°, the LEV at $t/T \approx 0.05$ is comparatively smaller and a weaker than at θ_o = 43° and 60°, where for θ_o = 43° the LEV is in a circular shape on the upper surface of the foil, while for θ_o = 60° two distinct vortex cores are identified where one is at the leading edge of the foil, while the other in a bit stretched form is on the foil's upper surface covering approximately 25% of the foil's chord. This difference can be observed in Figure 6.11 where at $t/T \approx 0.05$ the hydrodynamic lift force increases in small increments with increasing pitching amplitude. By $t/T \approx 0.10$ as the foil plunges

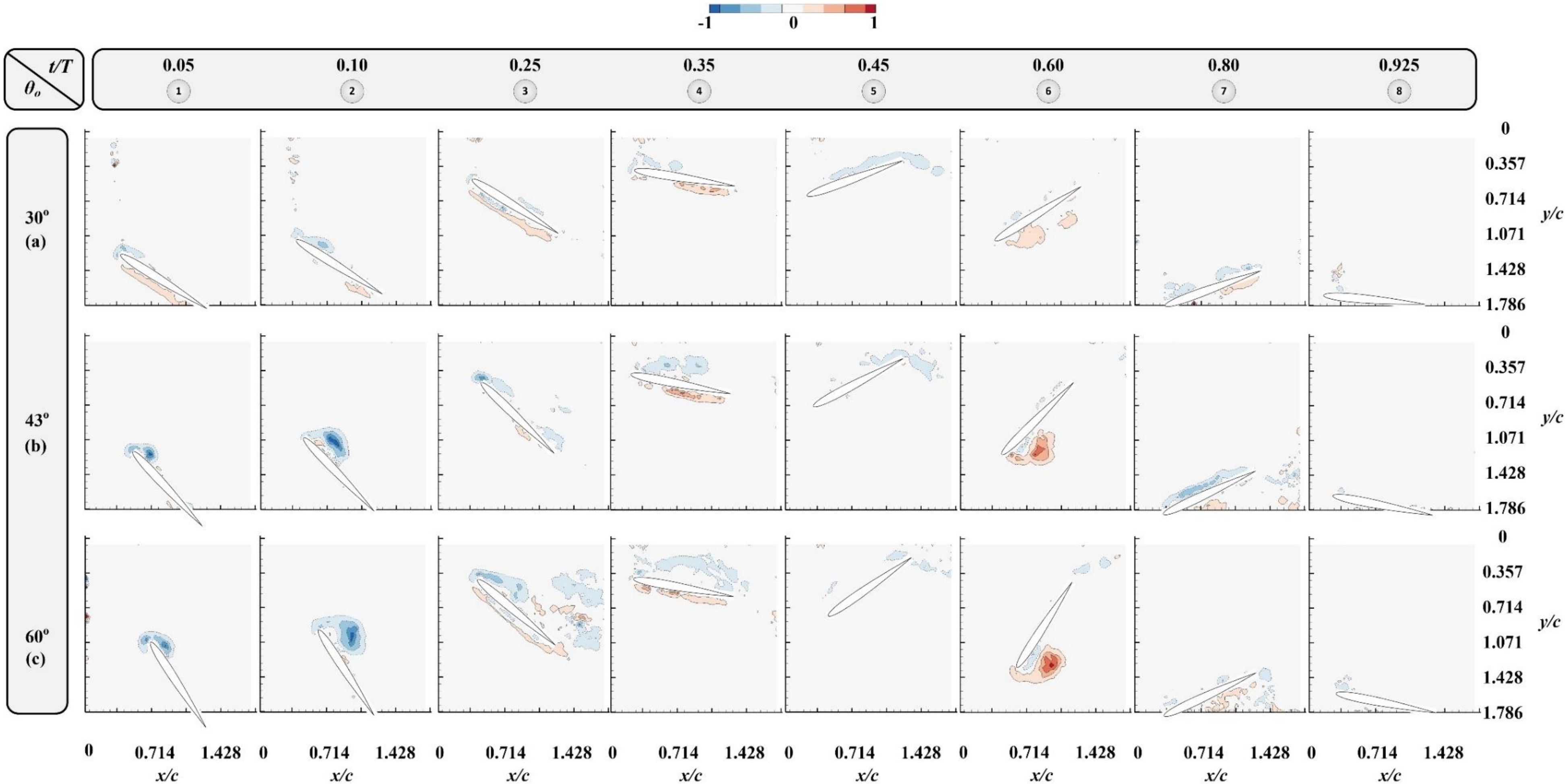

Figure 6.12: Figure showing vorticity contours of NACA0006 hydrofoil at eight different time instants during one flapping cycle with free-stream velocity of U_o = 0.65 m/s and pivot location x_p = 0.65c at three different pitching amplitudes: **(a)** θ_o = 30°, **(b)** θ_o = 43° and **(c)** θ_o = 60°. The x and y scale are dimensionalized with reference to the chord length (c = 0.14 m) of the hydrofoil.

upstroke, the LEV size starts to increase which can be observed quite clearly in Figure 6.12 (b) and (c). For θ_o = 30° (Figure 6.12 (a)) the primary LEV is still not fully developed and comparatively weaker than the developing vortical structures at the foil's leading edge with pitching amplitude θ_o = 43° and 60°. The hydrodynamic lift force starts to increase, due to the increased pressure difference experienced by the foil due to the presence of LEV on the foil's upper surface as can be seen in Figure 6.11. The respective plunging velocity also starts to increase which increases the C_{Py} value due to the good synchronization between the lift force and plunging velocity (Figure 6.10 (a)). Eventually between 0.10 < t/T < 0.25, the primary LEV sheds into the wake and formation of a secondary LEV at θ_o = 43° and 60° is quite evident at $t/T \approx 0.25$ in Figure 6.12 (b) and (c), while at θ_o = 30° it has not yet commenced. The shedding of the primary LEV causes the lift force to decline slightly and with the initiation of the secondary LEV, it increases a bit (Figure 6.11). Approximately after $t/T \approx 0.30$, the moment arm comes in contact with the plunge limiter, initiating stroke reversal. The secondary LEV especially at θ_o = 43° and 60° have not fully developed and as the foil performs the stroke reversal, the flow structures on the foil's upper surface are pushed against the tunnel's side wall, eventually breaking them down and shedding into the wake.

As the foil is pitching, no evident flow structures are observed 0.4 < t/T < 0.5 the rise in lift force in the opposite direction is the result stroke reversal. As the foil reaches its maximum pitching amplitude in the opposite direction and starts to plunge down, the plunging velocity with its direction changed synchronizes with the hydrodynamic lift force. By $t/T \approx 0.60$ the foil has started the downstroke motion. Compared to the upstroke motion (0.10 < t/T < 0.15), the LEV size at θ_o = 30° is larger hence the lift force profile in the second half of the flapping cycle is different than the first, although still smaller than the two higher pitching amplitudes. For θ_o = 43° at $t/T \approx 0.60$, LEV size increases considerably as compared to the θ_o = 30° case, while for θ_o = 60°, LEV size and vortex core strength is larger and higher respectively compared to the smaller pitching amplitudes. This leads to considerable increase in hydrodynamic lift force and eventually plunging velocity as seen in Figure 6.11 (c). Good synchronization between lift force and plunging velocity leads to increase in C_{Py} peak values compared to θ_o = 43° and 60°. With augmentation in energy harvesting performance from $C_{P\theta}$ as seen in Figure 6.10 (b) to C_{Py}, a considerable increase in C_P is observed for θ_o = 60° (Figure 6.9) (0.5 < t/T < 0.75).

As the primary LEV in the downstroke motion is shed into the wake, the foil undergoes a secondary stroke reversal, where it pushes down the flow under the foil surfaces and eventually breaking and shedding any remaining small flow structures into the wake. Formation of secondary LEV is not witnessed during the downstroke phase; hence, the lift force decreases once as the primary LEV is shed into the wake. Further, undulations observed in the hydrodynamic lift force profile is due to the formation, breaking and shedding of smaller flow structures on the foil's lower surface. Like the first stroke reversal, no evident flow structures are formed while the foil performs the second stroke reversal, however due to the rapid change in direction due to pitching motion, the lift force direction changes (to upstroke direction) attaining a peak value as seen in Figure 6.11, which increases with increasing pitching amplitude. Augmented by the peak occurring in the $C_{P\theta}$ profile during $0.8 < t/T < 1.0$ in all pitching amplitude cases, contributes towards increased energy harvesting, as observed in C_P profile in Figure 6.9 and eventually leading to a linear increase in C_{Pmean} with increasing pitching amplitude.

6.4 PERFORMANCE COMPARISON WITH THE FLATPLATE

The importance of flow evolution around a hydrofoil in achieving higher performance and kinetics has been noted in earlier studies including Kinsey and Dumas (2008), Peng and Zhu (2009), Ashraf et al. (2011) and Xiao et al. (2012). Also from numerical studies of Kinsey and Dumas (2008) and Ashraf et al. (2011), the shape of the LE of a flapping foil can play an important role in power generation through flapping motion. As sharp L.E. fixes the flow separation point and alters the evolution of the LEV, while different foil sections alter the subsequent progression of the LEV. However, these are important aspects of morphology effect on power generation, synchronization between force/torque and velocity and flow conditions is also a critical factor which determines the energy harvesting performance of a flapping foil. In this section, we will compare the flow evolution, subsequent kinetics and energy harvesting performance of three different hydrofoil profiles. Pivot location for this analysis was fixed at 0.65c, with different pitching amplitudes (30°, 43° and 60°) and free-stream velocities (0.57, 0.65 and 0.78 m/s).

Figure 6.13 shows the variation of C_{Pmean} of flatplate, NACA0006 and elliptical foil with varying pitching amplitude at three different free-stream velocities. From Figure 6.13 (a) we observe that at $\theta_o = 30^o$ C_{Pmean} for all foil shapes remains constant at each free-stream velocity. Both at $U_o = 0.57$ m/s and 0.65 m/s for $\theta_o = 30^o$, mean energy extraction performance for all foil shapes are very close to each other, although force-kinematics profiles of all three foils may vary from each other. Except for elliptical foil at $U_o = 0.57$ m/s where it was not able to perform sustainable flapping motions for energy harvesting hence force-motion data could not be acquired, as discussed earlier in this chapter. Furthermore, with increasing free-stream velocity energy extraction performance for each foil shape decreases, however C_{Pmean} trend line remains the same as seen on the smaller free-stream velocities. As pitching amplitude is increased to $\theta_o = 43^o$, C_{Pmean} values for all foil shapes increase as compared to $\theta_o = 30^o$ especially at $U_o = 0.57$ m/s as can be seen in Figure 6.13 (b). C_{Pmean} for flatplate and elliptical foil in Figure 6.13 (b) at $U_o = 0.57$ m/s are almost at the same level, while C_{Pmean} is higher for NACA 0006 than the other two foil shapes at this free-stream velocity. At $U_o = 0.65$ m/s, C_{Pmean} increases in a linear fashion with elliptical foil being the smallest and NACA0006 foil being the largest in Figure 6.13 (b). C_{Pmean} for elliptical foil is a little smaller than at $\theta_o = 30^o$, while for flatplate it is almost in the same range as for all foil shapes at $\theta_o = 30^o$. C_{Pmean} for NACA0006 in Figure 6.13 (b) is higher than all values exhibited in Figure 6.13 (a). Energy extraction performance decreases with increasing free-stream velocity as seen in Figure 6.13 (b) and C_{Pmean} at $U_o = 0.78$ m/s for all foil shapes is even less than C_{Pmean} values for all free-stream velocities when pitching amplitude is set at $\theta_o = 30^o$ (Figure 6.13 (a)), with the lowest demonstrated by the elliptical foil.

In Figure 6.13 (c) we see some improvement in energy extraction performance of foil shapes for free-stream velocities $U_o = 0.65$ and 0.78 m/s at $\theta_o = 60^o$ as compared to the smaller pitching amplitudes. C_{Pmean} trend for all free-stream velocities look like an inverted 'V' with a very wide base showing that the flatplate energy harvesting performance is better than elliptical and NACA0006 foils at $U_o = 0.65$ m/s as shown in Figure 6.13 (c). At $U_o = 0.57$ m/s, C_{Pmean} for flatplate foil is also better than elliptical and NACA0006 foil, however C_{Pmean} for NACA0006 foil is still close to that of flatplate foil. In the case of NACA0006 foil, it shows good energy harvesting performance at $U_o = 0.78$ m/s than the elliptical and especially the

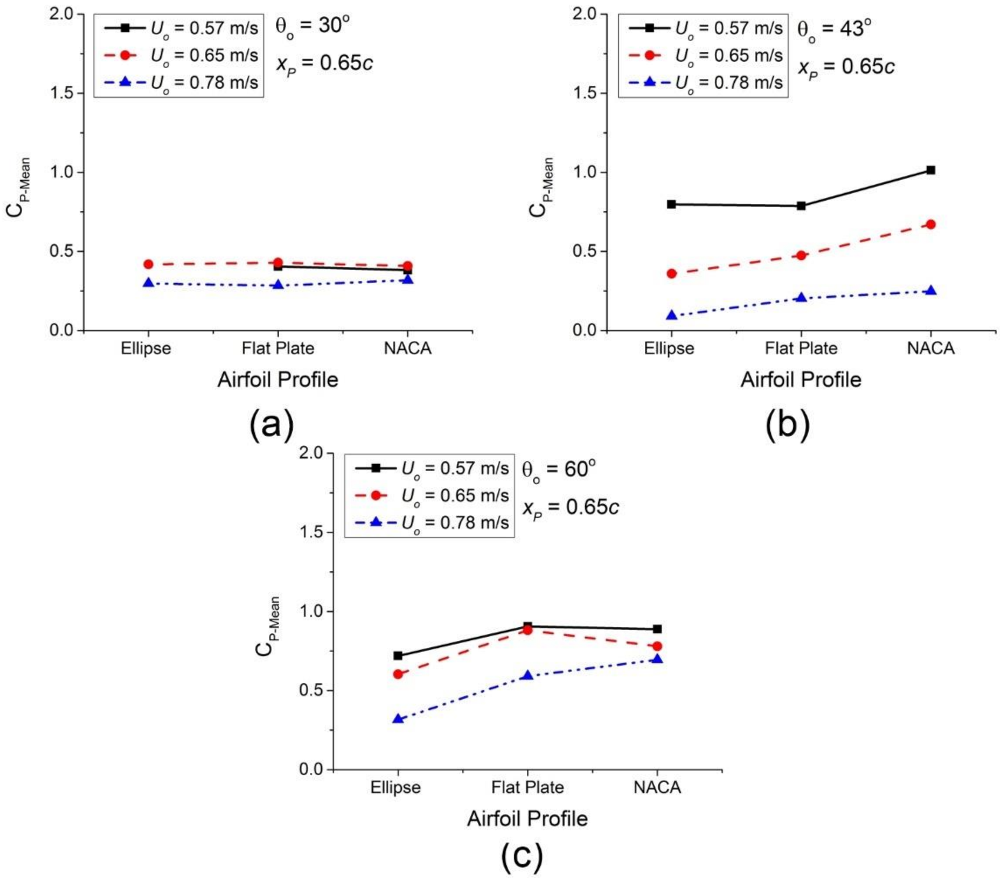

Figure 6.13: C_{Pmean} variation of flat-plate, NACA0006 and elliptical foil at three different frees stream velocities (U_o = 0.57 m/s, 0.65 m/s and 0.78 m/s) at **(a)** θ_o = 30°, **(b)** θ_o = 43° and **(c)** θ_o = 60°.

flatplate foil as compared to at U_o = 0.57 and 0.65m/s as shown in Figure 6.13 (c).

Figure 6.14 shows the phase-averaged time history of force-motion and energy extraction performance data for the three foil shapes for U_o = 0.65 m/s at pitching amplitude 30° and pivot location 0.65c. From the C_P trend of the three foil shapes in Figure 6.14 (a), we observe a similarity in the energy extraction profile during the flapping cycle among the three foil shapes. Two peaks because of stroke reversal process during the flapping cycle, while the additional peaks because of flow separation during the onset of both upstroke and downstroke plunging motion. The C_P profile for all three foil shapes is, as already established in this research, due to the contribution from plunging motion (C_{Py}), while the pitching motion enhances the energy extraction performance during stroke reversal time spans to the total energy extraction through flapping motion.

Figure 6.14 (b) shows the hydrodynamic lift force and plunging velocity time history for all three foil shapes. Plunging velocity profile for flatplate and

NACA0006 foil look similar, where at the onset of the upstroke plunging motion ((0 < t/T < 0.1) there is a huge increase in plunging velocity as observed in Figure 6.14 (b)-II & III compared to the elliptical foil in Figure 6.14 (b)-I. As the foil gets past the mid-stroke, the plunging velocity starts to decrease slowly, where then upon contact of the moment arm with the plunge limiter starts to decelerate rapidly due to the stroke reversal. For all three foils, the plunging velocity comes to zero for short time period as the foil reaches the zero-angle mark, from where it then starts to increase in the downstroke direction, as the foil continues its stroke reversal in the opposite direction (0.35 < t/T < 0.45). During the downstroke motion, the plunging velocity of the flatplate and NACA0006 foil is smaller than the elliptical foil. For the hydrodynamic lift force, the profile is similar during the most part of the upstroke motion for all profile shapes. However, the magnitude of the hydrodynamic lift force for the elliptical foil is higher than the flatplate and NACA0006 foil. Furthermore, for the elliptical and the flatplate foil the time take for the upstroke motion is relatively shorter than its downstroke motion, although for the NACA foil, the upstroke and downstroke motions are relatively symmetric than the elliptical and flatplate foil as seen in Figure 6.14 (b). Synchronization between the hydrodynamic lift force and the plunging velocity for all foil shapes is similar and good, leading to positive energy extraction for almost the whole flapping cycle. The four positive peaks observed in C_P plots in Figure 6.14 (a) for all foil shapes is synonymous to the peaks observed in the foil shapes relative C_{Py} plots in Figure 6.14 (b). This indicates, as already established before, that the maximum contribution towards total energy harvesting by the system is due to the plunging motion. The first peak in C_{Py} (0 < t/T < 0.1) in Figure 6.14 (b) is not only because of the LEV formation and shedding but also due to the good synchronization between the hydrodynamic lift force and plunging velocity. As the foil completes its upstroke motion and undergoes stroke reversal, it causes a surge in hydrodynamic lift force (0.275 < t/T < 0.475) as shown in Figure 6.14 (b) eventually leading to the second peak in C_{Py}. After the end of the stroke reversal, the hydrofoil (for all foil shapes) initiates its downstroke plunging motion, which causes the onset of LEV on the foil's lower surface. As the foil plunges downwards, the LEV grows (according to the set maximum pitching amplitude), travels along the foil's lower surface and sheds into the wake. This causes an increase in hydrodynamic lift force and then a

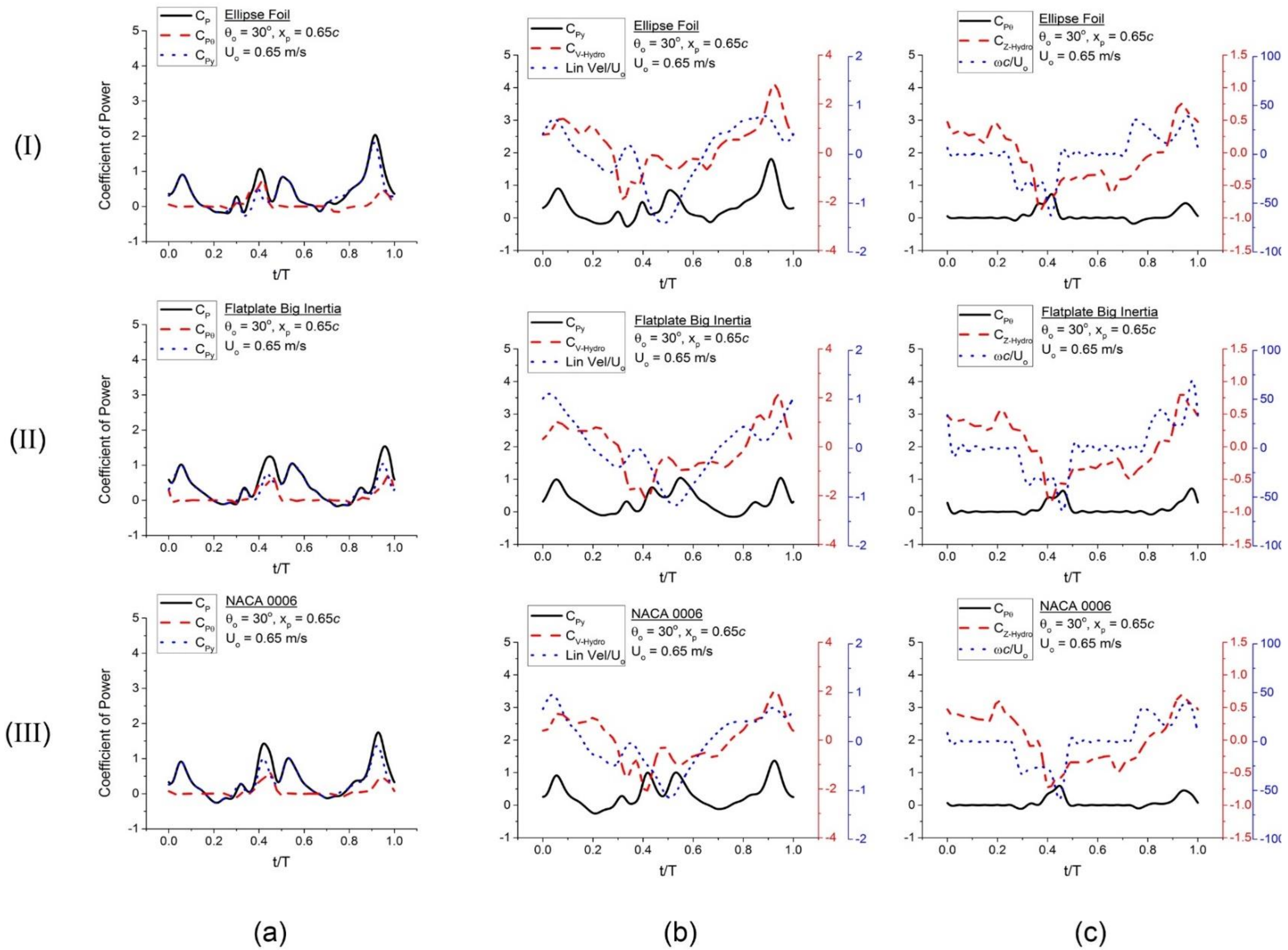

Figure 6.14: Graphs showing phase-averaged **(a)** Coefficient of Power (Total, Plunging and Pitching), **(b)** Coefficient of Power due to Plunging motion with corresponding Coefficient of Hydrodynamic Vertical Force and Linear Velocity and **(c)** Coefficient of Power due to Pitching Motion with corresponding Coefficient of Hydrodynamic Moment and Angular Velocity, for θ_o = 30$^{\mathrm{o}}$ and U_o = 0.65 m/s for foil shapes, **(I)** Elliptical Foil **(II)** Flatplate foil, and **(III)** NACA0006 foil.

sudden decrease due to vortex shedding. Along with good synchronization with the plunging velocity, this leads to the second positive peak in C_{Py} ($0.5 < t/T < 0.65$) for all foil shapes as shown in Figure 6.14 (b). As the foil plunges downwards, the moment arm strikes the plunge limiter initiating the second stroke reversal. This causes the foil to decelerate while undergoing pitching motion, leading to the decrease in plunging velocity as well as hydrodynamic lift force. Since, both parameters are still in synch with each other, C_{Py} does not cross the zero-line mark. Upon the completion of the pitching motion, a surge in hydrodynamic lift force is observed ($0.875 < t/T < 1.0$) with the elliptical foil being comparatively higher than the flatplate and NACA0006 foil. As a result, the last positive peak at the end of the flapping cycle is higher for the elliptical foil followed by NACA0006. The flatplate, although has comparable peak hydrodynamic lift force ($0.875 < t/T < 1.0$), but due to a sudden drop in plunging velocity ($0.83 < t/T < 0.92$) results in a smaller peak in its C_{Py} profile as compared to the elliptical and NACA0006 foil.

For pitching motion contribution in Figure 6.14 (c), hydrodynamic torque profile for all three foil shapes look similar during both upstroke and downstroke motion, while the magnitude of the resulting angular velocity for elliptical and flatplate hydrofoils also look similar. However, for the NACA00006 foil the angular velocity is comparatively a little lower than that of the other two foil shapes. Therefore, the peak values in $C_{P\theta}$ plot for NACA0006 foil is comparatively somewhat smaller than the flatplate and elliptical foil as shown in Figure 6.14 (c). The peak values observed in $C_{P\theta}$ ($0.375 < t/T < 0.475$ & $0.90 < t/T < 1.0$) for all foil shapes in Figure 6.14 (c) is due to the foils undergoing pitching motion and about to complete the stroke reversal process. For the rest of the duration in the flapping cycle, $C_{P\theta}$ remains zero since the foil undergoes plunging motion at the set maximum pitching amplitude ($\theta_o = 30^o$ for this discussion) indicating a non-sinusoidal angular displacement profile demonstrated by the test-rig.

Figure 6.15 shows the phase-averaged C_P plot of elliptical, flatplate and NACA0006 foils at $\theta_o = 60^o$, $x_p = 0.65c$ at $U_o = 0.65$ m/s and test-rig equipped with big inertial blocks ($m_{ib} = 1.35$ kg), where the region on the graphs shaded in red marks the energy expenditure (energy loss from system) area. The average of these C_P profiles is summarized in Figure 6.13 (c), where at $U_o = 0.65$ m/s C_{Pmean} gradually increases from elliptical to flatplate foil and then decreases when foil is

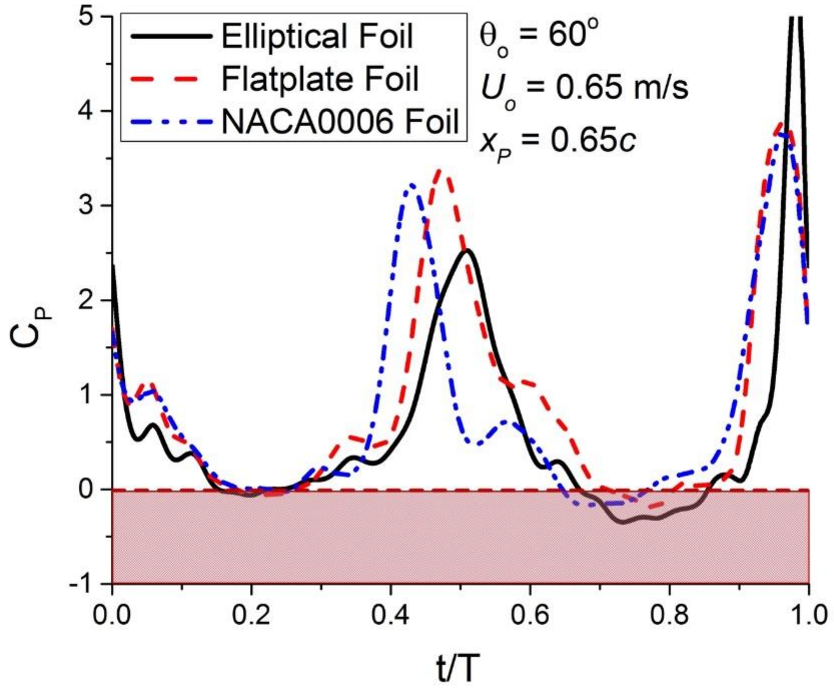

Figure 6.15: Phase-averaged C_P at θ_o =60°, U_o = 0.65 m/s for elliptical, flatplate and NACA0006 foil at pivot location x_p = 0.65c. Red regions marked in red below the zero line indicates the region where the flapping foil starts to expend energy from the system rather than extracting it from the surrounding fluid.

changed to NACA0006 foil. From Figure 6.15 we observe that for all foil shapes, two evident peaks exist during the flapping cycle rather than the four peaks when θ_o = 30° for all foil shapes as shown in Figure 6.14 (a). For the elliptical foil, C_P profile and first peak are comparatively smaller than the other two foil shapes and remains in the red-zone (energy loss from the system) during the downstroke plunging phase (0.675 < t/T < 0.875) till the onset of the second stroke reversal. C_P profiles for the other two foil shapes, are comparable to each other with the first peak for NACA0006 foil a little lower than the flatplate. The width of the first peak for the flatplate foil is wider (0.2 < t/T < 0.6) than that for NACA0006 foil (0.2 < t/T < 0.5), while the second shorter bump which follows this first peak is also higher and wider for the flatplate foil than that of NACA0006 foil. The first peak is because of the stroke reversal, while the shorter bump is due to the foil's downstroke plunging motion which leads to the formation of the LEV on the foil's lower surface. The C_P plots shown in Figure 6.15 are consistent with the C_{Pmean} data shown in Figure 5.13, where the flatplate foil performs better than the elliptical and NACA0006 foils.

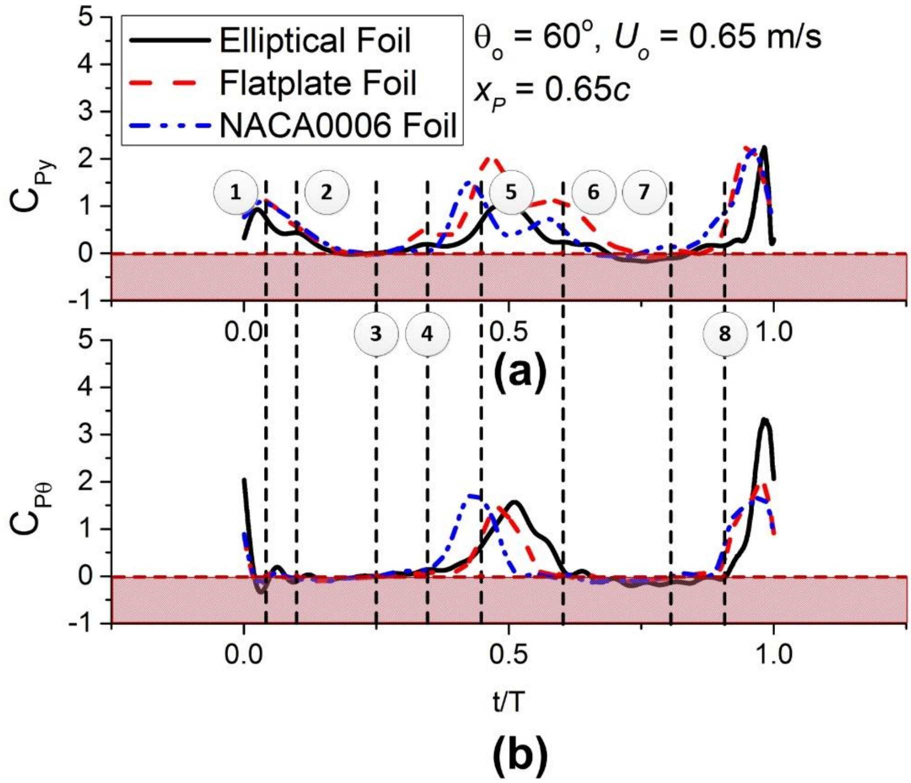

Figure 6.16: Phase-averaged **(a)** C_{Py} and **(b)** $C_{P\theta}$ at U_o = 0.65 m/s, x_p = 0.65c and θ_o = 60º for elliptical, flatplate and NACA0006 foils. Eight-time stamps are marked to correlate to the flow evolution around the NACA0006 foil as shown in Figure 6.18.

Figure 6.16 shows the individual contributions of plunging (C_{Py}) and pitching ($C_{P\theta}$) motions to the total energy extraction for all three foil shapes at U_o = 0.65 m/s, x_p = 0.65c and θ_o = 60º. The plots are also marked with eight different time stamps to correlate the flow behavior (Figure 6.18) around each of the foil shapes with the motion and hydrodynamic force-torque data to ascertain a comparative analysis on its impact on the foils' energy extraction performance. By comparing Figure 6.15 and Figure 6.16 (a), we can observe the plots are synonymous to each other, recognizing an established fact that the total energy extraction is totally dependent on the plunging motion when it comes to the trend during the flapping cycle, while the pitching motion at two distinct points (usually during the end of the stroke reversal) enhances the total energy harvesting performance of the system. From Figure 6.15 we can see that the second peak for the elliptical foil is much higher than that for the flatplate and NACA0006 foils. Although the peak value of C_{Py} for all three foil shapes in Figure 6.16 (a) is the same (but not the peak width which is shorter for the elliptical foil than the flatplate and NACA0006 foils), however due the higher $C_{P\theta}$ (0.925 < t/T < 1.0) for the elliptical foil (Figure 6.16 (b)), it enhances its C_{Py} counterpart resulting in a much higher peak as shown in Figure 6.15. All three foil shapes demonstrate an increase in C_{Py} during the start of the upstroke motion (0 < t/T < 0.15, indicating vortex formation on each of the foil's leading edge). Evidently after $t/T \approx 0.2$, C_{Py} starts to decrease which is due to contact made by the moment arm with the plunge limiter to initiate the stroke reversal. Since, the pitching amplitude is 60^{o} and due to the short plunging distance, the moment arm strikes the plunger limiter early than at 43^{o} and 30^{o}. The secondary peak observed in Figure 6.16 (a) is due to the first stroke reversal process, where its value increases in the following order; elliptical foil, NACA0006 foil and flatplate foil. A secondary bump observed after the second peak in C_{Py} (Figure 6.16 (a)) is evident for flatplate and NACA0006 foils but diminishes in the case of the elliptical foil as the three foils commence their downstroke plunging motion. Eventually, this bump in C_{Py} decreases as the foil plunges downwards until the moment comes in contact with the plunge limiter initiating a secondary stroke reversal. As the foil undergoes a change in direction due to pitching motion, both C_{Py} and $C_{P\theta}$ surge (0.80 < t/T < 1.0), hence the larger peaks in C_P during this time duration as shown in Figure 5.15.

Figure 6.17 shows the hydrodynamic lift force and plunging velocity profile for the three foil shapes at the same kinematic parameters as in Figure 6.15 & 6.16, and Figure 5.18 shows the vorticity plots for the three foil shapes to correlate with their respective force-motion data shown in Figure 6.16 and 6.17. From Figure 6.18 we can observe that at $t/T \approx 0.05$, the onset of LEV formation for the elliptical foil is comparatively a little early than the flatplate and the NACA0006 foil. This indicates that the comparatively shaper leading edge of the elliptical foil as compared to the other foil shapes results in the earlier formation of a strong and larger LEV. As the foils plunge in the upward direction, the larger pitching amplitude allows the LEV to grow and move on the foil's upper surface. In the case of elliptical foil due to it relatively sharper L.E, it allows the LEV to grow more than the flatplate and NACA0006 foil as can be seen at $t/T \approx 0.10$ in Figure 6.18. In Figure 6.17, we can see that as result of the formation of the LEV, the hydrodynamic lift force increases for all three foil shapes. Evidently, good synchronization of the hydrodynamic lift force with the plunging velocity yields in positive energy extraction (0 < t/T < 0.125).

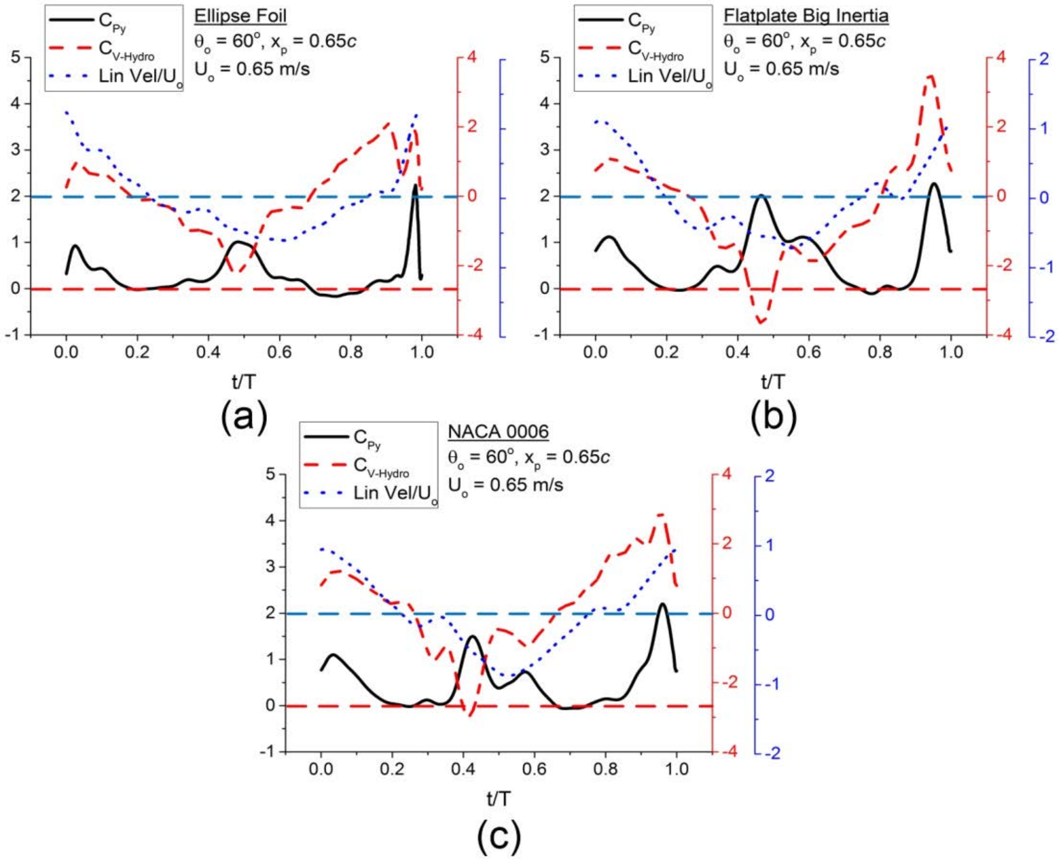

Figure 6.17: Phase-averaged C_{Py}, $C_{V\text{-}hydro}$ and Lin Vel/U_o at x_p = 0.65c, U_o = 0.65 m/s and θ_o = 60º for **(a)** Elliptical foil, **(b)** Flatplate foil and **(c)** NACA0006 foil.

Just before the mid-stroke (plunging motion) after t/T ≈ 0.10, as the foil moves upwards the LEV sheds into the wake. This happens early for the elliptical foil due to the early formation of the LEV and due to this early separation, the hydrodynamic lift force in Figure 6.17 (a) decreases and crosses the zero mark around t/T ≈ 0.13, while for the flatplate foil it is still positive with a gradual decrease until t/T ≈ 0.30. The same is for the NACA0006 foil, however the hydrodynamic lift force crosses the zero-mark earlier than the flatplate foil. Between t/T ≈ 0.10 and t/T ≈ 0.25, as the foil moves further upwards a secondary LEV is formed which almost fully develops in the case of elliptical foil as compared to the flatplate and NACA0006 foils. For the flatplate foil the secondary LEV shatters into two smaller chunks as shown at t/T ≈ 0.25 in Figure 6.18, while the it is fully intact and larger in the case of elliptical foil and for NACA0006 foil, however relatively little smaller than that of the elliptical foil. Furthermore, during this period the foils also initiate their first stroke reversal as a consequence of the moment arm contacting

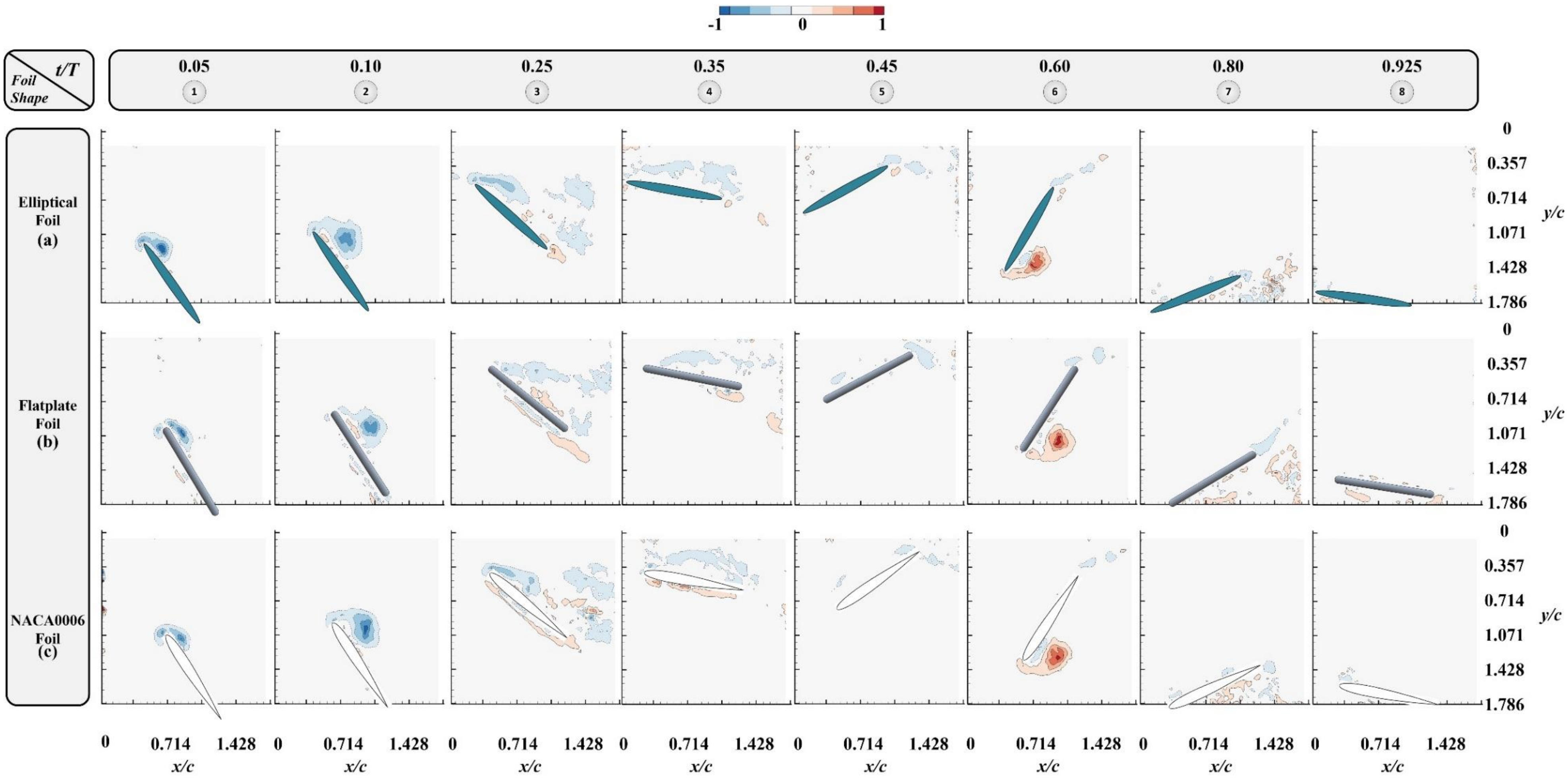

Figure 6.18: Figure showing vorticity contours of **(a)** Elliptical, **(b)** Flatplate and **(c)** NACA0006 hydrofoils at eight different time instants during one flapping cycle with free-stream velocity of U_o = 0.65 m/s and pivot location $x_p = 0.65c$ pitching amplitude $\theta_o = 60^o$. The *x* and *y* scale are dimensionalized with reference to the chord length (c = 0.14 m) of the hydrofoil.

the plunge limiter. Around $t/T \approx 0.35$, the secondary LEV and other small flow structures on the foil's upper surface break down further and start to shed in to the wake causing the hydrodynamic lift force to decrease further. The plunging velocity of the elliptical during the first stroke reversal period is relatively smaller than that of flatplate and NACA0006 foils as shown in Figure 6.17. Although good synchronization between the hydrodynamic lift force and plunging velocity remain, the C_{Py} peak is smaller due to the smaller plunging velocity in the case of the elliptical foil ($0.4 < t/T < 0.575$) (Figure 6.17 (a)). Furthermore, due to stroke reversal the resulting hydrodynamic lift force generated by the elliptical foil is comparatively lower than the NACA0006 foil and the flatplate foil (which has the highest) as shown in Figure 6.17. At $t/T \approx 0.45$, the foils are about to complete the first stroke reversal and during this pitching motion no significant flow structures are observed as seen in Figure 6.18. The surge in hydrodynamic lift force generated around $t/T \approx 0.465$ approximately for all foil shapes indicates that this rapid increase is due to the change in direction of the foil because of pitching motion. As the hydrofoils initiate their downstroke motion, the higher pitching amplitude leads to the formation of a larger separation region on the foil's lower surface. The LEV for the elliptical foil at $t/T \approx 0.60$ is relatively smaller than during upstroke motion and as compared to the NACA0006 and flatplate foil at $t/T \approx 0.60$. However, from Figure 6.18 the core strength of the vortex of the elliptical foil is comparable to the other foil shapes. The comparatively smaller size of the vortex leads to generation of lower hydrodynamic lift force compared to that of the flatplate and NACA0006 foil. The relatively thicker leading edge of the flatplate and the NACA0006 foil keeps the flow structures attached over 40% of the foil's lower surface (Figure 6.18). This results in the stability of the hydrodynamic lift force and its good synchronization with the plunging velocity leading to positive power generation (C_{Py}) during $0.55 < t/T < 0.63$ as shown in Figure 6.17 (b) and (c). However, for the NACA0006 foil the hydrodynamic lift force crosses the zero-mark (decrease in lift force) earlier than the flatplate due to the reduction of thickness from $0.40c$ to the trailing edge. This causes the LEV to convect further away from the foil's surface, hence decrease in lift force.

By $t/T \approx 0.80$ and $t/T \approx 0.925$ the hydrofoils undergo a second stroke reversal process and evidently compared to the upstroke motion, no secondary flow structures were developed after the formation and shedding of the primary LEV during the downstroke motion. Similarly, no flow structures were also formed as the foil performs the pitching motion. Hence, due to the rapid stroke reversal which causes a surge in hydrodynamic lift force and its good synchronization with the plunging velocity results in a positive peak observed in C_{Py} ($0.9 < t/T < 1.0$) for all foil shapes as shown in Figure 6.17.

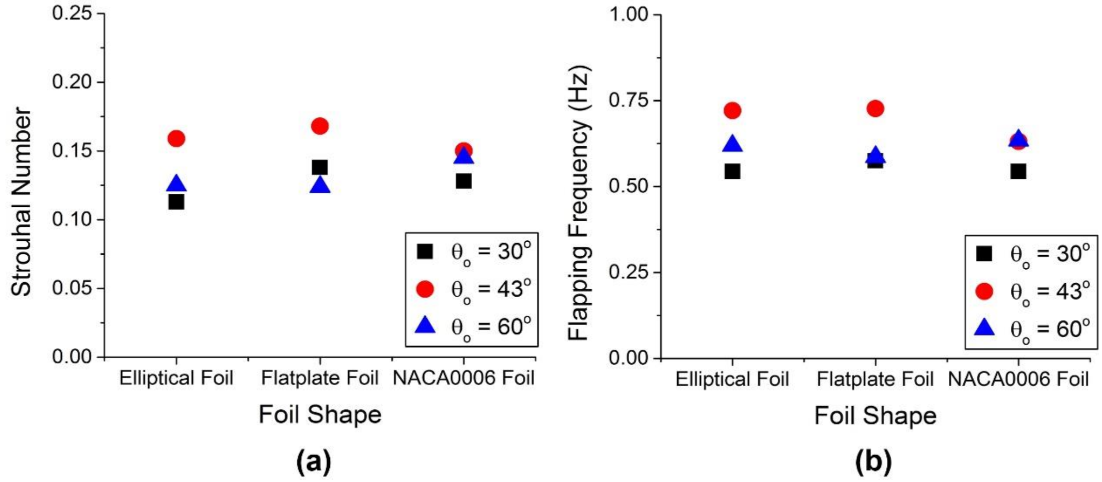

Figure 6.19: Scatter plot showing; (a) Strouhal number (St) and (b) flapping frequency (f – Hz) of different foil shapes at U_o = 0.65 m/s at three different pitching amplitudes (θ_o = 30°, 43° and 60°) and equipped with Big Inertia (m_{ib} = 1.35 kg).

Figure 6.19 shows the Strouhal number (St) and flapping frequency (f) trend for all three different foil shapes at different pitching amplitudes (θ_o = 30°, 43° and 60°) and pivot location $x_p = 0.65c$ and m_{ib} = 1.35 kg. From Table 6.1 it can be seen that A_{piv} for all three foil shapes remain in a narrow band for their respective pitching amplitudes at U_o = 0.65 m/s, leading to the fact that the trend observed in St in Figure 6.19 is attributed to the flapping frequency of the hydrofoil. From Figure 6.19 (a) we observe a comparatively higher St for flatplate foil compared to other foil shapes for each pitching amplitude category, indicating a healthy formation of LEV and its delay in flow separation compared to the other two foil shapes allowing generation of comparatively higher hydrodynamic lift force, and with its subsequent good synchronization with plunging velocity leading towards higher energy extraction performance. Furthermore, this LEV sheds into the wake in the form of von Karman street at the rate of the flapping frequency of the oscillating foil. This hydrodynamic lift force also causes the foil to complete its flapping motions quicker leading to higher flapping frequencies as observed in Figure 6.19 (b).

6.5 REMARKS

A detailed analysis of the effect of different foil shapes on energy extraction performance through passively oscillating motion regime has been investigated in this chapter. Elliptical foil and NACA0006 along with our baseline foil i.e. flatplate foil were used in our experimental campaign to study the morphology effect on energy harvesting performance. The flatplate foil was manufactured using plexi-glass, while the elliptical and NACA0006 foils were 3D printed so that the mass of the foils should remain consistent. Since, the elliptical and NACA0006 foils were not transparent, hence two lasers were used for qualitative and quantitative flow evolution study. The pivot location was fixed at $x_p = 0.65c$ and the test-rig was equipped with Big Inerital blocks ($m_{ib} = 1.35\ kg$) on the translating small aluminium block. The different foils were tested at three different pitching amplitudes ($\theta_o = 30^o$, 43^o and 60^o) and at each pitching amplitude, three different free-stream velocities (U_o = 0.57 m/s, 0.65 m/s and 0.78 m/s). Through our early testing, it was found out that the two foils other than the flatplate were not able to perform sustainable flapping motions for energy harvesting at lower water speeds and pitching amplitude with the Baseline Inertial blocks. Hence, the inertial blocks were switched to the Big Inertial blocks which provided better support, especially during stroke reversals. However, the elliptical foil at $\theta_o = 30^o$ and U_o = 0.57 m/s was still not able to perform sustainable flapping motions, hence no force-motion data could be acquired.

Comparative analysis revealed that the energy extraction performance of our test rig is dependent on the coupled effect of kinematic conditions and foil morphology. With each change in kinematic conditions such as free-stream velocity and pitching amplitude, the three foils behave differently. One trend observed in our experimental campaign and which is common to this sub-study also is that with increasing free-stream velocity, the energy harvesting performance of the system declines. At a lower pitching amplitude ($\theta_o = 30^o$) for each free-stream velocity, no significant improvement in energy harvesting was observed when foil shapes were changed. The only difference which was made was through change in free-stream velocity with C_{Pmean} (= 0.42, 0.43 and 0.41 for elliptical, flatplate and NACA0006 foils respectively) the highest at U_o = 0.65 m/s, with C_{Pmean} values at U_o = 0.57 m/s very close to that of U_o = 0.65 m/s, while the lowest recorded at U_o = 0.78 m/s (= 0.297, 0.284 and 0.31 for elliptical, flatplate and NACA0006 foils respectively). At

θ_o = 43°, we observed a different pattern in C_{Pmean} variation among the different foil shapes. For U_o = 0.65 and 0.78 m/s, C_{Pmean} showed a gradual linear increase as the foil shapes were changed from elliptical to flatplate to NACA0006 foil. While at U_o = 0.57 m/s, the elliptical foil and flatplate foil showed similar performance (C_{Pmean} = 0.797 & 0.787 respectively), while the NACA0006 foil recorded the highest energy extraction performance among all foil shapes and other free-stream velocities (C_{Pmean} = 1.01). However, at θ_o = 60° the flatplate foil at U_o = 0.57 & 0.65 m/s records a better performance than the NACA0006 foil's performance at all free-stream velocities, however NACA0006 outperforms the flatplate and elliptical foil at U_o = 0.78 m/s where the C_{Pmean} increases in a linear fashion.

Qualitatively, for each pitching amplitude and free-stream velocity the energy extraction performance of the flatplate and the NACA0006 foil are still comparable to each other even at higher pitching amplitudes. This may be since the flatplate and NACA0006 foils possess a thicker leading edge which helps to delay flow separation allowing comparatively higher hydrodynamic lift force leading to higher energy extraction performance. Furthermore, at times the uniform thickness of the flatplate and the rounded leading and trailing edge increases the proximity of the LEVs to the surface of the foil. This allows to increase the interactions between the LEVs and the foil's surface, making it favorable for energy extraction. The elliptical foil on the other hand due to its relatively sharper leading and trailing edges causes early separation of vortical structures (at the leading edge), while the trailing edge reduces the interaction of the shedding LEV and the foil surface. Comparatively, the streamlined leading edge of the NACA0006 foil promotes better timing for the formation of the LEV. A summary of important parameters for all cases pertaining to foil shape study is shown in Table 6.1.

Pivot Location (x_p) & Inertia Mass	Foil Type	Water Speed (U_∞)	Pitching Amplitude (θ_o)	P_{mean} (W)	C_{pmean}	η	C_{pymean}	C_{p0mean}	St	f (Hz)	A_{piv} (m)	ω	χ
0.65c & m_{ib} = 1.35 kg	Elliptical Foil	0.57 m/s	30	*No sustainable flapping motion for energy extraction*									
			43	2.066	0.797	37.178	0.563	0.234	0.156	0.634	0.141	3.984	1.665
			60	1.865	0.719	33.562	0.421	0.299	0.110	0.558	0.113	3.503	2.998
		0.65 m/s	30	1.608	0.242	11.296	0.200	0.042	0.113	0.544	0.163	3.418	1.543
			43	1.384	0.360	16.796	0.139	0.221	0.159	0.721	0.144	4.529	1.639
			60	2.177	0.566	26.429	0.257	0.309	0.125	0.619	0.131	3.890	2.662
		0.78 m/s	30	1.970	0.297	13.840	0.232	0.064	0.123	0.627	0.153	3.942	1.443
			43	0.605	0.091	4.247	-0.098	0.189	0.141	0.807	0.136	5.072	1.822
			60	2.097	0.316	14.731	0.053	0.262	0.121	0.697	0.135	4.380	2.729
	Flatplate Foil	0.57 m/s	30	1.051	0.405	18.917	0.316	0.090	0.142	0.505	0.160	3.170	1.259
			43	2.041	0.787	36.728	0.632	0.155	0.170	0.622	0.156	3.908	1.548
			60	2.347	0.905	42.251	0.678	0.227	0.131	0.525	0.143	3.296	2.520
		0.65 m/s	30	1.652	0.430	20.047	0.335	0.095	0.138	0.575	0.156	3.612	1.291
			43	2.052	0.534	24.912	0.298	0.236	0.168	0.727	0.150	4.566	1.568
			60	3.298	0.858	40.035	0.609	0.249	0.124	0.586	0.138	3.679	2.658
		0.78 m/s	30	1.886	0.284	13.250	0.204	0.080	0.129	0.640	0.158	4.024	1.384
			43	1.349	0.203	9.473	0.018	0.185	0.149	0.794	0.146	4.991	1.754
			60	3.922	0.590	27.551	0.367	0.223	0.138	0.693	0.156	4.353	2.415
	NACA0006 Foil	0.57 m/s	30	0.990	0.382	17.813	0.295	0.087	0.118	0.468	0.144	2.939	1.499
			43	2.627	1.013	47.284	0.790	0.224	0.162	0.593	0.156	3.725	1.598
			60	2.301	0.888	41.420	0.632	0.256	0.129	0.551	0.134	3.461	2.526
		0.65 m/s	30	1.566	0.407	19.012	0.336	0.071	0.128	0.544	0.152	3.416	1.399
			43	2.580	0.671	31.316	0.487	0.184	0.150	0.631	0.155	3.965	1.720
			60	2.993	0.778	36.326	0.495	0.283	0.145	0.634	0.149	3.982	2.297
		0.78 m/s	30	2.114	0.318	14.850	0.257	0.061	0.122	0.611	0.155	3.837	1.464
			43	1.647	0.248	11.571	0.091	0.157	0.153	0.741	0.161	4.658	1.696
			60	2.164	0.326	15.198	0.065	0.260	0.148	0.827	0.139	5.198	2.248

Table 6.1: Summary of key parameters for different foil shapes; Elliptical foil, Flatplate foil and NACA0006 foil at three different free-stream velocities (U_o = 0.57, 0.65 and 0.78 m/s) and three different pitching amplitudes (θ_o = 30°, 43° and 60°) at fixed pivot location x_p = 0.65c and inertial mass (m_{ib}) = 1.35 kg.

CHAPTER 7

CONCLUSION & RECOMMENDATIONS

7.1 CONCLUSION

In this thesis we have presented the concept of energy harvesting through flapping motion through a water tunnel experiment. Unlike previous numerical and experimental investigations, a pure passive system was realized where the flapping motions were possible when the test-rig was subjected to incoming free-stream flow. The test-rig designed to realize such flapping motions for energy harvesting did not consist of any elaborate mechanical design to enforce a particular type of flapping motion kinematics or induce phasing between the plunging and pitching motions. The test-rig mimics a 2-DoF flapping motion including pitching and plunging motion, which is only applicable when the hydrofoil is subjected to a suitable hydrodynamic force. The minimum magnitude of this hydrodynamic force is dependent on the free-stream velocity of the incoming water flow; hence the test-rig has a cut-off velocity ($U_{o\text{-}cutoff}$). The cut-off velocity is also dependent on the test-rig configuration where by attaching a rotary encoder to the vertical cantilevered shaft increases the $U_{o\text{-}cutoff}$ value to about 0.50 m/s, while without the sensor the test-rig can start to perform self-sustained flapping motions in the range of $U_{o\text{-}cutoff}$ = 0.37-0.40 m/s.

In this research, two dimensionality was maintained by the addition of endplates on each of the hydrofoil wing tips to reduce end effects, and no power-takeoff system was connected to the test rig hence instead of calculating the "*water-to-wire performance*" which takes into account the mechanical and electrical losses in the system, the "*hydrodynamic power extraction efficiency*" was determined. This was achieved through real-time data acquisition of raw data from three different sensors through a DAQ module and then post-processing them to determine the hydrodynamic power generation performance of the system. For force-torque measurement a six-axis force sensor was used while for angular and linear kinematics a rotary encoder and an accelerometer were used, respectively. All sensors were wired to their respective DAQ modules connected in a common chassis and connected to the computer which was used to acquire the real-time sensor data through an in-house code using LabView software. The code was designed in such a way that the force-motion data acquired from the sensors was synchronized upon acquisition due to the absence of any external trigger since the test-rig is a passive system. The raw data were exhaustively post-processed to determine the energy harvesting performance of the system and collect processed phase-averaged force-motion-power data. For qualitative (LIF) and quantitative (PIV) flow evolution data collection a Dantec Dynamics laser system with a high-speed camera were utilized. The images collected (for LIF) were synchronized with the force-motion data acquired from the sensors, since the camera would initialize to acquire images upon receiving an external TTL signal generated by the same in-house LabView code used for collecting sensor data. The images acquired for quantitative analysis was done separately due to the unavailability of a suitable synchronizer system which could receive the external TTL signal and control the camera through the PIV software (Dynamic Studio).

The test-rig designed realizes a 2-DoF flapping motion, where the pitching motion follows a non-sinusoidal profile while the plunging (translational) motion follows a sinusoidal profile under the influence of the hydrodynamic forces. The pitching amplitude, plunging distance and pivot location can be set which, with added flow conditions can affect the flapping motion kinematics and consequent hydrodynamic force/torque profile and energy extraction performance due to the passive design of the test-rig. The test-rig was also equipped with inertial blocks, which provided the necessary inertial force for performing self-sustained flapping motions, especially during the stroke reversal phase (pitching motion), when the hydrofoil (flatplate) was subjected to the hydrodynamic forces. Three different kinds of inertial mass blocks were selected categorized as; Small Inertial Block (m_{ib} = 0.45 kg), Baseline Inertial block (m_{ib} = 0.90 kg) and Big Inertial block (m_{ib} = 1.35 kg) and tested to see how the test-rig performs its sustainable flapping motions as the mass on its plunging system is changed. The Small Inertial block demonstrated a linear variation in its energy extraction performance when subjected to different kinematic conditions such as free-stream velocity (U_o = 0.57 m/s, 0.65 m/s and 0.78 m/s) and pitching amplitude (θ_o = 30°, 43° and 60°). With the increase in inertial mass, as some kinematic conditions the test-rig performed in an erratic fashion affecting its energy extraction performance, however it did impact the stroke reversal process by letting the foil perform rapid pitching reversals (pitching motion).

Another observation made in our experiments, which will become an established fact for all our cases in our research is the influence of plunging and pitching motions on the total energy extraction performance of the system under different kinematic conditions. In all our analysis we found that the C_P profile (phase-averaged total energy harvesting performance parameter during a flapping cycle) follows its respective C_{Py} profile (phase-averaged energy harvesting through plunging motion performance parameter during a flapping cycle), while the $C_{P\theta}$ (phase-averaged energy harvesting through pitching motion performance parameter during a flapping cycle) would only contribute to total energy extraction during time durations when the hydrofoil was undergoing stroke reversal. Depending on different kinematic conditions, there were instances that the flapping foil would expend energy rather than extract from the fluid. This could be attributed to the synchronization between the hydrodynamic lift force and plunging velocity, where a slight de-synchronization could produce negative C_P during a part of the flapping cycle. However, for all our cases in our experiments the mean energy extraction performance parameter (C_{Pmean}) remained positive indicating energy extraction from water flow.

For the pivot location and pitching amplitude study, the test-rig was equipped with baseline inertial blocks and flatplate was selected as our baseline foil. Three different pitching amplitudes including θ_o = 30°, 43° and 60° were analyzed and three different pivot locations (x_p = 0.60c, 0.70c & 0.80c) subjected to three different free-stream velocities (U_o = 0.57 m/s, 0.65 m/s & 0.78 m/s). For each pitching amplitude, as the pivot location was varied a considerable effect on the flapping motion kinematics and hydrodynamic force was observed. Total stroke reversal time $\Delta T_{SRTOTAL}$ was influenced by change in pivot location, where in each free-stream velocity it decreased with increase in pivot location indicating a quick change in pitching amplitude and more time spent undergoing plunging motion in one flapping cycle. An increase in energy harvesting performance was observed as the pivot location distance from leading edge was increased due to increase in plunging velocity magnitude and high torque (during stroke reversal) leading to increase contribution to C_P by $C_{P\theta}$ during stroke reversal periods. Furthermore, energy extraction performance became more sensitive as the pitching amplitude was increased from θ_o = 30° (gradual increase in C_{Pmean}) to θ_o = 60° (steep increase in C_{Pmean}) at each pivot location. Additionally, it was also observed that a higher pitching amplitude at any given pivot location performs better due to the generation of large forces because of increased separation area leading to the formation and shedding of a large LEV. However, desynchronization between hydrodynamic lift force and plunging velocity due to unsteadiness in the flow around the flapping foil created at large pitching amplitudes and increased pivot location distances led towards lower energy extraction performance.

Morphological effect on energy harvesting through passively actuated flapping motion is a very important factor and has potential for more exploration through an exhaustive experimental campaign. In this research a comparative analysis was demonstrated among three different foil shapes; flatplate foil (baseline foil shape for our research), elliptical foil and NACA0006 foil. The three foils were manufactured in such a way that their total mass was in the same range with each other ($m_{foil} \approx 0.175$ kg) which along with attached small shaft connected below the force sensor was totaled to be about ($M_{foil} \approx 0.20$ kg). An additional laser source was used for both qualitative and quantitative flow evolution analysis, since the elliptical and NACA0006 foil were not made of transparent material. The big inertial block (m_{ib} = 1.35 kg) was installed on to our test-rig since the new foils were having problems to perform sustainable flapping motions for energy extractions at smaller kinematic parameters when equipped with the other two inertial blocks. Comparative analysis revealed that energy extraction performance was dependent on the coupled effect of kinematic conditions and foil morphology. At a lower pitching amplitude (θ_o = 30°) for each free-stream velocity, no significant improvement in energy harvesting was observed when foil shapes were changed. When changed to θ_o = 43°, we observed that at U_o = 0.65 and 0.78 m/s, C_{Pmean} showed a gradual linear increase as the foil shapes were changed from elliptical to flatplate to NACA0006 foil. While at U_o = 0.57 m/s, the elliptical foil and flatplate foil showed similar performance, while the NACA0006 foil recorded the highest energy extraction performance among all foil shapes and other free-stream velocities. At θ_o = 60° the flatplate foil at U_o = 0.57 & 0.65 m/s records a better performance than the NACA0006 foil's performance at all free-stream velocities, however NACA0006 outperforms the flatplate and elliptical foil at U_o = 0.78 m/s where the C_{Pmean} increases in a linear fashion. The lower performance of the elliptical foil at all kinematic conditions compared to the flatplate and NACA0006 foil could to attributed to its relatively sharper leading and trailing edges causes early separation of LEV, while the trailing edge reduces the interaction of the shedding LEV and the foil surface. Comparatively, the flatplate and NACA0006 foils possess a thicker leading edge which helps to delay flow separation allowing comparatively higher hydrodynamic lift force leading to higher energy extraction performance.

7.2 RECOMMENDATIONS FOR FUTURE WORK

The concept of energy harvesting through oscillating foils is a relatively new research field which has sparked a keen interest to the aero/hydro-dynamists. Although in its elementary stage, given a few key groups have studied this concept, mostly numerically, in the past decade or so, there is still room for further insight into this domain. As already seen through the literature survey, most of the studies, numerical and experimental, have focused on active or semi-active flapping profiles for energy harvesting, which gave us the opportunity to explore the neglected energy harvesting through pure passively actuated flapping motion. This research serves as a very good groundwork to fully exploit the area of passively actuated flapping motion for energy extraction through a series of exhaustive experimental regime. The following areas of research are worthwhile to be pursued with the current research as the foundation;

1. The flatplate foil with a semi-circular leading and trailing edge was used as a baseline foil for our experimental investigations. The geometrical aspects were kept constant for all our cases including when compared with the other two foil shapes. Therefore, this presents with an opportunity to tweak the flatplate geometry including its thickness and shape of leading and trailing edges and determine the best possible design configuration with a high energy harvesting performance capacity.
2. A detailed study is required to further analyze the effect of a variety of different foil shapes including elliptical foils, streamlined foils and cambered foils on energy harvesting. Corrugations may also be included to the foil design as a numerical study conducted by Le et al. has proved its advantages. Furthermore, a new nearly N-shape flatplate foil could also be envisaged to study its effect on energy harvesting in open channel water.

3. No study on wing planform shape, numerical or experimental through either active, semi-active or passive actuation for energy harvesting through flapping motion has been recorded in literature. Through our test-rig we can exploit this and perform exhaustive experiments to witness the effect of planform shape and associated 3D effects on energy harvesting through passively flapping motion.
4. Foil/wing flexibility (chord and span-wise) is another important factor which has a deep impact on the kinematics and flow evolution of a flapping foil. Extensive studies involving flexibility in the domain of flapping foil propulsion for MAV applications have been carried out for quite some time. This could be extended to the energy harvesting domain through flapping motions since it carries a lot of potential. Chord-wise and span-wise flexibility experimental study through passively actuated flapping motion will open more opportunities in this area of research and further analysis including optimization can help improve the energy extraction performance of the system.
5. Effect of spacing between individual flapping foil turbines has only been investigated in part, with consideration of multiple foil tandem and parallel investigations. Most of these include where the multiple foils are coupled to each other to enforce a particular spacing phase difference in order to study their effect on energy harvesting performance of the overall system. These systems will be placed as individual entities but in the form of clusters or "turbine farms" where the foils will not be mechanically connected to each other. To explore this concept in detail, an additional identical setup may be manufactured to experimentally investigate this concept. This concept can also include either identical foil types or different foil types with various permutations of different geometric and kinematic parameters to analyze the best possible combination for optimized and highly efficient energy harvesting system.

REFERCENCES

Ashraf, M. A., Young, J., Lai, J. C. S. and Platzer, M. F. (2011). "*Numerical Analysis of an Oscillating-Wing Wind and Hydropower Generator.*" AIAA Journal **49**(7): 1374- 1386.

Baik, Y. S., Bernal, L. P., Granlund, K. and Ol, V. M. (2012). "*Unsteady Force Generation and Vortex Dynamics of Pitching Aerofoils.*" Journal of Fluid Mechanics **709**: 37 to 68.

Baik, Y. S., Rausch, M. J., Bernal, L. P. and Shyy, W. (2010). "*Experimental Study of Governing Parameters in Pitching and Plunging Airfoil at Low Reynolds Number.*" 48th AIAA Aerospace Sciences Meeting Orlando, Florida.

Branke, J., Asafuddoula, M., Bhattacharjee, K. S. and Tapabratta, R. (2014). "*Efficient Use of Partially Converged CFD Simulations in Evolutionary Optimization.*

Brodsky, A. K. (1994). "*The Evolution of Insect Flight.*" (New York, Oxford University Press).

Bryant M, Garcia E. (2011). "*Modeling and testing of a novel aeroelastic flutter energy harvester*." J Vib Acoust, **133**(1): 011010

Bryant, M., Shafer, W. M. and Garcia, E. (2012). "*Power and Efficiency Analysis of a Flapping Wing Wind Energy Harvester*". Proceedings of SPIE.

Bryant M, Gomez JC, Garcia E. (2013), "*Reduced order aerodynamic modeling of flapping wing energy harvesting at low Reynolds number*." AIAA J; **51** (12): 2771–2782

Bryant MJ, Schlichting AD, Garcia E. (2013), "*Toward efficient aeroelastic energy harvesting: device performance comparisons and improvements through synchronized switching*." In: Proceedings of SPIE, vol. 8688. International Society for Optics and Photonics, Bellingham, Washington, p. 868807-1–10, doi: http://dx.doi.org/10.1117/12.2009818.

Campobasso, M. S. and Drofelnik, J. (2012). "*Analysis of An Oscillating Airfoil in A Power-Extraction Regime Based on The Compressible Navier-Stokes Equations with Low-Speed Preconditioning*". ASME Turbo Expo 2012, Cpenhagen, Denmark.

Campobasso, M. S. and Drofelnik, J. (2012). "*Compressible Navier-Stokes Analysis of An Oscillating Wing in A Power-Extraction Regime Using Low-Speed Preconditioning.*" Journal of Computer and Fluids **67**(2012): 26 to 40.

Campobasso, M. S., Piskopakis, A., Drofelnik, J. and Jackson, A. (2013). "*Turbulent Navier-Stokes Analysis of An Osillating Wing in A Power-Extraction Regime Using the Shear Stress Transport Turbulence Model."* Journal of Computer and Fluids **88**(2012): 136 to 155.

Campobasso, M. S., Piskopakis, A. and Yan, M. (2013). "*Analysis of An Oscillating Wing in A Power-Extraction Regime Based on The Compressible Reynolds-Averaged Navier-Stokes Equations and the κ–ω SST Turbulence Model*". ASME Turbo Expo 2013, San Antonio, Texas. USA.

Caracoglia L. (2010), "*Feasibility assessment of a leading-edge-flutter wind power generator*." J Wind Eng Ind Aerodyn; 98 (10–11): 679–686

Chopra MG. (1974) "*Hydromechanics of lunate-tail swimming propulsion*." J Fluid Mech ;64(2):375–391.

Climatewire (2011) "*Offshore turbines keep growing in size - Mammoth wind turbines may soon dot the shallow coastal seas of the world.*" Scientific American.

Davids, S. T. (1999). "*Computational and Experimental Investigation of a Flutter Generator*". M.Sc, Naval Postgraduate School, Monterey.

Deng, J., Caulfield, C. P. and Shao, X. (2014). "*Effect of Aspect Ratio on the Energy of Three-dimensional Flapping Foils.*" Journal of Physics and Fluids **26**: 0431021 to 04310224.

Dickinson, M. H., Lehmann, F.-O. and Sane, S. P. (1999). "*Wing rotation and the aerodynamic basis of insect flight*." Science 284(5422): 1954-1960.

G. Dumas, T. Kinsey (2006). "*Eulerian simulations of oscillating airfoils in power extraction regime.*" Advances in Fluid Mechanics VI, WIT , pp. 245-254

Ellington, C. P. (1984a). "*The aerodynamics of hovering insect flight. I. The quasi-steady analysis*." Philosophical Transactions of the Royal Society of London. Series B **305**, 1–15.

Ellington, C. P., Van den Berg, C., Willmott, A. P., and Thomas, A. L. R. (1996). "*Leading-edge vortices in insect flight*." Nature (London) 384, 626–30.

European Wind Energy Association (2009). Wind Energy - The Facts.

Hisanori, A. and Akira, Y. (2012). "*Experimental Study on a Cascade Flapping Wing Hydroelectric Power Generator.*" Journal of Energy and Power **6**(2012): 1429 to 1436.

Hoke, C., Young, J. and Lai, C. S. J. (2014). "*Time-Varying Flexible Airfoil Shape Effect on Flapping Airfoil Power Extraction.*" AIAA SciTech. National Harbor, Maryland. USA.

Hover, F. S., Haugsdal, O. and Triantafyllou, M. S. (2004). "*Effect of Angle of Attack Profiles in Flapping Foil Propulsion.*" Journal of Fluids and Structures **19**(2004): 37 to 47.

Howell, R., Qin, N., Edwards, J. and Durrani, N. (2010). "*Wind tunnel and numerical study of a small vertical axis wind turbine.*" Renewable Energy **35**(2): 412-422.

Huxham, G. H., Cochard, S. and Patterson, J. (2012). "*Experimental Parametric Investigation of an Oscillating Hydrofoil Tidal Stream Energy Converter*." 18th Australasian Fluid Mechanics Conference. Launceston, Australia.

Isogai, K. and Abiru, H. (2012). "*Study of Multi-Wing Configuration of Elastically Supported Flapping Wing Power Generator.*" Trans. Japan Society Aeronautical and Space Sciences **55**(2): 133 to 142.

Isogai, M., Yamasaki, K., Matsubara, M. and Asaoka, T. (2003). "*Design Study of Elastically Supported Flapping Wing Power Generator.*" International Forum on Aeroelasticity and structural Dynamics, Amsterdam.

Jones, K. D., Davids, S. T. and Platzer, M. F. (1999). "*Oscillating Wing Power Generation*." 3rd ASME/JSME Joint Fluids Engineering Conference.

Jones, K. D., Lindsey, K. and Platzer, M. F. (2003). "*An investigation of the fluid-structure interaction in an oscillating-wing micro-hydropower generator.*" Fluid Structure Interaction II. Southampton, UK, WIT Press. **36:** 73 - 82.

Jones, K. D. and Platzer, M. F. (1997). “*Numerical computation of flapping–wing propulsion and power extraction*.” 35th AIAA Aerospace Sciences Meeting and Exhibit. Nevada, USA.

Kang, C.-k., Aono, H., Baik, Y. S., Bernal, L. P. and Shyy, W. (2013). "*Fluid Dynamics of Pitching and Plunging Flat Plate at Intermediate Reynolds Numbers*." AIAA Journal 51(2).

Katz, J., Weihs, D., (1978). “*Hydrodynamic propulsion by large amplitude oscillation of an airfoil with chordwise flexibility*.” Journal of Fluid Mechanics **88** (3), 485–497.

Kedare S, Date A. (1990), “*Performance characteristics of a reciprocating wind machine*.” J Wind Eng Ind Aerodyn; **34**(1): 1–25

Kerr, D., (2007). “*Marine energy*.” Philosophical Transactions of the Royal Society A 365, 971–992.

Kinsey, T. and Dumas, G. (2008). "*Parametric Study of an Oscillating Airfoil in a Power Extraction Regime.*" AIAA Journal **46**(6): 1318-1330.

Kinsey, T. and Dumas, G. (2010). “*Testing and Analysis of an Oscillating Hydrofoils Turbine Concept.*” Proceedings of ASME 2010 3rd Joint US-European Fluids Engineering Summer Meeting and 8th International Conference on Nanochannels, Microchannels, and Minichannels, Montreal, Canada, ASME.

Kinsey, T. and Dumas, G. (2010). "*Testing and Analysis of an Oscillating Hydrofoils Turbine Concept.*" ASME Conference Proceedings **2010**(49484): 9-22.

Kinsey, T. and Dumas, G. (2012). "*Computational Fluid Dynamics Analysis of a Hydrokinetic Turbine Based on Oscillating Hydrofoils.*" Journal of Fluids Engineering **134**(2): 16.

Kinsey, T. and Dumas, G. (2012). "*Optimal Tandem Configuration for Oscillating-Foils Hydrokinetic Turbine.*" Journal of Fluids Engineering **134**(3): 11.

Kinsey, T. and Dumas, G. (2012). "*Three-Dimensional Effects on an Oscillating-Foil Hydrokinetic Turbine.*" Journal of Fluids Engineering **134**.

Kinsey, T., Dumas, G., Lalande, G., Ruel, J., Mehut, A., Viarouge, P., Lemay, J. and Jean, Y. (2011). "*Prototype testing of a hydrokinetic turbine based on oscillating hydrofoils.*" Renewable Energy **36**(6): 1710 -1718.

Langhamer, O., Haikonen, K., Sundberg, J., (2010). "*Wave power – sustainable energy or environmentally costly? A review with special emphasis on linear wave energy converters*." Renewable and Sustainable Energy Reviews 14, 1329–1335.

Le, Q. T., Ko, H. J. and Byun, D. (2013). "*Morphological Effect of a Scallop Shell on A Flapping-type Tidal Stream Generator.*" BIOINSPIRATION & BIOMIMETICS **8** (2013).

Legrand, C. and Black & Veatch Ltd. (2009). "*Assessment of Tidal Energy Resource*". Marine Renewable Energy Guides. Ed. by The European Marine Energy Centre Ltd. London, UK: BSI.

Lindsey, K. (2002). "*A Feasibility Study of oscillating-Wing Power Generators.*" M.Sc, United States Naval Academy.

Liu, W., Xiao, Q. and Cheng, F. (2013). "*A Bio-Inspired Study on Tidal Energy Extraction with Flexible Flapping Wings.*" BIOINSPIRATION & BIOMIMETICS **8**

Liu, W., Xiao, Q. and Zhu, Q., (2016) "*Passive Flexibility Effect on Oscillating Foil Energy Harvester*," AIAA Journal, Vol. **54**, No. 4, pp. 1172-1187

Massoud, H., Alexeev, A., (2010) "*Resonance of flexible flapping wings at low Reynolds number*." Physical Review E **81**, 056304.

McKinney, W. and DeLaurier, J. (1981). "*The Wingmill: An Oscillating-Wing Windmill.*" Journal of Energy **5**.

Michelin, S., Stefan, G., Llewellyn, S., (2009). "*Resonance and propulsion performance of a heaving flexible wing*." Physics of Fluids **21**, 071902

Mueller, T. J. and DeLaurier, J. D. (2003). "*Aerodynamics of small vehicles*." Annual. Rev. Fluid Mech. 35: 89-111.

Peng, Z. and Zhu, Q. (2009). "*Energy harvesting through flow-induced oscillations of a foil.*" Physics of Fluids **21**(12): 123602-123601 to 123609.

Platzer, M. F., and Sarigul-Klijn, N., "*A Novel Approach to Extract Power from Free Flowing Water and High Altitude Jet Streams*," Proceedings of the 3rd International Conference on ASME Energy Sustainability, Vol. 1, San Francisco, CA, 2009, pp. 493–499.

Platzer, F. M., Ashraf, M. A., Young, J. and Lai, C. S. J. (2009). "*Development of a New Oscillating-Wing Wind and Hydropower Generator*." 47th AIAA Aerospace Sciences Meeting. Orlando, Florida**:** 1-13.

Platzer, F. M., Ashraf, M. A., Young, J. and Lai, C. S. J. (2010). "*Extracting Power in Jet Streams: Pushing the Performance of Flapping Wing Technology.*" 27th International Congress of the Aeronautical Sciences (ICAS 2010). Nice, France.

Platzer, F. M., Sarigul-Klijn, N., Young, J., Ashraf, A. M. and Lai, C. S. J. (2014). "*Renewable Hydrogen Production Using Sailing Ships.*" Journal of Energy Resources Technology **136**.

Platzer, F. M., Young, J. and Lai, C. S. J. (2008). "*Flapping-Wing Technology: The Potential for Air Vehicle Propulsion and Airborne Power Generation.*" 26th International Congress of the Aeronautical Sciences (ICAS 2008). Anchorage, Alaska**:** 1-10.

Platzer, M. F. and Bradley, R. A. (2009). "*Oscillating-wing power generator with flow induced pitch-plunge phasing*." I. C. A. D. F. U. C. U. Patent.

Prater, R. and Lian, Y. (2012). "*Aerodynamic Response of Stationary and Flapping Wings in Oscillatory Low Reynolds Number Flows*." 50th AIAA Conference. Nashville, Tennessee.

Ragheb, M. and Ragheb, A. M. (2011). "*Wind Turbines Theory - The Betz Equation and Optimal Rotor Tip Speed Ratio, Fundamental and Advanced Topics in Wind Power."* InTech.

Semler, C. S., "*Experimental Investigation of an Oscillating Flow Generator*," MSc Thesis, U.S. Naval Postgraduate School, Monterey,CA, 2010

Shimizu, E., Isogai, K. and Obayashi, S. (2008). "*Multi objective Design Study of a Flapping Wing Power Generator.*" Journal of Fluids Engineering **130**.

Simpson B.J., Hover, F.S., Triantafyllou, M.S., (2008a). “*Experiments in direct energy extraction through flapping foils*.” In: Proceedings of the Eighteenth International Offshore and Polar Engineering Conference. July 6–11, 2008, Canada.

Simpson, B.J., Licht, S., Hover, F.S., Triantafyllou, M.S., (2008b). “*Energy extraction through flapping foils*.” In: Proceedings of 27th International Conference on Offshore Mechanics and Arctic Engineering, OMAE-2008-58043.

Shyy, W. and Liu, H. (2007). "*Flapping Wings and Aerodynamic Lift: The Role of Leading Edge Vortices.*" AIAA Journal Aerospace Letters **45**(12).

Triantafyllou, M.S., Techet, A.H., Hover, F.S., (2004). “*Review of experimental work in biomimetic foils*.” IEEE Journal of Ocean Engineering 29, 585–594.

Usoh, C. O., Young, J., Lai, C. S. J. and Ashraf, A. M. (2014). “*Effective Angle of Attack Control of a Flat Plate Flapping-foil Turbine*.” 32nd AIAA Applied Aerodynamics Conference. Atlanta, USA.

Usoh, C. O., Young, J., Lai, J. C. S. and Ashraf, M. A. (2012). “*Numerical Analysis of a Non-Profiled Plate for Flapping Wing Turbines.*” Proceedings of the18th Australasian Fluid Mechanics Conference AFMC., Launceston, Australia.

Westwood, A., (2004). “*Ocean power wave and tidal energy review.*” Refocus 5, 50–55.

Wen, X., Tang, Hui., and Duan, Fei., (2015). “*Vortex dynamics of in-line twin synthetic jets in laminar boundary layer*.” Physics of Fluids **27**, 083601.

Willert. C.E., and Gharib. M., (1991). “*Digital particle image velocimetry.*” Experiments in Fluids **10**, 181-193

Wu, J., Qiu, L. Y., Shu, C. and Zhao, N. (2014). "*Pitching-motion-activated flapping foil near solid walls for power extraction: A numerical investigation.*" Journal of Physics and Fluids **26**: 0836011 to 08360118.

Xiao, Q., Liao, W. and Dou, H.-S. (2010). "*Enhancement on Propulsion Performance: Modifying Angle of Attack Profile.*" Modern Physics Letters B **24**(13).

Xiao, Q., Liao, W., Yang, S. and Peng, Y. (2012). "*How motion trajectory affects energy extraction performance of a biomimic energy generator with an oscillating foil.*" Renewable Energy **37**(1): 61-75.

Xiao, Q., and Zhu, Qiang. (2014). "*A review on flow energy harvesters based on flapping foils.*" Journal of Fluids and Structures **46**: 174-191.

Yin, B., Luo, H., (2010). "*Effect of wing inertia on hovering performance of flexible flapping wings*." Physics of Fluids **22**, 111902.

Young, J., Ashraf, M. A., Lai, J. C. S. and Platzer, M. F. (2010). "*Numerical Simulation of Flow-Driven Flapping-Wing Turbines for Wind and Water Power Generation.*" 17th Australasian Fluid Mechanics Conference. Auckland, New Zealand, 5-9 December**:** 1-4.

Young, J., Ashraf, M. A., Lai, J. C. S. and Platzer, M. F. (2013). "*Numerical Simulation of Fully Passive Flapping Foil Power Generation.*" AIAA Journal **51**(11): 2727 - 2739.

Zhu, Q. (2011). "*Optimal frequency for flow energy harvesting of a flapping foil.*" Journal of Fluid Mechanics **675**: 495-517.

Zhu, Q. (2012). "*Energy Harvesting by a Purely Passive Flapping Foil from Shear Flows.*" Journal of Fluids and Structures **34**.

Zhu, Q., Haase, M. and Wu, H. C. (2009). "*Modeling the Capacity of a Novel Flow-energy Harvester.*" Applied Mathematical Modelling **33**: 2207 - 2217.

Zhu, Q. and Peng, Z. (2009). "*Mode coupling and flow energy harvesting by a flapping foil.*" Physics of Fluids **21**(3): 033601-033601 to 033610.